博士論文

Reusable Rocket Engine Thrust Chamber Life Extension Analysis

（再使用ロケットエンジン燃焼室の寿命延長に関する考察）

リチャードソン　マシュー　ポール

Matthew Paul Richardson

Acknowledgements

This project would not have been possible without the support and confidence of my supervising professors. Professor Yoshifumi Inatani (Institute of Space and Astronautical Science and The University of Tokyo) accepted a not-inconsequential risk in taking me on as a graduate student in his lab in September, 2016. Had he not taken that chance; I would not be in the position I am today. I also find myself indebted to Associate Professor Hiroyuki Ogawa (Institute of Space and Astronautical Science and The University of Tokyo), whose willingness to adopt me after Professor Inatani's retirement saved me from graduate student purgatory. I am honoured to simultaneously be Professor Inatani's last doctoral student, and Associate Professor Ogawa's first. I would also like to thank Associate Professor Hiroaki Kobayashi (Institute of Space and Astronautical Science and The Graduate University for Advanced Studies), for taking a keen interest in my work, and providing invaluable data, advice and support.

I'd like to extend my gratitude to the members of my review committee: Associate Professor Toshiya Kimura (Japan Aerospace Exploration Agency), Associate Professor Takehiro Himeno (The University of Tokyo) and Associate Professor Tomohiro Yokozeki (The University of Tokyo). I appreciate your time, consideration and feedback. In particular, I would like to acknowledge Associate Professor Yokozeki for standing in for my official supervisor at the formal department meeting in August, 2019. Thanks also to Yuka Yoneda (Institute of Space and Astronautical Science), Yukimi Umeda (The University of Tokyo) and Rika Sakai (The University of Tokyo) for always helping me in so many ways.

I acknowledge the School of Engineering at the University of Tokyo, the Japan Aerospace Exploration Agency, the Japanese Rocket Society, the Secure World Foundation, the Japan Society of the Promotion of Science, the Japan Society for Aeronautical and Space Sciences and the Institute of Electronics, Information and Communication Engineers for their support of this project or other opportunities I have pursued as a graduate student.

Thanks to my Sempai, Danielle Delatte, for being the "canary in the coal mine" – you helped me avoid more pitfalls than I care to remember. Thanks to my extended family, in particular my mother, father, mother in-law and father in-law for your emotional and material support. Finally, I have boundless gratitude for my wife, Kana. I can never fully repay you for the sacrifices you've made over the past three years. Your support, wisdom and patience have been endless, and I could not have done this without you.

Abstract

Extending the life of thrust chambers is considered crucial to improving the reusability of RLVs. Since the mid-1970's many studies have focused on analysing, testing and extending thrust chamber life. Many concepts and solutions for extending thrust chamber life have been proposed in the decades since. However, these concepts and improvements tend to focus on the design of the thrust chamber: using better materials, developing better structures, and so on. It is also important to consider the operating conditions to which the thrust chamber is exposed.

The aim of this study is to identify which operating conditions affect thrust chamber life and engine performance, and how these operating conditions have an effect. The reusable rocket engine developed at ISAS/JAXA is used as a case study to investigate this problem. A preliminary analysis of all possible variables which could affect thrust chamber life or engine performance was undertaken. Through a logical process of elimination and a sensitivity analysis, five variables were identified as potentially having an effect on either engine performance, thrust chamber life, or both. These variables are cooling channel pressure, cooling channel flow rate, mixture ratio, propellant flow rate and combustion pressure. It was established that combustion pressure and propellant flow rate are intrinsically coupled. Thus, they were treated as a single variable.

To investigate the effects of these operating conditions in detail, a model was developed to simulate engine performance and thrust chamber life. The engine plant model comprises CFD models for the thrust chamber and cooling channels, and simple analytical models for all other components. A structural model for the thrust chamber wall was sourced from a NASA study. The structural model accounts for three failure modes: plastic instability, low-cycle fatigue and creep deformation. These models were integrated together and used to analyse the effects of varying the above-mentioned operating conditions individually. The models were also used to determine the limits of engine operation.

The results of this analysis indicate that coolant pressure has only a marginal effect on plastic instability & creep deformation, and no significant effect on low-cycle fatigue. Coolant flow rate has similar negligible effects, with the notable exception of its effect on maximum wall temperature. If coolant flow rate is significantly reduced, the maximum wall temperature may increase above the creep threshold for the thrust chamber wall material. This in turn dramatically increases plastic deformation and reduces thrust chamber life. Both mixture ratio and combustion pressure were found to be effective methods of reducing heat flux into the thrust chamber wall, thereby reducing thermal loads and extending life. Such improvements usually lead to losses in engine performance, however. For

example, by reducing propellant flow rate, it was assessed that a 50% increase in thrust chamber fatigue life could be achieved. However, this would also reduce engine thrust by 16%, and specific impulse by 3%.

An optimization of the above-mentioned operating condition variables was conducted, to improve thrust chamber life as much as possible without sacrificing engine performance. This optimization determined that life could be extended by 18.3–26.6% (depending on the failure mode being considered) without any loss in thrust or specific impulse. A sensitivity analysis was conducted on these results by relaxing the specific impulse requirement. By relaxing the specific impulse requirement by 3.6%, thrust chamber life could be extended by 24.3–38.5% (depending on the failure mode being considered) over the baseline value.

The key findings of this study include the importance of finding the "critical failure point" in the thrust chamber, the effectiveness of regenerative cooling for thrust chamber life extension, the effect of changing mixture ratio on gas properties, temperature and wall heat transfer, and the trade-off between mixture ratio and propellant flow rate in terms of both engine performance and thrust chamber life. Generally speaking, some of the qualitative results of this study can inform future reusable liquid rocket engine thrust chamber design. Specifically, key findings related to the location of the critical failure point, the effect of mixture ratio on heat transfer, and the trade-off between mixture ratio and combustion pressure (in terms of thrust chamber life and engine performance) are applicable to other engine designs. Future work will focus on improving the models developed for this project, investigating critical failure point location in more detail, quantifying the effects of mixture ratio on thrust chamber heat transfer for a variety of propellant types, and investigating previously-proposed design improvements for reusable rocket engine thrust chambers.

Contents

List of Tables

List of Figures

Nomenclature

Abbreviations

AIAA - American Institute of Aeronautics and Astronautics

CEA   - Chemical Equilibrium with Applications

CFD   - Computational Fluid Dynamics

Cr   - Chromium

Cu   - Copper

ELV   - Expendable Launch Vehicle

FEM   - Finite Element Method

FTP   - Fuel Turbopump

GH_2 - Gaseous Hydrogen

ISAS   - Institute of Space and Astronautical Science

LH_2 - Liquid Hydrogen

LOx   - Liquid Oxygen

JAXA - Japan Aerospace Exploration Agency

MFVT - Main Fuel Valve (Throttling)

MRCV- Mixture Ratio Control Valve

NASA - National Aeronautics and Space Administration

NIST   - National Institute of Standards and Technology

OFHC - Oxygen-Free High-Conductivity

OMC   - Okegawa Mold Copper

OTP   - Oxidizer Turbopump

RLV   - Reusable Launch Vehicle

RNG   - Renormalization Group

RVT   - Reusable Vehicle Testing

SSME - Space Shuttle Main Engine

TCV   - Thrust Control Valve

UDF   - User-Defined Function

VTVL - Vertical Take-off/Vertical Landing

Zr   - Zirconium

Alphanumeric Symbols

a - Inverse effective Prandtl number

A - Area

$\bar{A}$ - Thrust chamber wall temperature differential constant

B - Norton law constant

c - Specific heat capacity

C - Norton creep law exponent

D - Diameter

E - Modulus of elasticity

f - Normalized force

F - Force

$\bar{F}(C)$ - Creep exponent function

g - Standard Gravity (9.087 m/s^2)

G - Turbulence generation

h - Specific enthalpy

H - Thrust chamber wall ligament half-thickness

htc - Heat transfer coefficient

i - Number of injectors

I - Impulse

k - Turbulent kinetic energy

K - Curvature

l - Thrust chamber wall ligament width

m - Normalized moment

$\dot{m}$ - Mass Flow Rate

M - Moment

Ma - Mach Number

MR - Mixture Ratio

n - Strain hardening parameter

N - Number of combustion cycles

p - Pressure

Pr - Prandtl number

Q - Volumetric flow rate

r - Radius

R - Gas Constant

$\mathcal{R}$ - RNG Term

Re - Reynolds number

s - Specific entropy

S - Material Strength

t - Time

T - Temperature

u - Velocity

U - Speed

v - Beam deflection

V - Specific molar volume

w - Thrust chamber wall rib thickness

$\dot{W}$ - Shaft power

x - Thrust chamber hoop (tangential) direction

y - Thrust chamber axial direction

z - Thrust chamber radial direction

Greek Symbols

α - Coefficient of thermal expansion

γ - Ratio of specific heats

δ - Thrust chamber wall ligament inelastic deflection

ΔH - Pump pressure head

Δp - Differential pressure load

ΔT - Temperature differential

$\Delta \dot{W}$ - Shaft power balance

$\Delta \epsilon$ - Strain range

$\Delta \sigma$ - Relaxation stress

ε - Turbulence dissipation rate

ϵ - Strain

$\bar{\epsilon}$ - Total strain range

η - Efficiency

κ - Thermal conductivity

μ - Dynamic viscosity

ν - Poisson's ratio

ρ - Density

σ - Stress

τ - Thrust chamber wall ligament thickness

ϕ - Correction factor

ψ - Acentric factor

ω - Rotational Speed

Subscripts & Superscripts

a - Atmospheric conditions

avg - Average

be - Bending

bl - Boundary layer

c - Critical

C - Combustion

CC - Cooling Channel

$CC1$ - Cooling Channel Inlet

$CC2$ - Cooling Channel Outlet

cf - Coolant film

cr - Creep

$curv$ - Curvature

E - Exhaust Nozzle Exit

eff - Effective

ET	- Engine total	$MFVT1$	- Main Fuel Valve (Throttling) Inlet
EV	- Exhaust (bleed) valve	$MRCV1$	- Mixture Ratio Control Valve Inlet
f	- Fatigue	min	- Minimum
F	- Failure	$M1$	- Mixer Inlets
FI	- Fuel Injector	$M1G$	- Mixer Inlet (GH$_2$ side)
FP	- Fuel Pump	$M1L$	- Mixer Inlet (LH$_2$ side)
FPL	- Fuel Pump Leakage	$M2$	- Mixer Outlet
$FP1$	- Fuel Pump Inlet	l	- Thrust chamber wall ligament
$FP2$	- Fuel Pump Outlet	LOW	- Low point
FT	- Fuel Turbine	$l1$	- Thrust chamber wall ligament, thrust chamber side
FTP	- Fuel Turbopump		
$FT1$	- Fuel Turbine Inlet	$l2$	- Thrust chamber wall ligament, cooling channel side
$FT2$	- Fuel Turbine Outlet		
$HIGH$	- High point	OI	- Oxidizer Injector
ho	- Hoop	OP	- Oxidizer Pump
hyd	- Hydraulic	$OP1$	- Oxidizer Pump Inlet
i	- Free variable (Einstein notation)	$OP2$	- Oxidizer Pump Outlet
in	- Initial	OT	- Oxidizer Turbine
INT	- Interpolated point	OTP	- Oxidizer Turbopump
j	- Free variable (Einstein notation)	$OT1$	- Oxidizer Turbine Inlet
k	- Turbulent kinetic energy	$OT2$	- Oxidizer Turbine Outlet
max	- Maximum	P	- Constant-pressure
$MFVTB$	- Main Fuel Valve (Throttling) Bypass	PI	- Plastic Instability
		r	- Rupture
		ref	- Reference

ri - Rib

s - Isentropic

sh - Shear

SH - Strain Hardening

SP - Specific

SS - Steady State

T - Thrust

TC - Thrust Chamber (Combustion)

$TCVB$ - Thrust Control Valve Bypass

$TCV1$ - Thrust Control Valve Inlet

Th - Thermal

tot - Total

U - Ultimate (tensile)

w - Thrust chamber wall

$w1$ - Thrust chamber wall, ligament side

$w2$ - Thrust chamber wall, close-out wall side

x - Thrust chamber hoop (tangential) direction

y - Thrust chamber axial direction

Y - Yield

z - Thrust chamber radial direction

0 - Stagnation point

$*$ - Exhaust Nozzle Throat

ε - Turbulence dissipation rate

1.   Introduction

In this chapter, relevant background information and the motivation for this research project are discussed. Section 1.1 provides a brief background and historical context of Reusable Launch Vehicle (RLV) development. Section 1.2 introduces the issues of maintenance, overhaul and service life, and how they impact RLV operations, with a particular focus on liquid rocket engines. These engines are compared to their aviation counterparts (gas turbines), to highlight the differences in service life and operating conditions.

1.1   Background

RLVs have long been considered crucial for reducing space transportation costs and removing barriers to space access. A traditional Expendable Launch Vehicle (ELV) business model requires all costs to be recovered in a single flight. On the other hand, RLVs can be recovered and reused a number of times. This allows manufacturing costs to be amortized over multiple flights. Such a change could reduce space transportation costs by an order of magnitude[1, 2].

Concepts and studies for RLVs date back to the late 1950's[3], but the first operational RLV was the Space Transportation System (colloquially known as the "Space Shuttle", shown in Figure 1-1(a)), which was operated by the United States National Aeronautics and Space Administration (NASA). The Space Shuttle was a partially-reusable two-stage-to-orbit launch vehicle capable of transporting both cargo and crew. A fleet of five Space Shuttles were built, which completed a combined total of 135 missions from 1981 until 2011[4]. Despite the promise of RLVs as a low-cost, reliable space transportation solution, the Space Shuttle increased costs and had a high failure rate. The average cost of a Space Shuttle flight was estimated to be $1.5 billion in 2011 USD at the conclusion of the program[5]. Additionally, the Space Shuttle suffered two catastrophic mission failures in its lifetime, which resulted in both fatalities and hull losses[4]. This represents a failure rate of almost 1.5%. The cost, complexity and time required for maintenance, repair and overhaul outweighed any of the Space Shuttle's reusability benefits.

The SpaceX Falcon 9, shown in Figure 1-1(b), followed the Space Shuttle as the second partial RLV to enter into service. Like the Space Shuttle, the Falcon 9 is a partially-reusable two-stage-to-orbit launch vehicle. Unlike the NASA-operated Space Shuttle however, Falcon 9 is a commercial launch vehicle. The Falcon 9 first flew in 2010, and initially operated as an ELV[6]. the first "re-flight" of a reusable Falcon 9 booster occurred in March 2017[2]. Since then reusable boosters have been used to launch both Falcon 9 and larger Falcon Heavy rockets at reduced costs. Other commercial launch

providers have begun focusing on RLV development, such as Blue Origin and United Launch
Alliance[2, 6]. Despite the early setbacks of the Space Shuttle, the future of the space transportation
industry seems to be trending towards the development and operation of RLVs.

(a)   *(b)*
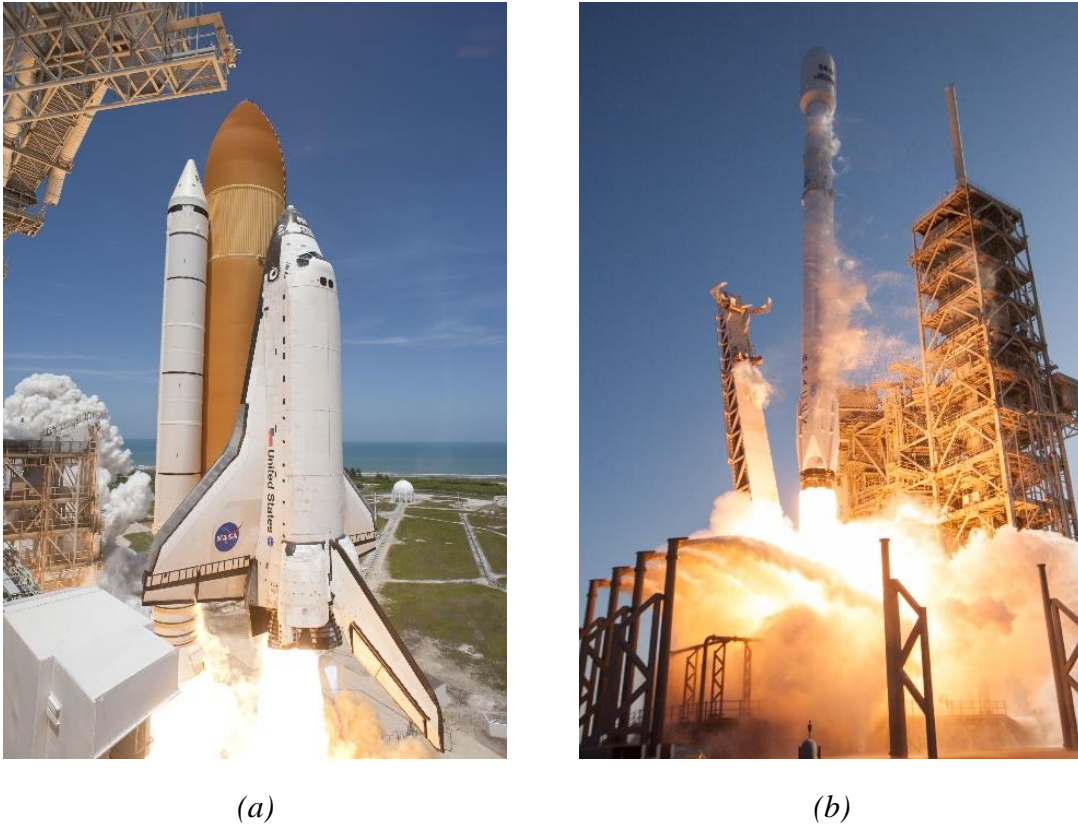
Figure 1-1: Partial RLVs – (a) NASA Space Shuttle and (b) SpaceX Falcon 9[7, 8]

1.2   Motivation

RLVs offer the potential to change the entire culture of the launch industry, not only through
lower costs, but streamlined, simplified launch operations, fast turnaround and increased launch
availability. However, such a shift would necessitate "aircraft-type operations"[1], wherein the space
transportation industry would emulate the high levels of reliability, safety and operational efficiency
which have been achieved in the air transportation industry. A key area in which RLV operators should
seek to achieve aircraft-like operations is in maintenance, repair and overhaul. Complicated and time-
consuming maintenance is often cited as a reason for the Space Shuttle's high cost and low flight
frequency[9].

To minimize the cost of maintenance and overhaul of RLVs, it is logical to focus on the most
expensive subsystems and components, and those which are most prone to failure. Liquid rocket
engines are typically the most expensive individual subsystems in a launch vehicle. For example,
considering the Atlas launch vehicle, engines represent more than 50% of the total cost of the first

stage, and more than 25% of the second stage cost[3]. Multiple studies have identified thrust chambers (alongside turbopump bearings, seals and turbine blades) as components which limit the life of liquid rocket engines[10, 11]. If the useful life of a thrust chamber could be extended, then the maintenance, repair and overhaul requirements of the engine could be reduced. Thus, extending the life of liquid rocket engine thrust chambers could be an effective method for improving the reusability of liquid rocket engines, and allowing RLVs to achieve aircraft-type operations.

For a variety of reasons, it is difficult to directly compare the function and operation of liquid rocket engines and the gas turbine engines which are typically used in commercial aircraft. However, in considering how an RLV might achieve aircraft-type operations, it is useful to compare the state of the art in reusable liquid rocket engines to their aircraft counterparts (gas turbines). Decades of high-volume operational experience in commercial air transport has aided in the refinement of gas turbine technology, and critical components in modern gas turbines can be expected to have a useful life of approximately 15,000 – 30,000 flight cycles[12]. On the other hand, an expendable rocket engine is typically designed to a "Four Mission Duty Cycle" (4-MDC) standard, meaning the design life is effectively four flights[13]. The Space Shuttle's RS-25 liquid rocket engines improved on the expendable standard, and had a useful life of 55 flights[14]. SpaceX is forecasting a life of 100 flight cycles for the reusable Merlin engines used in the Falcon 9 booster[15]. Likewise, the Japan Aerospace Exploration Agency (JAXA) has developed a reusable rocket engine with a 100-flight design life requirement[16]. Despite these recent advances, state of the art for life in liquid rocket engines is still orders of magnitude lower than their gas turbine counterparts.

In a liquid rocket engine, the thrust chamber is used to mix and combust propellants, and accelerate the resulting product gasses to exhaust velocity to generate thrust. In a gas turbine engine, components such as the combustor, exhaust nozzle and (in engines with reheat capability) the afterburner duct perform an analogous function[17]. Despite their functional similarity, these gas turbine components typically have a much longer life than the thrust chamber in a liquid rocket engine. There may be many differences in the design and operation of a rocket engine and a gas turbine which may contribute to this discrepancy.

One clear difference is the operating conditions under which these components operate. Assuming a cruising altitude of 10 km and a velocity of 900 km/h (typical values for a commercial aircraft[18, 19]) as well as a compressor pressure ratio of 30 (based on the General Electric CF6-80C2 turbofan gas turbine engine[20]), a simple stagnation pressure calculation indicates that a gas turbine combustor would be exposed to fluid pressures of approximately 1.2 MPa during normal operation.

Additionally, modern gas turbine combustors are limited to fluid temperatures of 2,000K, to protect the turbine downstream of the combustor from excessive temperatures. This requirement is relaxed for afterburner ducts, but gas temperatures are still typically limited to 2,220K[17]. For comparison, the thrust chamber in the Space Shuttle's RS-25 liquid rocket engine operated at a combustion pressure of 2,994 psi (20.64 MPa) and a temperature of 6,000°F (3,589 K)[14].

Perhaps the severity of these operating conditions (in comparison to a gas turbine) is an underlying reason for the comparatively short life of liquid rocket engine thrust chambers. While prior research focused on thrust chamber life has focused on how thrust chamber life can be improved through design concepts (such as material selection or structural geometry), the present study instead focuses on how the operating conditions to which a thrust chamber is exposed, such as high pressures and temperatures, can affect its life. Changing these operating conditions would likely also affect engine performance (measured as thrust and specific impulse). Thus, the trade-off between thrust chamber life and engine performance is also evaluated. This study seeks to answer the following borad research questions:

1. Which operating conditions have an effect on thrust chamber life (measured in terms of combustion cycles to failure)?
2. How and to what extent can these operating conditions be changed?
3. What is the effect of these changes on engine performance (measured in terms of thrust and specific impulse)?

2.   Literature Review

In this chapter, literature relevant to the present study is evaluated. Relevant literature is arranged into two separate categories: prior studies and fundamental theory. Section 2.1 describes prior studies have focused on issues of thrust chamber life evaluation and reusable liquid rocket engines more generally. Section 2.2 describes fundamental engineering theories which form the theoretical basis for this study.

2.1   Prior Art

This section describes the history and current state of the art in long-life reusable liquid rocket engine thrust chamber research. The studies described herein are important foundational works which have led to and enabled the current research described in this dissertation. Subsection 2.1.1 describes research in this field conducted by NASA's Lewis Research Center (now the Glenn Research Center) dating back to the late 1970's. Similarly, Subsection 2.1.2 describes work undertaken by JAXA's Institute of Space and Astronautical Science (ISAS) since the late 1990's. Finally, Subsection 2.1.3 describes other works which are also considered to be important contributions in this field.

2.1.1 NASA Studies

In the 1970's, during the development of the RS-25 Space Shuttle Main Engine (SSME) researchers at NASA's Lewis Research Center in Cleveland, Ohio began considering the development of future reusable liquid propulsion systems. It was expected at the time that future RLV design requirements would call for regeneratively-cooled thrust chambers with a service life of 100 to 300 cycles[21, 22]. Numerical studies of thrust chamber thermo-mechanical structural behaviour[23] and evaluation of various materials for thrust chambers[24] were conducted in the mid-1970's. A subscale rocket engine test apparatus was set up to experimentally evaluate the life of various thrust chamber designs. This apparatus, shown in Figure 2-1 was used to test multiple different thrust chamber test articles. The apparatus provides GH_2 fuel and LOx oxidizer to the thrust chamber, as well as a separate supply of LH_2 which acts as a coolant and is then vented through a burn stack. Ignition is achieved through back-lighting: an external igniter is used at the exhaust, triggering a flame front that flows back up through the nozzle and into the combustion chamber. The test stand was also fitted with an exhaust gas muffler and scrubber[21, 22].
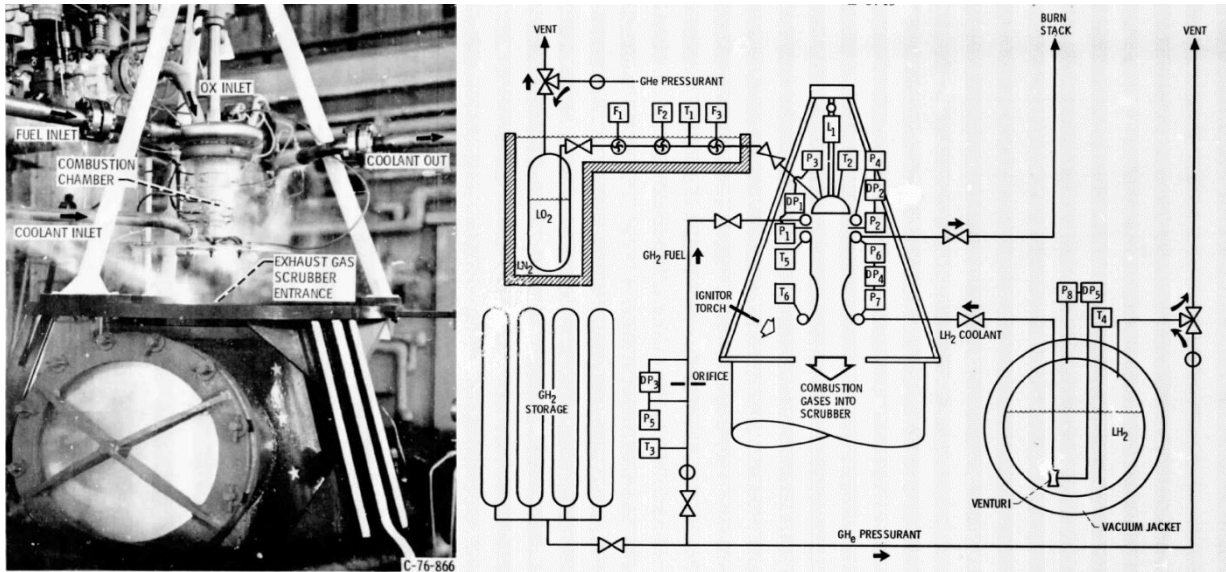
Figure 2-1: NASA Lewis Research Center Subscale Rocket Engine Test Apparatus[21]

Hannum, Kasper and Pavli[21] used the test apparatus to evaluate a range of thrust chamber designs, with the goal of determining how different configurations might affect thrust chamber life. 13 thrust chambers were manufactured: six had liners made from Oxygen-Free High-Conductivity (OFHC) copper and seven had liners made from Amzirc. All chambers had electroformed nickel closeout walls. Two different contours for the walls were tested, but the basic dimensions (overall length, throat position, throat diameter, exhaust diameter) of all test articles were the same. GH$_2$ was injected through a porous "rigimesh" faceplate, while LOx was injected through a network of 85 showerhead tubes which passed through the faceplate. Thermocouples were both attached to the outside of the thrust chambers, and placed in pre-drilled holes. One of the thrust chamber test articles is shown in Figure 2-2.
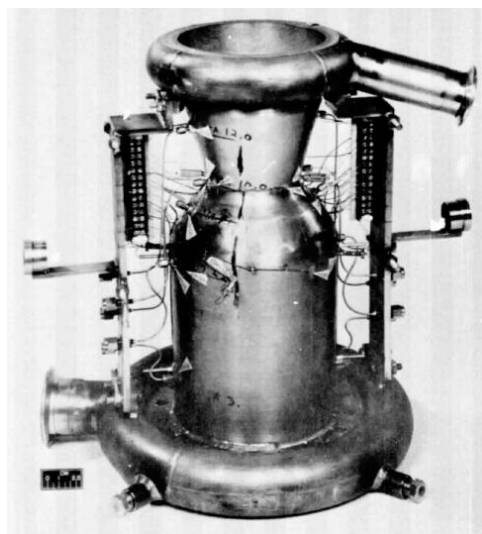
Figure 2-2: Experimental thrust chamber[21]

The 13 thrust chambers were tested to failure. In addition to the differing geometries and materials, tests were conducted at chamber pressures of 4.14 MPa and 5.52 MPa, and coolant flow rates of 0.91 kg/s and 0.59 kg/s. The number of cycles to failure varied from 21 (for an Amzirc thrust chamber at a chamber pressure of 5.52 MPa and coolant flow rate of 0.59 kg/s) to 165 (for an OFHC copper thrust chamber at a chamber pressure of 4.14 MPa and coolant flow rate of 0.91 kg/s). Failures were characterized by the radially-inward bulging and rupture of the ligaments separating the cooling channels from the thrust chamber, as shown in Figure 2-3. Figure 2-3 also shows that these deformations were most severe at the throat. Generally, the experimental results for thrust chamber life did not agree with theoretical predictions. The authors argued that better structural and heat transfer analysis was required to improve theoretical predictions[21].
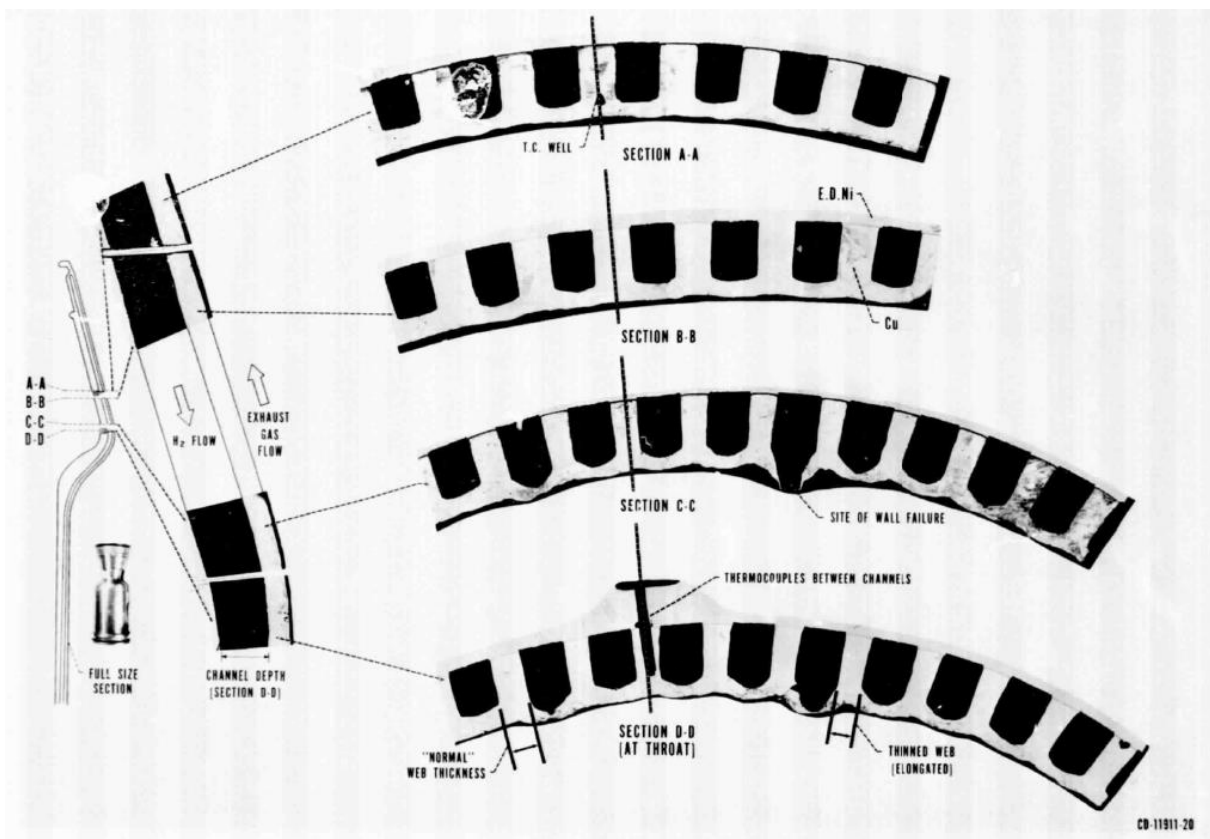
Figure 2-3: Thrust chamber ligament rupture failures[21]

Building on the work of Hannum, Kasper and Pavli[21], Quentmeyer[22] also used the Subscale Rocket Engine Test Apparatus to conduct multiple destructive tests of thrust chambers, with the specific aim of collecting more data to better understand thrust chamber failure mechanisms, such that theoretical and experimental predictions of thrust chamber life could be reconciled. Unlike Hannum, Kasper and Pavli[21], Quentmeyer[22] used cylindrical test sections (rather than a converging-diverging nozzle), which allows for numerous tests to be conducted with low fabrication costs for the test

sections[25]. To achieve a converging-diverging flow cross section, a variable geometry centerbody was fitted to the test section, as shown in Figure 2-4. The centerbody was water-cooled and treated with a zirconium-oxide surface coating to prolong its life such that it could be used for multiple tests. The coating was repaired every 100-200 cycles, and the centerbody typically failed after 1,000 – 2,000 cycles. As with the thrust chambers tested by Hannum, Kasper and Pavli[21], a porous "rigimesh" faceplate was used for GH_2 injection, with a network of 70 showerhead tubes for LOx injection.
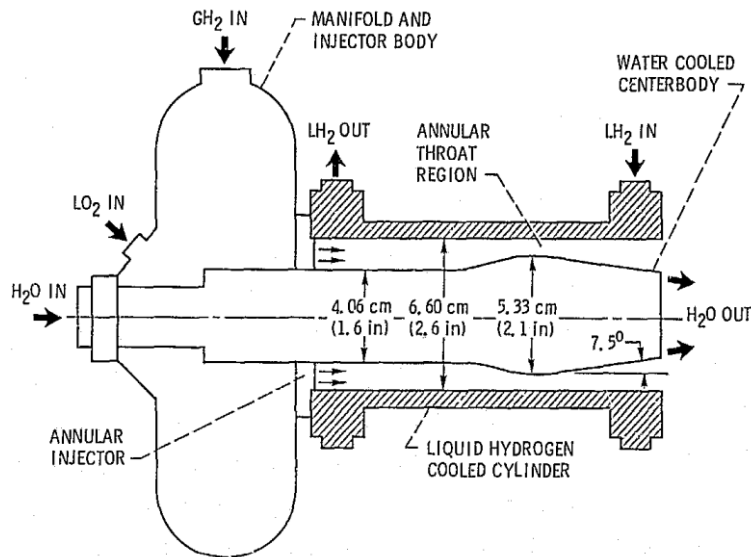
Figure 2-4: Cylindrical Thrust Chamber Assembly[22]

22 test section liners were fabricated from different materials: 12 were fabricated from OFHC copper, three from NARloy-Z, six from half-hard Amzirc, and one from aged Amzirc. Cooling channels were machined into the liners and a copper closeout wall was electroformed on the outer edge of each liner. In all tests, thrust chamber pressure was set to 4.14 MPa, and coolant flow rate was varied to achieve a desired temperature in the cooling channel ribs. Thermocouples were fitted to both the outer wall and into holes drilled into the ribs[22].

21 of the test sections were tested to failure (one of the OFHC test sections was tested to over 2,000 cycles without failure). Of the test sections which failed, the cycles to failure varied from 58 for one of the OFHC copper test sections, to 944 for one of the half-hard Amzirc test sections. All failures were characterized by a thinning of the ligament, leading to rupture, as shown in Figure 2-5. A correlation between cycles to failure and both maximum wall temperature and (ligament-to-closeout) wall temperature difference was also observed, as shown in Figure 2-6. Once again, the author noted that the results did not agree with theoretical predictions, and noted the deficiency of contemporary theoretical models of thrust chamber structural behaviour[22].
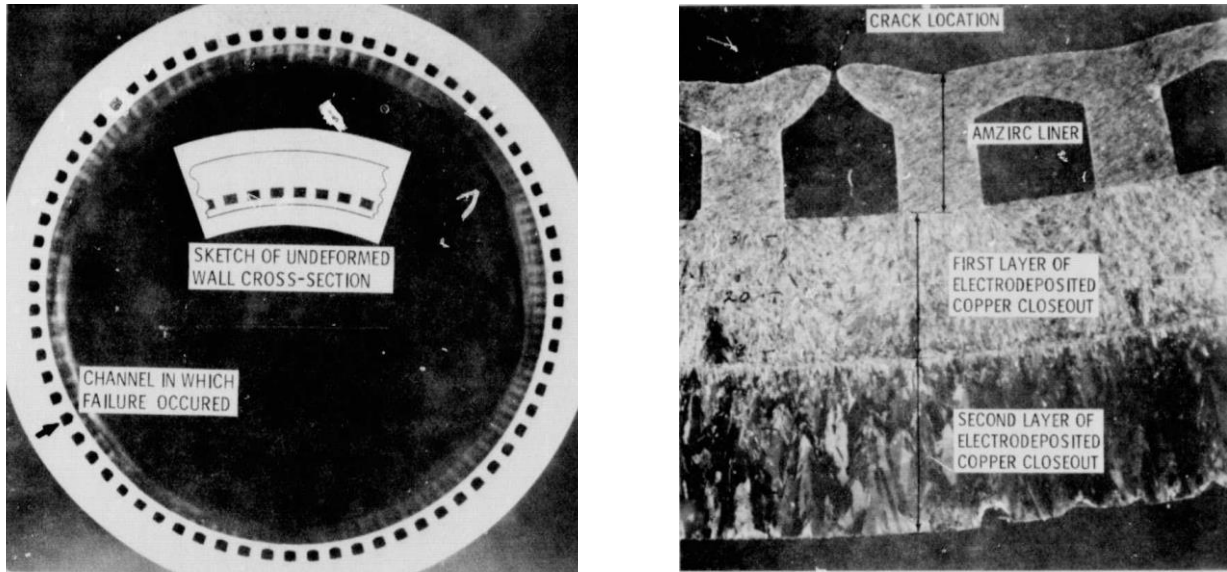
Figure 2-5: Cylindrical thrust chamber ligament rupture failures[22]
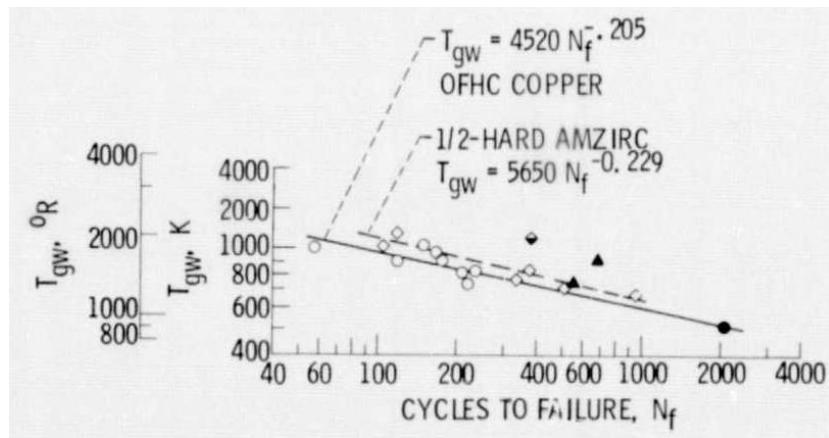
(a)
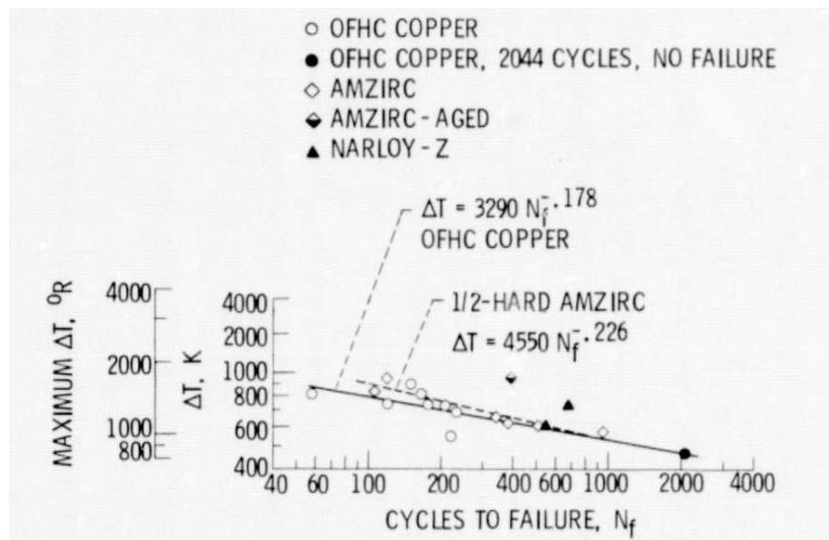
(b)

Figure 2-6: Correlation between cycles to failure and (a) maximum wall temperature & (b) wall temperature difference[22]

Based on the results Subscale Rocket Engine Test Apparatus experiments, it was clear that an improved structural model was required to accurately predict thrust chamber life. In the Early 1980's, Porowski et al.[26, 27] developed a structural model to account for the progressive bulging and thinning of thrust chamber wall ligaments which lead to rupture, as observed by Hannum, Kasper and Pavli[21] and Quentmeyer[22]. This model used Tresca's yield criterion to estimate the plastic strain range in the ligaments which cause the observed progressive bulging and thinning of the ligament. The plastic strain is influence by bending and sheer strains, induced by both the pressure load on the ligament, and thermally-induced bending due to the temperature difference across the ligament. The temperature difference between the ligament and closeout wall leads to differential thermal expansion, which in turn contributes to the bending strain in the ligament. The sum of the ligament plastic deflections due to hoop and bending strains was used to estimate the shape of the deformed ligament. A later version of the model also included a term for estimating plastic deflections due to creep deformation[28]. The structural model developed by Porowski et al.[26-28] is described in detail in Subsection 2.2.2 of this report.

Porowski et al.[26-28] also established three separate failure modes to evaluate thrust chamber life: one each for plastic instability (necking), low-cycle fatigue and creep deformation. The plastic instability failure criterion is based on determination of whether or not the ligament thickness has reached a critical level at which instability would occur. The low-cycle fatigue failure criterion is based on determining the total strain range after each cycle, calculating the instantaneous cycles to failure, and using this value with a cumulative damage rule to assess when failure occurs[26, 27]. The creep deformation failure criterion is based on determining the initial bending stress in the ligament (which increases as the ligament gets progressively thinner), and using this stress to estimate time to failure based on a stress-rupture plot. The time to failure is then used in a cumulative damage calculation based on the Robinson rule to determine if creep failure has occurred[28]. The failure modes established by Porowski et al.[26-28] are described in detail in Subsection 2.2.3 of this report.

Research on thrust chambers continued at Lewis Research Center into the early 1990's. This research was primarily focused on design improvements as a method for extending thrust chamber life. Such improvements included using thermal barrier coatings (such as zirconium-oxide, ZrO_2), tungsten ligament reinforcement, wall geometry modifications (such as wall slots and tubular bundles), high-aspect ratio cooling channels, transpiration cooling at the throat, and reducing the stiffness of the closeout wall (to allow for less constrained ligament thermal expansion). Other research topics included low-cost fabrication techniques, and reducing corrosion when using hydrocarbon fuels for regenerative cooling[25].

2.1.2 JAXA Studies

ISAS began experimental research into RLVs with the Reusable Vehicle Testing (RVT) Program in the late 1990's. The RVT was a small-scale reusable Vertical Take-off/Vertical Landing (VTVL) test vehicle, initially developed to build knowledge in rocket turnaround operations and to develop propulsive landing technology, with the eventual goal of developing a reusable sounding rocket[1]. Four variants of the RVT (shown in Figure 2-7) were built and tested over the next decade, with the complexity gradually increasing with each new variant. RVT #1 first flew in 1999, demonstrating VTVL using a throttleable LH_2/LOx-fed rocket engine. One-day turnaround was achieved with RVT #2 in 2001. RVT #3 featured an upgraded engine and propellant system: nickel electroforming was used to manufacture more durable engine components, quick re-ignition capability was also introduced and a composite LH_2 tank was developed. These advancements helped RVT #3 achieve an extended flight envelope, reaching a maximum altitude of 42m. One significant change with the introduction of RVT #4 was a redesigned engine. While all previous variants used a simple pressure-fed engine, a more advanced expander-cycle engine was developed for RVT #4[29].

RVT#1 (1999)   RVT#2 (2001)   RVT#3 (2003)   RVT#4
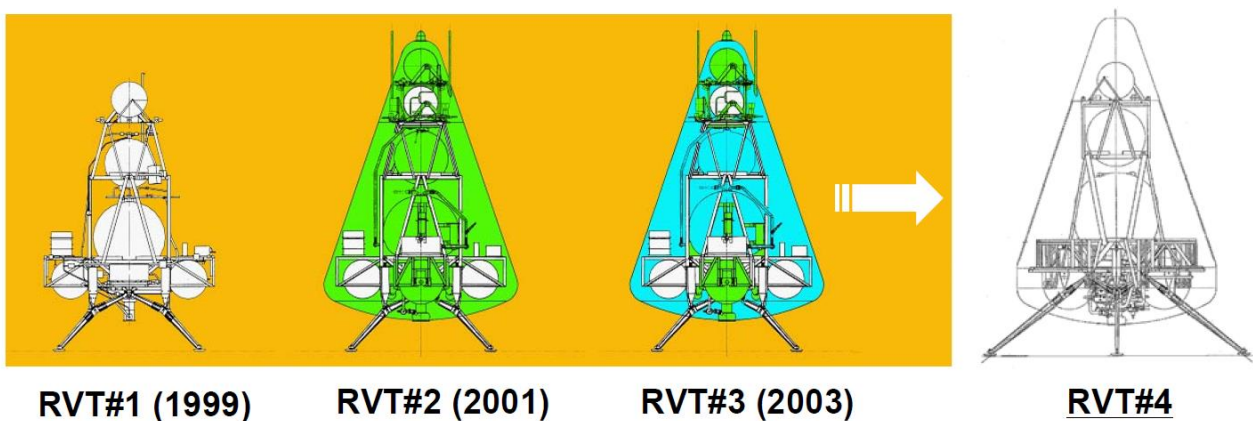
Figure 2-7: RVT Variants[29]

As the RVT program concluded in the late 2000's, ISAS researchers transitioned to the original program goal of developing a reusable sounding rocket. Knowledge gained through the RVT program, including the development of the RVT #4 expander-cycle engine, was used in the design and development of the reusable sounding rocket. In particular, a state-of-the-art reusable rocket engine was developed and tested for the reusable sounding rocket, as shown in Figure 2-8. This 40kN expander-bleed cycle engine was designed to meet various requirements related to its reusability. Such requirements focused on performance, restartability & deep throttling, health monitoring, reliability, ease of inspection & maintenance, and long life. The engine was designed to meet a life requirement of 100 flight cycles. In considering the life of the engine, two types of critical life-limiting components were identified: turbopump frictional components (bearings and seals), and the thrust chamber[10].
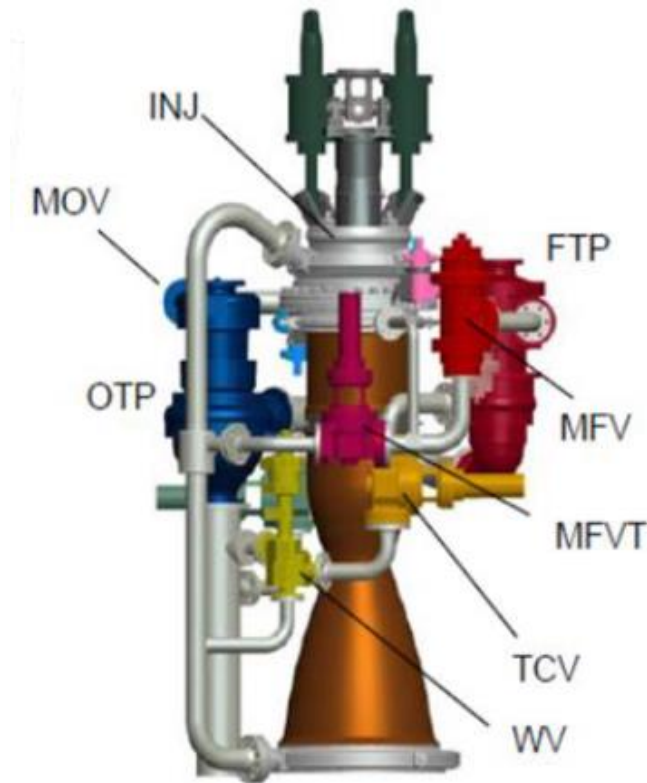
Figure 2-8: Reusable Sounding Rocket engine[10]

In order to confirm that the engine would meet its life requirement of 100 flight cycles, a detailed lifetime evaluation of the thrust chamber was conducted, involving both numerical simulation and prototype testing[16]. A 2D Finite Element Method (FEM) model of the thrust chamber wall at the throat was used to assess thrust chamber life, accounting for both creep and fatigue damage. The domain of the FEM model, shown in Figure 2-9, was a symmetrical half-section of a single cooling channel and rib. In contrast to the NASA experiments and theoretical analyses described in Section 2.1.1, which focused on failures at the ligament center, the results of this analysis showed that damage was greater at the rib center. The results also showed that that low-cycle fatigue damage was the dominant mechanism, being two orders of magnitude larger than creep damage[16].
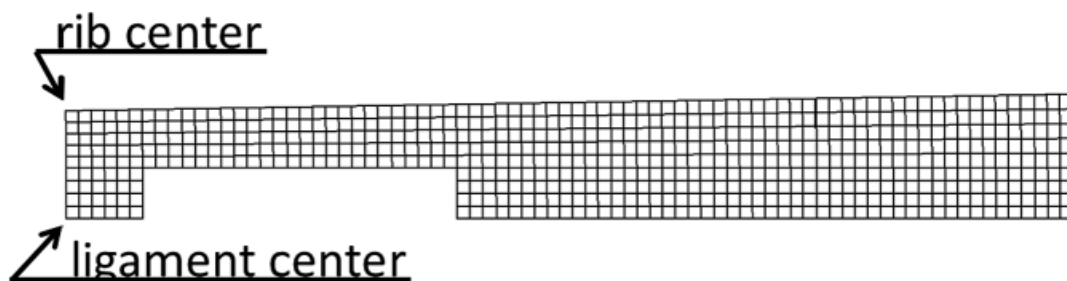
Figure 2-9: Reusable sounding rocket engine thrust chamber FEM model domain[16]

A total of 54 engine firing tests were conducted at JAXA's Kakuda Space Center, as shown in Figure 2-10. 22 of these were multiple firing tests. The total number of individual engine firings, including both "high thrust" and "low thrust" firings, was 142. Based on a typical flight profile for the reusable sounding rocket, the cumulative damage from these tests was determined to be the equivalent of approximately 117 nominal flight cycles, after which the thrust chamber showed no signs of damage. As such, it was determined that the engine met its design requirement of a life of at least 100 flight cycles[16]. The life of the turbopump frictional components was evaluated separately. It was determined that replacement of the turbopump seals and bearings would be necessary to meet a 100-flight design requirement[30].
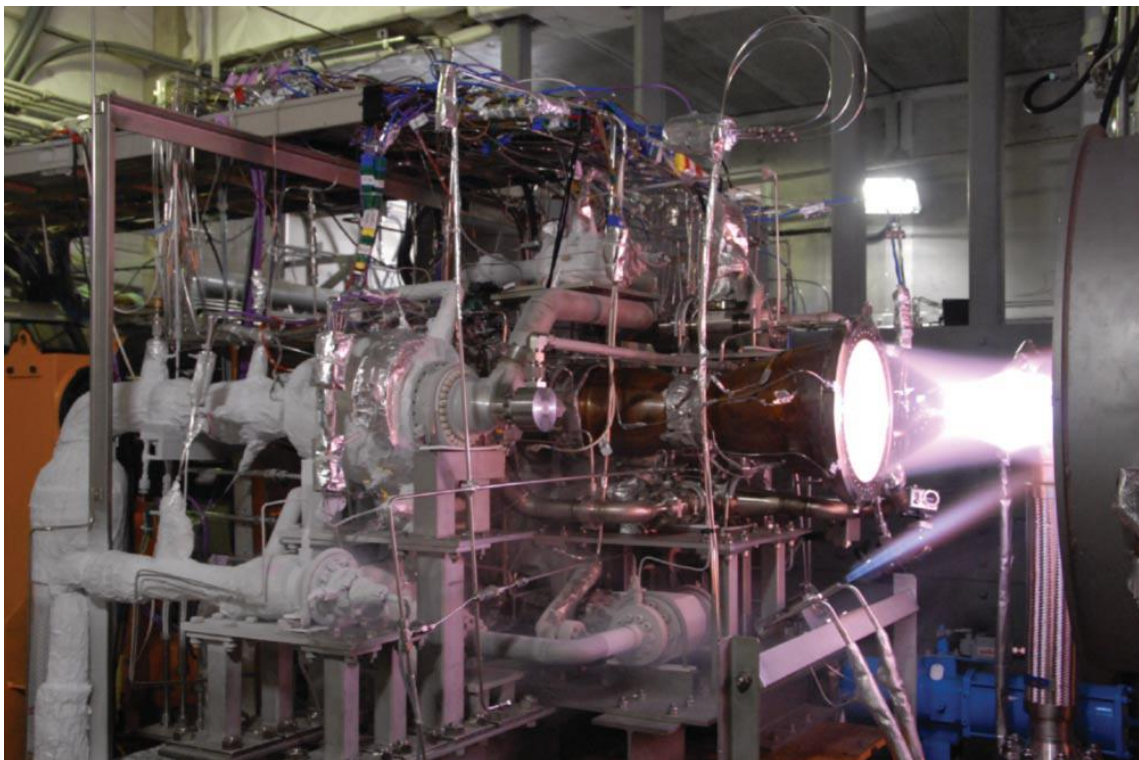
Figure 2-10: Reusable Sounding Rocket engine firing test[16]

In order to accelerate the development timeline, a scaled-down version of the reusable sounding rocket has been built by ISAS. This vehicle, called the RV-X, will use a single engine, rather than the four engines called for in the design of the reusable sounding rocket. Thus, the vehicle will be smaller, lighter and have a reduced flight envelope. The goal of the RV-X project is to return ISAS RLV research to flight testing as quickly as possible. To that end, systems and components developed for the reusable sounding rocket are being adapted for use on the RV-X. The reusable rocket engine is one such system[31]. Thus, the first flight test of this engine can be expected in the near future.

2.1.3 Other Studies

In addition to the theoretical and experimental research focusing on regeneratively-cooled thrust chamber reusability and life conducted by NASA and JAXA (as described in Sections 2.1.1 and 2.1.2, respectively), other studies have also focused on this issue. Two such examples are presented in this subsection.

Popp and Schmidt[32] proposed a variety of design concepts for extending the life of both expendable and reusable thrust chambers. In the case of expendable cooling chambers, the authors argued that using these design concepts could reduce regenerative cooling requirements and thereby increase performance. Specifically, Popp and Schmidt[32] discussed material improvements, changing the structure of cooling channels (a higher number of high-aspect ratio channels), transpiration cooling, thermal barrier coatings and elastic cooling structures. Many of these concepts had been proposed or investigated previously. Material improvements and cooling channel structure changes were assessed to be unlikely to yield significant improvements in life. Transpiration cooling raised concerns due to a lack of flight heritage. Thermal barrier coatings and elastic cooling structures were assessed as having the greatest potential to improve thrust chamber life. It was estimated that these design improvements could theoretically increase thrust chamber life by a factor of 3 to 30. Notably all of the concepts mentioned were previously described in a summary of thrust chamber research performed at NASA Langley Research Center[25]. Popp and Schmidt argued that, while these concepts were not novel, there was insufficient experimental evidence to validate the effectiveness or feasibility of the concepts. As such, more research was required[32].

Chen et al.[33] investigated the relative influence of cooling channel design and coolant inlet properties on cooling channel pressure loss, maximum wall temperature and thrust chamber life. The results of their analysis indicated that the number of cooling channels, cooling channel aspect ratio and coolant flow rate had the most significant impact on pressure loss, whereas inlet pressure only had a marginal impact. Maximum wall temperature was most significantly impacted by the number of cooling channels and the coolant flow rate, while cooling channel aspect ratio and pressure only had a marginal impact. Finally, thrust chamber life was most significantly impacted by the number of cooling channels and cooling channel aspect ratio, while coolant inlet pressure and mass flow had a marginal impact. Chen et al.[33] also performed a design optimization of a SSME-like reusable liquid rocket engine thrust chamber. Rather than being an objective function, thrust chamber life was set as an optimization constraint. Instead, the objective of the optimization was to minimize coolant pressure loss[33]. The logic of using cooling channel pressure loss (rather than thrust chamber life) as an optimization objective is not justified beyond the stated reason of reducing turbopump loads.

2.2 Fundamental Theory

This section describes the fundamental theories and empirical relationships upon which the rationale of this study is based. The topics described include a one-dimensional analysis of rocket exhaust gas flow based on compressible flow theory (Subsection 2.2.1), structural behaviour (Subsection 2.2.2) and failure modes (Subsection 2.2.3) for thrust chamber wall ligaments based on the Porowski model, as well as heat transfer from the exhaust gas to the walls and cooling channel based on the Bartz correlation, the Porowski model and the Colburn correlation (Subsection 2.2.4). While based on simplified analysis assumptions in some cases, the formulas in this section provide sufficient insight for the rationale discussion in Chapter 3.

2.2.1 Rocket Nozzle Gas Flow

The net thrust produced by a rocket engine is obtained by integrating the surface stresses over all solid surfaces of the rocket. For the purposes of calculation, this can be simplified to the force contributions (pressure, viscosity and momentum) acting on the exit plane of the exhaust nozzle. The contribution of viscous forces is typically considered negligible, thus the formula for rocket thrust can be expressed considering only momentum and pressure force contributions, as shown in Equation (2-1)[34].

$$F_T = \dot{m}_{TC} u_E + (p_E - p_a) A_E \tag{2-1}$$

Specific impulse is a common metric of rocket performance, used to measure how "efficiently" a rocket generates thrust. Specific impulse essentially measures how much thrust is generated per unit mass of propellant used. It is typically normalized by standard gravity, such that the result can be expressed in units of "seconds". The formula for specific impulse is shown in Equation (2-2)[34]. Note: in most cases, total propellant flow rate is equal to thrust chamber propellant flow rate (i.e. $\dot{m}_{ET} = \dot{m}_{TC}$). In engines with propellant bleed systems, however, not all propellant flows through the thrust chamber. Thus, these values can be different.

$$I_{SP} = \frac{F_T}{\dot{m}_{ET} g} \tag{2-2}$$

Equations (2-1) and (2-2) show that in order to calculate thrust and specific impulse, it is necessary to determine exhaust nozzle exit velocity and pressure. Assuming the gas conditions in the combustion chamber can be approximated as stagnant, and gas flow through the nozzle is isentropic, then the exhaust pressure can be estimated using isentropic flow theory, as shown in Equation (2-3)[34].

Rearranging Equation (2-3) gives an expression for exhaust pressure as a function of combustion pressure, specific heat ratio, and nozzle exit Mach number, as shown in Equation (2-4).

$$\frac{p_{TC}}{p_E} = \left(1 + \frac{\gamma - 1}{2} Ma_E{}^2\right)^{\gamma/(\gamma-1)} \tag{2-3}$$

$$\Rightarrow \qquad \frac{p_E}{p_{TC}} = \left(1 + \frac{\gamma - 1}{2} Ma_E{}^2\right)^{\gamma/(1-\gamma)}$$

$$\Rightarrow \qquad p_E = p_{TC}\left(1 + \frac{\gamma - 1}{2} Ma_E{}^2\right)^{\gamma/(1-\gamma)} \tag{2-4}$$

Nozzle exit Mach number is defined as shown in Equation (2-5)[34]. This formula can be rearranged to give an expression for nozzle exit exhaust velocity in terms of nozzle exit temperature, specific heat ratio, gas constant and nozzle exit Mach number. This is shown in Equation (2-6). Note that the gas constant referred to in Equation (2-6) is the specific gas constant.

$$Ma_E \equiv \frac{u_E}{\sqrt{\gamma R T_E}} \tag{2-5}$$

$$u_E = Ma_E\sqrt{\gamma R T_E} \tag{2-6}$$

In order to solve Equations (2-4) and (2-6), an expression for the nozzle exit Mach number is required. Assuming sonic properties at the nozzle throat and isentropic flow, the relationship between nozzle area ratio (defined as exit area divided by throat area), specific heat ratio and nozzle exit Mach number can be expressed as shown in Equation (2-7)[34]. For a given area ratio and specific heat ratio, this equation can be solved iteratively to determine nozzle exit Mach number.

$$\frac{A_E}{A^*} = \frac{\left[\frac{2}{\gamma + 1}\left(1 + \frac{\gamma - 1}{2} Ma_E{}^2\right)\right]^{(\gamma+1)/[2(\gamma-1)]}}{Ma_E} \tag{2-7}$$

Finally, in order to solve Equation (2-6), an expression for nozzle exit temperature is required. Once again assuming the gas conditions in the combustion chamber can be approximated as stagnant, and gas flow through the nozzle is isentropic, then the exhaust temperature can be estimated using isentropic flow theory, as shown in Equation (2-8)[34]. Rearranging Equation (2-8) gives an expression for exhaust temperature as a function of combustion temperature, specific heat ratio, and nozzle exit Mach number, as shown in Equation (2-9).

$$\frac{T_{TC}}{T_E} = 1 + \frac{\gamma - 1}{2} Ma_E{}^2 \tag{2-8}$$

$$\Rightarrow \qquad \frac{T_E}{T_{TC}} = \frac{1}{1 + \dfrac{\gamma - 1}{2} Ma_E{}^2}$$

$$\Rightarrow \qquad T_E = \frac{T_C}{1 + \dfrac{\gamma - 1}{2} Ma_E{}^2} \tag{2-9}$$

Equations (2-1) through (2-9) provide a simplified method for estimating rocket engine performance (as measured by thrust and specific impulse). Standard gravity, atmospheric pressure, thrust chamber gas properties, propellant flow rates and nozzle geometry are required input variables. While modelling non-Isentropic nozzle gas flow is not such a trivial exercise, the above-described method provides a good approximation, and is instructive for establishing the relevant variables which influence rocket engine performance.

2.2.2 Thrust Chamber Structural Behaviour

NASA developed the Porowski model in the early 1980's as a simplified procedure to evaluate thrust chamber life, as discussed in Subsection 2.1.1. This procedure includes both a model of structural behaviour in the thrust chamber walls, and several failure modes used to evaluate thrust chamber life. The Porowski model failure modes are discussed in Subsection 2.2.3. In this Subsection, the Porowski model's structural behaviour modelling is introduced. The relevant dimensions, locations and coordinates are shown in Figure 2-11.
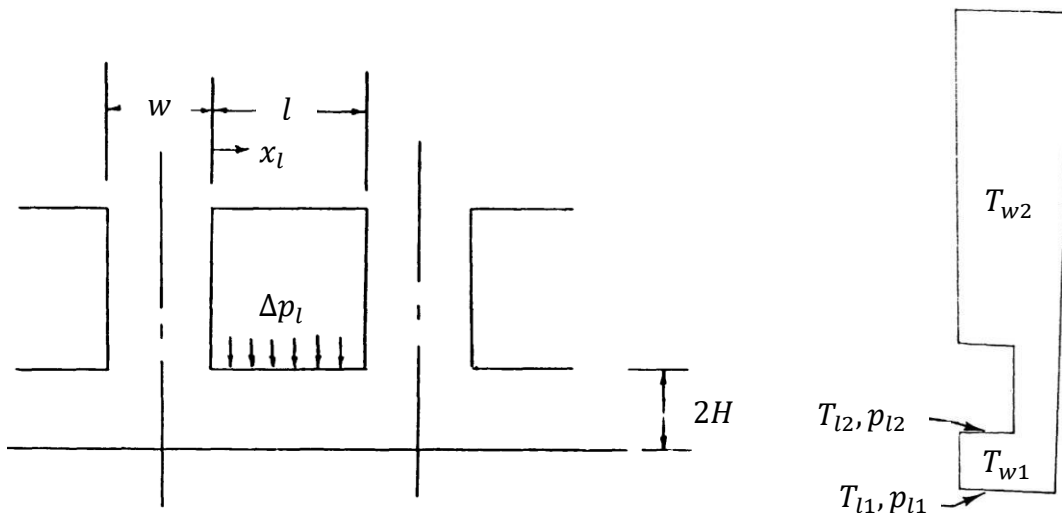
Figure 2-11: Thrust chamber wall geometry[26] (Edited)

As described in Subsection 2.1.1, liquid thrust chambers typically fail when the wall ligaments which separate the thrust chamber from the cooling channels rupture inward. Several mechanisms cause the inelastic deflections which eventually lead to ligament rupture. These mechanisms include pressure-induced bending, shear and hoop strains in the ligament, thermally-induced bending in the ligament, hoop strain induced by the temperature difference between the ligament and the close-out wall, and creep deformation in the ligament[26-28]. Strains acting on the ligament are shown in Figure 2-12.
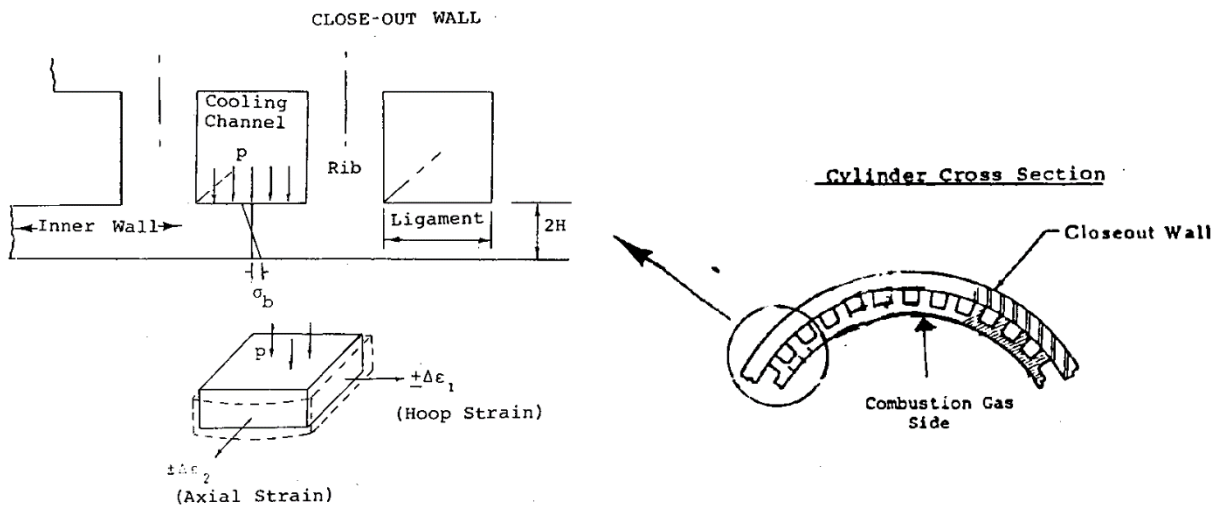
Figure 2-12: Thrust chamber wall ligament loading[27, 28] (Edited)

The total inelastic deflection of the ligament per combustion cycle is important for evaluating cumulative damage and predicting ligament failure, as described in Subsection 2.2.3. This total deflection can be estimated as the sum of the inelastic deflections induced by bending, shear and creep individually, as shown in Equation (2-10)[28]. Thus, in order to determine total deflection, estimates for the bending, shear and creep deflections are required.

$$\delta_{tot} = \delta_{be} + \delta_{sh} + \delta_{cr} \tag{2-10}$$

The pressure-induced bending moment in the ligament can be estimated using Euler–Bernoulli beam theory. The ligament is approximated as a statically indeterminate beam, with its ends "clamped" to the adjacent ribs. The pressure in the cooling channel is higher than the thrust chamber pressure, causing the resultant pressure differential load to act inwards on the ligament. Assuming this pressure differential is constant along the width of the ligament, it can be multiplied by a unit length, to give a load in Newtons per meter to give a uniformly distributed load, as shown in Equation (2-11).

$$\Delta p_l = (p_{l2} - p_{l1}) \times 1 \tag{2-11}$$

According to Euler–Bernoulli beam theory, the pressure-induced bending moment distribution in the ligament is given be Equation (2-12), while the shear force distribution is given be Equation (2-13)[26].

$$M_{be}(x_l) = \frac{-\Delta p_l l^2}{2}\left(\frac{1}{6} + \frac{x_l}{l} + \frac{x_l^2}{l^2}\right) \tag{2-12}$$

$$F_{sh}(x_l) = \frac{\Delta p_l l}{2} - \Delta p_l x_l \tag{2-13}$$

The ligament bending moment and shear force given by Equations (2-12) and (2-13) can be normalized by their respective yield values, as shown in Equation (2-14) (for bending moment) and Equation (2-15) (for shear force)[27].

$$m_{be} = \frac{M_{be}}{H^2 S_Y} \tag{2-14}$$

$$f_{sh} = \frac{F_{sh}}{H S_Y} \tag{2-15}$$

For a structure approximated as a beam (like the ligament) which is subjected to bending and hoop forces, the yield surface is parabolic, with plastic flow vectors acting perpendicular to the yield surface. The yield surface can be modelled based on Tresca's yield criterion, as shown in Equation (2-16)[27]. Equation (2-16) can be rearranged to give an expression for normalized hoop force, as shown in Equation (2-17).

$$m_{be} + \frac{f_{ho}^2}{\sqrt{1 - f_{sh}^2}} - \sqrt{1 - f_{sh}^2} = 0 \tag{2-16}$$

$$\Rightarrow \qquad \frac{f_{ho}^2}{\sqrt{1 - f_{sh}^2}} = \sqrt{1 - f_{ho}^2} - m_{be}$$

$$\Rightarrow \qquad f_{ho} = \sqrt{1 - f_{sh}^2 - m_{be}\left(1 - f_{sh}^2\right)^{1/2}} \tag{2-17}$$

There are two components to thermal strain range in the ligament: hoop strain range due to the temperature difference between the ligament and the close-out wall, and bending strain range due to

the temperature difference across the ligament. The total thermal strain range is the sum of these two components, as shown in Equation (2-18)[27].

$$\Delta\epsilon_{Th} = \Delta\epsilon_{Th,w} + \Delta\epsilon_{Th,l} \tag{2-18}$$

If the ligament and close-out wall are manufactured from the same material, then the hoop strain range due to the temperature difference between the ligament and the close-out wall can be determined as shown in Equation (2-19)[27]. The relaxation stress term in Equation (2-19) can be conservatively approximated as the yield stress[28]. Given that creep deformation is most severe at higher temperatures, $S_{Y,max}$ should be used.

$$\Delta\epsilon_{Th,w} = [\alpha(\Delta T_w)_{max} - \alpha(\Delta T_w)_{min}] - \left(\frac{S_{Y,max} + S_{Y,min}}{E}\right) + \frac{\Delta\sigma}{E} \tag{2-19}$$

The temperature difference in Equation (2-19) is defined as shown in Equation (2-20).

$$\Delta T_w \equiv T_{w1} - T_{w2} \tag{2-20}$$

The bending strain range due to the temperature difference across the ligament can be determined as shown in Equation (2-21)[27].

$$\Delta\epsilon_{Th,l} = \frac{E(\alpha\Delta T_l)^2}{12(1-v)^2 S_Y} \tag{2-21}$$

The temperature difference in Equation (2-21) is defined as shown in Equation (2-22).

$$\Delta T_l \equiv T_{l1} - T_{l2} \tag{2-22}$$

The normalized expressions for bending moment (Equation (2-14)), shear force (Equation (2-15)) and hoop force (Equation (2-17)), as well as the total thermal strain range (Equation (2-18)) are used to determine inelastic deflections for both bending and shear. The curvature of ligament bending deflection can be calculated as shown in Equation (2-23)[26], where the normalized shear and hoop forces represent the values at the point of maximum bending deflection (i.e. in the centre of the ligament).

$$K = \frac{1}{r_{be}} = \frac{2\sqrt{1-f_{sh}^2}}{f_{ho}} \frac{(\Delta\epsilon_{Th})}{H} \tag{2-23}$$

Experiments have shown that the shape of deformed ligaments can be approximated by a linear deformation profile[27], as shown in Figure 2-13. Thus, an expression for the ligament bending deflection can be derived from simple trigonometric analysis. The resultant formula is shown in Equation (2-24)[26].
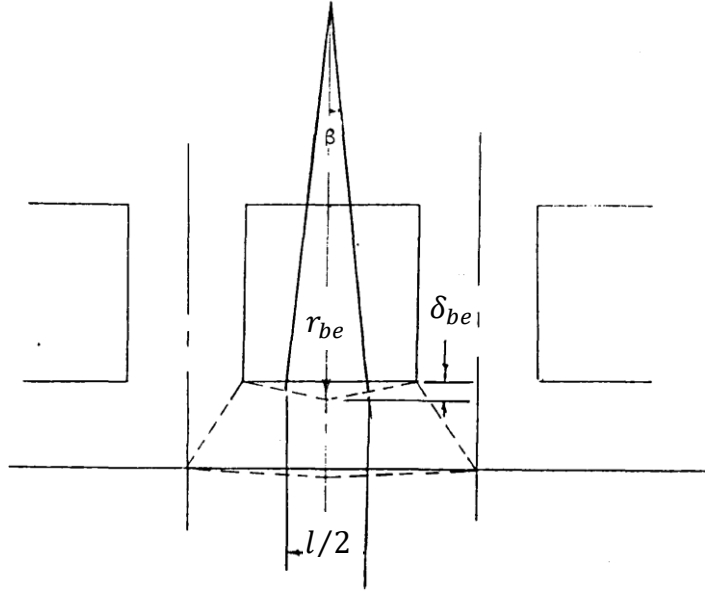
Figure 2-13: Ligament bending radius[28] (Edited)

$$\delta_{be} = 2\left(r_{be} - \sqrt{\left(\frac{l}{4}\right)^2 - r_{be}{}^2} \right) \tag{2-24}$$

The shear strain distribution along the length of the ligament can be expressed as a function of position, as shown in Equation (2-25)[27]. Integrating this function along the length of the ligament gives the ligament shear deflection[27], as shown in Equation (2-26).

$$\epsilon_{sh}(x_l) = 2\left(2f_{sh} - \frac{m_{be}f_{sh}}{\sqrt{1 - f_{sh}{}^2}} \right)\frac{(\Delta\epsilon_{Th})}{f_{ho}} \tag{2-25}$$

$$\delta_{sh} = \int_0^{l/2} \epsilon_{sh}(x_l)\,dx_l \tag{2-26}$$

According to Euler-Bernoulli beam theory, the strain in the axial direction of a loaded beam is proportional to the second derivative of its deflection. The strain rate can be described by talking the time derivative of this relationship, as shown in Equation (2-27)[28].

$$\frac{\partial \epsilon_y}{\partial t} = \dot{\epsilon}_y = -z\frac{\partial^3 v}{\partial y^2 \partial t} = -z\dot{v}'' \tag{2-27}$$

According to Norton's creep law, the strain rate can be expressed as shown in Equation (2-28)[28].

$$\dot{\epsilon}_y = B\sigma_y{}^C \tag{2-28}$$

The bending moment can be determined by taking the area integral of the axial stress distribution, as shown in Equation (2-29)[28].

$$M_{be} = \int z\sigma_y \, dA \tag{2-29}$$

Thus, the maximum creep deflection can be expressed in terms of the Norton's creep law as shown in Equation (2-30)[28].

$$\delta_{cr} = v_{max} = -\frac{Bt_C l^2}{4H}\left(\frac{\Delta p_l l^2}{16H^2}\right)^C \bar{F}(C) \tag{2-30}$$

The value of the creep exponent function, $\bar{F}(C)$, in Equation (2-30) is interpolated from the curve in FIG. This curve was plotted using tabulated reference data[28].
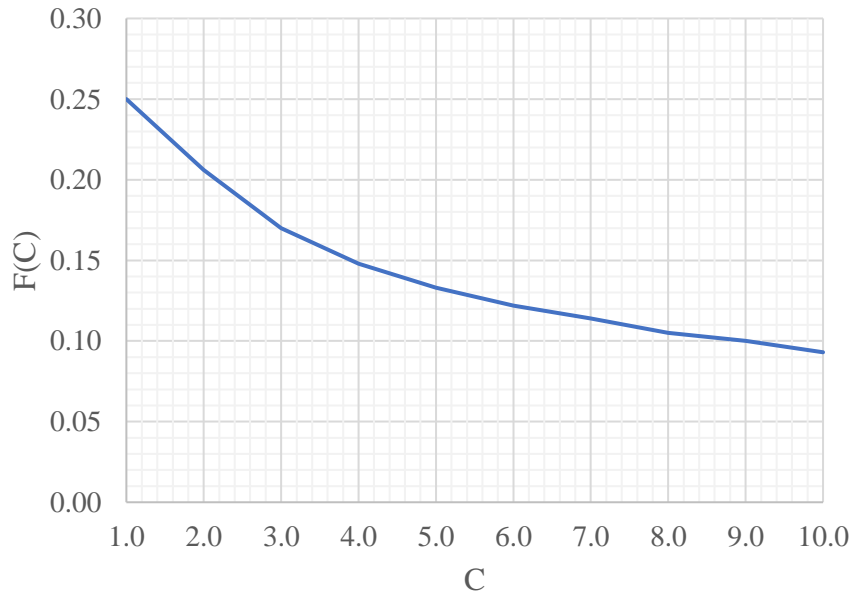
Figure 2-14: Creep exponent function

2.2.3 Thrust Chamber Failure Modes

As discussed in Subsection 2.1.1, the Porowski model provides a procedure for evaluating thrust chamber service life, based on structural behaviour and failure predictions of the wall ligaments. The structural behaviour of the ligaments is described in Subsection 2.2.2. In this subsection, the Porowski model failure modes are described. The model accounts for three separate failure modes: plastic instability (necking), low-cycle fatigue and creep deformation. The number of cycles to failure for each failure mode is evaluated. This information is used to determine the critical failure mode (i.e. which of the three failure modes occurs first), and to quantify thrust chamber life (measured as cycles to failure)[26-28].

The cumulative effect of the inelastic deflections described Subsection 2.2.2 are ligaments which become incrementally thinner over the life of the thrust chamber, until failure occurs. Thus, to evaluate when failure occurs and hence estimate thrust chamber life, it is necessary to determine how this thinning occurs. As described in Subsection 2.2.2, the deformed ligaments can be approximated by a linear deformation profile, which can be used to determine the maximum and minimum thicknesses of the ligament during a single combustion cycle, as shown in Figure 2-15. Based on this linear variation in thickness, the maximum and minimum ligament thicknesses after N combustion cycles can be calculated as shown in Equations (2-31) and (2-32), respectively.

$$t(x) = (t_{max} - t_{min}) \frac{2x}{\ell} + t_{min}$$
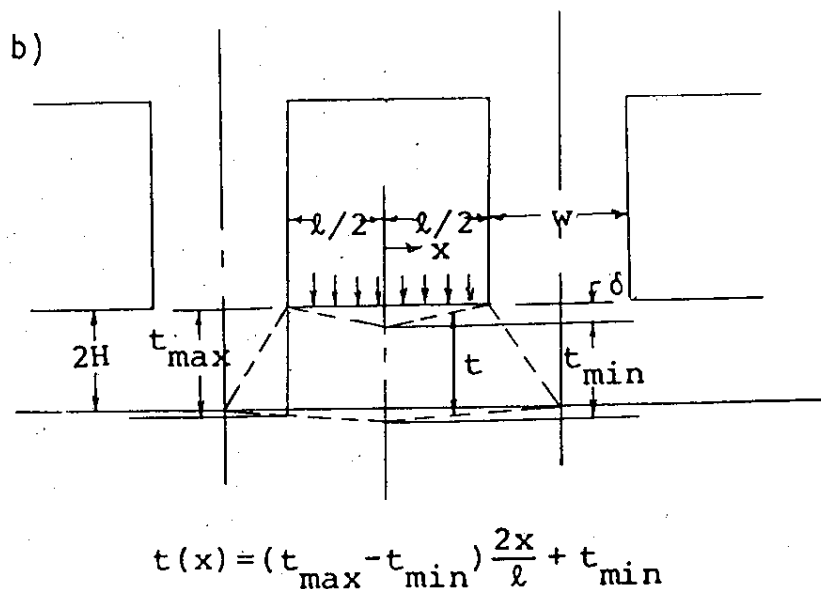
Figure 2-15: Maximum and minimum ligament thicknesses[27]

$$\tau_{min} = 2H - \frac{N\delta_{tot}w}{(l+w)} \tag{2-31}$$

$$\tau_{max} = 2H - \frac{N\delta_{tot}lw}{(l+w)^2} \tag{2-32}$$

Unless prevented, plastic instability typically occurs after a short number of cycles. By assuming the ligament as a biaxially loaded shell, the Porowski model provides a simple formula for evaluating the "critical thickness", below which the ligament will fail due to plastic instability. The formula for this critical thickness is shown in Equation (2-33)[27].

$$\tau_{PI} = 2He^{-n} \tag{2-33}$$

If the minimum thickness, as determined by Equation (2-31), decreases to a point where it becomes smaller than the critical thickness, the ligament is assumed to fail due to plastic instability, and the life of the thrust chamber is determined to be the number of cycles until this failure occurs.

The fatigue failure criterion on the Porowski model is based on a simple cumulative damage rule. After each cycle, the cycles to failure is evaluated by interpolation of a fatigue curve. Failure is assumed to occur once the sum of the inverse of these values reaches unity, as shown in Equation (2-34). If this sum exceeds unity, the ligament is assumed to fail due to low-cycle fatigue, and the life of the thrust chamber is determined to be the number of cycles until this failure occurs.

$$\sum_{i=1}^{N_{F,f}} \left(\frac{1}{N_F}\right)_i = 1.0 \tag{2-34}$$

In order to interpolate the fatigue curve, a total strain range for the cycle is required. The Porowski model uses the multiaxial strain formula in Equation (2-35) for the total strain range in the minimum thickness ligament section[27], based on incompressibility of the ligament material.

$$\bar{\epsilon}_{min} = \frac{2}{\sqrt{3}}\sqrt{\epsilon_{x,min}^2 + \epsilon_{x,min}\epsilon_{y,min} + \epsilon_{y,min}^2} \tag{2-35}$$

The axial strain in the minimum thickness ligament section is calculated as shown in Equation (2-36)[27].

$$\epsilon_{y,min} = \alpha\Delta T_w \tag{2-36}$$

The hoop strain in the minimum thickness ligament section is calculated as shown in Equation (2-37)[27].

$$\epsilon_{x,min} = \epsilon_{x,avg} \frac{\frac{n-1}{n}\left(\frac{\tau_{max}}{\tau_{min}} - 1\right)}{\left(\frac{\tau_{max}}{\tau_{min}}\right)^{\frac{n-1}{n}} - 1} \tag{2-37}$$

The average hoop strain in the ligament is estimated to be equal to the axial strain in the minimum thickness ligament section, as shown in Equation (2-38)[26].

$$\epsilon_{x,avg} = \epsilon_{y,min} = \alpha\Delta T_w \tag{2-38}$$

For kinematically hardening materials, cyclical loading eventually results in fully alternating plastic strain. In other words, working of the material through cyclical loading gradually increases its resistance to plastic instability, and prevents the strain range from increasing further. Eventually the material reaches a state where plastic strains become stable, cyclic thinning of the ligament ceases and instability cannot occur. This state is described in the Porowski model as strain hardening, and it affects both the plastic instability and fatigue failure modes in the Porowski model. Once strain hardening is achieved, plastic instability is prevented, and the total strain range calculated in Equation (2-35) becomes constant. The number of cycles required to achieve this outcome is given by the formula in Equation (2-39)[27].

$$N_{SH} = 750n^{1.25} \tag{2-39}$$

The strain hardening parameter, n, used in both Equations (2-33) and (2-39), can be estimated as shown in Equation (2-40)[26].

$$n = 0.2\left(\frac{S_U - S_Y}{S_Y}\right)^{0.6} \tag{2-40}$$

Creep deformation is considered to be significant as a failure mode if the creep period (assumed to be the engine firing time in this case) is less than 10% of the time to reach the steady state stress. The time to reach the steady state stress may be determined as shown in Equation (2-41)[28].

$$t_{SS} = \frac{1}{B\sigma_{SS}{}^C} \frac{2.3}{C} \frac{\sigma_{in}}{E} \tag{2-41}$$

The steady state stress can be conservatively estimated as equal to initial stress, as shown in Equation (2-42)[28].

$$\sigma_{SS} \approx \sigma_{in} \qquad (2\text{-}42)$$

The initial stress can be estimated as the bending stress due to pressure loading in the centre of the ligament, assuming that the pressure acts uniformly over the length of the ligament, which is approximated as a clamped-clamped beam with a rectangular cross section of unit width. This is shown in Equation (2-43).

$$\sigma_{in} = \frac{\Delta p_l \left(l + \frac{w}{4}\right)^2}{4(2H)^2} \qquad (2\text{-}43)$$

As damage accumulates in the ligaments over multiple combustion cycles, the ligaments get thinner, resulting in increased initial stress in the minimum-thickness section. After N cycles, the initial stress can be estimated using the calculated minimum thickness, as shown in Equation (2-44).

$$\sigma_{in} = \frac{\Delta p_l \left(l + \frac{w}{4}\right)^2}{4(\tau_{min})^2} \qquad (2\text{-}44)$$

If creep deformation is considered significant, then cumulative damage over multiple combustion cycles can be quantified as a failure mode criterion using Robinson's life fraction rule, as shown in Equation (2-45), where the current stress level, which is estimated using Equation (2-44), is constantly updated based on the changing ligament thickness from Equation (2-31).

$$\sum_{i=1}^{N_{F,cr}} \left(\frac{t_C}{t_r}\right)_i = 1.0 \qquad (2\text{-}45)$$

2.2.4 Thrust Chamber Heat Transfer

In this section, conductive heat transfer through the thrust chamber wall, and convective heat transfer through both the thrust chamber and the cooling channel are discussed. In addition to a procedure for determining thrust chamber life, the Porowski model included a one-dimensional heat transfer model of the wall, to allow the required temperatures inside the wall to be estimated[26]. The relevant locations and coordinates are shown in Figure 2-16.
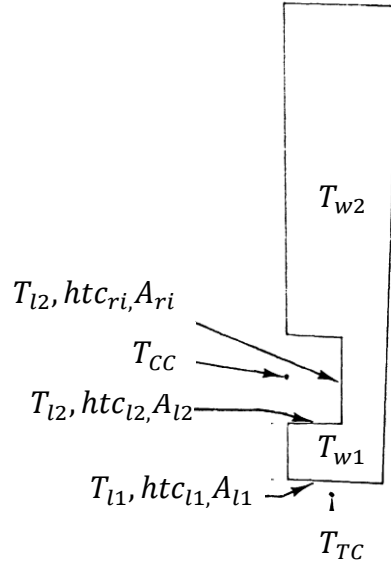
Figure 2-16: Thrust chamber wall heat transfer locations[26] (Edited)

According to the Porowski heat transfer model, the temperature on the inner (thrust chamber) side of the ligament can be estimated as shown in Equation (2-46)[26].

$$T_{l1} = \frac{\left(\frac{4H}{\kappa}\frac{1}{A_{l1}+A_{l2}+A_{ri}} + \frac{1}{htc_{l2}A_{l2}+htc_{ri}A_{ri}}\right)htc_{l1}A_{l1}T_{TC} + T_{CC}}{1 + htc_{l1}A_{l1}\left(\frac{4H}{\kappa}\frac{1}{A_{l1}+A_{l2}+A_{ri}} + \frac{1}{htc_{l2}A_{l2}+htc_{ri}A_{ri}}\right)} \tag{2-46}$$

Similarly, the temperature on the outer (cooling channel) side of the ligament can be estimated as shown in Equation (2-47)[26].

$$T_{l2} = T_{CC} + \frac{htc_{l1}A_{l1}}{htc_{l2}A_{l2}+htc_{ri}A_{ri}}(T_{TC}-T_{l1}) \tag{2-47}$$

The average temperature in the ligament can then be estimated using the inner and outer ligament temperatures, as shown in Equation (2-48)[26].

$$T_{w1} = \frac{T_{l1}+T_{l2}}{2} \tag{2-48}$$

The average temperature in the closeout wall is approximately proportional to the average ligament temperature. As such, it can be estimated using as a linear function of average ligament temperature, as shown in Equation (2-49)[26].

$$T_{w2} = \bar{A}T_{w1} \tag{2-49}$$

In order to solve Equations (2-46) and (2-47), the heat transfer coefficient between the thrust chamber and the wall, and the heat transfer coefficients between the cooling channels and the walls must be determined. The Bartz correlation was developed over 60 years ago for estimating of thrust chamber heat transfer, and is still commonly used to provide simplified estimates, without the need for computationally expensive simulations[35]. The Bartz correlation gives the formula for heat transfer coefficient shown in Equation (2-50)[36].

$$htc_{l1} = \left[\frac{0.026}{D^{*0.2}} \left(\frac{\mu_{TC}{}^{0.2} c_{P,TC}}{Pr_{TC}{}^{0.6}} \right)_0 \left(\frac{p_{TC,0} g}{u_{char}} \right)^{0.8} \left(\frac{D^*}{r^*} \right)^{0.1} \right] \left(\frac{A^*}{A} \right)^{0.1} \phi_{bl} \qquad (2\text{-}50)$$

The boundary layer correction factor shown in Equation (2-50), can be calculated as shown in Equation (2-51)[36].

$$\phi_{bl} = \frac{1}{\left[\frac{1}{2} \frac{T_{l1}}{T_{TC,0}} \left(1 + \frac{\gamma - 1}{2} Ma^2 \right) + \frac{1}{2} \right]^{0.68} \left[1 + \frac{\gamma - 1}{2} Ma^2 \right]^{0.12}} \qquad (2\text{-}51)$$

The Prandtl number for the thrust chamber flow can be calculated as shown in Equation (2-52)[36].

$$Pr_{TC} = \frac{c_{P,TC} \mu_{TC}}{\kappa_{TC}} \qquad (2\text{-}52)$$

The characteristic velocity for the thrust chamber flow can be calculated as shown in Equation (2-53)[34]. Note that the gas constant referred to in Equation (2-53) is the specific gas constant.

$$u_{char} = \frac{p_{TC,0} A^*}{\dot{m}_{TC}} = \left(\frac{\gamma + 1}{2} \right)^{(\gamma+1)/2(\gamma+1)} \sqrt{\frac{R T^*_0}{\gamma}} \qquad (2\text{-}53)$$

The Bartz correlation is not applicable to cooling channel flow. However, other correlations are available. The Colburn correlation has been used previously for modelling heat transfer in noncircular regenerative cooling channels[37]. The Colburn correlation gives the formula for ligament outer heat transfer coefficient shown in Equation (2-54)[37].

$$htc_{l2} = 0.023 \frac{\kappa_{CC,cf}}{D_{CC,hyd}} \left(\frac{c_{P,CC,cf}}{k_{CC,cf} \mu_{CC,cf}} \right)^{0.4} \left(\frac{\dot{m}_{CC} D_{CC,hyd}}{A_{CC}} \right)^{0.8} \phi_{curv} \qquad (2\text{-}54)$$

The Colburn correlation can also be used to estimate heat transfer through the ribs by removing the curvature correction factor (as the rib surfaces are not curved). This is shown in Equation (2-55).

$$htc_{ri} = 0.023 \frac{\kappa_{CC,cf}}{D_{CC,hyd}} \left(\frac{c_{P,CC,cf}}{k_{CC,cf}\mu_{CC,cf}}\right)^{0.4} \left(\frac{\dot{m}_{CC}D_{CC,hyd}}{A_{CC}}\right)^{0.8} \tag{2-55}$$

The coolant film temperature for the cooling channel flow, which impacts several of the terms in Equation (2-54), can be calculated as shown in Equation (2-56)[37].

$$T_{CC,cf} = \frac{T_{CC} - T_{l2}}{2} \tag{2-56}$$

The curvature correction for the cooling channel flow from Equation (2-54) can be calculated as shown in Equation (2-57)[37].

$$\phi_{curv} = \left[Re_{CC}\left(\frac{0.5D_{CC,hyd}}{r_{CC}}\right)^2\right]^{0.05} \tag{2-57}$$

The Reynolds number for the cooling channel flow can be calculated as shown in Equation (2-58)[38].

$$Re_{CC} = \frac{\rho_{CC}u_{CC}D_{CC,hyd}}{\mu_{CC}} \tag{2-58}$$

Finally, the cooling channel flow velocity can be calculated as shown in Equation (2-59)[38].

$$u_{CC} = \frac{\dot{m}_{CC}}{\rho_{CC}A_{CC}} \tag{2-59}$$

Equations (2-46), (2-47), (2-50) and (2-54) can be solved iteratively to establish a solution for thrust chamber wall heat transfer. Alternatively, a Computational Fluid Dynamics (CFD) model can be used to establish a temperature distribution in the thrust chamber, wall and cooling channel. This approach is described in more detail in Sections 4.4 and 4.5.

3.   Rationale

This chapter describes the rationale and hypothesis upon which this study is based. Using the theory outlined in Section 2.2, the factors which affect engine performance, thrust chamber life and wall heat transfer are evaluated by inspection of the underlying equations, and then by quantitative sensitivity analysis to identify the variables which have the most significant impact. Section 3.1 describes the analysis of engine performance, Section 3.2 describes the analysis of thrust chamber life, and Section 3.3 describes the analysis of thrust chamber wall heat transfer. The analysis of these functional relationships forms the basis for the research hypothesis, which is postulated in Section 3.4.

3.1   Factors Affecting Engine Performance

For the purposes of this study, "engine performance" is defined as thrust and specific impulse. Expressions for thrust and specific impulse are described in Section 2.2.1. Through a process of substitution of relevant functions from Section 2.2.1, elimination of parameters that are constant or invariable (for the purposes of this analysis), and assuming an isobaric, adiabatic combustion reaction with discrete, specified reactants (fuel and oxidizer) in the thrust chamber, the expressions for thrust and specific impulse can be distilled to a set of relevant operating condition variables (namely combustion mixture ratio, thrust chamber and engine total propellant flow rates, combustion pressure and propellant injection temperatures), as shown in Equations (3-1) and (3-2). This functional analysis is described in detail in Appendix A-1.

$$F_T = f(MR_C, \dot{m}_{TC}, p_{TC}, T_{FI}, T_{OI}) \tag{3-1}$$

$$I_{SP} = f(MR_C, \dot{m}_{TC}, \dot{m}_{ET}, p_{TC}, T_{FI}, T_{OI}) \tag{3-2}$$

Propellant flow rates and mixture ratio can be controlled directly as an engine control inputs. Likewise, propellant injection temperatures can be taken as engine inlet conditions, or controlled using devices such as heat exchangers or mixers. Combustion pressure can be controlled using turbopump power output, which is typically correlated with pressurization levels. Thus, Equations (3-1) and (3-2) show the operating conditions upon which the functions for engine thrust and specific impulse depend.

The relative influence of each of the above-mentioned operating conditions can be quantitatively demonstrated through a simplified sensitivity analysis of the functional variables shown in Equations (3-1) and (3-2). This analysis has been performed using CEA[39] to simulate constant-pressure, adiabatic combustion reactions, and the equations in Subsection 2.2.1 to model gas flow. The constant values used in this analysis loosely reflect the design specifications for the GH₂/LOx-fed

thrust chamber in the JAXA reusable rocket engine operating at 100% thrust, as described in Subsection 2.1.2. The variable values represent deviations of the operating conditions from these specifications. Although the JAXA reusable rocket engine is an expander-bleed cycle, for the purposes of this analysis it is assumed that propellant bleed flow rate can be neglected, so $\dot{m}_{ET} = \dot{m}_{TC}$.

The results of the engine performance sensitivity analysis are shown in Figure 3-1, Figure 3-2 and Figure 3-3. Figure 3-1(a) shows that while there is a positive linear correlation between thrust chamber propellant flow rate and thrust (i.e. thrust increases with increasing flow rate), there appears to be no correlation between propellant flow rate and specific impulse. This result could be expected by inspection of Equations (2-1) and (2-2). In Equation (2-1), the momentum thrust component ($\dot{m}_{TC}u_E$), which typically dominates net thrust in rocket engines, varies linearly with thrust chamber propellant flow rate. However, the influence of propellant flow rate is largely cancelled out by the total engine propellant flow rate term in Equation (2-2). Even in engines with propellant bleed systems, bleed flow rates are typically minimal, and total engine propellant flow rate is dominated by thrust chamber propellant flow rate.

(a)   *(b)*
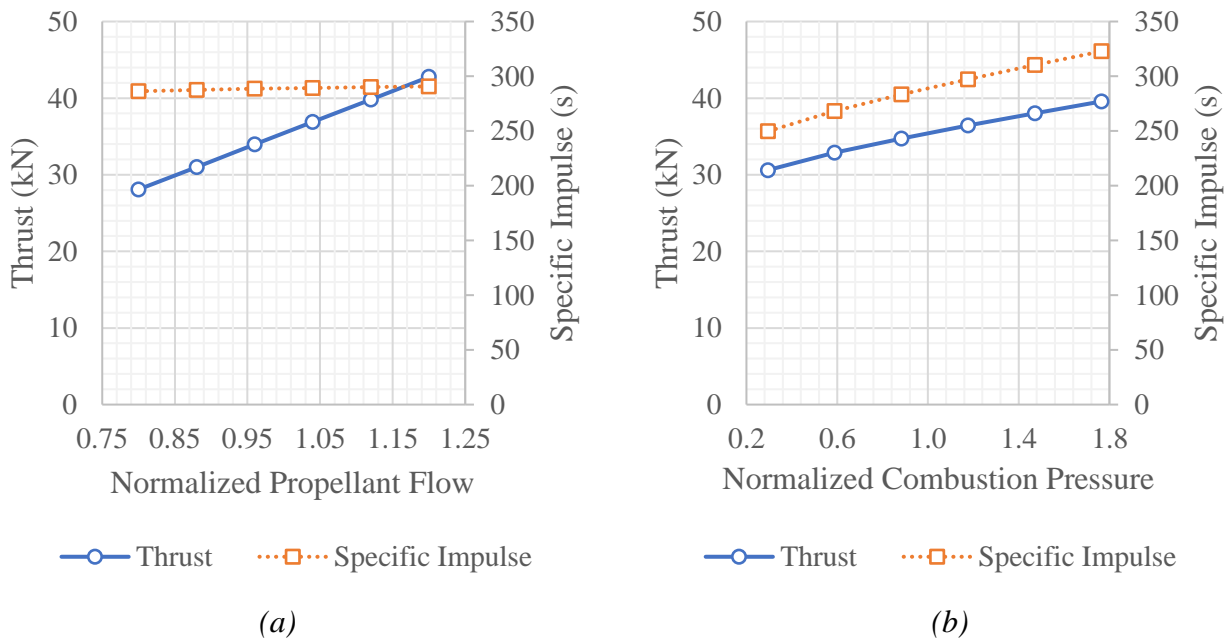
Figure 3-1: Influence of propellant flow and combustion pressure on thrust and specific impulse

Figure 3-1(b) shows that there is an approximate positive linear correlation between combustion pressure and both thrust and specific impulse. This can also be expected. Increased combustion pressure also increases exhaust pressure, which would increase thrust as shown in Equation (2-1), and in doing so would also increase specific impulse, as shown in Equation (2-2). The pressure thrust component in Equation (2-1) ($(p_E - p_a)A_E$) does not typically have a significant impact on net thrust, but increased combustion pressure also increases the "pressure energy" available

to be converted into kinetic energy by the exhaust nozzle, in accordance with the second law of thermodynamics. As a result, increased combustion pressure results in not only increased exhaust pressure, but also increased exhaust velocity.

Figure 3-2(a) shows that there is no significant correlation between fuel injection temperature and either thrust or specific impulse. Similarly, Figure 3-2(b) shows that there is no relationship between oxidizer injection temperature and either thrust or specific impulse. As such, the influence of these variables on the functions for thrust and specific impulse described in Equations (3-1) and (3-2) is negligible.

(a)   *(b)*
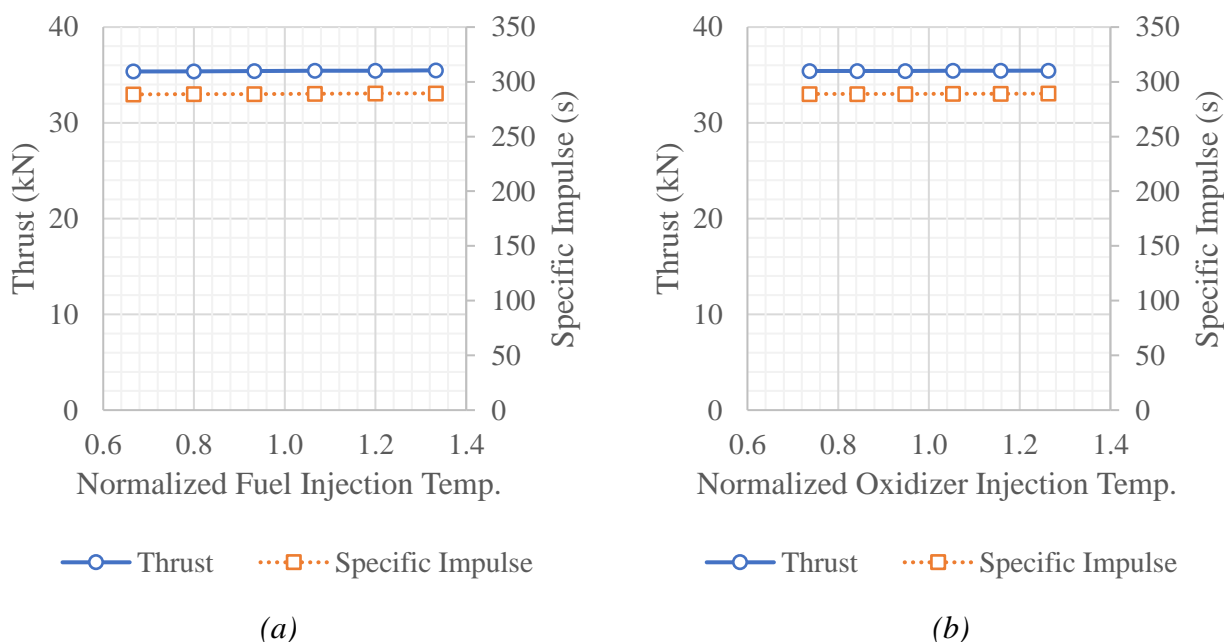
Figure 3-2: Influence of (a) fuel and (b) oxidizer injection temperatures on thrust and specific impulse

Figure 3-3 shows that there is a negative correlation between combustion mixture ratio and both thrust & specific impulse (i.e. thrust and specific impulse increase with decreasing mixture ratio). Decreasing mixture ratio results in increased combustion temperature, lowering combustion heat release. Based on the first law of thermodynamics, lower heat release results in less energy available to accelerate exhaust gasses in the nozzle, resulting in lower exhaust velocity. However, changing the mixture ratio also changes the composition of the exhaust gasses. A lower mixture ratio therefore increases the presence of hydrogen in the exhaust gas flow. The low molecular weight of hydrogen reduces the energy required to accelerate a hydrogen-rich exhaust gas. The effect of lower exhaust gas molecular weight appears to outweigh the effect of lower combustion energy release, resulting in a higher exhaust gas velocity and improved thrust and specific impulse at lower mixture ratios.
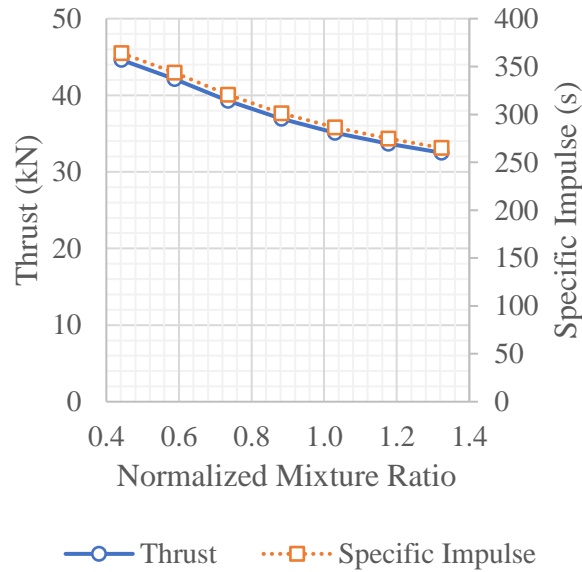
Figure 3-3: Influence of combustion mixture ratio on thrust and specific impulse

This simplified sensitivity analysis does neglect some factors and effects. By using isentropic flow theory, heat transfer into the walls and nozzle efficiency are not considered. Also, isentropic flow theory assumes an ideal gas equation of state. The exhaust gasses are predominantly comprised of water vapor, which is not typically considered an ideal gas. Viscous effects, injector performance and species transport are also neglected. While these simplifications are clearly introducing some error in the analysis, the general trends of variables which impact engine performance are clear. As a result of this analysis, Equations (3-1) and (3-2) can be rewritten to remove variables with no significant impact on the respective functions. This is shown in Equations (3-3) and (3-4).

$$F_T \approx f(MR_C, \dot{m}_{TC}, p_C) \qquad (3\text{-}3)$$

$$I_{SP} \approx f(MR_C, p_C) \qquad (3\text{-}4)$$

3.2   Factors Affecting Thrust Chamber Life

For the purposes of this study, "thrust chamber life" is defined as the number of combustion cycles to failure for each of the three failure modes described in the Porowski model (plastic instability, low-cycle fatigue and creep deformation). Methods for calculating combustion cycles to failure for each failure mode are described in Sections 2.2.2 and 2.2.3. Through a process of substitution of relevant functions from Sections 2.2.2 and 2.2.3 and elimination of parameters that are constant or invariable (for the purposes of this analysis), the expressions for the number of combustion cycles to

failure for all three failure modes can be distilled to functions of a set of relevant variables, as shown in Equations (3-5) to (3-7). This functional analysis is described in detail in Appendix A-2.

$$N_{F,PI} = f(t_C, T_{l1}, \Delta p_l, \Delta T_l, \Delta T_w) \tag{3-5}$$

$$N_{F,f} = f(t_C, T_{l1}, \Delta p_l, \Delta T_l, \Delta T_w) \tag{3-6}$$

$$N_{F,cr} = f(t_C, T_{l1}, \Delta p_l, \Delta T_l, \Delta T_w) \tag{3-7}$$

Equations (3-5) to (3-7) show that the number of cycles to failure for all three failure modes are functions of the same variables. These variables are combustion time, maximum wall ligament temperature, differential pressure loading, temperature difference across the ligament and temperature difference between the ligament and the close-out wall. The relative influence of each of the variables shown in Equations (3-5) to (3-7) can be quantitatively demonstrated through simplified sensitivity analysis. This analysis has been performed using the equations in Subsections 2.2.2 and 2.2.3 to estimate cycles to failure for each failure mode. Once again, the constant values used in this analysis loosely reflect the GH_2/LOx-fed thrust chamber in the JAXA reusable rocket engine operating at 100% thrust, or by using reasonable estimates where there is no data available (i.e. Δp_l and ΔT_l). The material data described in Subsection 4.6.2 was also used in this analysis. Calculations are performed at the nozzle throat, assuming this is the location of maximum heat transfer, and therefore minimum cycles to failure. The variable values shown in Equations (3-5) to (3-7) represent deviations from the nominal values at 100% thrust.

The results of this sensitivity analysis are shown in Figure 3-4 to Figure 3-8. Figure 3-4 shows that combustion time has no significant impact on any of the three failure modes. This is likely due to combustion time only affecting creep deformation, as shown in Equation (2-30). This variable has no effect on other deflections, which may be a more significant source of plastic deformation in the ligament. As such, the impact of combustion time on service life can be considered negligible.

Figure 3-5 shows the relationship between maximum ligament temperature and cycles to failure. There is clearly a negative correlation between maximum ligament temperature and plastic instability failure (i.e. as maximum temperature increases, cycles to plastic instability failure decreases). At temperatures below nominal (i.e. a normalized value of 1.0), Figure 3-5 also shows no significant relationship between maximum ligament temperature and fatigue failure, and a similar lack of correlation between maximum ligament temperature and creep failure at lower temperatures.
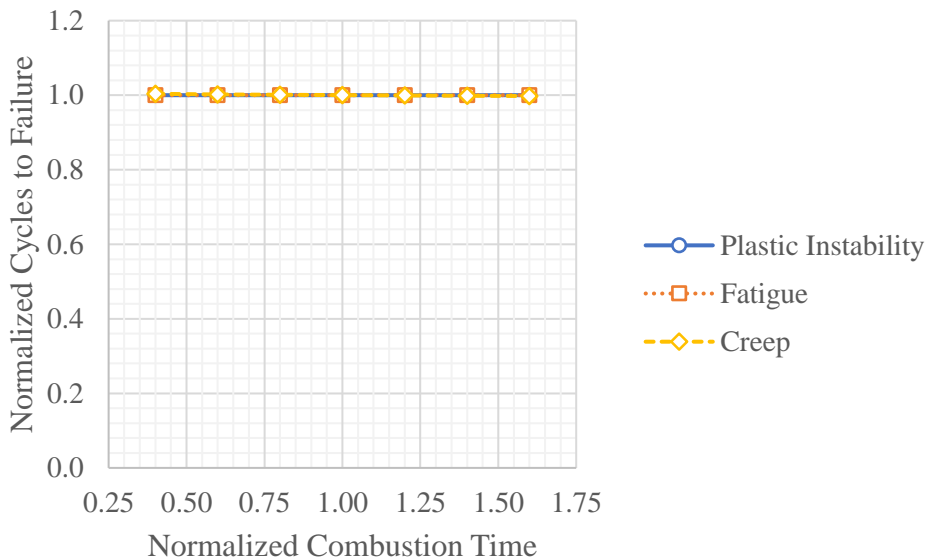
Figure 3-4: Influence of combustion time on thrust chamber failure modes
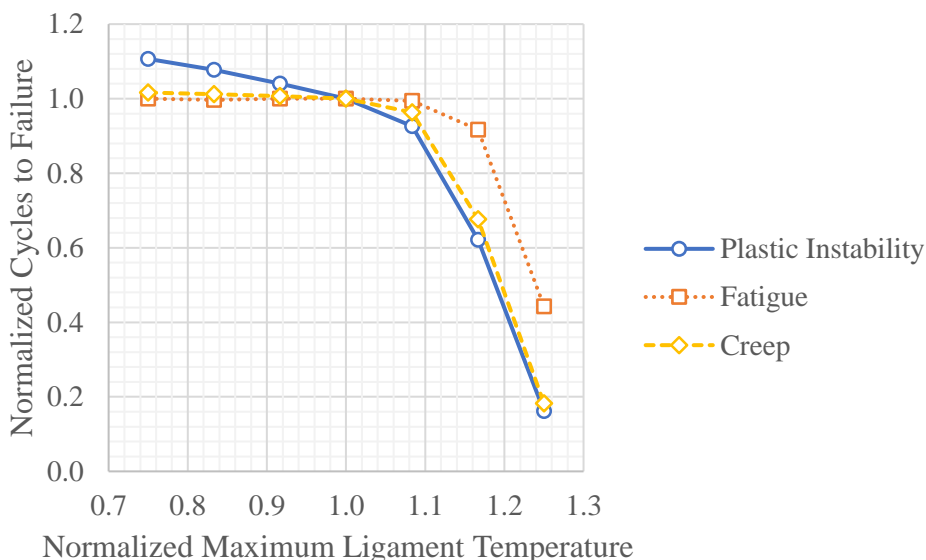
Figure 3-5: Influence of maximum ligament temperature on thrust chamber failure modes

For all three failure modes, Figure 3-5 shows a precipitous decline in cycles to failure at temperatures above a normalized value of 1.1. This is likely due to an increase in temperature-dependent creep deformation. The Norton law constant, which governs strain rate, is actually a function of temperature, as described in Subsection 4.6.2. Due to this exponential relationship, the value of this constant increases substantially above the "creep threshold" temperature. This leads to creep deformation becoming the dominant source of deflection in Equation (2-10). As such, it can be seen that there is a relationship between maximum ligament temperature and all three failure modes.

Figure 3-6 shows the relationship between differential pressure load and cycles to failure. There is no significant correlation between differential pressure load and the number of cycles to fatigue failure. However, there is a negative correlation between differential pressure load and plastic instability failure. Figure 3-6 also shows a similar negative correlation between differential pressure load and creep failure. Thus, while there is a relationship between differential pressure load and the creep and plastic instability failure modes, there is no such relationship between differential pressure load and fatigue failure.
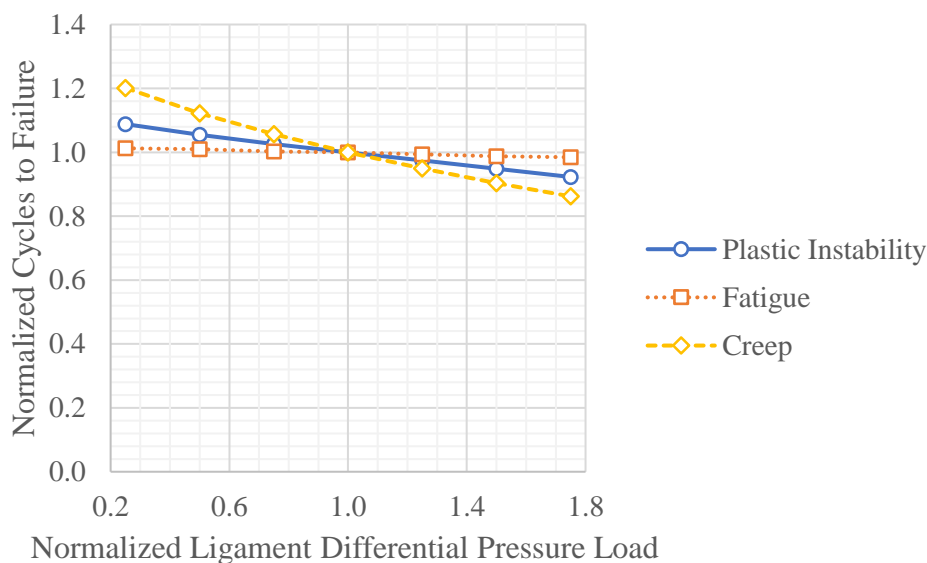
Figure 3-6: Influence of differential pressure load on thrust chamber failure modes

Figure 3-7 shows the relationship between ligament temperature difference and cycles to failure. There is no significant correlation between ligament temperature difference and the number of cycles to fatigue failure. However, there is a negative correlation between ligament temperature difference and plastic instability failure. Figure 3-7 also shows a similar negative correlation between ligament temperature difference and creep failure. Thus, while there is a relationship between ligament temperature difference and the creep & plastic instability failure modes, there is no such relationship between ligament temperature difference and fatigue failure.

Figure 3-8 shows the relationship between wall temperature difference and cycles to failure. There is a strong negative correlation between wall temperature difference and all three failure modes. These correlations are likely due to the impact of thermally-induced hoop strains arising from the difference in temperature between the ligament and close-out wall, as shown in Equation (2-19). As such, it can be seen that there is a relationship between wall temperature difference and all three failure modes.
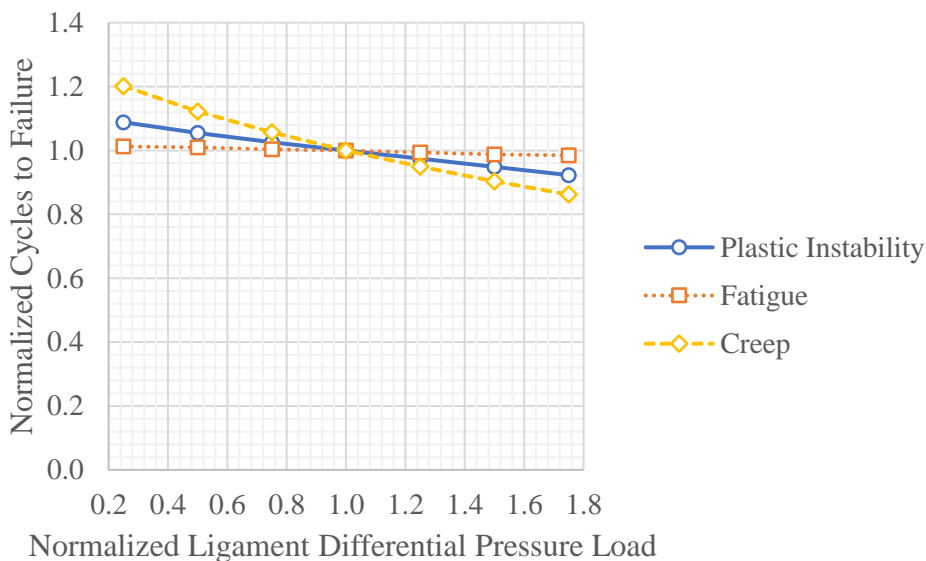
Figure 3-7: Influence of ligament temperature difference on thrust chamber failure modes
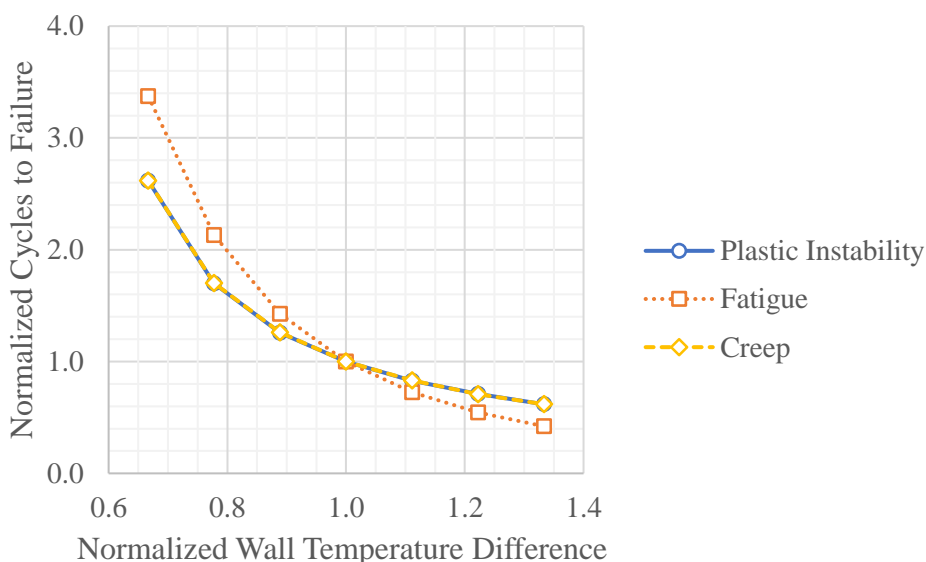
Figure 3-8: Influence of wall temperature difference on thrust chamber failure modes

As with the sensitivity analysis described in Section 3.1, some of the simplifications in the Porowski model may introduce some error in this analysis. For example, without a detailed FEM model, other important structural behaviours may be overlooked, such as cumulative damage at not only the ligament centre but also the rib centre, which other studies have taken into account[16]. It should be noted however, that the Porowski model has previously been verified against FEM results[26-28]. Thus, while simplifications may introduce some error in this analysis, the general trends of variables which impact the number of cycles to failure for each failure mode are clear. As a result of this analysis,

Equations (3-5) to (3-7) can be rewritten to remove variables with no significant impact on the respective functions. This is shown in Equations (3-8) to (3-10).

$$N_{F,PI} \approx f(T_{l1}, \Delta p_l, \Delta T_l, \Delta T_w) \tag{3-8}$$

$$N_{F,f} \approx f(T_{l1}, \Delta T_w) \tag{3-9}$$

$$N_{F,cr} \approx f(T_{l1}, \Delta p_l, \Delta T_l, \Delta T_w) \tag{3-10}$$

3.3 Factors Affecting Thrust Chamber Heat Transfer

Section 3.2 shows that maximum wall temperature, temperature difference across the ligament and temperature difference between the ligament and closeout wall influence thrust chamber life (as measured by the number of cycles to failure). These three temperature values are all influenced by heat transfer through the wall. Thrust chamber wall heat transfer formulas are described in Section 2.2.4. Through a process of substitution of relevant functions from Section 2.2.4, elimination of parameters that are constant or invariable (for the purposes of this analysis), and assuming an isobaric, adiabatic combustion reaction with discrete, specified reactants (fuel and oxidizer) in the thrust chamber, expressions for the three temperature values can be distilled to a functions of a set of relevant operating condition variables, as shown in Equations (3-11) to (3-13). This functional analysis is described in detail in Appendix A-3.

$$T_{l1} = f(MR_{TC}, \dot{m}_{CC}, p_{CC}, p_{TC}, T_{CC}, T_{FI}, T_{OI}) \tag{3-11}$$

$$\Delta T_l = f(MR_{TC}, \dot{m}_{CC}, p_{CC}, p_{TC}, T_{CC}, T_{FI}, T_{OI}) \tag{3-12}$$

$$\Delta T_w = f(MR_{TC}, \dot{m}_{CC}, p_{CC}, p_{TC}, T_{CC}, T_{FI}, T_{OI}) \tag{3-13}$$

Equations (3-11) to (3-13) show that maximum ligament temperature, ligament temperature difference and wall temperature difference are all functions of the same variables: combustion mixture ratio, cooling channel mass flow rate and pressure, combustion pressure and cooling channel, fuel injection & oxidizer injection temperatures. A simplified sensitivity analysis can be used to quantify the effect of these variables individually on the thrust chamber wall temperature distribution. As with the analyses in Sections 3.1 and 3.2, this analysis is based on the JAXA reusable rocket engine thrust chamber and cooling channels operating at 100% thrust. The equations described in Subsection 2.2.4 can be used along with CEA (for combustion calculations) and interpolation of a coolant state variable database (assuming the coolant is pure H_2) as described in Subsection 4.3.2.

The constant values used in this analysis loosely reflect the GH2/LOx-fed thrust chamber and LH2-fed cooling channels in the JAXA reusable rocket engine operating at 100% thrust, or by using reasonable estimates where there is no data available (i.e. $\bar{A}$). The variable values shown in Equations (3-11) to (3-13) represent deviations from the nominal values at 100% thrust. The material data described in Subsection 4.4.6 was also used in this analysis. Calculations are performed at the nozzle throat, assuming this is the location of maximum heat transfer. Surface areas are estimated by multiplying the relevant dimension by a unit length. Solutions for the wall temperature distribution functions are determined iteratively based on the variables listed in Equations (3-11) to (3-13).

The results of the sensitivity analysis are shown in Figure 3-9 to Figure 3-15. Figure 3-9 shows that there is a nonlinear relationship between combustion mixture ratio and thrust chamber temperature distribution, in terms of maximum wall temperature, ligament temperature difference and ligament-closeout wall temperature difference. All three relationships show a maximum value at a combustion mixture ratio between 6.0 and 7.0. At both higher and lower values, the values decrease, with these decreases being more significant at mixture values lower than 6.0, in comparison to values higher than 7.0. Thus, combustion mixture ratio as a variable influences the wall temperature distribution functions in Equations (3-11) to (3-13).
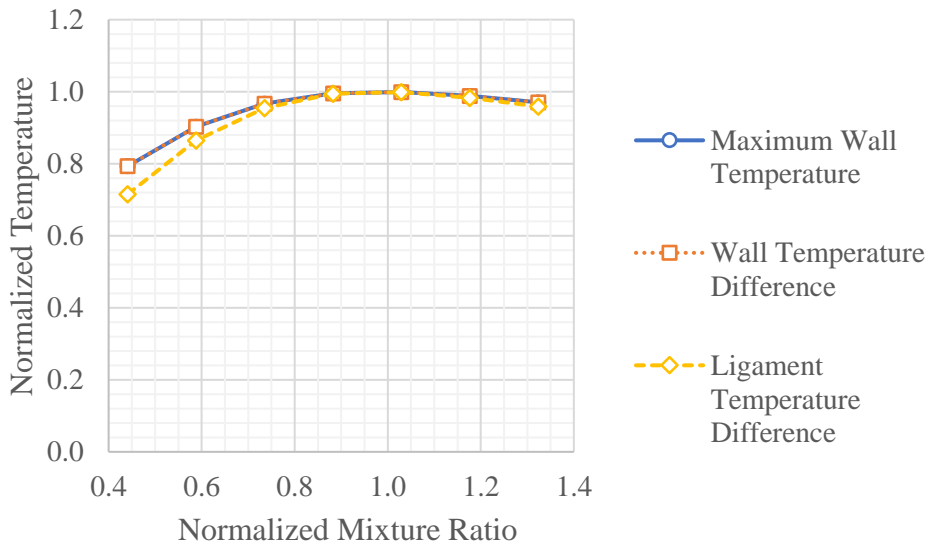
Figure 3-9: Influence of combustion mixture ratio on thrust chamber wall temperature distribution

Figure 3-10 shows a positive correlation between combustion pressure and thrust chamber temperature distribution. As combustion pressure increases, wall temperature, ligament temperature difference and ligament-closeout wall temperature difference also increase. This is to be expected due to the influence of thrust chamber stagnation pressure on the Bartz heat transfer coefficient, as shown

in Equation (2-50). Thus, combustion mixture ratio as a variable influences the wall temperature distribution functions in Equations (3-11) to (3-13).
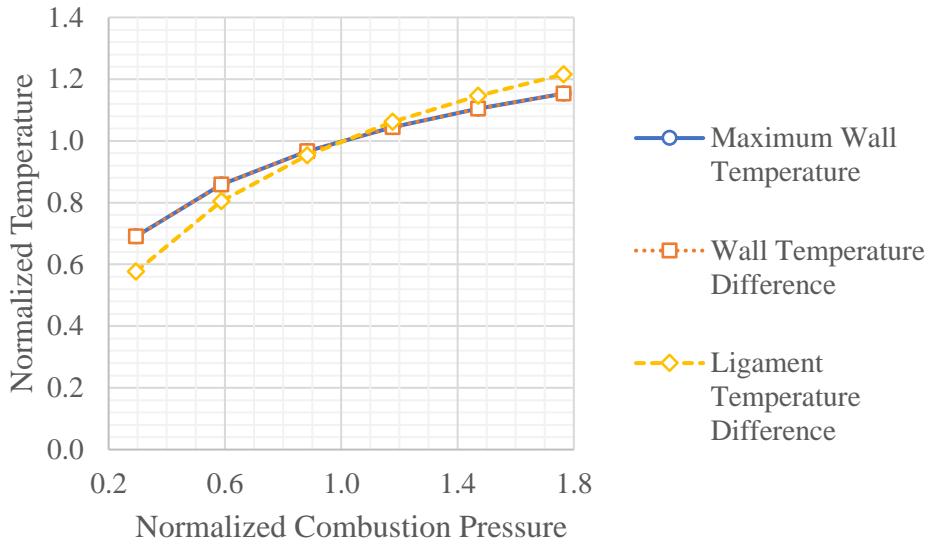
Figure 3-10: Influence of combustion pressure on thrust chamber wall temperature distribution

Figure 3-11 shows the relationship between fuel injection temperature and thrust chamber temperature distribution. Similarly, Figure 3-12 shows the relationship between oxidizer injection temperature and thrust chamber temperature distribution. It can be seen that neither fuel nor oxidizer injection temperature has a significant influence on wall temperature distribution. Thus, these injection temperatures as variables do not influence the wall temperature distribution functions in Equations (3-11) to (3-13), and can be removed from these functions as independent variables.
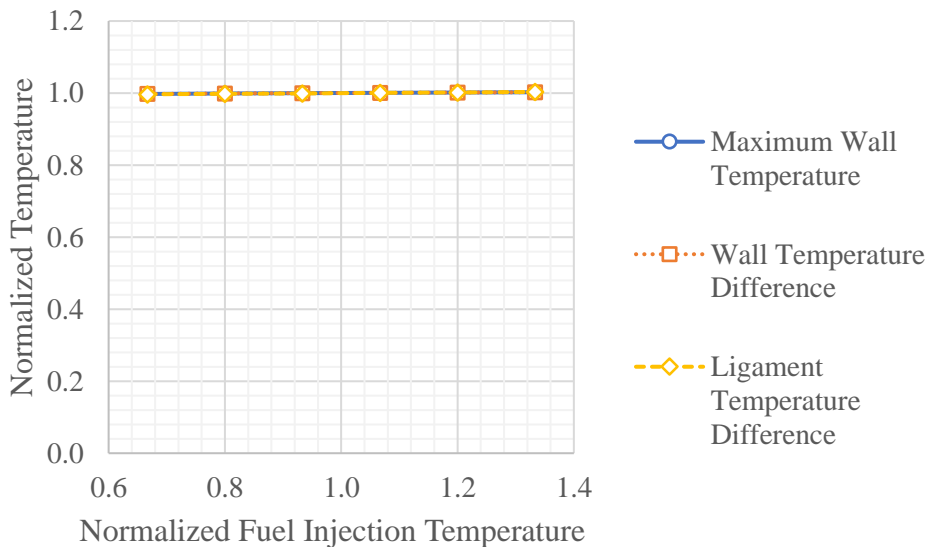
Figure 3-11: Influence of fuel injection temperature on thrust chamber wall temperature distribution
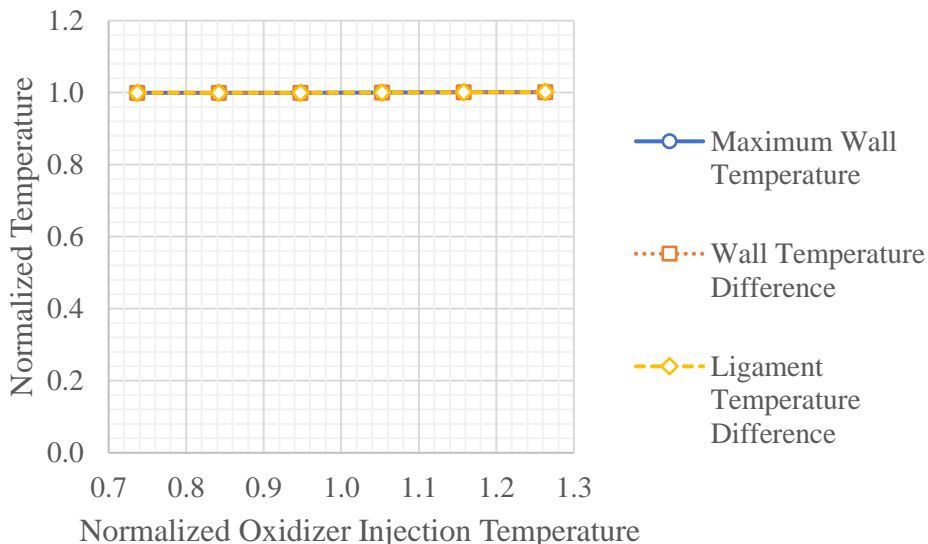
Figure 3-12: Influence of oxidizer injection temperature on thrust chamber wall temperature distribution

Figure 3-13 shows the relationship between coolant flow rate and wall temperature distribution. There is a negative correlation between coolant flow rate and maximum wall temperature – as coolant flow rate increases, maximum wall temperature decreases. This is to be expected as a higher coolant flow would remove more heat from the wall, reducing the maximum temperature. There is also a positive correlation between coolant flow rate and the temperature difference across the ligament. This is also to be expected as the higher coolant flow would have a larger cooling effect on the outer ligament surface, rather than the inner ligament surface. This leads to a higher temperature difference.
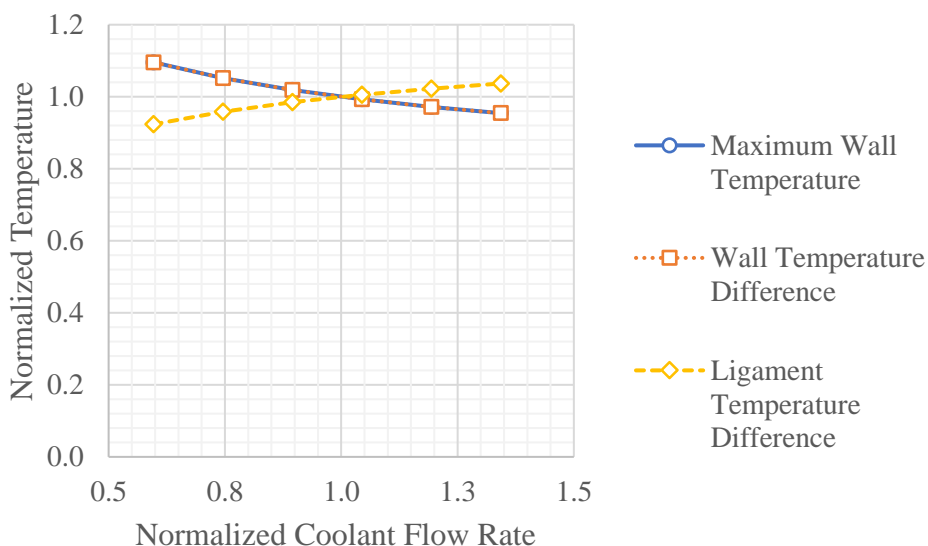
Figure 3-13: Influence of coolant flow rate on thrust chamber wall temperature distribution

Figure 3-13 also shows a negative correlation between coolant flow rate and ligament-closeout wall temperature difference – as coolant flow rate increases, maximum wall temperature decreases. This may not be accurate, as a higher coolant flow could be expected to reduce heat flux into the closeout wall, increasing the temperature difference. However, the Porowski wall heat transfer model expresses closeout wall temperature simply as a linear function of ligament temperature, as shown in Equation (2-49). As such, this model cannot accurately capture changes in wall temperature distribution due to changes in cooling channel flow. Regardless, Figure 3-13 clearly shows that coolant flow rate as a variable influences the wall temperature distribution functions in Equations (3-11) to (3-13).

Figure 3-14 shows the relationship between coolant pressure and thrust chamber temperature distribution. It can be seen that coolant pressure does not have a significant influence on wall temperature distribution. This is to be expected as coolant pressure only influences coolant heat transfer as a state variable for estimating fluid properties which are used in the Colburn heat transfer coefficient, as shown in Equation (2-54). Even large changes in pressure may not result in significant property variations. Thus, coolant pressure as a variable does not influence the wall temperature distribution functions in Equations (3-11) to (3-13), and can be removed from these functions as an independent variable.
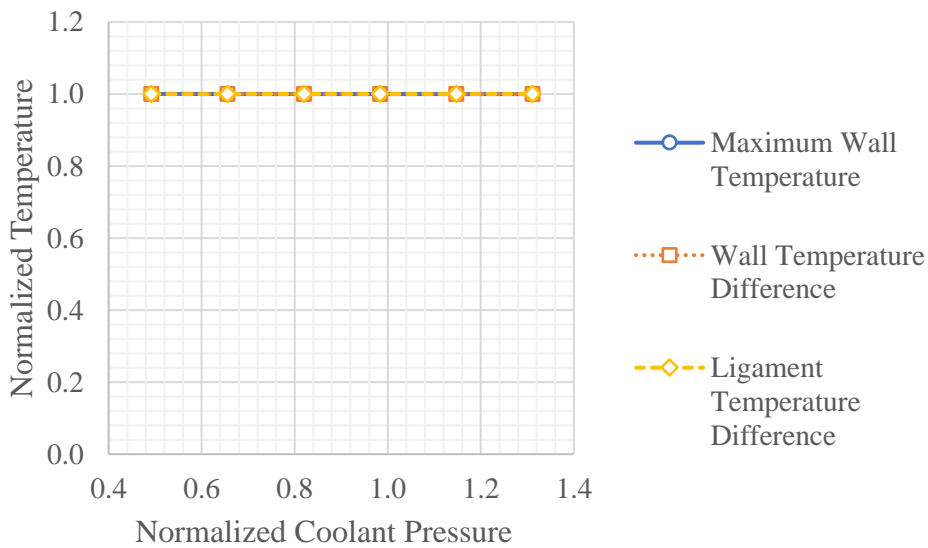
Figure 3-14: Influence of coolant pressure on thrust chamber wall temperature distribution

Figure 3-15 shows the relationship between coolant temperature and thrust chamber temperature distribution. There is a positive correlation between coolant temperature and maximum wall temperature – as coolant temperature increases, maximum wall temperature also increases. This is to be expected as a higher coolant temperature would lower heat flux into the coolant, allowing the

maximum temperature to remain high. There is also a negative correlation between coolant temperature and ligament temperature difference – as coolant temperature increases, ligament temperature difference decreases. This is also to be expected as a higher coolant temperature would allow the outer ligament temperature to be maintained at a higher level, reducing the difference between the inner and outer temperatures.
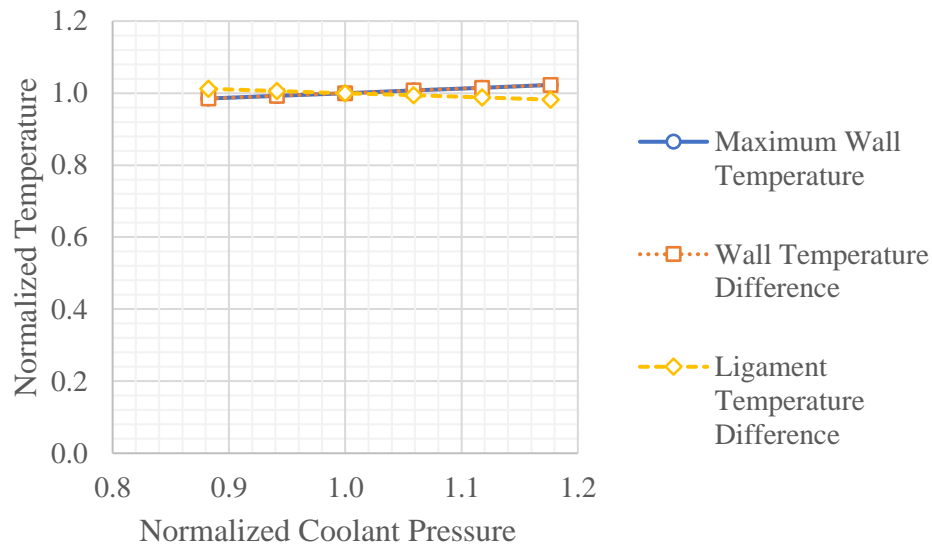
Figure 3-15: Influence of coolant temperature on thrust chamber wall temperature distribution

Figure 3-15 shows a positive correlation between coolant temperature and ligament-closeout wall temperature difference – as coolant temperature increases, maximum wall temperature also increases. As with the coolant flow rate result shown in Figure 3-13(b), this may not be accurate, as a higher coolant temperature could be expected to increase heat flux into the closeout wall, reducing the temperature difference. Once again, this discrepancy is likely due to oversimplification of the Porowski wall heat transfer model in Equation (2-49). Notwithstanding the results shown in Figure 3-15, coolant temperature at the throat cannot be controlled directly. The most effective way of controlling the coolant temperature at the throat is likely by varying the coolant flow rate, which increases or decreases the heat flow into the coolant in the upstream of the throat. Thus, coolant temperature at the throat can be considered as a function of coolant flow rate, which is already accounted for in the wall temperature distribution functions in Equations (3-11) to (3-13). As such, coolant temperature can be removed from these functions as an independent variable.

While the assumptions and simplifications used in this analysis may be introducing some quantitative error into the results, the general trends of variables which impact thrust chamber wall heat transfer are clear. As a result of this analysis, Equations (3-11) to (3-13) can be rewritten to remove

variables with no significant impact on the respective functions. This is shown in Equations (3-14) to (3-16).

$$T_{l1} \approx f(MR_{TC}, \dot{m}_{CC}, p_{TC}) \tag{3-14}$$

$$\Delta T_l \approx f(MR_{TC}, \dot{m}_{CC}, p_{TC}) \tag{3-15}$$

$$\Delta T_w \approx f(MR_{TC}, \dot{m}_{CC}, p_{TC}) \tag{3-16}$$

3.4   Hypothesis

Equation (3-3) shows that thrust can be considered as a function of combustion mixture ratio, thrust chamber propellant flow rate and combustion pressure. Similarly, Equation (3-4) shows that specific impulse can be considered as a function of combustion mixture ratio and pressure. For ease of reference, these results are repeated in Equation (3-17) (for thrust) and Equation (3-18) (for specific impulse).

$$F_T \approx f(MR_{TC}, \dot{m}_{TC}, p_{TC}) \tag{3-17}$$

$$I_{SP} \approx f(MR_{TC}, p_{TC}) \tag{3-18}$$

The results of the analysis in Section 3.2 (Equations (3-8) to (3-10)) show that the cycles to failure for the three failure modes (plastic instability, low-cycle fatigue and creep) can be expressed variously as functions of ligament inner temperature, ligament temperature difference, ligament differential pressure load and wall (ligament to close-out) temperature difference. The results of the analysis in Section 3.3 (Equations (3-14) to (3-16)) show that the ligament inner temperature, ligament temperature difference and wall temperature difference can be expressed as functions of combustion mixture ratio, cooling channel mass flow rate and combustion pressure. Also, Equation (2-11) shows that differential pressure load is a function of thrust chamber pressure (which itself is influenced by combustion pressure) and coolant pressure. The results from Sections 3.2 and 3.3 can therefore be combined by substituting Equations (3-14) to (3-16) into Equations (3-8) to (3-10). This is shown in Equations (3-19) to (3-21).

$$N_{F,PI} \approx f(MR_{TC}, \dot{m}_{CC}, p_{TC}, p_{CC}) \tag{3-19}$$
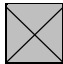
$$N_{F,f} \approx f(MR_{TC}, \dot{m}_{CC}, p_{TC}) \tag{3-20}$$
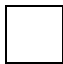
$$N_{F,cr} \approx f(MR_{TC}, \dot{m}_{CC}, p_{TC}, p_{CC}) \tag{3-21}$$

Table 3-1 shows the functional relationships described in Equations (3-17) to (3-21). The dependent variables can be broadly grouped into two categories: "engine performance" (thrust and/or specific impulse) and "thrust chamber life" (cycles to plastic instability, fatigue and/or creep failure). Table 3-1 shows Coolant flow rate and pressure affect thrust chamber life, but have a negligible impact on engine performance. Combustion mixture ratio influences both engine performance and thrust chamber life. Propellant flow rate only influences engine performance, and has a negligible impact on thrust chamber life. However, due to the requirement to maintain sonic flow conditions at the throat, and geometry constraints, combustion pressure and propellant flow rate must be coupled – any variation in one of these values necessitates an adjustment of the other. As such, these two variables cannot be isolated from each other. Thus, all discussions henceforth will describe variations in combustion pressure, with the implication that such variations will also affect propellant flow rate. Table 3-1 shows that changes in combustion pressure can influence both engine performance and thrust chamber life.

Table 3-1: Engine performance and thrust chamber life functional relationships

	Thrust	Specific Impulse	Plastic Instability	Fatigue	Creep
Combustion Mixture Ratio	⊠	⊠	⊠	⊠	⊠
Propellant Flow Rate	⊠				
Combustion Pressure	⊠	⊠	⊠	⊠	⊠
Coolant Flow Rate			⊠	⊠	⊠
Coolant Pressure			⊠		⊠

⊠ = Functional Relationship

☐ = Negligible Functional Relationship

These preliminary results indicate that it may be possible to extend thrust chamber life without detrimentally impacting engine performance by adjusting one or more of these operating conditions (combustion mixture ratio, combustion pressure/propellant flow rate, coolant flow rate and/or coolant pressure). The aim of this study is to individually and quantitatively investigate the influence of these operating conditions on thrust chamber life and engine performance. This is achieved by developing a model of engine behaviour to simulate system-level responses (such as engine performance) to changes

in operating conditions, and adopting a structural model for the thrust chamber to assess cumulative damage, failure and life. In particular, this study will assess engine performance and thrust chamber life using the JAXA reusable rocket engine as a case study, under the following conditions:

a)   Control case (normal operating conditions)

b)   Variable coolant pressure case (all other functional variables held constant)

c)   Variable coolant flow rate case (all other functional variables held constant)

d)   Variable mixture ratio case (all other functional variables held constant)

e)   Variable combustion pressure & propellant flow rate case (all other functional variables held constant)*

Note: Combustion pressure and propellant flow rate are coupled as described above.

In the design of launch vehicles, engine performance is a high-level design requirement which impacts the design of various systems, and is not typically considered flexible. Thus, an optimization of thrust chamber life will also be conducted, with engine performance considered as a constraint. Thrust will be held at a constant level, and specific impulse will be constrained to be above a minimum level, in accordance with design specifications. Using the results of the other cases as a guide, operating conditions for optimal thrust chamber life will be explored under these constraints. It is anticipated that the results of this investigation will show that thrust chamber life can be extended by some margin without performance losses through some combination of operating condition adjustments.

4.   Method

In this chapter, the methods used to collect data in this study are described. Section 4.1 gives an overview of the case study used in this project. Section 4.2 describes how the models described in Sections 4.3 to 4.6 were integrated together for data collection. Section 4.3 describes the models of all engine subsystems other than the thrust chamber and cooling channels. Section 4.4 describes the CFD model of the thrust chamber. Section 4.5 describes the CFD model of the cooling channels. Section 4.6 describes how the Porowski model was implemented as the thrust chamber structural model. Finally, Section 4.7 describes the individual data collection procedure used for each of the cases described in Section 3.4.

4.1   Case Study

As described in Section 3.4, this project involves a case study of the JAXA reusable rocket engine design. All models described in this chapter represent this engine. The JAXA reusable engine was selected as a representation of the state of the art in reusable rocket engine design, it's similarity to future reusable propulsion systems, and availability of requisite design and reference data. Having achieved a verified design life of 100 flight cycles, the JAXA reusable rocket represents cutting-edge reusable liquid rocket engine technology, developed with a strong design focus on reusability and service life[16]. As a result, the engine far exceeds the 4-MDC standard of similar expendable engines.

As a LH_2/LOx-fed engine, the JAXA reusable rocket engine arguably represents the future of reusable propulsion systems. As the rocket launch industry moves towards daily operations of reusable vehicles, exhaust gas emissions (which are currently negligible on a global scale) will become a more significant concern. "Zero-carbon" fuels, such as LH_2, have a distinct advantage here, and will therefore likely play a key role in future high-volume reusable space transportation. Finally, as this project was undertaken at ISAS/JAXA, detailed design information and reference data for the engine, which is typically not publicly available, could be used as reference information to develop detailed and accurate models. For these reasons, the JAXA reusable rocket engine was selected as a case study for this project.

Operationally, when used in a VTVL vehicle such as the RV-X or the Reusable Sounding Rocket, the JAXA reusable rocket engine is subject to a complex load profile – the engine is throttled up to 100% during launch, then shut down during ballistic flight. The engine is then reignited and throttled down to 40% for landing[16]. For simplicity, this study only considers a simple combustion cycle of 100% nominal thrust for a duration of 50 seconds, rather than a more complex load profile based on the flight cycle described above.

4.2 Model Integration

This section gives an overview of how the integrated engine plant and wall structural models are integrated using algorithm flowcharts. Figure 4-1 shows a simplified, high-level diagram of these two models, how they interact, and their respective inputs and outputs. A detailed computation algorithm for the wall structural model is provided in Subsection 4.6.3. Figure 4-2 shows a data and control flow diagram for the engine plant model. Algorithm flowcharts for each individual analytical model shown in Figure 4-2 are included in the relevant sections of Appendix B.
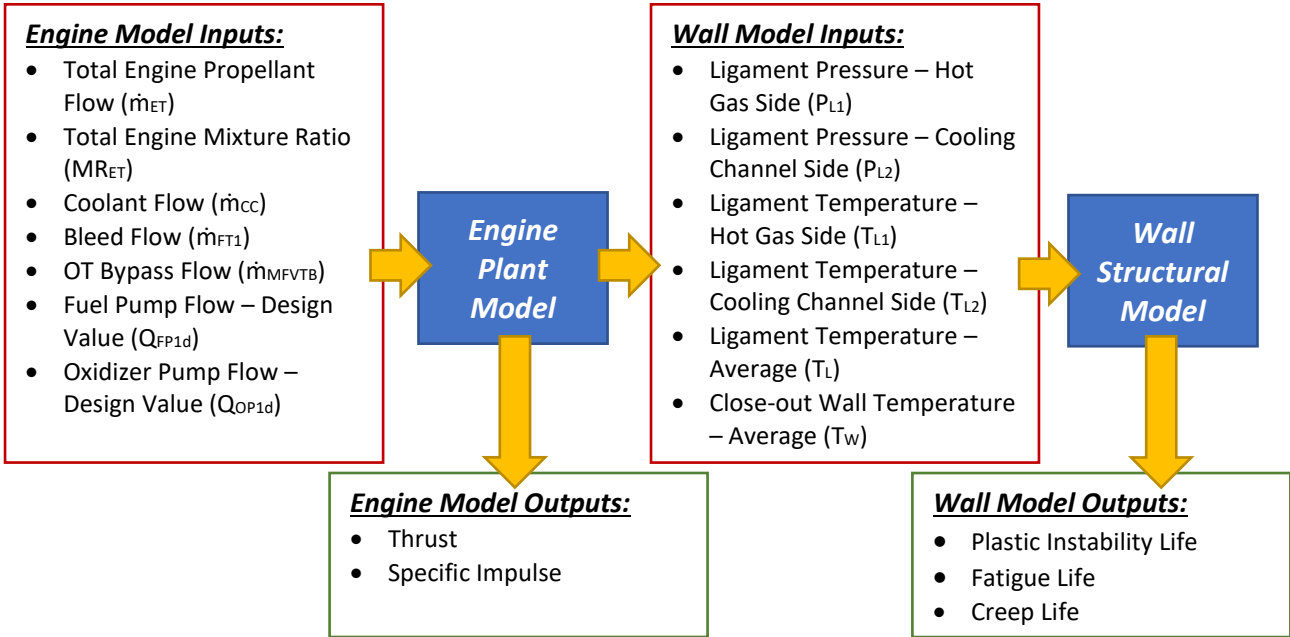
Figure 4-1: Model overview
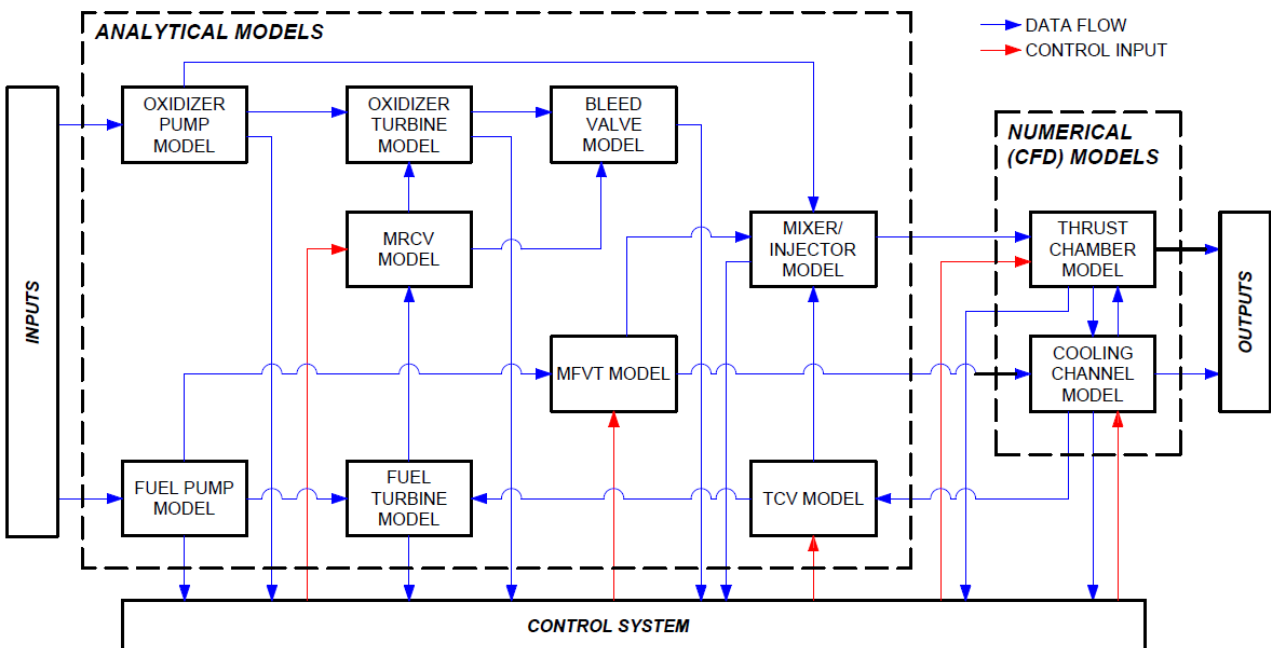
Figure 4-2: Engine plant model data flow diagram

4.3 Engine Subsystem Models

This section introduces the simplified analytical models of all engine subsystems and components, other than the thrust chamber and cooling channels, which are modelled using more detailed and computationally expensive CFD simulations. This includes models of the fuel and oxidizer turbopumps, main fuel valve (throttling) thrust control valve, mixture ratio control valve, the fuel mixer and the injectors. The engine subsystem model codes were written and executed in Microsoft Excel. Refer to Appendix B for detailed descriptions of each model covered by this section.

4.3.1 Engine Subsystem Model Overview

The models described in this section are used to create an integrated plant model of the engine, such that operating limits and flow-on effects of operating condition changes can be analysed. The analytical models of engine components described in this section have been developed using engine design data, test result data, propellant chemical property data and fundamental engineering theorems. Much of the data used to develop these models has not been published and is not otherwise publicly available. As such, the sources of the data are not referenced in this report. In addition, in the interests of protecting intellectual property, most of the original data is withheld from this report, or presented as normalized values. The integration of these models with each other, as well as with the CFD models, is described in Section 4.2.

The engine has been designed to function under specific operating conditions, and the components have been sized accordingly. For example, the turbopumps are of an appropriate size to efficiently pressurize propellants at given flow rates, which correspond to the designed operating conditions. It is expected that this will constrain the range of conditions at which the various operating conditions can be held constant. For example, changing pump flow rates to adjust the mixture ratio may have the unintended consequence of changing the pump head, resulting in a variation in fluid pressures.

The nomenclature established for modelling the various engine components is described in Figure 4-3. The symbols in Figure 4-3 are defined in the Nomenclature section. These symbols are used as subscripts to represent various properties and different locations within the engine. For example, the symbol for the fuel pump discharge has been designated FP2, thus the pressure at the fuel pump inlet is designated as p_{FP2}.
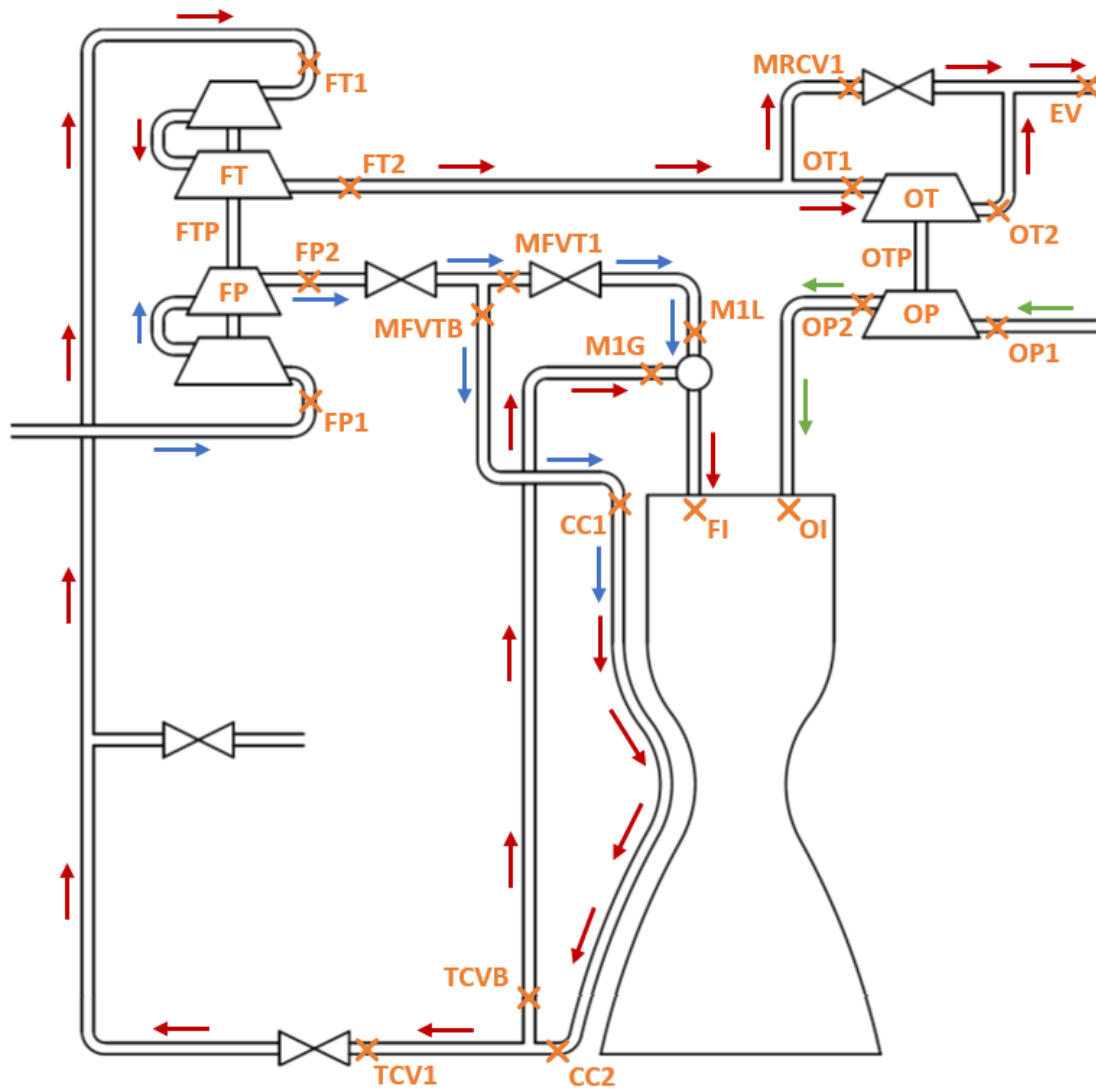
Figure 4-3: Engine component modelling nomenclature

In order to investigate the effect of varying only one operating condition at a time, it is necessary to assume that the engine could be redesigned to function in a way such that operating conditions other than the one of interest remained constant. As such, the component models are designed to be "scalable" – selected input variables are normalized by design values, such as volumetric flow rates, such that the "design point" of the component can be adjusted. It is assumed that smaller or larger components can be designed with similar levels of efficiency, pressure loss and so on, such that the component models remain valid at smaller or larger scales.

4.3.2 Chemical Property Data

A method for determining the properties of the fuel and oxidizer at different states as they flow through the engine is required. Specifically, the relationship between temperature, pressure, density, specific enthalpy, specific entropy, viscosity, specific heat ratio and the speed of sound needs to be determined at several different points. Interpolation of thermo-physical chemical property tables is

considered more appropriate than alternative methods, such as gas law modelling. This data is more accurate than a using gas law estimate, such as the ideal gas law, and allows for all the required properties at a point to be determined using just two known state variables.

Interpolation of property data requires the tabulation of this data for both molecular hydrogen and molecular oxygen at a wide range of different states. Data was sourced from the United States National Institute of Standards and Technology (NIST) REFPROP database[40]. For each table, pressures were specified in the first column, and temperatures were specified in the first row. The tables were then populated with density, specific enthalpy and specific entropy data for both hydrogen and oxygen as well as viscosity, specific heat ratio and the speed of sound (for hydrogen only). This led to the generation of nine separate tables: six for hydrogen, and three for oxygen.

Although this project only focuses on operating the engine at 100% thrust level, the range of data covered by the tables was selected based on the range of temperatures and pressures of the fuel and oxidiser expected at all points in the engine under normal operating conditions (40% - 100% thrust), with the exception of exhaust gasses in the combustion chamber. Some margin was added to these ranges to round off the numbers and allow modelling of non-normal operating conditions outside of these values. The resulting data ranges for the property tables are shown in Table 4-1. In order to populate the interpolation tables, the density, specific enthalpy, specific entropy, viscosity, specific heat ratio and speed of sound data in these ranges must be discretized. The data was discretized to create a sufficiently high resolution which would reduce interpolation errors, while avoiding computational limitations arising from interpolation of large data tables. Considering these factors, the tables were populated with data over the increments described in Table 4-1. This discretization scheme results in tables of 38,577 cells for the fuel properties, and 5,511 cells for oxidizer properties. Given the greater role fuel plays in engine functions (also acting as a coolant and turbine working fluid) it is reasonable for the fuel property tables to be larger and cover a wider range of data.

Table 4-1: Propellant chemical property data table ranges and increments

Propellant Property	Minimum Value	Maximum Value	Data Increment	Number of Rows/Columns
Fuel (H$_2$) Temperature	20.0 K	600.0 K	(20.0 – 40.0 K): 1.0 K (40.0 – 600.0 K): 10.0 K	77
Fuel (H$_2$) Pressure	0.00 MPa	10.00 MPa	0.02 MPa	501
Oxidizer (H$_2$) Temperature	90.0 K	100.0 K	1.0 K	11
Oxidizer (H$_2$) Pressure	0.00 MPa	10.00 MPa	0.02 MPa	501

The propellant data tables were interpolated using bi-linear interpolation. This two-dimensional interpolation method allows properties to be determined at states not explicitly specified in the data tables. Bi-linear interpolation involves three linear interpolations using the four adjacent data points from the property tables. This process is shown in Figure 4-4, for determining density at point "INT", where the temperature at "INT" is higher than the temperature at point "LOW", but lower than the temperature at point "HIGH" (i.e. $T_{LOW} < T_{INT} < T_{HIGH}$). Also, the pressure at point "INT" is higher than the pressure at point "LOW", but lower than the pressure at point "HIGH" (i.e. $P_{LOW} < P_{INT} < P_{HIGH}$). Although density is used as an example here, the same process is used for determining all chemical properties using these tables.
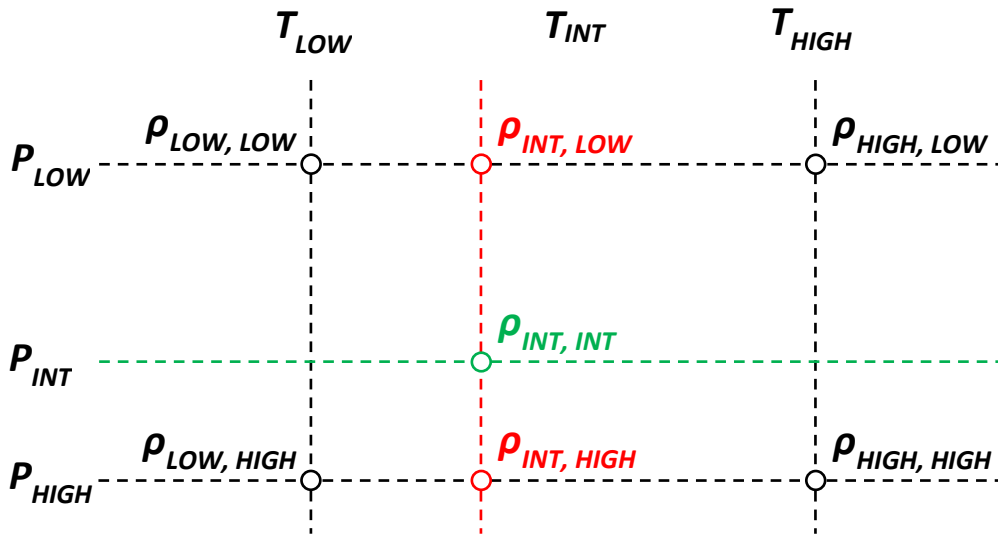
Figure 4-4: Bi-linear interpolation

The goal of the interpolation is to determine a value for the density at a temperature of T_{INT} and a pressure of P_{INT}. The notation $\rho(T_{INT}, P_{INT}) = \rho_{INT,INT}$ is adopted to represent this point, as shown in Figure 4-4. It is possible to use the data tables to look up the density values at the four points closest to $\rho_{INT,INT}$, as shown in Figure 4-4:

- A temperature of T_{LOW} and a pressure of P_{LOW}, i.e. $\rho(T_{LOW}, P_{LOW}) = \rho_{LOW,LOW}$,

- A temperature of T_{HIGH} and a pressure of P_{LOW}, i.e. $\rho(T_{HIGH}, P_{LOW}) = \rho_{HIGH,LOW}$,

- A temperature of T_{LOW} and a pressure of P_{HIGH}, i.e. $\rho(T_{LOW}, P_{HIGH}) = \rho_{LOW,HIGH}$,

- A temperature of T_{LOW} and a pressure of P_{HIGH}, i.e. $\rho(T_{LOW}, P_{HIGH}) = \rho_{LOW,HIGH}$,

The first of three interpolations is used to determine the density at a temperature of T_{INT} and a pressure of P_{LOW}, i.e. $\rho(T_{INT}, p_{LOW}) = \rho_{INT,LOW}$. This point is shown in Figure 4-4. The value $\rho_{INT,LOW}$ can be interpolated from points $\rho_{LOW,LOW}$ and $\rho_{HIGH,LOW}$, as shown in Equation (4-1).

$$\rho_{INT,LOW} = \rho_{LOW,LOW} + \left(\rho_{HIGH,LOW} - \rho_{LOW,LOW}\right)\left(\frac{T_{INT} - T_{LOW}}{T_{HIGH} - T_{LOW}}\right) \qquad (4\text{-}1)$$

The second interpolation is used to determine the density at a temperature of T_{INT} and a pressure of P_{HIGH}, i.e. $\rho(T_{INT}, p_{HIGH}) = \rho_{INT,HIGH}$. This point is also shown in Figure 4-4. The value $\rho_{INT,HIGH}$ can be interpolated from points $\rho_{LOW,HIGH}$ and $\rho_{HIGH,HIGH}$, as shown in Equation (4-2).

$$\rho_{INT,HIGH} = \rho_{LOW,HIGH} + \left(\rho_{HIGH,HIGH} - \rho_{LOW,HIGH}\right)\left(\frac{T_{INT} - T_{LOW}}{T_{HIGH} - T_{LOW}}\right) \qquad (4\text{-}2)$$

Finally, the density $\rho_{INT,INT}$ can be determined by interpolation between points $\rho_{INT,LOW}$ and $\rho_{INT,HIGH}$, as determined from Equations (4-1) and (4-2), respectively. This is shown in Equation (4-3).

$$\rho_{INT,INT} = \rho_{INT,LOW} + \left(\rho_{INT,HIGH} - \rho_{INT,LOW}\right)\left(\frac{p_{INT} - p_{LOW}}{p_{HIGH} - p_{LOW}}\right) \qquad (4\text{-}3)$$

It is also possible to use a similar method to reverse the roles that pressure and temperature play in the interpolation process. Using this method, the first interpolation is performed between $\rho_{LOW,LOW}$ and $\rho_{LOW,HIGH}$, using pressure instead of temperature as the second variable. The second interpolation is performed between $\rho_{HIGH,LOW}$ and $\rho_{HIGH,HIGH}$, once again using pressure instead of temperature as the second variable. The final interpolation is performed between these two points, using temperature instead of pressure as the second variable. This process produces the same result as that described in Figure 4-4 and Equations (4-1) to (4-3).

Typically, a specified pressure and temperature will be used to determine the density, specific enthalpy or specific entropy at a particular point. However, it is also possible to reverse this process to determine pressure or temperature using other properties. For example, if the pressure and specific entropy of the fuel or oxidizer at a point are known, this information can be used to determine the temperature at this point. In this case, the same interpolation process described above is used, however the temperature or pressure becomes an unknown, and the "interpolated" quantity becomes known.

4.4   Thrust Chamber Model

This section describes the CFD model of the thrust chamber developed for this study. The model was developed using ANSYS Fluent[41], a commercial CFD software package.

4.4.1 Domain

The thrust chamber model uses a 2D axisymmetric domain comprised of a fluid region and a solid region. The domain of the model is shown in Figure 4-5. The thin solid region representing the ligament can be seen in the inset of Figure 4-5.
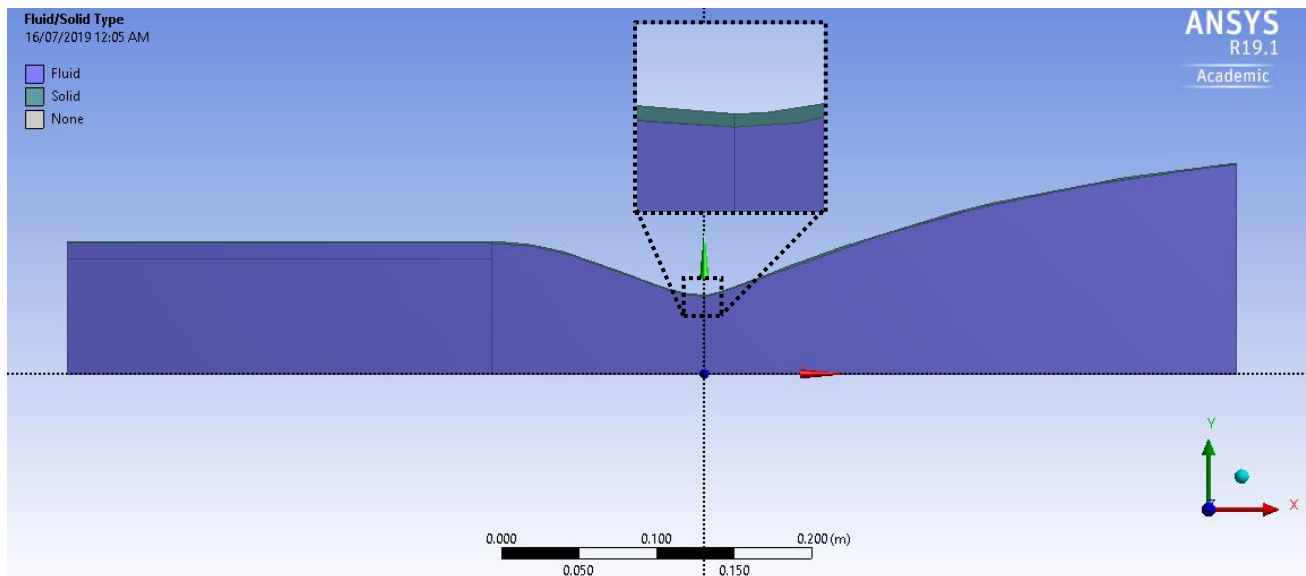
Figure 4-5: Thrust chamber model domain

The fluid region represents the interior of the thrust chamber. It is bounded by the injector faceplate in the upstream direction, the exhaust nozzle exit in the downstream direction, the thrust chamber centreline in the inner radial direction and the solid region in the outer radial direction. The solid region represents the thin ligament separating the thrust chamber from the cooling channel. It is bounded by the injector faceplate plane in the upstream direction, the exhaust nozzle exit plane in the downstream direction, the fluid region (representing the hot gas side of the thrust chamber) in the inner radial direction, and the cooling channel in the outer radial direction. A cartesian coordinate system was adopted, with the origin at the intersection of the throat plane and the thrust chamber centreline. The centreline forms the x axis, with the downstream direction being positive. The y axis is in the radial direction.

A structured mesh was adopted for both the solid and fluid domains. For the fluid mesh, a maximum cell edge length of 0.5mm in the axial direction was specified. In the radial direction, edge biasing was used to achieve a refined mesh near the wall, with 120 divisions and a bias factor of 10.0. The resulting fluid mesh has 178,800 cells. For the solid mesh, the maximum cell edge length in the axial direction was also set to 0.5mm. The number of divisions in the radial direction was set to 4. The resulting solid mesh has 6,140 cells, bringing the total mesh size of the domain to 184,940 cells. The

minimum orthogonal quality of the mesh was 0.22598, and the maximum aspect ratio is 10.971. The resultant mesh is shown in FIG. The solid domain mesh is visible in the inset.
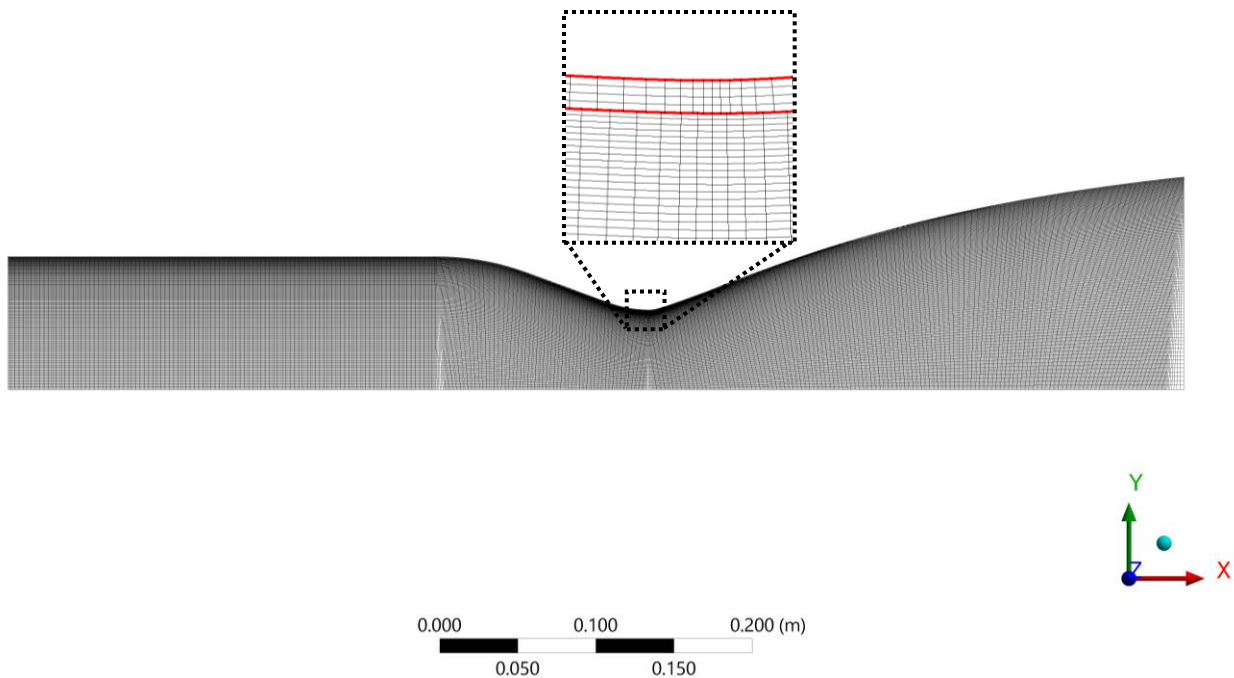
Figure 4-6: Thrust chamber model mesh

4.4.2 Combustion Model

The JAXA reusable rocket engine injector faceplate houses dozens of LOx/GH$_2$ coaxial injectors. Accurately simulating injection, mixing and combustion of propellants in all or small patternable section of all these injectors is beyond the computational capability of the software or hardware used on this project. Instead, CEA[39] was used to simulate combustion reactions, assuming an adiabatic, isobaric reaction. Combustion pressure, mixture ratio and propellant injection temperatures are specified as inputs. An "infinite area combustor" is assumed, such that combustion calculations can be performed without specifying propellant flow rates.

CEA provides output data which is used as inputs into the thrust chamber CFD model. The output is a text file, which was imported into the engine model. Inlet temperature is specified based on the combustion temperature calculated in CEA. The mole fraction composition of the combustion products is also provided. This data is used with a molar mixture law to calculate viscosity and the equation of state, as described in Subsections 4.4.3 and 4.4.5. The CEA simulation was also used to calculate fluid properties at varying temperatures, by sampling results at different nozzle area ratios. This data was used to create temperature-dependent functions for specific heat and thermal conductivity, as described in Subsection 4.4.4.

4.4.3 Turbulence Model

Thrust chamber gas turbulence is modelled using the Renormalization Group (RNG) k-ε model, a two-equation Reynolds-Averaged Naiver Stokes (RANS) turbulence model[42]. The RNG k-ε model has a range of features which make it generally more accurate and reliable than the standard k-ε model. The transport equations for turbulent kinetic energy and turbulent dissipation rate in the RNG k-ε model are shown in Equations (4-4) and (4-5), respectively. The forms of these equations represent how they are implemented in ANSYS Fluent[41]. Terms not relevant to this project, such as those representing buoyancy or multiphase flows, are not shown.

$$\frac{\partial}{\partial t}(\rho k) + \frac{\partial}{\partial x_i}(\rho k u_i) = \frac{\partial}{\partial x_j}\left(a_k \mu_{eff} \frac{\partial k}{\partial x_j}\right) + G_k - \rho \varepsilon - \frac{2\rho \varepsilon k}{\gamma RT} + k_{in} \tag{4-4}$$

$$\frac{\partial}{\partial t}(\rho \varepsilon) + \frac{\partial}{\partial x_i}(\rho \varepsilon u_i) = \frac{\partial}{\partial x_j}\left(a_\varepsilon \mu_{eff} \frac{\partial \varepsilon}{\partial x_j}\right) + 1.42\frac{\varepsilon}{k}G_k - 1.68\rho\frac{\varepsilon^2}{k} - \mathcal{R} + \varepsilon_{in} \tag{4-5}$$

The viscosity of the thrust chamber gas is modelled as a function of temperature using the three-coefficient form of Sutherland's Law[43], as shown in Equation (4-6). The reference temperature, effective temperature and effective viscosity are calculated based on a molar mixture law, using combustion product mole fraction data from the CEA model described in Subsection 4.4.2.

$$\mu = \mu_{ref}\left(\frac{T}{T_{ref}}\right)^{3/2}\frac{T_{ref} + T_{eff}}{T + T_{eff}} \tag{4-6}$$

4.4.4 Fluid Thermal Properties

The constant-pressure specific heat and thermal conductivity of the thrust chamber gas are modelled as functions of temperature. As described in Subsection 4.4.2, the CEA simulation was used to estimate fluid properties at varying temperatures. Regressions were performed on these datasets to establish temperature-dependent functions for constant-pressure specific heat and thermal conductivity. An example is shown in Figure 4-7. These datasets were sourced from the outputs of CEA simulation for the control case described in Section 5.1.
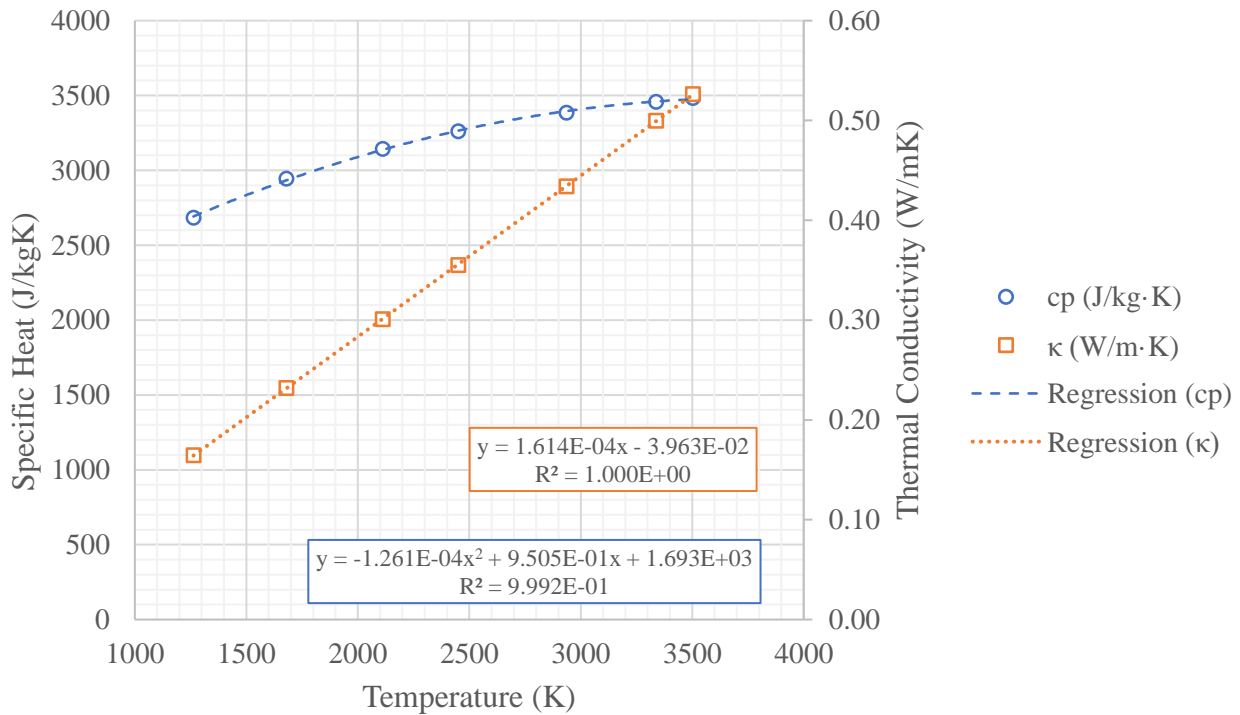
Figure 4-7: Thrust chamber fluid thermal properties

While the absolute values of these functions varied for each CEA simulation, the general trends were the same: constant-pressure specific heat was modelled as a second-order polynomial function of temperature, and thermal conductivity was modelled as a linear function of temperature. In every regression, the coefficient of determination was higher than 0.99. Thus, the regression functions always matched the CEA data well.

4.4.5 Equation of State

The thrust chamber gas is modelled as a single phase, but in reality, multiple species (such as water vapor, unburned hydrogen and hydroxide) are present in the gas flow. Given that each CEA simulation produces a unique thrust chamber gas composition, it is not possible to use a fluid database to determine state variables of the gas. Also, as the exhaust gas contains a significant amount of water vapor in all cases, it cannot be reliably modelled as an ideal gas. As such, a real gas equation of state has been adopted for the thrust chamber model. Specifically, the Soave-Redlich-Kwong real gas model[44] is used. The Soave-Redlich-Kwong real gas model is a robust equation of state which can model not only vapour phases, but also liquids and supercritical fluids. The form of the Soave-Redlich-Kwong implemented in ANSYS Fluent[41] is shown in Equation (4-7). Note that the gas constant referred to in Equation (4-7) is the universal gas constant. The critical temperature, critical pressure and acentric factor are calculated based on a molar mixture law, using combustion product mole fraction data from the CEA model described in Subsection 4.4.2.

$$p = \frac{RT\left(\dfrac{0.42747R^2T_c^{\,2}}{p_c}\right)}{V - \dfrac{0.08664RT_c}{p_c}} \cdot \frac{\left[1 + (0.48 + 1.574\psi - 0.176\psi^2)\left(1 - \left(\dfrac{T}{T_c}\right)^{0.5}\right)\right]^2}{V^2 + \dfrac{0.08664RT_c}{p_c}V} \qquad (4\text{-}7)$$

4.4.6 Solid Properties

The solid region of the thrust chamber model domain represents the ligaments. The thrust chamber liner, into which the ligaments are machined, is fabricated from a copper-chromium-zirconium (Cu-CR-Zr) alloy called Okegawa Mold Copper (OMC). OMC is an uncommon alloy, and material data & specifications are not widely available. However, Table 4-2 shows that the composition of OMC is similar to other Cu-CR-Zr alloys based on U.S. and European material standards. As such, for the purposes of this project, it is assumed that OMC can be modelled using material properties and data from these similar alloys. The relevant material properties used in the thrust chamber model are listed in Table 4-3. These properties align closely with the values for pure copper used as default settings in ANSYS Fluent[41], although thermal conductivity is notably lower than the default value of 387.6 W/m·K.

Table 4-2: Comparison of Cu-CR-Zr alloys

Alloy	Cu (%)	Cr (%)	Zr (%)	Source
OMC (Japan)	99.12	0.7	0.1	[45]
CW106C (Europe)	(Balance)	0.5 ~ 1.2	0.05 ~ 0.25	[46]
C18150 (United States)	(Balance)	0.5 ~ 1.2	0.03 ~ 0.30	

Table 4-3: Thrust chamber model solid material properties (Cu-Cr-Zr alloy)[46]

Property	Value
Density	8,900 kg/m^3
Specific heat capacity	380 J/kg·K
Thermal conductivity	320 W/m·K

4.4.7 Boundary Conditions

The boundary conditions of the thrust chamber model are shown in Figure 4-8.
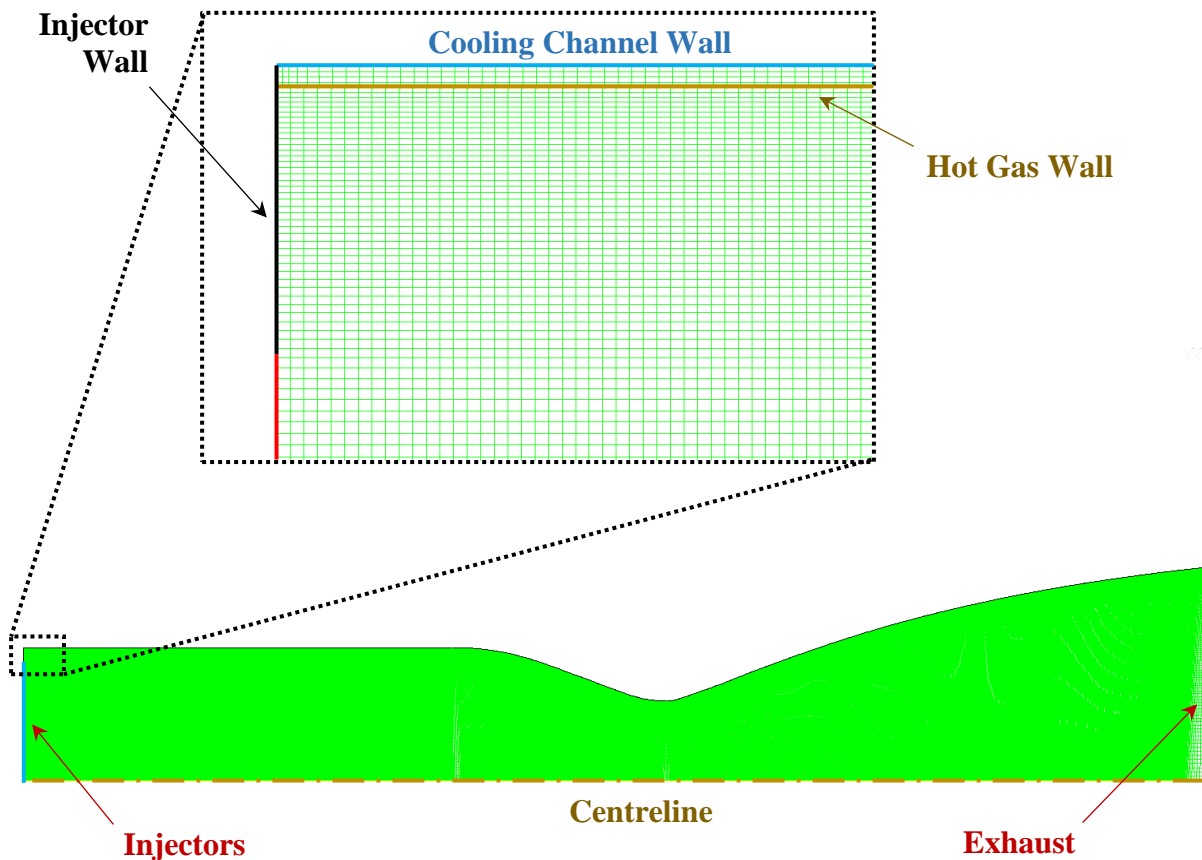
Figure 4-8: Thrust chamber model boundary conditions

The exhaust shown in Figure 4-8 is a pressure outlet. Exhaust pressure is estimated based on a quasi-1D isentropic flow calculation, using the formulas described in Subsection 2.2.1. This pressure is specified at the exhaust as an initial estimate, however due to the transition between subsonic and supersonic flow in the model, the solver automatically adjusts this pressure estimate to match the specified mass flow rate and sonic conditions at the throat. The centreline of the thrust chamber shown in Figure 4-8 is treated as an axis for the purposes of making the model domain axisymmetric.

The injectors shown in Figure 4-8 are treated as a single mass flow inlet. Mass flow into the thrust chamber is specified at this point. Combustion pressure is also specified as an initial estimate, but like exhaust pressure this value is automatically adjusted by the model. The temperature at the injectors is specified as the combustion temperature determined by the CEA simulation. However, as mixing and combustion of the propellants is not directly simulated in the CFD model, making the injector temperature constant would result in the model significantly overestimating heat transfer in the constant-area section of the thrust chamber. This effect is mitigated by creating a temperature

gradient at the injectors. The temperature at the outer edge of the injectors is equal to the fuel injector temperature, and the bulk inlet temperature is equal to the combustion temperature. This gradient occurs over the distance from the outer edge of the injectors to the centreline of the outer ring of injectors. The inlet temperature distribution is shown in Figure 4-9.
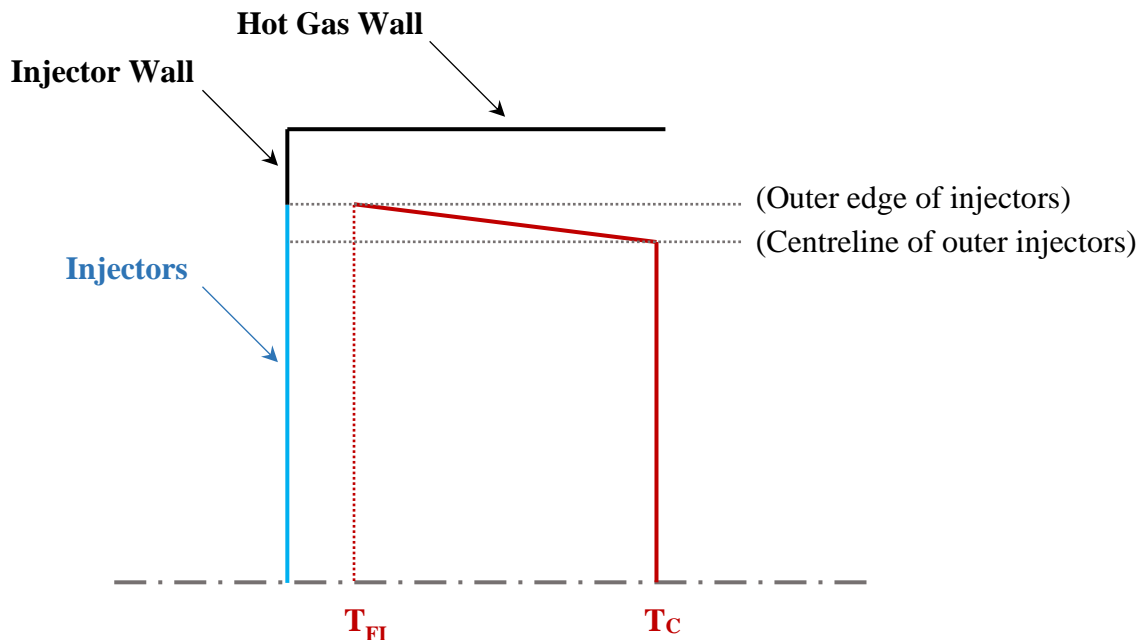
Figure 4-9: Injector boundary condition: temperature distribution

The cooling channel wall shown in Figure 4-8 is a solid wall boundary condition. The temperature of this wall varies in the axial direction. This temperature distribution is created based on the output of the cooling channel model at this point, and loaded into the thrust chamber model as a User-Defined Function (UDF). Refer to Section 4.2 for more information. The hot gas wall shown in Figure 4-8 is the boundary between the solid and fluid regions. For heat transfer purposes, it is treated as a thermally-coupled wall. For momentum purposes, it is treated as a no-slip wall. Due to software limitations, it was not possible to refine the fluid region near-wall mesh to fully resolve the boundary layer. As such, a near-wall treatment option in ANSYS Fluent[41] was adopted. Specifically, non-equilibrium wall functions are used. This wall treatment makes use of the law of the wall for mean temperature, but uses a pressure gradient-sensitized log-law for mean velocity. The non-equilibrium wall functions also use a two-layer concept for computing turbulent kinetic energy in wall-adjacent cells, where the wall-neighbouring cells are assumed to consist of a viscous sub-layer and a fully-turbulent layer[47]. These improvements over other wall functions allow the non-equilibrium wall functions to better account for pressure gradients and heat transfer in the near-wall region.

The injector wall shown in Figure 4-8 represents the edge of the injector faceplate. This wall is treated as adiabatic for heat transfer purposes. Like the hot gas wall, it is treated as a no-slip wall for momentum purposes. Also like the hot gas wall, non-equilibrium wall functions are used in lieu of fully resolving the boundary layer with a fine mesh.

4.4.8 Numerical Methods

The thrust chamber model is solved numerically using ANSYS Fluent's[41] pressure-based solver. A coupled algorithm is used to solve momentum and pressure-based continuity equations together. Gradients are calculated using a Green-Gauss cell-based method. Second-order discretization is used to solve the convection terms. The convergence criteria are set to 10^{-4} for continuity, velocity, k and ε. The stricter default ANSYS Fluent[41] convergence criteria of 10^{-6} for energy is maintained.

4.5   Cooling Channel Model

This section describes the CFD model of the cooling channel developed for this study. As with the thrust chamber model described in Section 4.4, the model was developed using ANSYS Fluent[41].

4.5.1 Domain

The cooling channel model uses a 3D symmetric domain representing a half-section of a single cooling channel-rib pair. The domain is comprised of a fluid region and a solid region. The domain of the model is shown in Figure 4-10. The fluid region represents the interior of the cooling channel. It is bounded by the cooling channel inlet in the upstream direction, the cooling channel outlet in the downstream direction, the ligament in the inner radial direction, and the closeout wall in the outer radial direction. In the hoop direction, one edge of the fluid domain is bounded by the symmetry plane through the mid-section of the cooling channel and ligament, and the other edge is bounded by the rib. The solid region represents all sections of the thrust chamber wall (i.e. the ligament, rib and closeout wall). It is bounded by the cooling channel inlet plane in the upstream direction, the cooling channel outlet plane in the downstream direction, the hot gas wall in the inner radial direction, and the outer edge of the closeout wall in the outer radial direction. In the hoop direction, the solid domain is bounded by two symmetry planes: one through the mid-section of the cooling channel and ligament, and the other through the mid-section of the rib. A cartesian coordinate system was adopted, with the origin at the intersection of the throat plane and the thrust chamber centreline. The centreline forms the x axis, with the downstream direction being positive. The y axis is in the radial direction, and z-axis is in the tangential (hoop) direction.
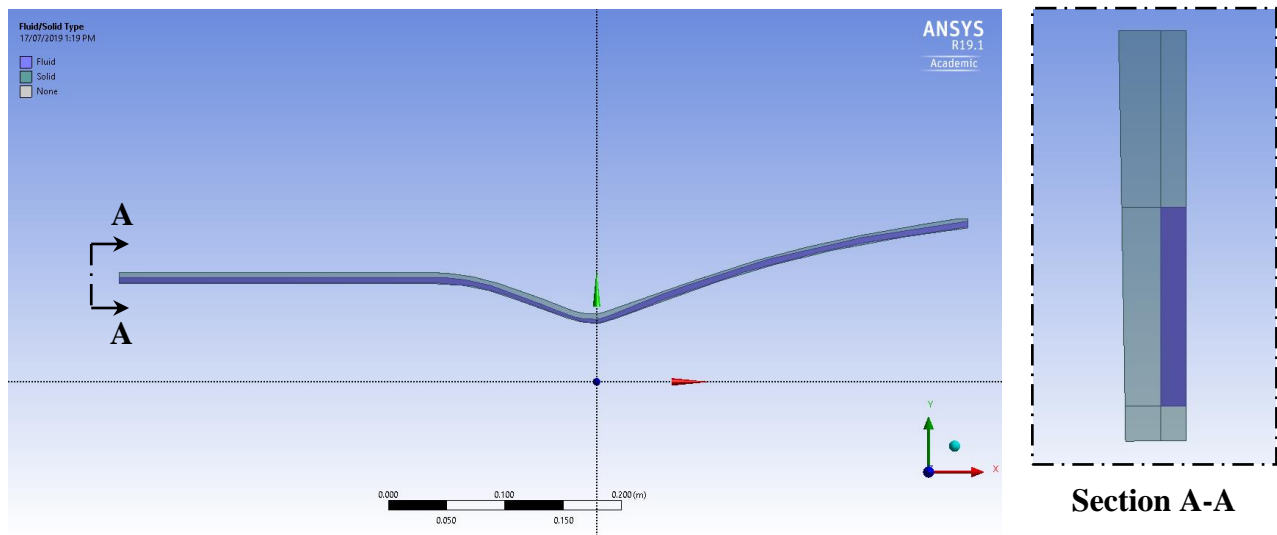
Figure 4-10: Cooling channel model domain

A structured mesh was adopted for both the solid and fluid domains. For the fluid mesh, a maximum cell edge length of 1.0mm in the axial direction was specified, although this was refined to 0.2mm in the converging-diverging region near the throat. In the radial direction, edge biasing was used to achieve a refined mesh near the ligament and closeout wall edges, with 20 divisions and a bias factor of 4.0. In hoop direction, the mesh sizing was uniform, with 8 divisions. The resultant mesh is shown in Figure 4-11.
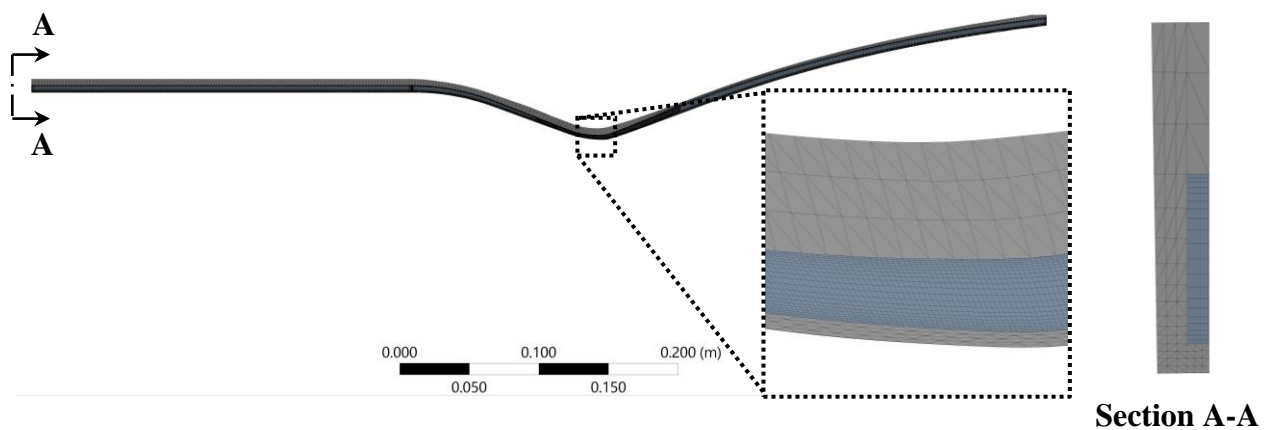
Figure 4-11: Cooling channel model mesh

The cooling channel model fluid mesh has 188,640 cells. For the solid mesh, the maximum cell edge length in the axial direction was also set to 1.0mm. The number of divisions in the radial direction was set to 4 for the ligament section only. In order to Other than the structured mesh requirement, no other constraints were placed on the solid mesh in the radial or hoop directions. The resulting solid mesh has 120,282 cells, bringing the total mesh size of the domain to 308,922 cells. The minimum orthogonal quality of the mesh was 0.00442, and the maximum aspect ratio is 151.2.

4.5.2 Turbulence Model

Cooling channel coolant turbulence is modelled using the same RNG k-ε RANS turbulence model as the thrust chamber model. Refer to Section 4.4.3 for more details. Unlike the thrust chamber model, in the cooling channel model viscosity is calculated as a function of temperature. Instead, it is considered a state variable and determined based on a database lookup, as described in Section 4.5.3.

4.5.3 Fluid Properties

The coolant fluid used in the cooling channels is hydrogen, supplied to the engine as fuel in a cryogenic state. In the cooling channel, the coolant is exposed to supercritical pressures and a wide range of temperatures. To accurately determine fluid properties (i.e. density, viscosity, specific heat and thermal conductivity) under these varying conditions, a fluid property database was considered the most accurate and reliable method, with the properties treated as state variables to be interpolated based on pressure and temperature. Given that the coolant is pure hydrogen, the NIST REFPROP database[48] which is built-in to ANSYS Fluent[41] was used to determine these properties.

The version of the REFPROP database built-in to ANSYS fluent[41] is slightly newer than the version used in the engine subsystem models (as described in Subsection 4.3.2), but significant discrepancies in the data between the versions is not expected. The range of applicability for the REFPROP hydrogen database is temperatures between 13.957 K and 1,000 K, and pressures up to 2,000 MPa. The database was therefore considered applicable to all possible states which the fluid might take in the cooling channel.

4.5.4 Solid Properties

The thrust chamber liner is fabricated from OMC, as described in Subsection 4.4.6. The Copper is then electroformed onto the outside of the liner to form the closeout wall. For simplicity, it is assumed that the closeout wall material properties are identical to that of the liner. As described in Subsection 4.4.6, due to a lack of available data for OMC, the material properties are approximated based on similar Cu-Cr-Zr alloys. The relevant material properties used in the cooling channel model are listed in Table 4-4.

Table 4-4: Cooling channel model solid material properties (Cu-Cr-Zr alloy)[46]

Property	Value
Density	8,900 kg/m^3
Specific heat capacity	380 J/kg·K
Thermal conductivity	320 W/m·K

4.5.5 Boundary Conditions

The boundary conditions of the cooling channel model are shown in Figure 4-12.
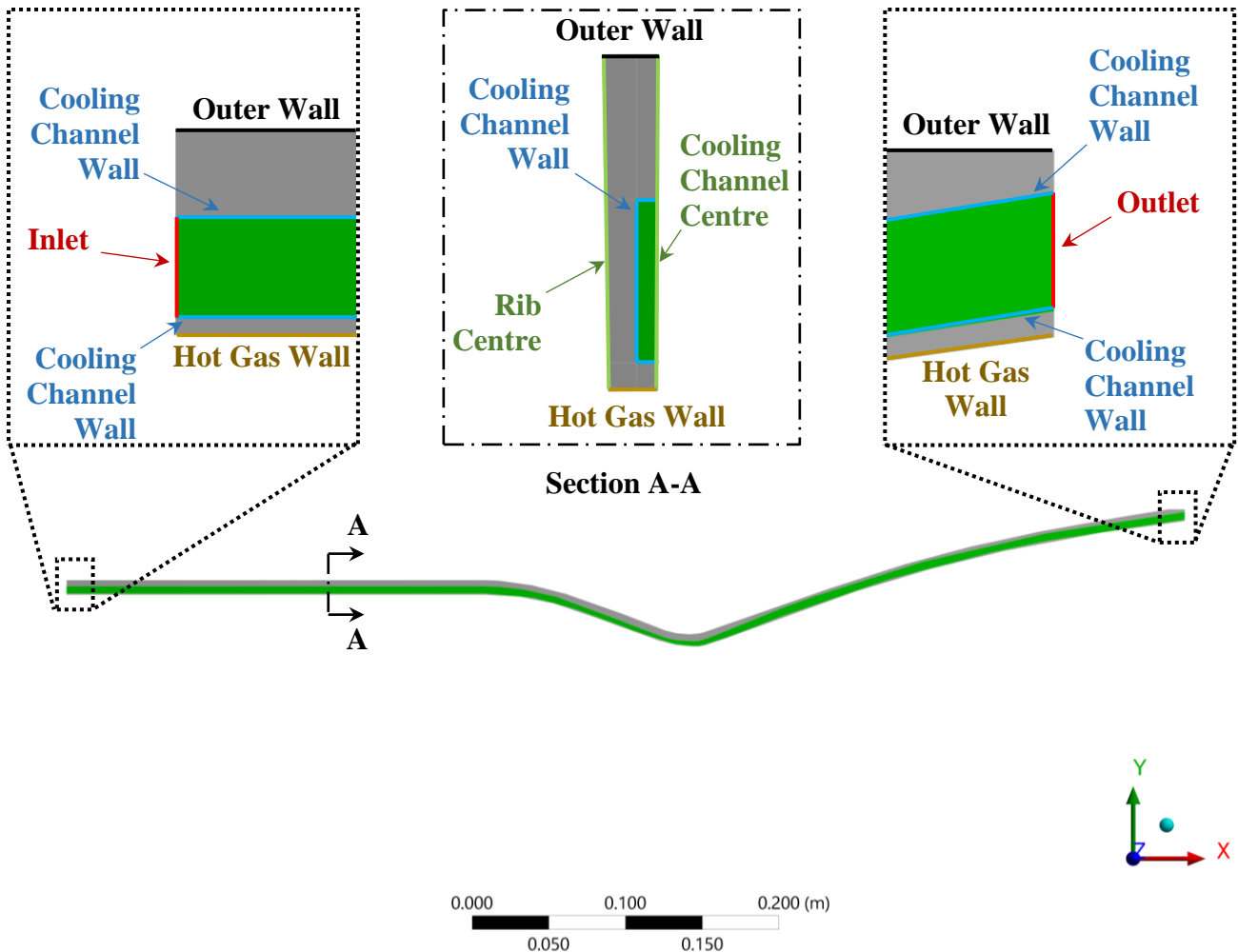
Figure 4-12: Cooling channel model boundary conditions

The outlet shown in Figure 4-12 is a mass flow outlet. The coolant mass flow rate is specified at this point. The inlet shown in Figure 4-12 is a pressure inlet. Static pressure and temperature at this point are specified based on inputs from the larger engine plant model. Stagnation pressure is estimated based on the inlet velocity, which is calculated based on the coolant flow rate. The rib centre and cooling channel centre boundaries shown in Figure 4-12 represent symmetry boundary conditions for both the solid and fluid regions. This symmetry allows a half-section of a single cooling channel to be simulated to represent the entire network of cooling channels in the thrust chamber walls.

The hot gas wall shown in Figure 4-12 is a solid wall boundary condition. The temperature of this wall varies in the axial direction. This temperature distribution is created based on the output of the thrust chamber model at this point, and loaded into the thrust chamber model as a User-Defined Function (UDF). Refer to Section 4.2 for more information. The outer wall shown in Figure 4-12 is a

solid wall boundary condition. For heat transfer purposes, this wall is treated as adiabatic. This is considered reasonable because the cooling channels are the primary mechanism by which heat is removed from the thrust chamber wall. Any conduction, convection or radiation from the outer wall boundary would be small by comparison.

The cooling channel wall shown in Figure 4-12 is the boundary between the solid and fluid regions. For heat transfer purposes, it is treated as a thermally-coupled wall. For momentum purposes, it is treated as a no-slip wall. Due to software limitations, it was not possible to refine the fluid region near-wall mesh to fully resolve the boundary layer. As such, a near-wall treatment option in ANSYS Fluent[41] was adopted. Specifically, enhanced wall treatment is used. This approach combines a two-layer model of the boundary layer with enhanced wall functions. A blending function is used to facilitate smooth transitions between the two regimes.

4.5.6 Numerical Methods

Like the thrust chamber model, the cooling channel model is solved numerically using ANSYS Fluent's[41] pressure-based solver. A coupled algorithm is used to solve momentum and pressure-based continuity equations together. Gradients are calculated using a least squares cell-based method. Second-order discretization is used to solve the convection terms. The convergence criteria are set to 10^{-4} for continuity, velocity, k and ε. The stricter default ANSYS Fluent[41] convergence criteria of 10^{-6} for energy is maintained.

4.6 Wall Structural Model

This section describes the structural model of the thrust chamber wall that was adapted the estimate thrust chamber life in this study. The wall structural model code was written and executed in Microsoft Excel.

4.6.1 Theoretical Basis

Both the structural behaviour and the failure modes included in this model are based on the Porowski model[26-28]. Refer to Subsection 2.2.2 for a summary of the structural behaviour included in the Porowski model. Refer to Subsection 2.2.3 for a summary of the Porowski model failure modes.

4.6.2 Source Data

The source data required for the structural model computation can be loosely sorted into three categories: operational loading data (e.g. temperatures, pressures, etc.), wall cross section geometry and wall material data. For this study, the structural model code has been designed to accept outputs

from the thrust chamber and cooling channel CFD models as input data. Specifically, the wall cross section temperature distribution and cooling channel-side ligament pressure are sourced from the cooling channel model, and the hot gas-side ligament pressure is sourced from the thrust chamber model. The wall cross section temperature distribution is used to determine the relevant temperatures (i.e. ligament inner and outer temperatures, ligament average temperature and closeout wall average temperature). Combustion time is specified as a user input. Wall cross section geometry is determined based on the axial position of interest within the thrust chamber. The inputs from the cooling channel model can also be used to infer the relevant geometry data.

As described in Subsection 4.4.6, due to a lack of available data for OMC, the thrust chamber wall material properties are based on more common alloys with similar compositions. This assumption is also used for wall material data in the structural model. Figure 4-13 shows the effect of temperature on the ultimate and yield strengths of Cu-Cr-Zr alloys. Using this data, temperature-dependent functions have been derived for ultimate strength and yield strength. These functions are shown in Equations (4-8) and (4-9), respectively.
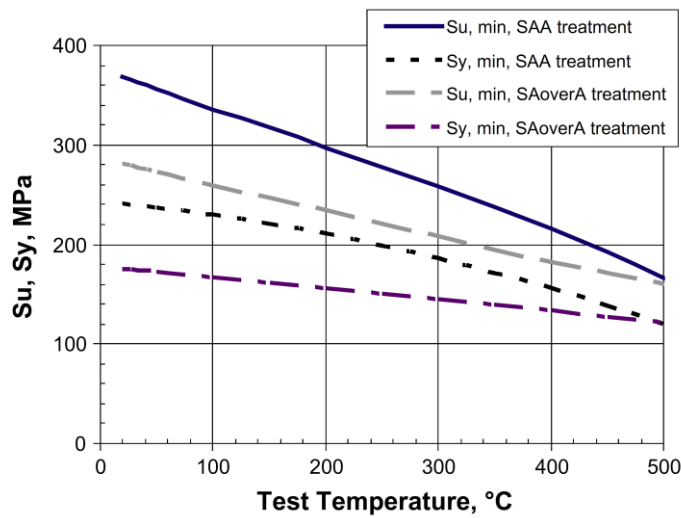
Figure 4-13: Ultimate and yield strength temperature dependence for Cu-Cr-Zr alloys[49]

$$S_U = 351.8 - 0.2414T \qquad (4\text{-}8)$$

$$S_Y = 206.5 - 0.1071T \qquad (4\text{-}9)$$

Figure 4-14 shows a fatigue plot for Cu-Cr-Zr alloys at various temperatures. By conservatively using the data for fatigue life at 500°C in Figure 4-14, a function for the number of cycles to fatigue failure has been derived. This is shown in Equation (4-10).
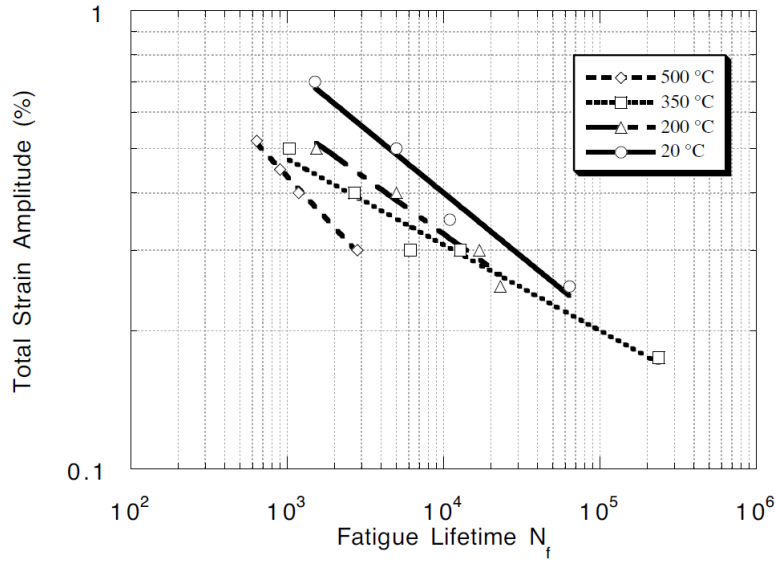
Figure 4-14: Cu-Cr-Zr alloy fatigue plots at varying temperatures[50]

$$N_{F,f} = 2.77 \times (\bar{\epsilon}_{min} \times 100)^{-2.7323} \tag{4-10}$$

Li, Thomas and Stubbins[50] provide multiple formulas for estimating creep strain rate in Cu-Cr-Zr alloys, which can be adapted to the form of Norton's creep law shown in Equation (2-28) (refer to page 22). Based on the anticipated temperatures in the thrust chamber ligament, the formula in Equation (4-11) has been selected. The temperature input required for Equation (4-11) is conservatively assumed to be the maximum ligament temperature.

$$\dot{\epsilon}_y = 7.51 \times 10^{12} \times \exp\left(-\frac{197,000}{8.314 \times T_{l1}}\right) \sigma_y^{1.70} \tag{4-11}$$

Values for the Norton law constant and exponent can be extracted from Equation (4-11) for use in the various creep deformation equations used in the structural model. This is shown in Equations (4-12) and (4-13).

$$B = 7.51 \times 10^{12} \times \exp\left(-\frac{197,000}{8.314 \times T_{l1}}\right) \tag{4-12}$$

$$C = 1.7 \tag{4-13}$$

Figure 4-15 shows a stress-rupture plot for Cu-Cr-Zr alloy. These plots can be used with the output of Equation (2-44) (page 26) to determine time to rupture. As a conservative estimate, the lowest stress-rupture curve in Figure 4-15 is used. The corresponding formula is shown in Equation (4-14).
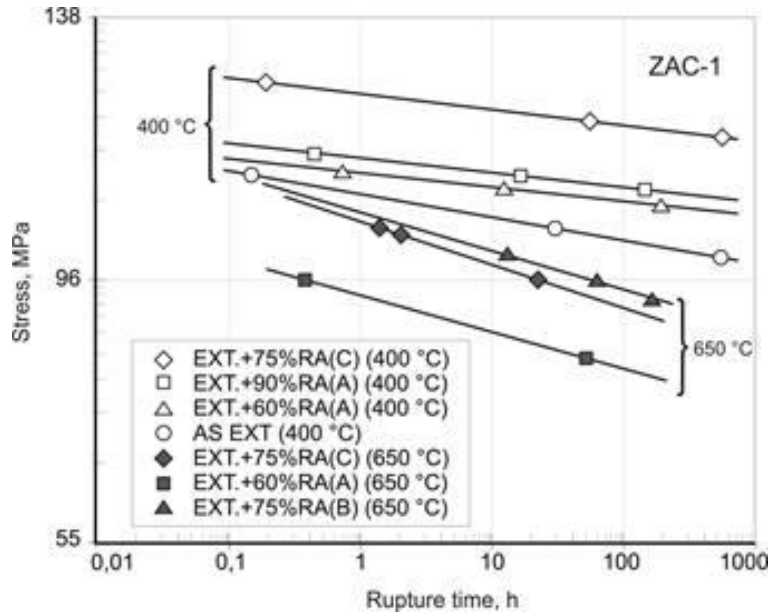
Figure 4-15: Cu-Cr-Zr alloy stress-rupture plots at varying temperatures[46]

$$t_r = 3,600 \times \left[10^{(94.24-\sigma_{in})/5.972}\right] \tag{4-14}$$

In addition to the variable material properties described in Equations (4-8) to (4-14), Table 4-5 shows constant material properties for Cu-Cr-Zr alloy which are used in the structural model.

Table 4-5: Cu-Cr-Zr alloy material properties (Structural model)[46]

Property	Value
Coefficient of Thermal Expansion	1.7 $\times 10^{-5}$ K^{-1}
Modulus of Elasticity	128 GPa
Poisson's ratio	0.3

4.6.3 Computation

The computation procedure for the structural model is based on the formulas in Subsections 2.2.2, 2.2.3 and 4.6.2. First, the net plastic deflection, cycles to strain hardening and critical thickness are calculated. Then, an iterative procedure is used to calculate the number of cycles to each failure mode. An algorithm for the wall structural model computation procedure is shown in Figure 4-16.
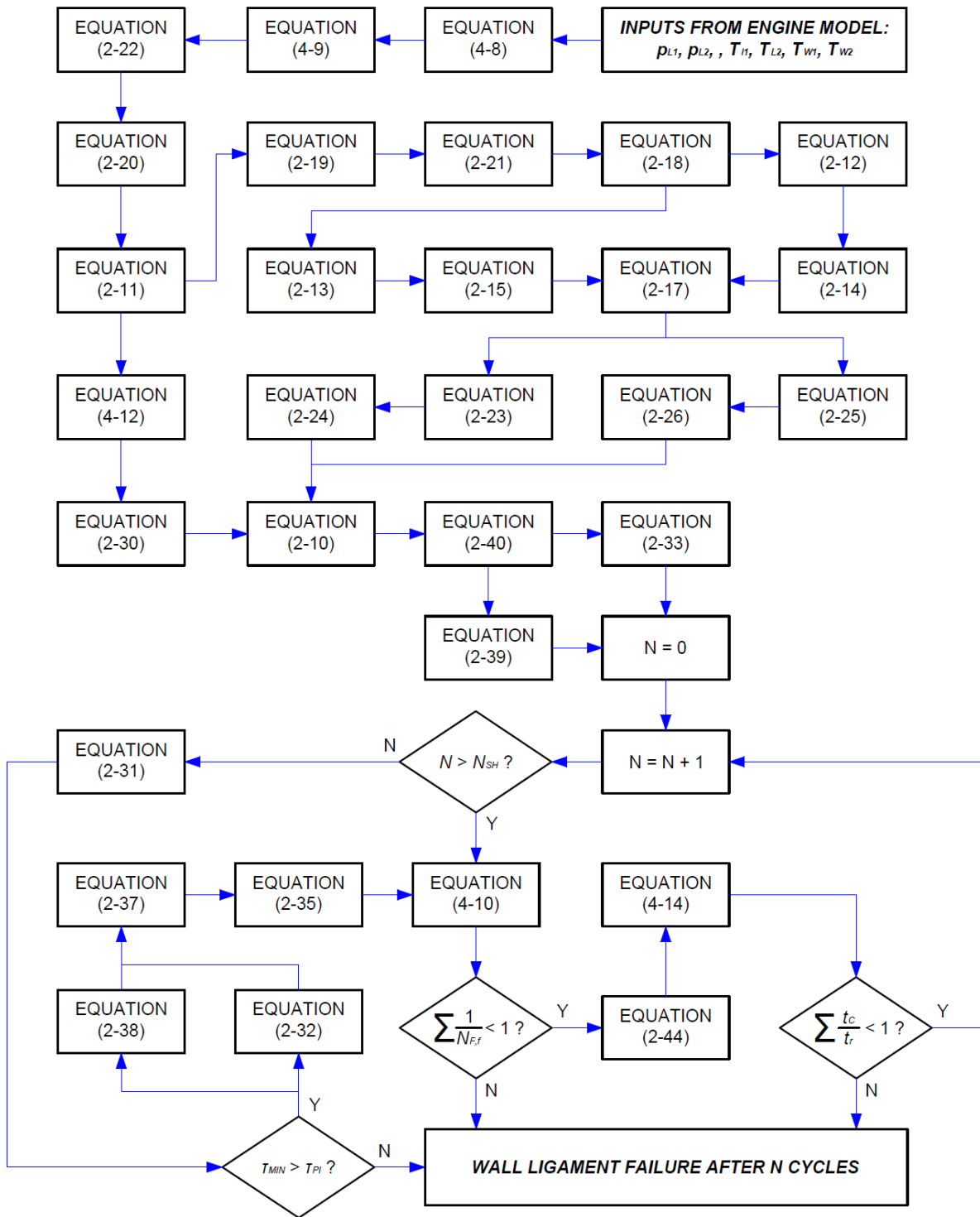
Figure 4-16: Wall structural model algorithm

4.7   Data Collection Method

This section outlines how the models described in this chapter are used to collect engine performance and thrust chamber life data for the cases identified in Section 3.4. Subsection 4.7.1 describes the general procedure used to control the model with varying input variables. Subsection

4.7.3 specifies how the input variables were controlled to collect data for the control case. Subsection 4.7.4 specifies how the input variables were controlled to collect data for the variable coolant pressure case. Subsection 4.7.5 specifies how the input variables were controlled to collect data for the variable coolant flow rate case. Subsection 4.7.6 specifies how the input variables were controlled to collect data for the variable mixture ratio case. Finally, subsection 4.7.7 specifies how the input variables were controlled to collect data for the variable propellant flow rate case.

4.7.1 General Control Procedure

Figure 4-17 shows an algorithm describing the control procedure for the engine plant model. This algorithm describes how the engine model is adjusted to match predetermined target variables. The engine subsystem models, thrust chamber model, cooling channel model and wall structural model are included as single processes in this algorithm. Refer to the relevant sections of this chapter for more information on these models individually.
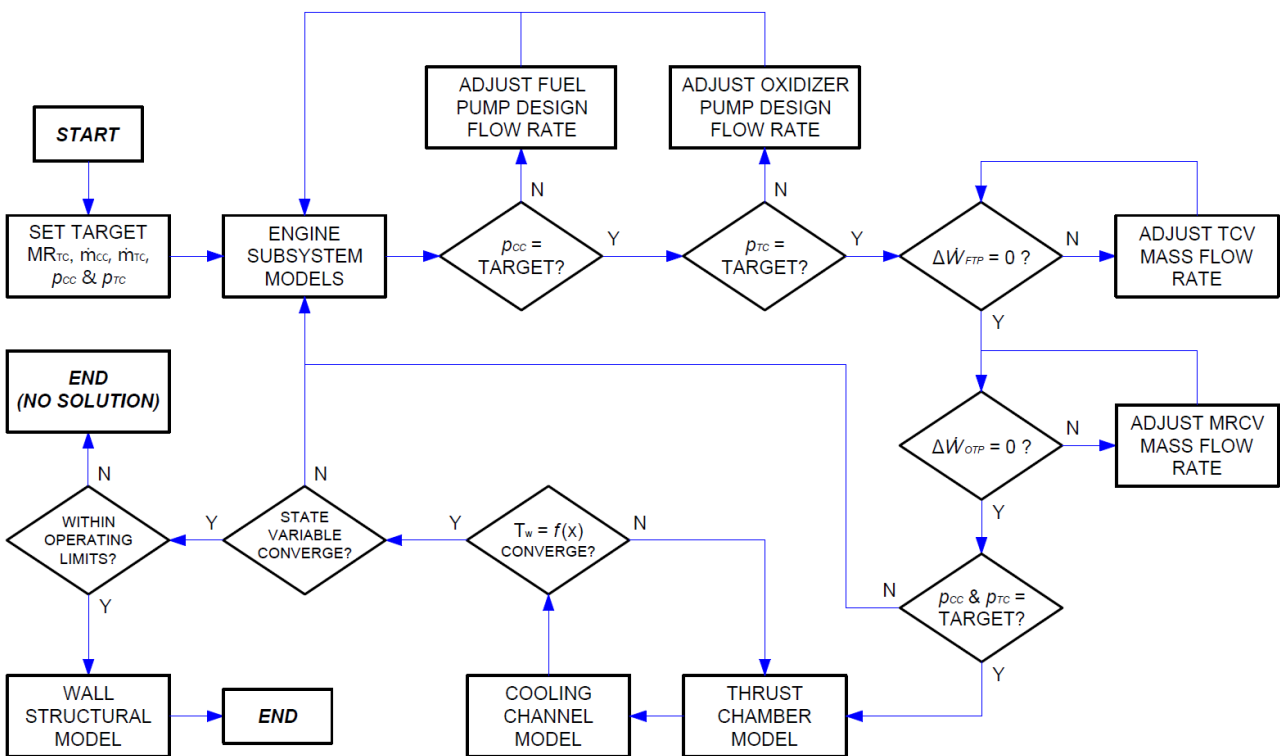
Figure 4-17: General solution algorithm

In order to analyse the cases identified in Section 3.4, it is necessary to isolate each of the identified operating conditions (cooling channel pressure, cooling channel flow rate, mixture ratio & propellant flow rate/combustion pressure), such that they can be varied individually while other parameters are held constant. The primary control inputs which can be varied in the integrated model are fuel pump design flow rate, oxidizer pump design flow rate, propellant flow rate, mixture ratio,

coolant flow rate, bleed flow rate (i.e. fuel turbine flow rate) and oxidizer turbine flow rate. Cooling channel flow rate, mixture ratio and propellant flow rate are all either directly or indirectly determined by mass flow rates at different points in the engine. As such, these operating conditions can be controlled using valve settings.

4.7.2 Turbopump Scaling

Cooling channel pressure and combustion pressure depend on fuel and oxidizer pump pressurization. Controlling these operating conditions is not so trivial in a practical sense. Figure 4-18 (copied from Figure B-1-3 in Appendix B-1, page 150) and Figure 4-19 (copied from Figure B-2-2 in Appendix B-2, page 160) show that fuel and oxidizer pressurization is a function of the normalized volumetric flow rates through the respective pumps as well as mass flow rate, as shown in Equations (4-15) and (4-16). If the pump pressurization is to be changed without changing flow rate (e.g. to change coolant pressure while holding coolant flow rate constant), the pump design volumetric flow rate must be adjusted. This would allow the normalized volumetric flow rates in Figure 4-18 and Figure 4-19 to be changed (leading to a change in pressurization) without changing the actual volumetric flow rate. The reverse is also possible – if pump flow rate needs to be adjusted without changing pressurization (e.g. to mixture ratio while holding combustion pressure constant), this can be achieved by adjusting the design volumetric flow rate, such that the normalized volumetric flow rate (and therefore pump pressurization) is held constant.
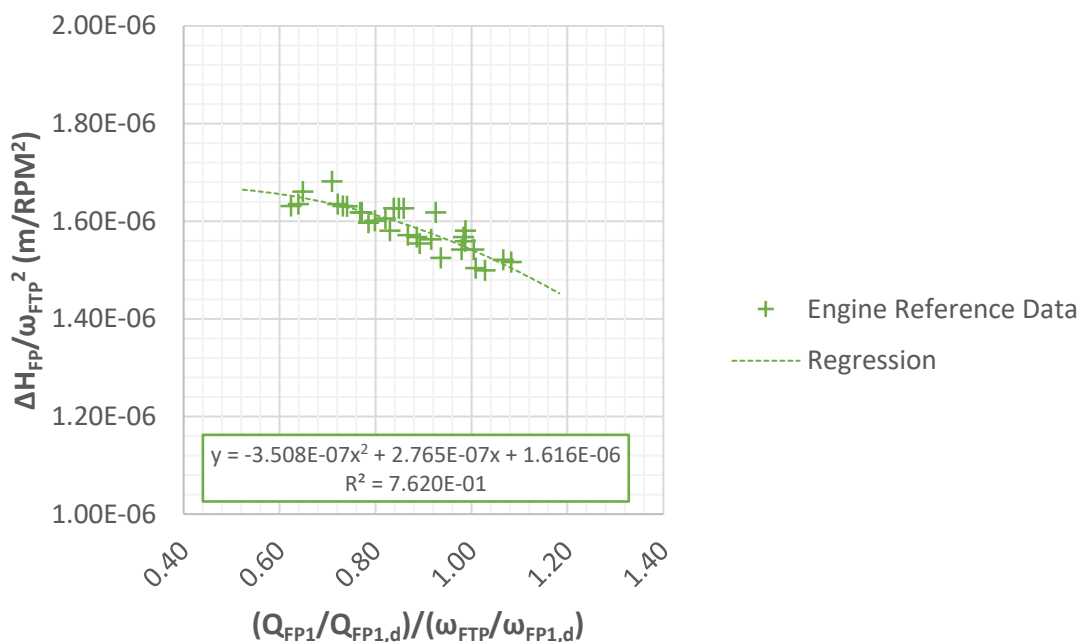
Figure 4-18: Regression of FTP pump head data
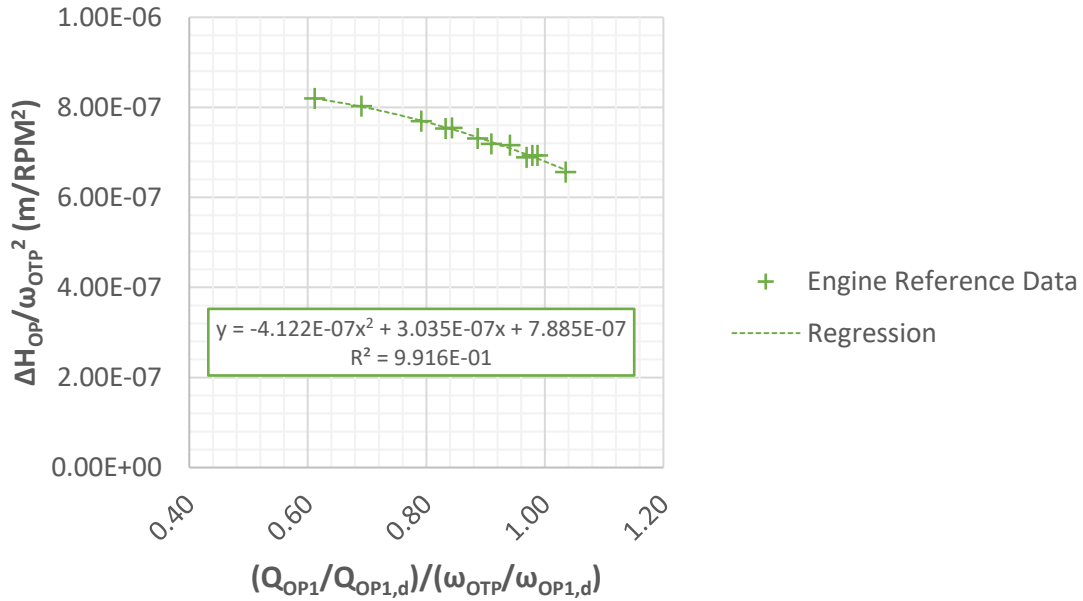
Figure 4-19: Regression of OTP pump head data

$$p_{FP2} = f\left(Q_{FP1}, Q_{FP1,d}, \omega_{FP1}\right) = f\left(Q_{FP1,d}, \dot{m}_{FP1}\right) \tag{4-15}$$

$$p_{OP2} = f\left(Q_{OP1}, Q_{OP1,d}, \omega_{OP1}\right) = f\left(Q_{FP1,d}, \dot{m}_{OP1}\right) \tag{4-16}$$

This change effectively simulates a redesign of the turbopumps. The pumps are "scaled up" or "scaled down" to meet the requirements of keeping thrust chamber and cooling channel properties constant in a variety of scenarios. While it may not be feasible in a practical or experimental sense to design and fit a wide variety of turbopumps to the engine, it is considered acceptable as a theoretical exercise to isolate the effects of various parameters on thrust chamber life. Thrust chamber and cooling channel geometry and material are unchanged. In effect, this functionality allows the engine to be "redesigned" around an unchanged thrust chamber design, to allow all operating conditions except the parameters of interest in each case to be held constant.

4.7.3 Control Case

Unlike the other cases described in this section, which investigate a range of points within the engine's operating limits, the control case represents a single operating point, intended to reflect the nominal operation of the engine at a thrust level of 100%. As such, the setting of the operating conditions and the corresponding control inputs is a relatively trivial exercise. These settings are shown in Table 4-6.

Table 4-6: Control case control inputs

Control Input	Normalized Values	Notes
Fuel Pump Design Flow Rate	100.0%	Based on design value
Oxidizer Pump Design Flow Rate	100.0%	Based on design value
Propellant Flow Rate	100.0%	Based on design value
Mixture Ratio (Combustion)	100.0%	Based on design value
Coolant Flow Rate	100.0%	Based on design value
Bleed Flow Rate	90.1%	Adjust to balance FTP power
Oxidizer Turbine Flow Rate	92.3%	Adjust to balance OTP power

4.7.4 Variable Coolant Pressure Case

In the variable coolant pressure case, fuel pump design flow rate is varied to create changes in coolant pressure without changing fuel flow rate. Fuel pressurization affects not only coolant pressure, but fuel injection pressure into the thrust chamber. Thus, oxidizer pump design flow rate is also varied to compensate for any changes in combustion pressure arising from changes in fuel injector pressure. Propellant flow rate, mixture ratio and coolant flow rate are all held constant based on their respective design values. Finally, bleed flow rate and oxidizer turbine flow rate are adjusted to balance shaft power in the fuel and oxidizer turbopumps, respectively. These settings are shown in Table 4-7. The normalized ranges shown in Table 4-7 are based on the established limits for this case as described in Subsection 5.2.3.

Table 4-7: Variable coolant pressure case control inputs

Control Input	Normalized Range	Notes
Fuel Pump Design Flow Rate	85.9% - 111.5%	***Adjust to vary coolant inlet pressure***
Oxidizer Pump Design Flow Rate	118.8% - 88.9%	Adjust to compensate for fuel pressure change in thrust chamber
Propellant Flow Rate	100.0% -100.0%	Based on Design Value
Mixture Ratio (Combustion)	100.0% -100.1%	Based on Design Value
Coolant Flow Rate	100.0% -100.0%	Based on Design Value
Bleed Flow Rate	79.7% - 142.8%	Adjust to balance FTP Power
Oxidizer Turbine Flow Rate	56.2% - 157.5%	Adjust to balance OTP Power

4.7.5 Variable Coolant Flow Rate Case

In the variable coolant flow rate case, the fuel pump design flow rate is varied to maintain a constant coolant pressure as the coolant flow rate changes. Changing coolant flow rate affects cooling channel pressure loss, leading to changes in fuel injection pressure into the thrust chamber (as some of the used coolant flows through the mixer and into the fuel injector manifold). Thus, oxidizer pump design flow rate is also varied to compensate for any changes in combustion pressure arising from changes in coolant discharge pressure. Propellant flow rate and mixture ratio are held constant based on their respective design values. Finally, bleed flow rate and oxidizer turbine flow rate are adjusted to balance shaft power in the fuel and oxidizer turbopumps, respectively. These settings are shown in Table 4-8. The normalized ranges shown in Table 4-8 are based on the established limits for this case as described in Subsection 5.3.3.

Table 4-8: Variable coolant flow rate case control inputs

Control Input	Normalized Range	Notes
Fuel Pump Design Flow Rate	100.4% - 94.0%	Adjust to prevent changes in pump flow rate from affecting coolant pressure
Oxidizer Pump Design Flow Rate	98.7% - 108.2%	Adjust to compensate for fuel pressure change in thrust chamber
Propellant Flow Rate	99.9% - 100.0%	Based on Design Value
Mixture Ratio (Combustion)	100.0% - 100.1%	Based on Design Value
Coolant Flow Rate	71.4% - 198.4%	***Adjust to vary coolant flow rate***
Bleed Flow Rate	75.8% - 215.3%	Adjust to balance FTP Power
Oxidizer Turbine Flow Rate	91.4% - 119.5%	Adjust to balance OTP Power

4.7.6 Variable Mixture Ratio Case

In the variable mixture ratio case, both fuel and oxidizer pump design flow rates are varied maintain constant pressurization as both the fuel and oxidizer flow rates change to create a variable mixture ratio without changing net propellant flow. The fuel pump design flow rate is adjusted to maintain the coolant pressure at the design value. The oxidizer pump design flow rate is then adjusted to maintain the combustion pressure at the design value. Propellant flow rate and coolant flow rate are held constant based on their respective design values. Finally, bleed flow rate and oxidizer turbine flow rate are adjusted to balance shaft power in the fuel and oxidizer turbopumps, respectively. These

settings are shown in Table 4-9. The normalized ranges shown in Table 4-9 are based on the established limits for this case as described in Subsection 5.4.3.

Table 4-9: Variable mixture ratio case control inputs

Control Input	Normalized Range	Notes
Fuel Pump Design Flow Rate	78.2% - 102.4%	Adjust to prevent changes in pump flow rate from affecting coolant pressure
Oxidizer Pump Design Flow Rate	160.2% - 80.9%	Adjust to prevent changes in pump flow rate from affecting combustion pressure
Propellant Flow Rate	99.9% - 100.0%	Based on Design Value
Mixture Ratio (Combustion)	57.3% - 127.8%	***Adjust to vary mixture ratio***
Coolant Flow Rate	100.0% -100.0%	Based on Design Value
Bleed Flow Rate	141.9% - 91.9%	Adjust to balance FTP Power
Oxidizer Turbine Flow Rate	73.1% - 108.1%	Adjust to balance OTP Power

4.7.7 Variable Combustion Pressure Case

In the variable combustion pressure case, both fuel and oxidizer pump design flow rates are varied, albeit for different reasons. As described in Section 3.4, variations in combustion pressure must be coupled with variations in propellant flow rate. The fuel pump design flow rate is varied to maintain constant coolant pressure as the fuel flow rate changes to create this variable propellant flow rate. The oxidizer pump design flow rate is then varied to proportionally adjust combustion pressure to match changes in propellant flow rate. As propellant flow rate & combustion pressure are coupled operating conditions, any variations in one of the two parameters cannot be isolated from variations in the other. Mixture ratio and coolant flow rate are held constant based on their respective design values. Finally, bleed flow rate and oxidizer turbine flow rate are adjusted to balance shaft power in the fuel and oxidizer turbopumps, respectively. These settings are shown in Table 4-10. The normalized ranges shown in Table 4-10 are based on the established limits for this case as described in Subsection 5.5.3.

Table 4-10: Variable combustion pressure case control inputs

Control Input	Normalized Range	Notes
Fuel Pump Design Flow Rate	113.6% - 93.2%	Adjust to prevent changes in pump flow rate from affecting coolant pressure
Oxidizer Pump Design Flow Rate	87.3% - 109.6%	***Adjust to vary combustion pressure***
Propellant Flow Rate	86.2% - 110.1%	***Adjust to vary propellant flow rate (coupled to combustion pressure)***
Mixture Ratio (Combustion)	100.0% - 100.0%	Based on Design Value
Coolant Flow Rate	100.0% -100.0%	Based on Design Value
Bleed Flow Rate	100.5% - 102.7%	Adjust to balance FTP Power
Oxidizer Turbine Flow Rate	115.7% - 86.9%	Adjust to balance OTP Power

5.   Results

The results of this study are presented in this chapter. The results of the control case are presented in Section 5.1. The results of the variable coolant pressure case are presented in Section 5.2. The results of the variable coolant flow rate case are presented in Section 5.3. The results of the variable mixture ratio case are resented in Section 5.4. Finally, the results of the variable combustion pressure case are presented in Section 5.3.

5.1   Control Case

In this section, the results of the control case are presented. Unlike the other cases presented in this chapter which cover a range of operating points, the control case represents a single operating point, corresponding to the JAXA reusable rocket engine under nominal operating conditions producing 100% thrust. Data collected at this point is used to verify the accuracy of the engine model (refer to Subsection 5.1.1), determine the axial location of the critical failure point in the thrust chamber (refer to Subsection 5.1.2), and to provide source data to normalize other data presented in this document as required. Figure 5-1 and Figure 5-2 show CFD model results for the control case, from the thrust chamber and cooling channel models, respectively.
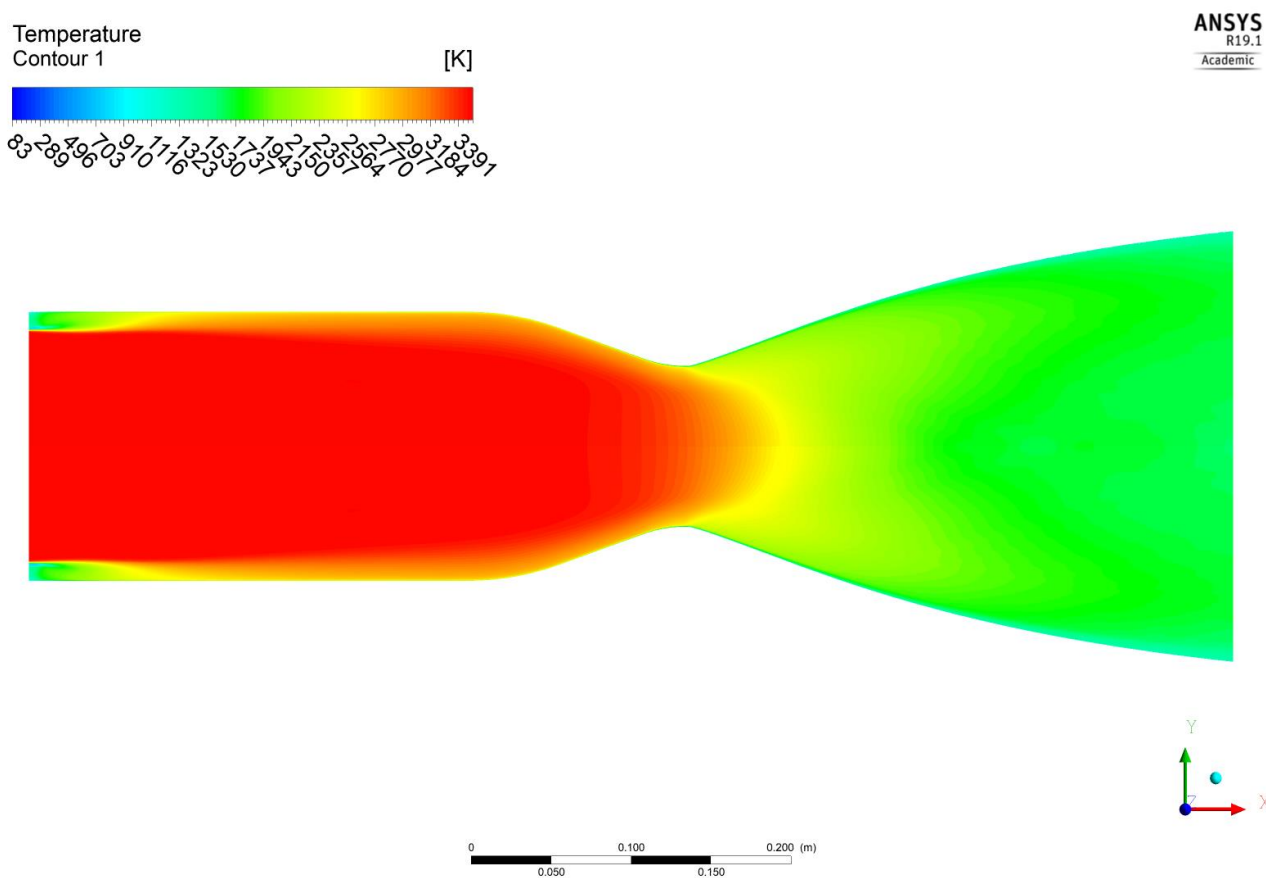
Figure 5-1: Thrust chamber model results – temperature distribution

Temperature
ThroatContour

608
596
584
572
560
548
535
523
511
499
487
475
463
451
438
426
414

[K]

Temperature
ThroatContour

489
474
459
443
428
413
398
383
368
352
337
322
307
292
276
261
246

[K]

| 0 | | 0.0015 | | 0.003 (m) |
| | 0.00075 | | 0.00225 | |

(a)   *(b)*
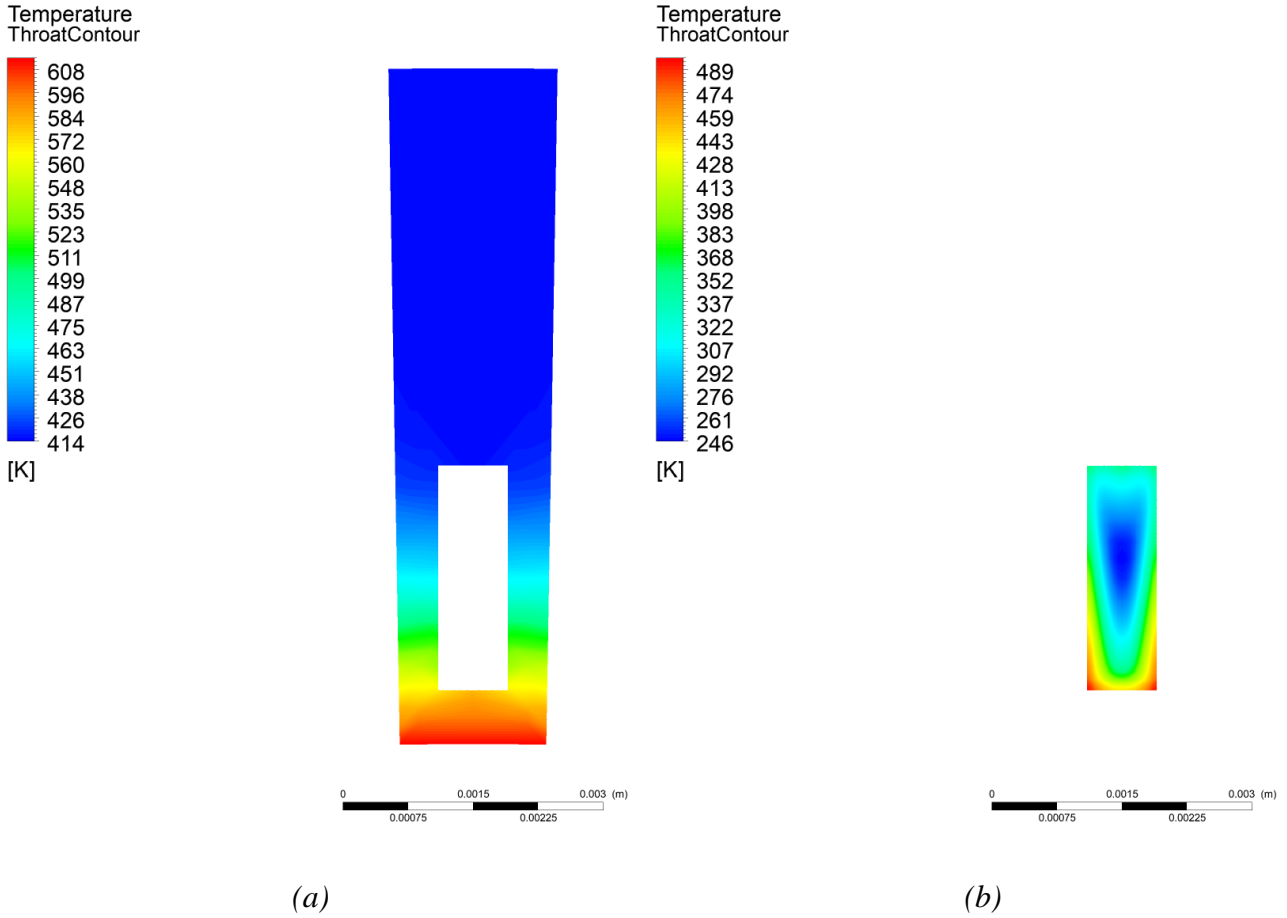
Figure 5-2: Cooling model results – temperature distribution in (a) the wall (b) the cooling channel

5.1.1 Verification

The control case results of the engine plant model are compared to reference data for the JAXA reusable rocket engine, to verify accuracy. The results of this comparison are shown in Table 5-1. 37 engine operating parameters were analysed. The largest error was an over-prediction of mixer inlet pressure by 14.65%. The average absolute error across the 37 parameters is 3.52%. Generally speaking, the largest errors seem to occur in the engine model at points downstream of the cooling channel outlet, where the outputs of the cooling channel CFD model are integrated back into the engine plant model. Table 5-1 shows that at this point, pressure is overestimated by 2.70% and temperature is underestimated by 6.19%. These errors have a "flow on" effect, and carry through into components downstream of the cooling channel, such as the fuel and oxidizer turbines and the fuel mixer.

Table 5-1: Error in engine plant model outputs

Parameter	Error	Parameter	Error
Mixer Gas Inlet Pressure	14.65%	**Oxidizer Pump Head**	-0.08%
Fuel Turbine Flow Rate	11.00%	**OTP Shaft Speed**	-0.11%
Oxidizer Turbine Flow Rate	8.29%	**Thrust Chamber Propellant Flow Rate**	-0.22%
Fuel Turbine Discharge Pressure	5.62%	**Cooling Channel Inlet Temperature**	-0.25%
Oxidizer Turbine Inlet Pressure	5.31%	**Mixer Liquid Inlet Pressure**	-0.32%
Oxidizer Turbine Discharge Pressure	4.63%	**Oxidizer Pump Discharge Pressure**	-0.40%
Fuel Turbine Inlet Pressure	4.32%	**Mixer Liquid Inlet Flow Rate**	-0.51%
Fuel Pump Head	3.41%	**Oxidizer Injection Pressure**	-0.52%
Fuel Injection Pressure	3.33%	**Sea-Level Thrust**	-2.64%
Cooling Channel Discharge Pressure	2.70%	**Sea-Level Specific Impulse**	-2.65%
Combustion Mixture Ratio	1.97%	**Mixer Gas Inlet Flow Rate**	-5.12%
Combustion Pressure	1.46%	**Cooling Channel Discharge Temperature**	-6.19%
FTP Shaft Speed	0.49%	**Fuel Turbine Inlet Temperature**	-6.19%
Oxidizer Injection Temperature	0.05%	**Mixer Gas Inlet Temperature**	-6.23%
Mixer Liquid Inlet Temperature	0.02%	**Fuel Turbine Discharge Temperature**	-7.46%
Fuel Pump Discharge Pressure	0.01%	**Oxidizer Turbine Inlet Temperature**	-7.46%
Cooling Channel Inlet Pressure	0.00%	**Oxidizer Turbine Discharge Temperature**	-7.58%
Fuel Pump Discharge Temperature	-0.01%	**Fuel Injection Temperature**	-9.22%
Oxidizer Pump Discharge Temperature	-0.02%		

5.1.2 Failure Point Analysis

The point of maximum heat flux in a rocket engine thrust chamber wall is typically at or near the throat. As such, the throat is usually considered to be the "weak point" in the thrust chamber wall. Estimates and analysis of thrust chamber life therefore conventionally focus on the throat, as it is assumed that the wall will fail in this location first. However, given that thrust chamber life is affected by a range of thermal and pressure loading conditions, as described in Equations (3-8) to (3-10) (page

38), it is logical to challenge the assumption that throat is the life-limiting critical failure point. Additionally, the geometry of the cooling channels and ligaments changes near the throat in the JAXA engine. This geometry change improves cooling capability near the throat, but could also lead to a change in the location critical failure point.

Using the results of the CFD simulations for the control case, temperature and pressure data at the thrust chamber wall was sampled at numerous points in the converging-diverging nozzle section of the thrust chamber. The resulting axial variations in wall maximum temperature are plotted in Figure 5-3. Similarly, axial variations in overall wall (ligament-to-closeout) temperature difference are plotted in Figure 5-4. Axial variations in ligament temperature difference are plotted in Figure 5-5. Finally, axial variations in ligament differential pressure load are plotted in Figure 5-6.

Figure 5-3 shows that maximum wall temperature does occur at the throat, but there is another peak in wall temperature of almost the same magnitude at a normalized axial position of -0.08. Figure 5-4 also shows a significant increase in wall temperature difference in this region. The wall temperature difference at this point is approximately 40 K higher than the same value at the throat. This axial position of -0.08 corresponds to the region immediately upstream of the aforementioned cooling channel and ligament geometry change. Downstream of this point, both maximum wall temperature and wall temperature difference decrease, indicating that the geometry change is having the desired effect of reducing thermal loading near the throat.
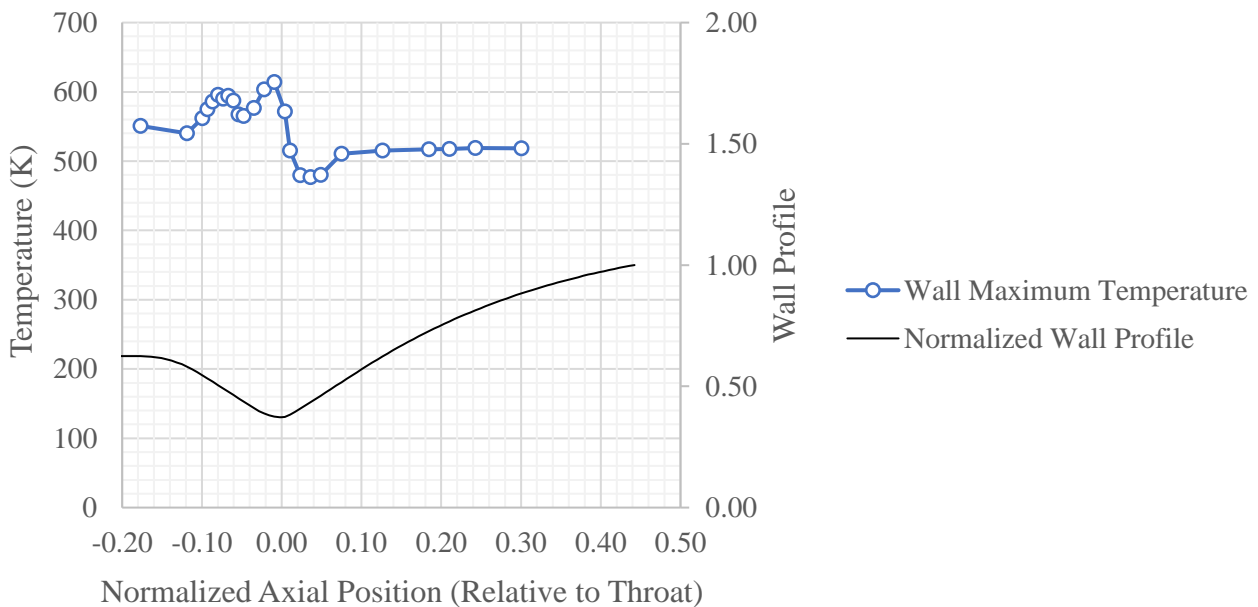
Figure 5-3: Axial variation of wall maximum temperature
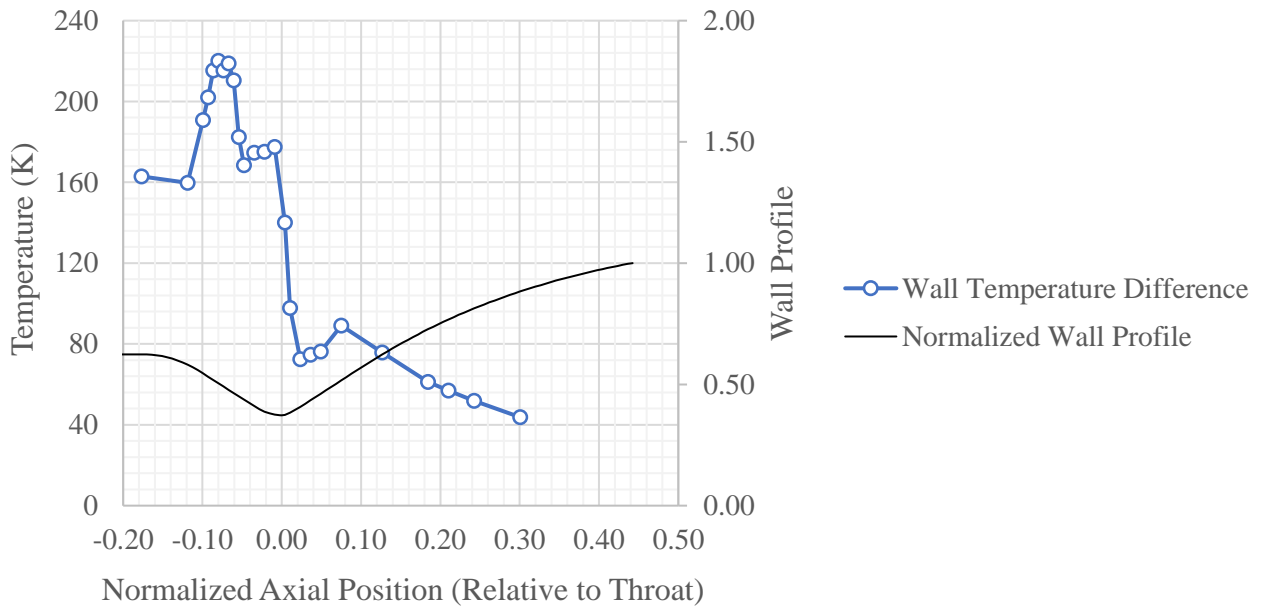
Figure 5-4: Axial variation of wall temperature difference

Figure 5-5 shows that ligament temperature difference reaches a maximum near the throat, but remains high in the converging section of the nozzle (from an axial position of -0.10 to 0.00). Figure 5-6 shows that the maximum pressure difference occurs in the diverging section (a normalized axial position of +0.30). This is to be expected, as by design the pressure in the thrust chamber declines significantly in the diverging section of the nozzle. The pressure in the cooling channel also decreases as the coolant passes through the throat, but this decline is not as significant as the thrust chamber pressure decrease. This results in a differential pressure load approximately 2,500 kN/m higher than the converging section in the diverging section of the nozzle.
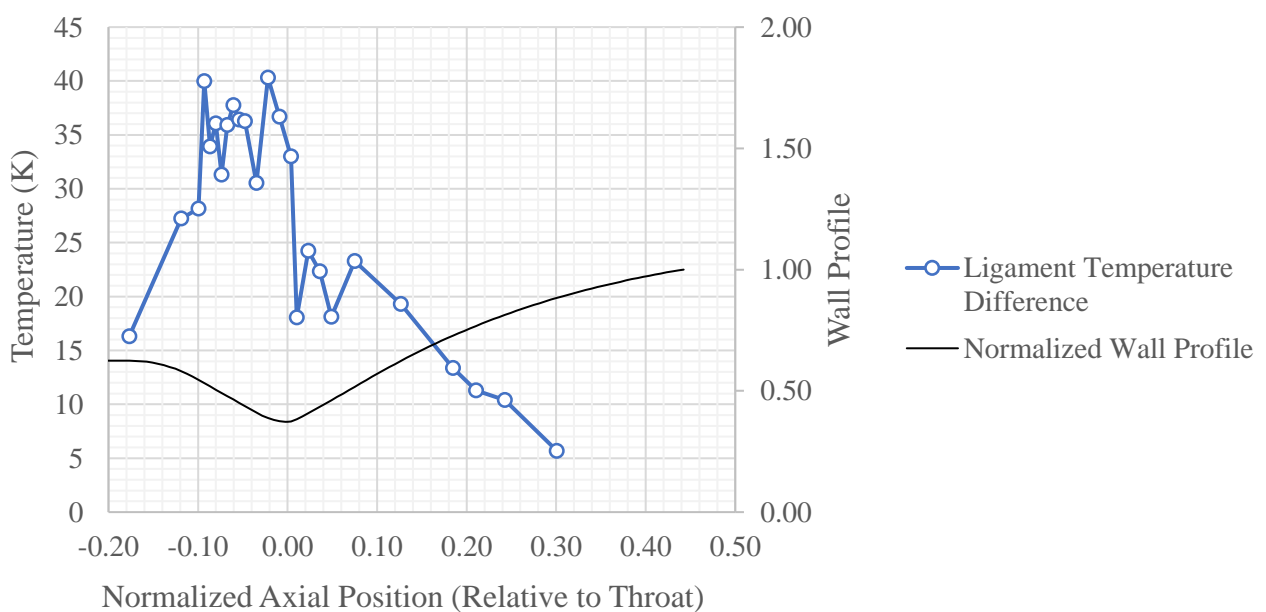
Figure 5-5: Axial variation of ligament temperature difference
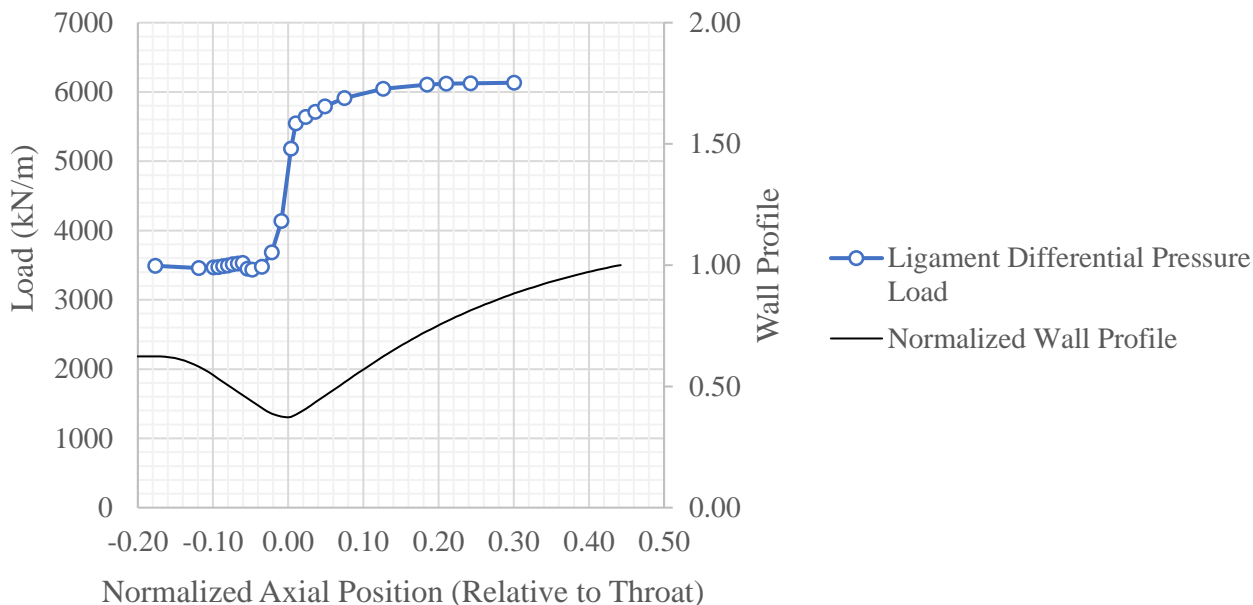
Figure 5-6: Axial variation of ligament differential pressure load

Using the data in Figure 5-3 to Figure 5-6, and accounting for variations in wall geometry, the wall structural model can be used to determine how the localized life of the thrust chamber varies with axial position. The number of cycles to plastic instability at the various axial locations are plotted in Figure 5-7. Similarly, the number of cycles to low-cycle fatigue failure at the various axial locations are plotted in Figure 5-8. Finally, the number of cycles to creep deformation failure at the various axial locations are plotted in Figure 5-9.
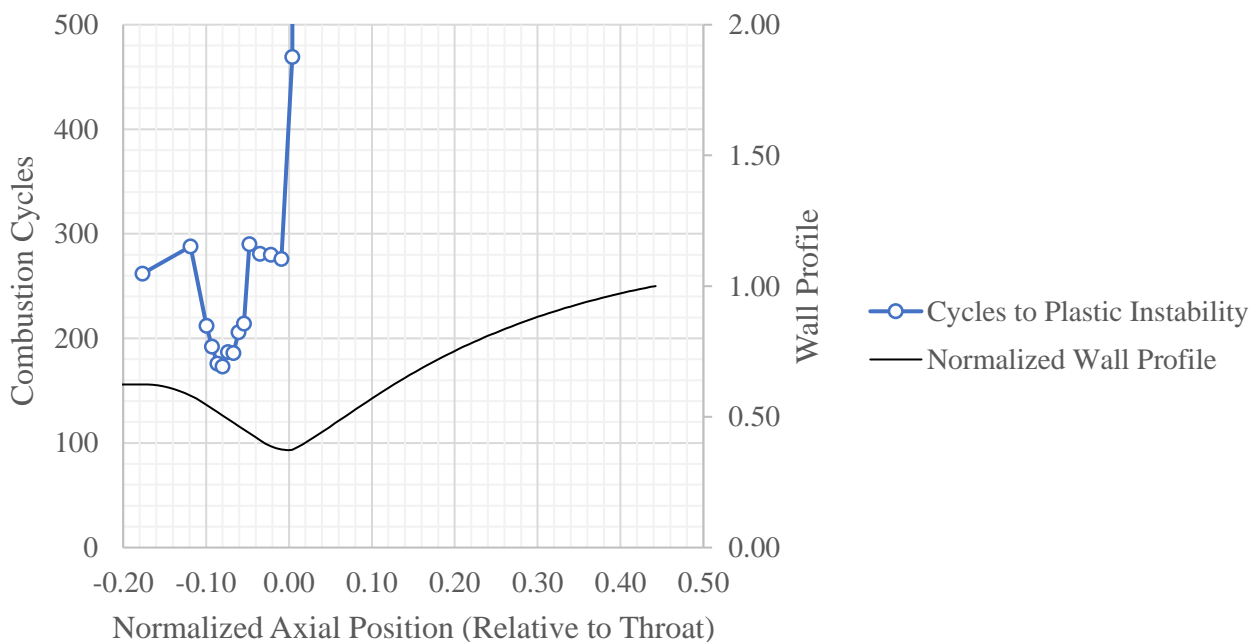
Figure 5-7: Axial variation of thrust chamber wall life (plastic instability failure)
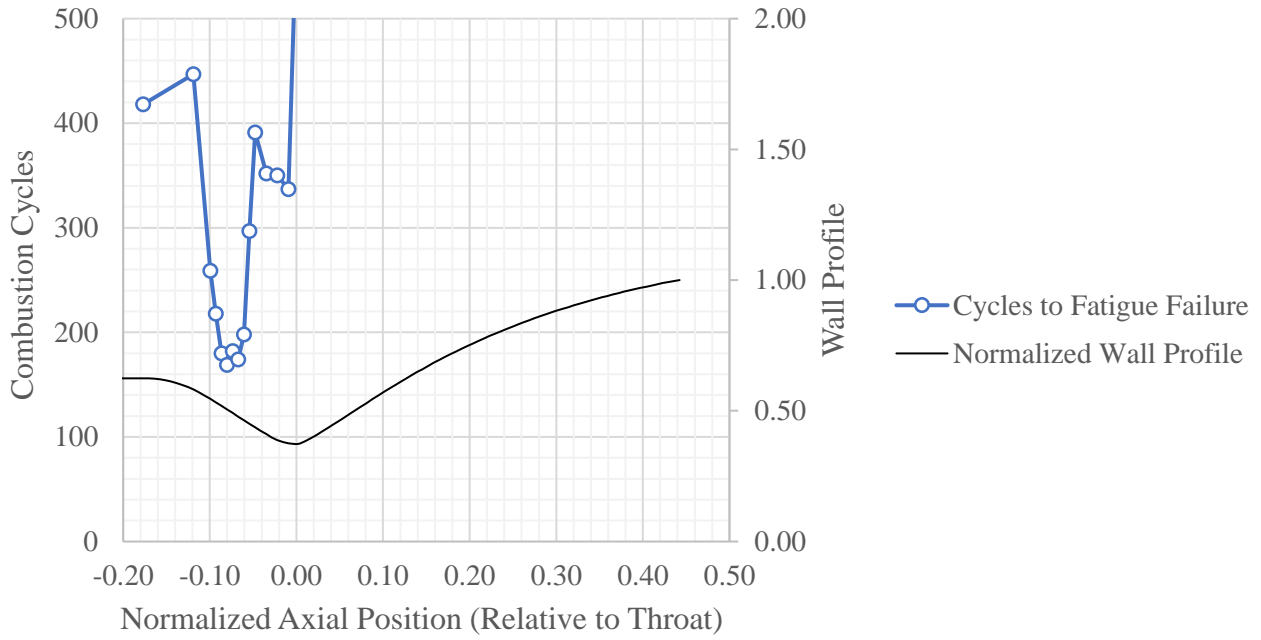
Figure 5-8: Axial variation of thrust chamber wall life (low-cycle fatigue failure)
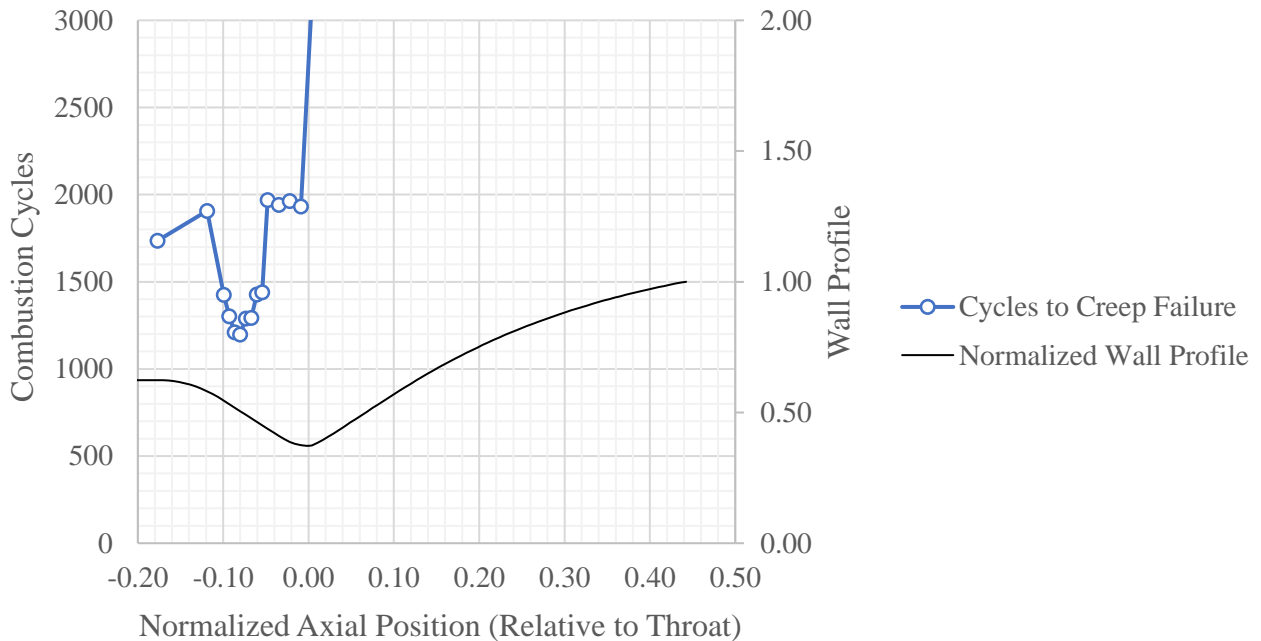
Figure 5-9: Axial variation of thrust chamber wall life (creep deformation failure)

It is clear that, for all three failure modes, a "critical failure point" exists at a normalized axial position of -0.80, not at the throat. This result appears to be primarily due to the sharp increase in overall wall temperature difference at this point, as shown in Figure 5-4. This finding goes against the conventional assumption that thrust chambers will usually fail first at or near the throat, and highlights the importance of analysing the number of cycles to ligament failure at multiple locations in the thrust chamber to determine thrust chamber life with confidence. Figure 5-7 to Figure 5-9 also show the

number of cycles to failure increasing dramatically in the diverging section of the nozzle, indicating that the higher pressure differential loading at this point does not pose a serious problem.

5.2   Variable Coolant Pressure

In this section, the results of the variable coolant pressure case are presented. Subsection 5.2.1 shows the effect of varying coolant pressure on engine performance. Subsection 5.2.2 shows the effect of varying coolant pressure on thrust chamber life. Finally, Subsection 5.2.3 shows the extent to which coolant pressure can be varied within the engine operating limits.

5.2.1 Effect on Engine Performance

Figure 5-10 shows the effect of changing coolant pressure on engine performance. It can be seen that the effect of changing coolant pressure on thrust is negligible. This is to be expected, as there is no direct mechanism by which coolant pressure could significantly influence propellant flow in the thrust chamber. While some of the coolant flows through the fuel mixer and into the combustion chamber, any resulting change in fuel pressure at the injectors resulting from a change in coolant pressure is compensated for by an adjustment in oxidizer pump pressurization. This change is necessary to maintain a constant combustion pressure, as described in Section 4.7.1. Figure 5-11 shows the effect of changing coolant pressure on fuel injection pressure, and how oxidizer injection pressure is adjusted accordingly.
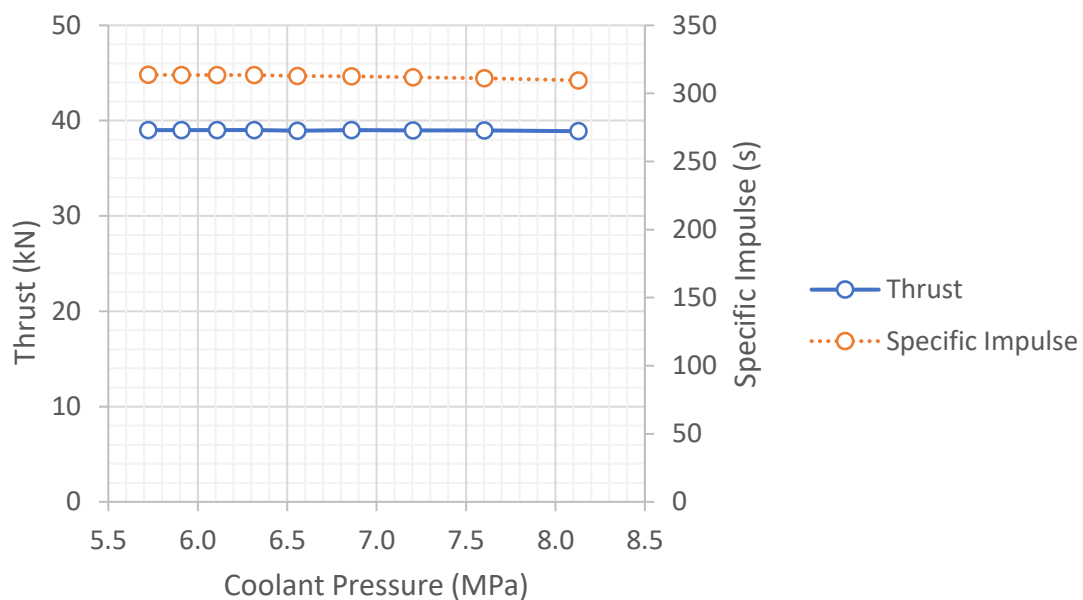
Figure 5-10: Effect of coolant pressure on thrust & specific impulse
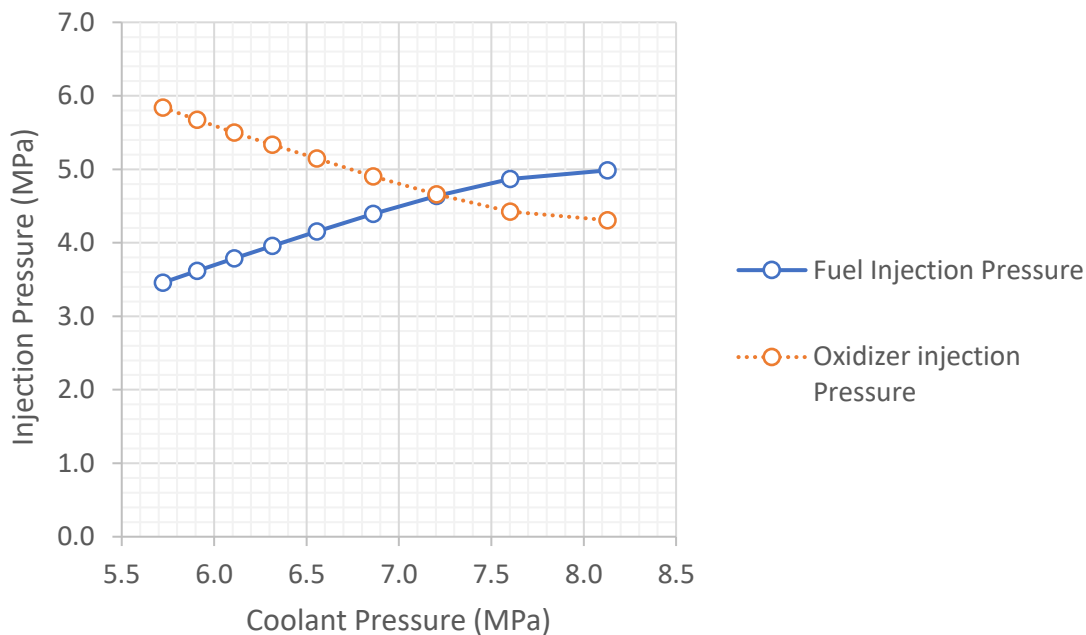
Figure 5-11: Effect of coolant pressure on fuel & oxidizer injection pressure

Figure 5-10 also shows a very slight change in specific impulse as a result of changing coolant pressure. This is likely due to a change in bleed flow requirements resulting from the change in FTP pressurization, as shown in Figure 5-12.
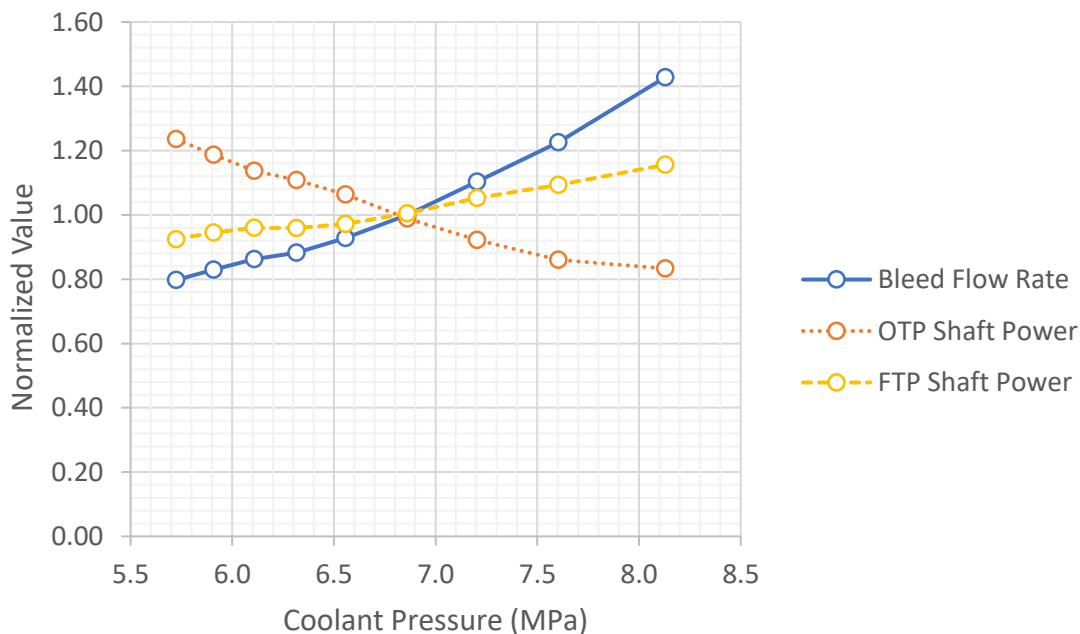
Figure 5-12: Effect of coolant pressure on bleed flow rate and turbopump power

Figure 5-12 shows that as coolant pressure increases, FTP power also increases. A higher pressure head requires the fuel pump to extract more energy from the fuel turbine. As a result, the turbine requires more working fluid. This results in an increase in bleed flow, as shown in Figure 5-12.

In the expander-bleed cycle, bleed flow is vented overboard without directly generating thrust. As such, an increase in bleed flow will decrease specific impulse, although bleed flow only represents a small proportion of net engine propellant flow, so the resulting effect is small, as Figure 5-10 indicates. Figure 5-12 also shows a decrease in OTP power as coolant pressure increases. This is likely due to a lower pressure requirement as oxidizer injector pressure is reduced to compensate for increased fuel injector pressure, as shown in Figure 5-11.

5.2.2 Effect on Thrust Chamber Life

Figure 5-13 and Figure 5-14 show the effect of changing coolant pressure on thrust chamber life. As shown in Figure 5-13(a), there appears to be some relationship between the number of combustion cycles to plastic instability and coolant pressure. Similarly, Figure 5-14 shows a correlation between the number of combustion cycles to creep failure and coolant pressure. However, Figure 5-13(b) shows that there appears to be no significant relationship between coolant pressure and the cycles to fatigue failure. Additionally, for all three failure modes, the life at the critical failure point is significantly shorter than the life at the throat.

(a)   *(b)*
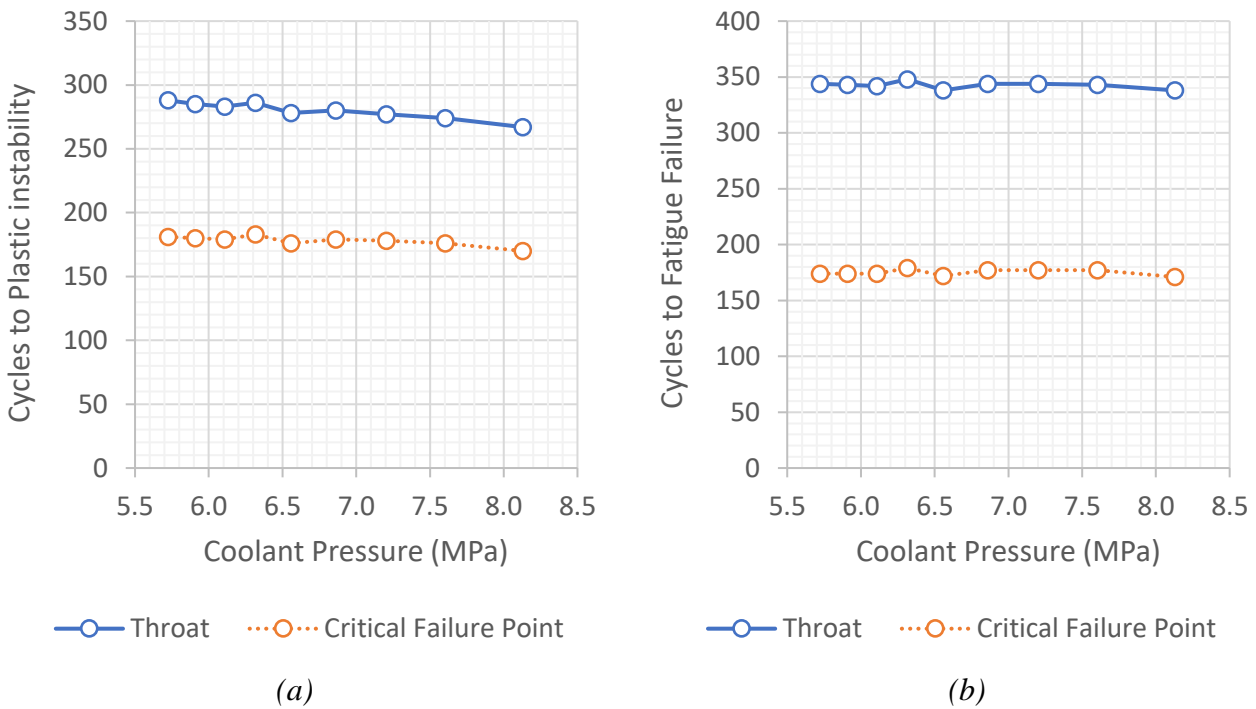
Figure 5-13: Effect of Coolant pressure on cycles to (a) plastic instability and (b) fatigue failure

Figure 5-14: Effect of coolant pressure on cycles to creep failure

Figure 5-15 and Figure 5-16 show the effect of changing coolant pressure on the parameters identified in the preliminary analysis results (refer to Equations (3-8) to (3-10), page 38), which affect life. Specifically, Figure 5-15(a) shows the effect on maximum wall temperature, Figure 5-15(b) shows the effect on overall wall (i.e. ligament to closeout wall) temperature difference. Figure 5-16(a) shows the effect on ligament pressure differential loading. Finally, Figure 5-16(b) shows the effect on ligament temperature difference.

(a)

(b)
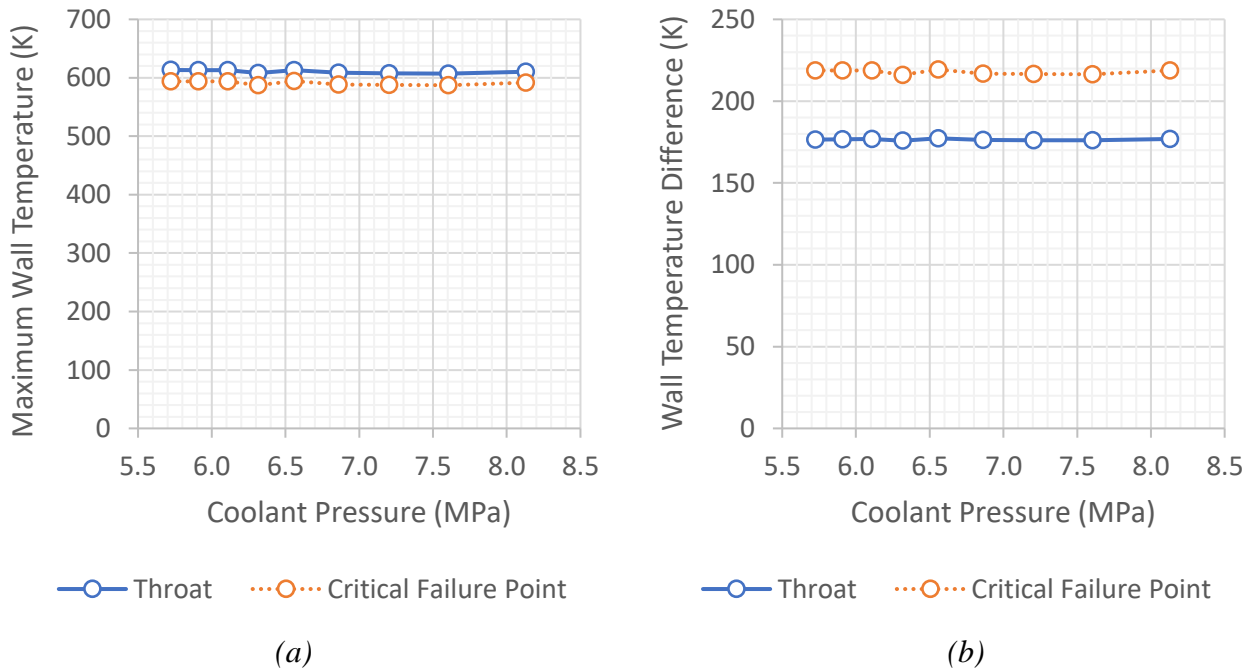
Figure 5-15: Effect of coolant pressure on (a) maximum wall temperature and (b) wall temperature difference

Figure 5-15(a), Figure 5-15(b), and Figure 5-16(b) show that changing the coolant pressure has little impact on the general temperature distribution in the thrust chamber wall. This indicates that coolant pressure does not strongly influence heat transfer into the coolant. This result is not surprising: the Colburn correlation in Equation (2-55) (page 29) shows that pressure is not a direct factor in determining the coolant heat transfer coefficient. Changing pressure may affect some relevant state variables, such as thermal conductivity, constant-pressure specific heat and viscosity, but the end result on heat transfer is negligible. It can also be seen that, while maximum temperature and ligament temperature difference are roughly equal at both the throat and the critical failure point, the overall wall temperature difference is higher at the critical failure point. This further indicates that a higher wall temperature difference is the likely reason for shorter life at the critical failure point.

(a)   *(b)*
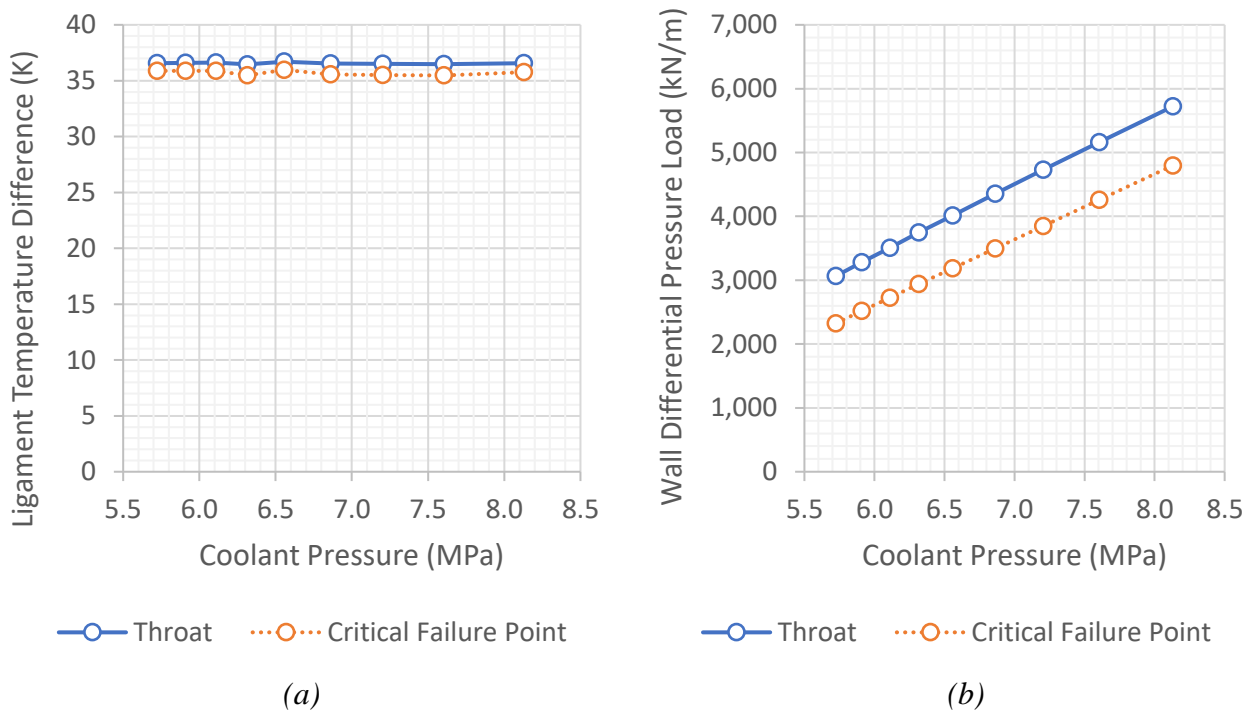
Figure 5-16: Effect of Coolant Pressure on (a) ligament differential pressure load and (b) ligament temperature difference

Figure 5-16(a) shows a clearly linear correlation between coolant pressure and ligament pressure differential loading. This is to be expected - the differential pressure loading arises from the local pressure difference between the coolant and hot gas sides of the ligament. Based on the preliminary analysis results shown in Equations (3-8) to (3-10) (page 38), it was expected that changing differential pressure load would affect combustion cycles to plastic instability and creep failure, but would have little effect on fatigue life. The results of this case reflect that assumption: Figure 5-15 and Figure 5-16 show that changing coolant pressure only affects differential pressure load – not wall

temperature distribution. At the same time, Figure 5-13 and Figure 5-14 show an effect on plastic instability and creep life, but a negligible effect on fatigue life.

5.2.3 Operating Limits

Coolant pressure can be increased to a maximum value of 8.1 MPa. This upper limit is constrained by FTP shaft speed, as shown in Figure 5-17. At a coolant pressure of 8.1 MPa, FTP shaft speed reaches its maximum allowable limit for the JAXA reusable rocket engine. Conversely, coolant pressure can be reduced to a minimum of 5.7 MPa. This lower limit is constrained by OTP shaft speed, as shown in Figure 5-17. At a coolant pressure of 5.7 MPa, OTP shaft speed reaches its maximum allowable limit for the JAXA reusable rocket engine.
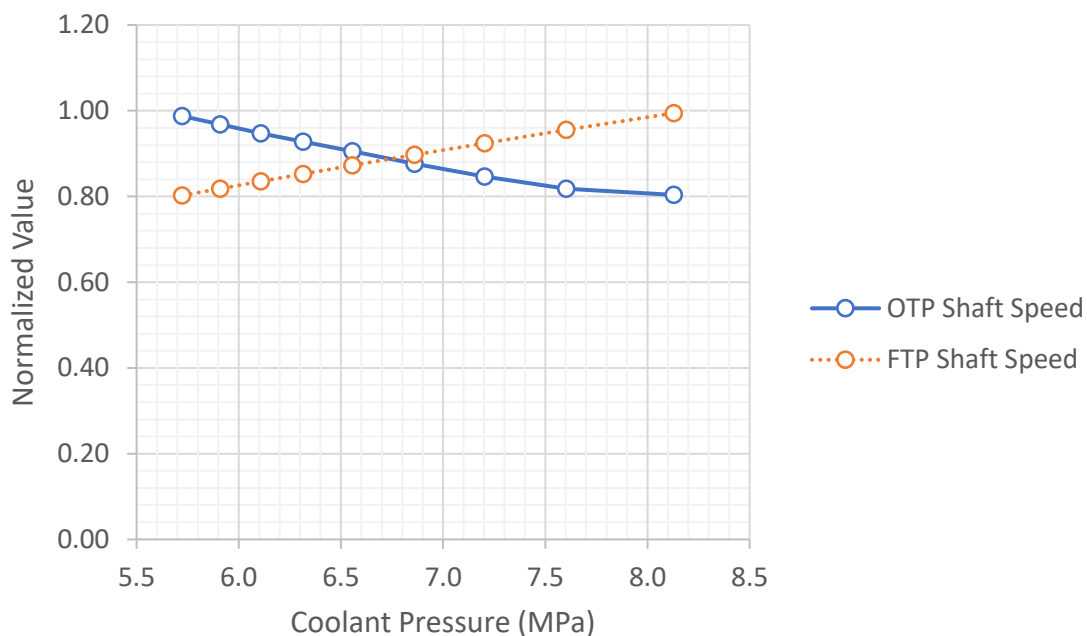
Figure 5-17: Effect of coolant pressure on turbopump shaft speeds

5.3   Variable Coolant Flow Rate

In this section, the results of the variable coolant flow rate case are presented. Subsection 5.3.1 shows the effect of varying coolant flow rate on engine performance. Subsection 5.3.2 shows the effect of varying coolant flow rate on thrust chamber life. Finally, Subsection 5.3.3 shows the extent to which coolant flow rate can be varied within the engine operating limits.

5.3.1 Effect on Engine Performance

Figure 5-18 shows the effect of changing coolant flow rate on engine performance. As with the variable coolant pressure case described in Section 5.2.1, it can be seen that the effect of changing

coolant flow rate on thrust is negligible. Once again, this is to be expected, as there is no direct mechanism by which coolant flow rate could significantly influence propellant flow in the thrust chamber. Theoretically, changing the coolant flow rate will change cooling channel outlet temperature and the heated fuel flow rate into the mixer, which could affect fuel injection temperature, but as established in the preliminary investigation in Section 3.1, changing injector temperatures has a negligible impact on performance.
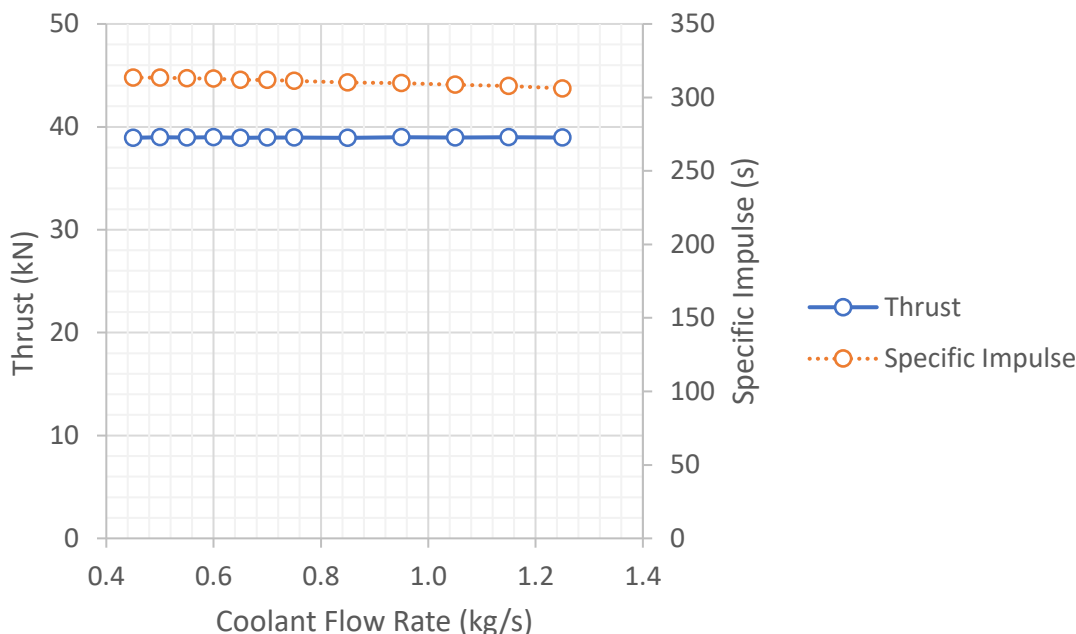
Figure 5-18: Effect of coolant flow rate on thrust and specific impulse

As with the variable coolant pressure case described in Section 5.2.1, Figure 5-18 also shows a very slight change in specific impulse as a result of changing coolant flow rate. This is likely due to a change in bleed flow requirements resulting from the change cooling channel outlet temperature. If the coolant flow rate is increased, the coolant temperature will logically decrease, as the higher volume of coolant can carry more heat with a lower temperature increase. The result of this can be seen on Figure 5-19: As coolant flow rate increases, the temperature at the cooling channel outlet decreases. However, the turbopumps require the high-enthalpy heated coolant as a working fluid for their turbines. If the temperature of the fluid flowing into the turbines is lower, more working fluid is required to generate the same level of shaft power. This increases the required bleed flow rate, as shown in Figure 5-19. This in turn decreases specific impulse. It should be noted however, that bleed flow only represents a small proportion of net engine propellant flow, so the resulting effect is small, as Figure 5-18 indicates.
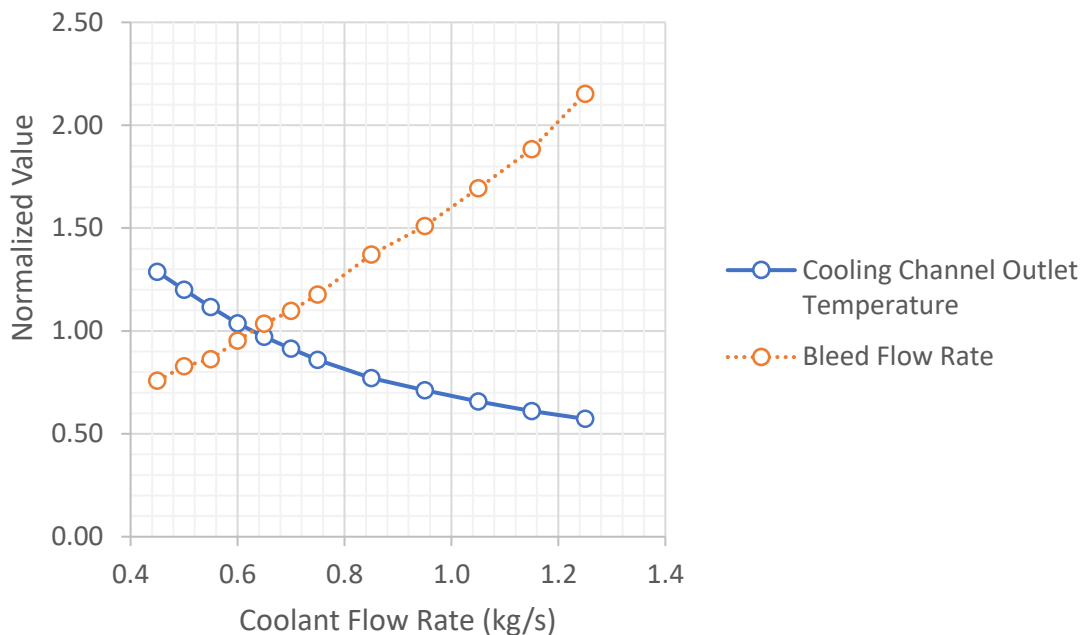
Figure 5-19: Effect of coolant flow rate on cooling channel outlet temperature and bleed flow rate

5.3.2 Effect on Thrust Chamber Life

Figure 5-20 and Figure 5-21 show the effect of changing coolant flow rate on thrust chamber life. In all three cases, there is a clear relationship between coolant flow rate and the number of cycles to failure. There are both similarities and differences in how coolant flow rate affects life for the three failure modes. Figure 5-20(a) shows that at both the throat and the critical failure point, increasing coolant flow rate will increase life. On the other hand, decreasing coolant flow rate decreases life, and this effect becomes significantly more pronounced below a coolant flow rate of 0.6 kg/s. Figure 5-20(b) shows that decreasing coolant flow rate will increase fatigue life at the throat up to a point, at a coolant flow rate of 0.5 kg/s. below this level, life decreases significantly. On the other hand, at the critical failure point fatigue life increases slightly with increasing coolant flow rate, but reaches a maximum value at a coolant flow rate of approximately 1.1 kg/s. Figure 5-21 shows that creep life at both the throat and the critical failure point is insensitive to changes in coolant flow rate, until the coolant flow rate declines to appoint below 0.6 kg/s. At this point, creep life decreases significantly as coolant flow rate is reduced.

(a)

(b)
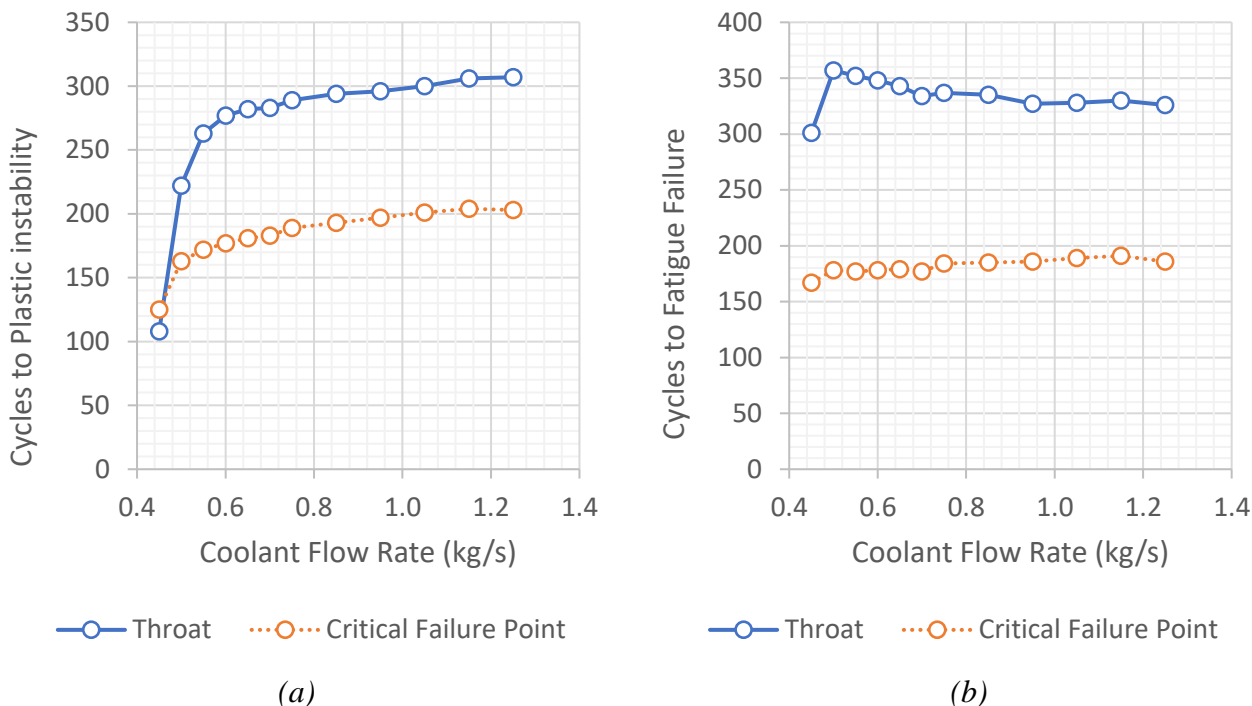
Figure 5-20: Effect of coolant flow rate on cycles to (a) plastic instability and (b) fatigue failure
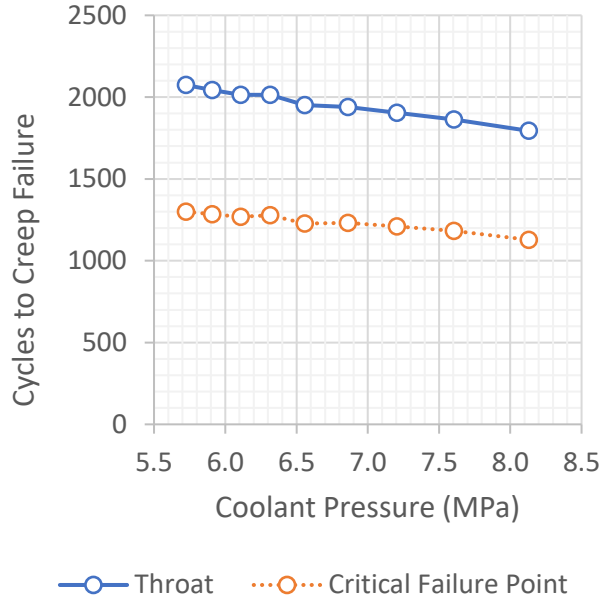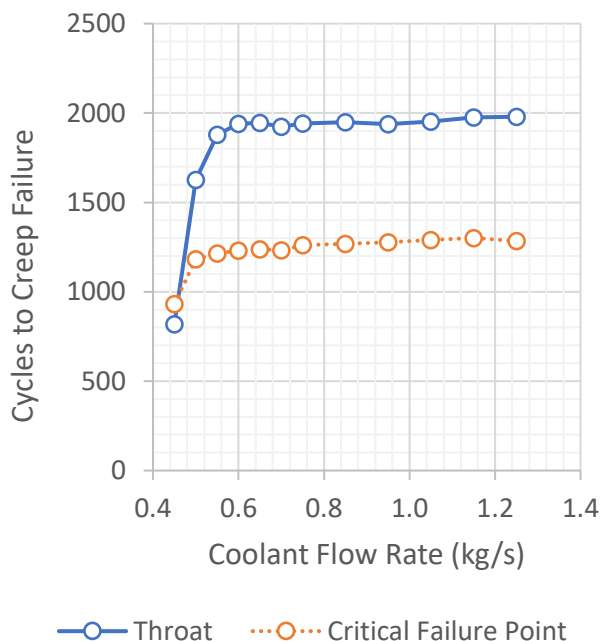

Figure 5-21: Effect of coolant flow rate on cycles to creep failure

Figure 5-22 and Figure 5-23 show the effect of changing coolant pressure on the parameters identified in the preliminary analysis results (refer to Equations (3-8) to (3-10), page 38), which affect life. Specifically, Figure 5-22(a) shows the effect on maximum wall temperature, Figure 5-22(b) shows the effect on overall wall (i.e. ligament to closeout wall) temperature difference. Figure 5-23(a) shows

the effect on ligament pressure differential loading. Finally, Figure 5-23(b) shows the effect on ligament temperature difference.

(a)   *(b)*
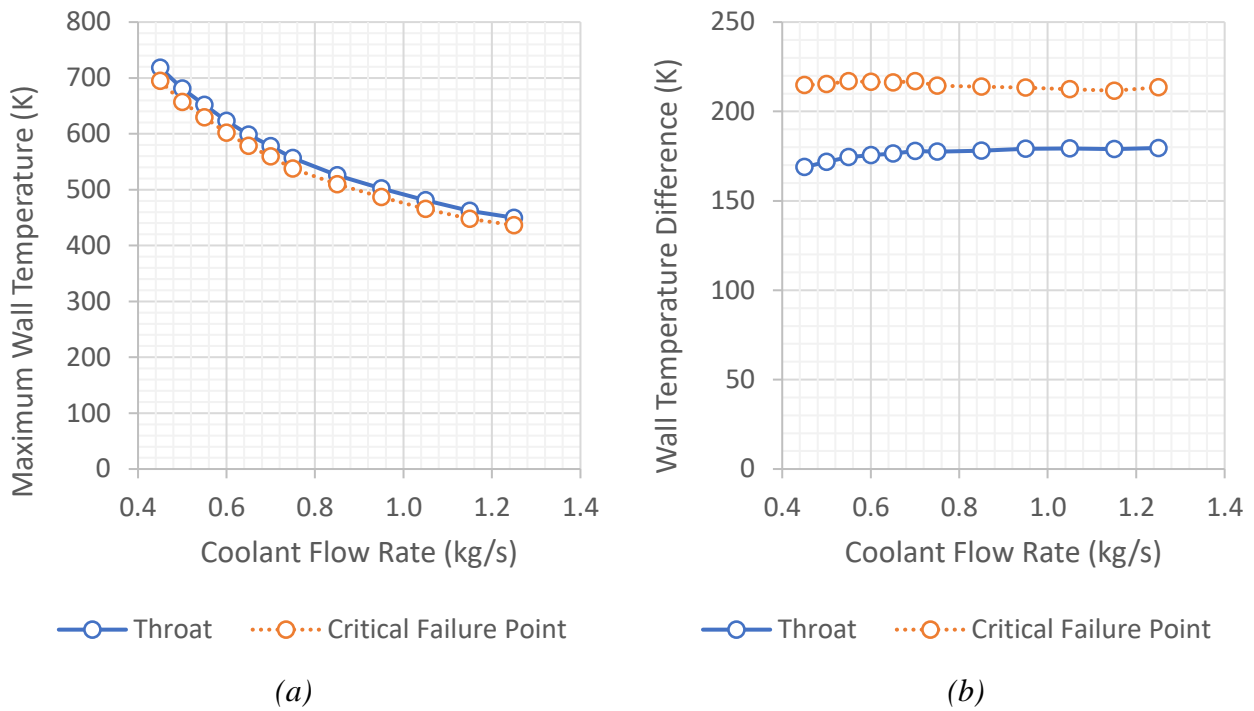
Figure 5-22: Effect of coolant flow rate on (a) maximum wall temperature and (b) wall temperature difference

Figure 5-22(a) shows that at both the throat and the critical failure point, maximum wall temperature increases as coolant flow rate is decreased. This result is intuitive – reducing coolant flow rate will reduce the rate at which heat can be removed from the thrust chamber wall, leading to an increase in temperature. The results in Figure 5-22(a) may also serve to explain the sudden decreases in thrust chamber life at low coolant flow rates, which are visible in Figure 5-20 and Figure 5-21. Creep deformation is highly temperature-sensitive. In materials which exhibit creep deformation, there is typically a "threshold temperature" above which creep behaviour becomes much more pronounced. This threshold for Cu-Cr-Zr alloy appears to be at a temperature of 650 – 700 K, which occurs at the throat at coolant flow rates below approximately 0.5 kg/s. Figure 5-24 shows the relative contribution of bending strain, hoop stain and creep strain to total ligament plastic deflection per cycle at the throat. It can be seen that above wall temperatures of 650 K, creep-induced deflection increases exponentially. This provides further evidence that the sudden decreases in life at low coolant flow rates is due to an increase in creep deflection.

(a)

(b)
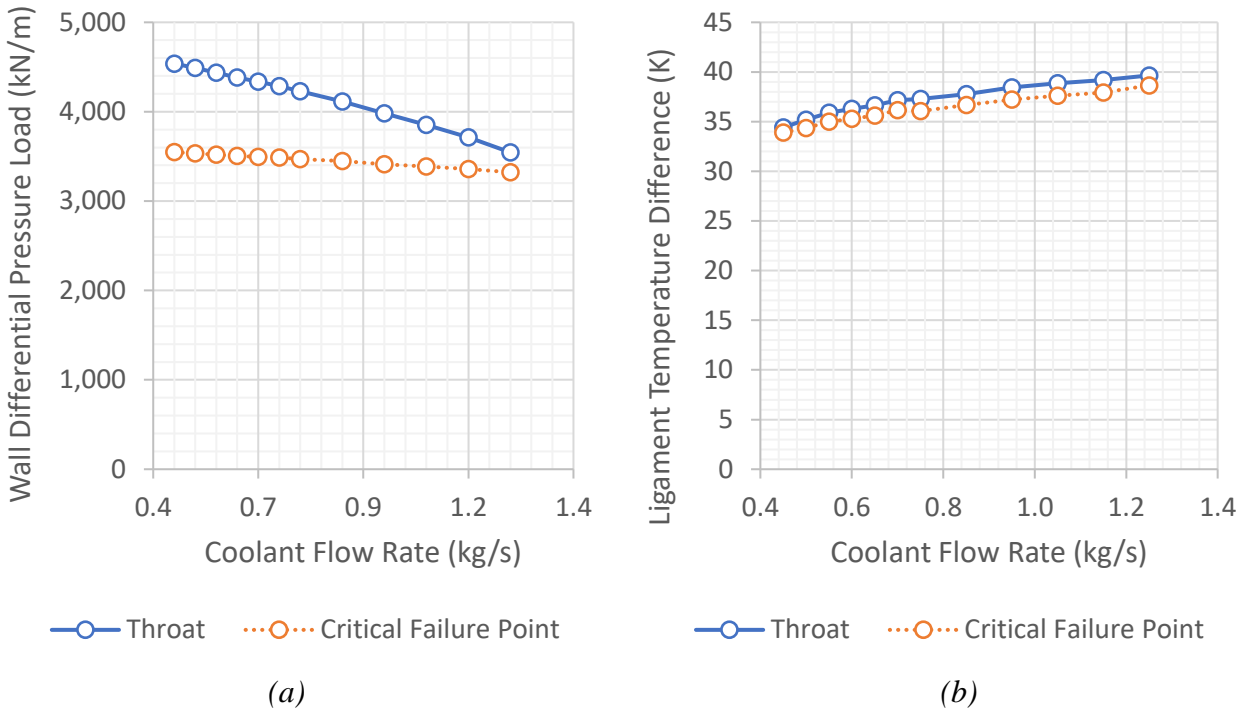
Figure 5-23: Effect of coolant flow rate on (a) ligament differential pressure load and (b) ligament temperature difference
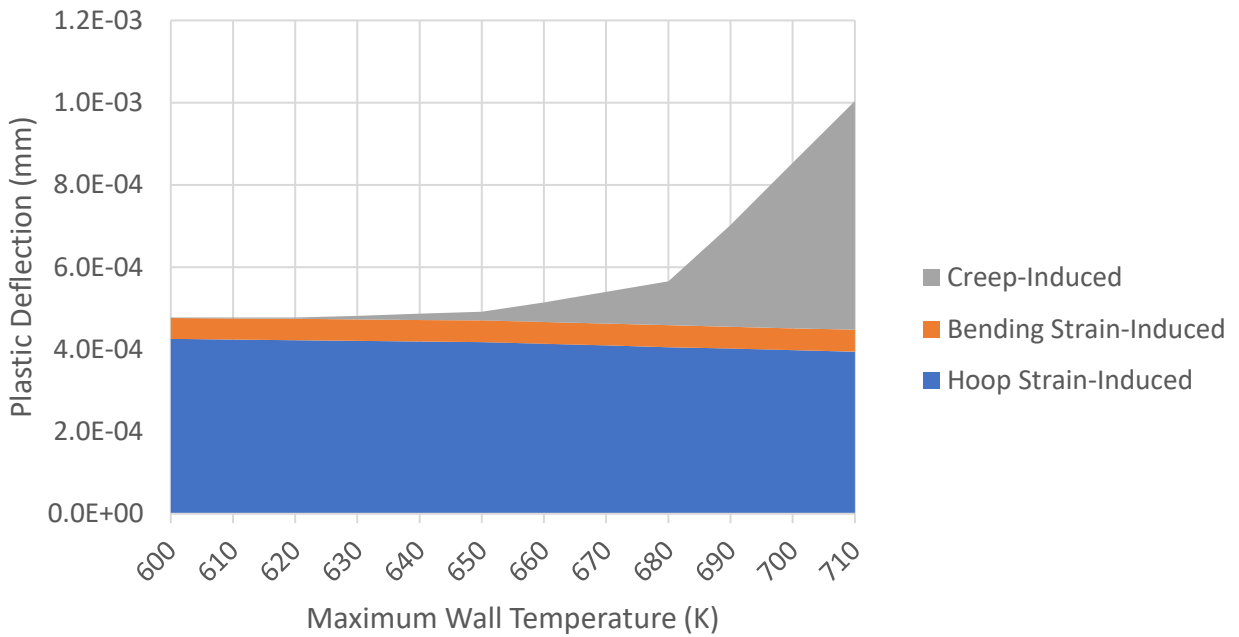
Figure 5-24: Effect of coolant flow rate on ligament plastic deflection

Figure 5-22(b) shows that decreasing coolant flow rate does not have a significant impact on wall temperature difference at either the throat or the critical failure point. At the throat, this temperature difference decreases slightly with decreased coolant flow rate, whereas at the critical failure point, the temperature difference increases slightly with increasing coolant flow rate. This result is somewhat unexpected. It was anticipated that wall temperature difference would be particularly

sensitive to coolant flow rates, as changing the coolant flow rate would change the amount of heat transferred into the coolant. This in turn would increase or decrease the amount of heat transferred into the closeout wall, affecting its temperature relative to the ligament temperature. However, closeout wall temperature seems to change at roughly the same rate as the ligament temperature, meaning coolant flow rate does not have a significant impact on wall temperature difference.

Figure 5-23(a) shows that coolant flow rate affects wall differential pressure load at both the throat and the critical failure point, but this effect is more pronounced at the throat. In accordance with the setup of this case described in Section 4.7.5, cooling channel inlet pressure and thrust chamber pressure are held constant in this case. Thus, the change in differential pressure load shown in Figure 5-23(a) must be a result of either the changing flow rate in the cooling channel affecting flow velocity, convective heat transfer or both. This result is noteworthy, as it was established in Section 5.2.2 that changing coolant pressure has a negligible effect on wall heat transfer. However, it appears that the reverse situation is different: wall heat transfer can have an effect on coolant pressure. Figure 5-23(b) shows that that coolant flow rate affects ligament temperature difference at both the throat and the critical failure point in roughly the same way: at both locations, ligament temperature difference decreases with decreasing coolant flow rate. This result is intuitive – a lower coolant flow rate will result in a higher local coolant temperature, reducing the temperature gradient across the ligament.

5.3.3 Operating Limits

Coolant flow rate can be increased to a maximum value of 1.25 kg/s. This upper limit is constrained by oxidizer turbine working fluid enthalpy. As described in Subsection 5.3.1, increasing coolant flow rate reduces cooling channel outlet temperature, leaving less energy available in the bleed flow to drive the turbopumps. Figure 5-25 shows that as coolant flow rate increases, both oxidizer turbine discharge temperature and pressure ratio also decrease, leading to a decrease in enthalpy. At the same time, OTP power requirements are slightly increasing. At the maximum coolant flow rate, the amount of energy which the turbine can extract from the flow is not enough to meet the pump power requirements, effectively creating an upper limit on cooling channel flow rate.

Coolant flow rate can be decreased to a minimum value of 0.45 kg/s. This lower limit is constrained by bleed flow rate. As there is no fuel turbine bypass valve in the JAXA reusable rocket engine, all oxidizer turbine working fluid must first flow through the fuel turbine. This creates an operational constraint in that the oxidizer turbine flow rate cannot exceed the fuel turbine flow rate. Figure 5-26 shows that at the minimum coolant flow rate, the fuel turbine flow rate decreases to a point

where it becomes equal to the oxidizer turbine flow rate. As such, the engine cannot operate at a lower

coolant flow rate without over-powering the fuel turbine, or under-powering the oxidizer turbine.
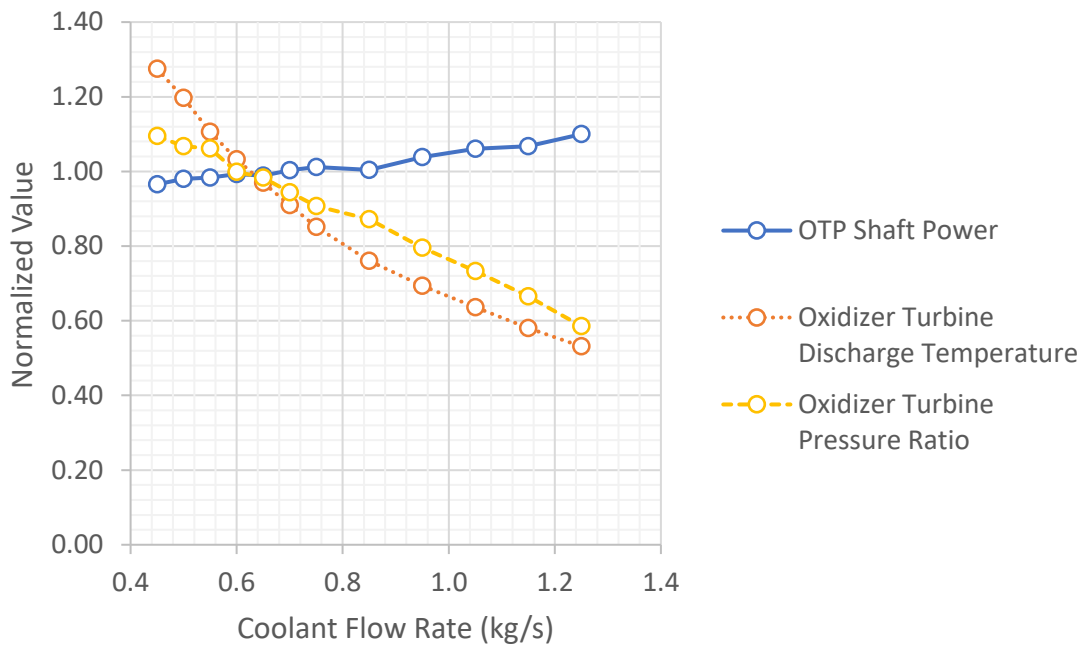
Figure 5-25: Effect of coolant flow rate on oxidizer turbine performance
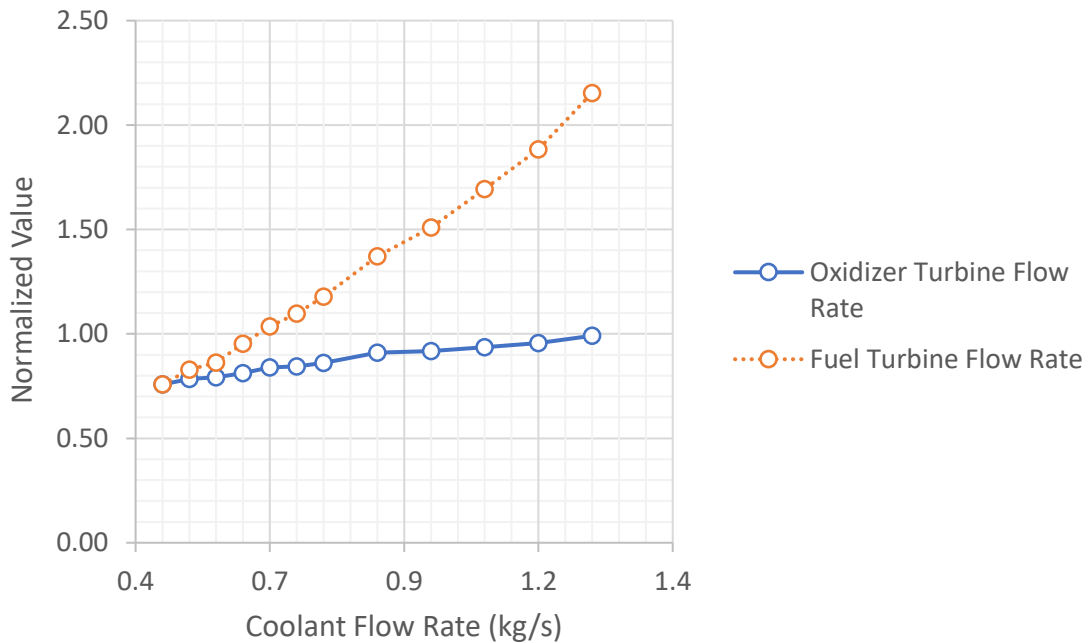
Figure 5-26: Effect of coolant flow rate on required turbine flow rates

5.4 Variable Mixture Ratio

In this section, the results of the variable mixture ratio case are presented. Subsection 5.4.1 shows the effect of varying mixture ratio on engine performance. Subsection 5.4.2 shows the effect of varying mixture ratio on thrust chamber life. Finally, Subsection 5.4.3 shows the extent to which mixture ratio can be varied within the engine operating limits.

5.4.1 Effect on Engine Performance

Figure 5-27 shows the effect of changing mixture ratio on engine performance. It can be seen that changing mixture ratio has an almost-identical effect on both thrust and specific impulse: increasing the mixture ratio will reduce thrust and specific impulse, while reducing mixture ratio will increase performance.
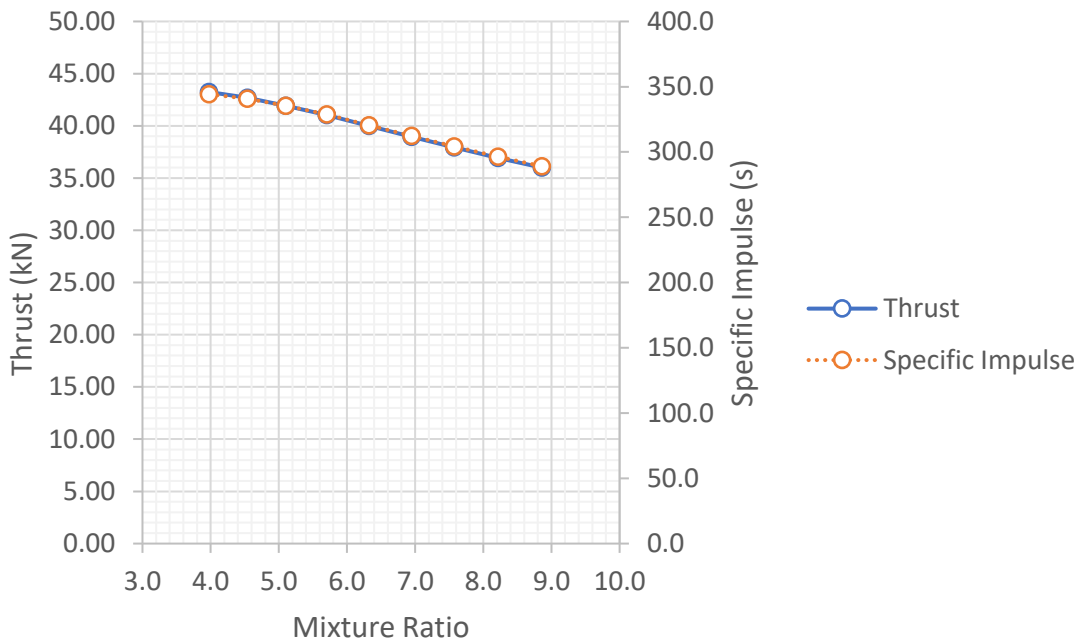
Figure 5-27: Effect of mixture ratio on thrust & specific impulse

The mechanisms here are well-understood for LH_2/LOx rocket engines. Figure 5-28 shows how the exhaust gas composition changes with varying mixture ratio. At low mixture ratios, the exhaust gas is effectively a 50-50 blend of water vapor and lightweight, unburnt molecular hydrogen. The higher proportion of hydrogen in the exhaust gas reduces the average molecular weight of the gas. Thus, less energy is required to accelerate the exhaust gasses, and a higher exhaust gas velocity can be achieved, as shown in Figure 5-29. On the other hand, as mixture ratio increases, the composition of the exhaust gas changes. There is a higher proportion of water vapour, and the concentration of species such as hydroxyl and unburnt molecular oxygen increases, while the proportion of hydrogen decreases. This increases average molecular weight and reduces exhaust velocity, as shown in Figure 5-29.
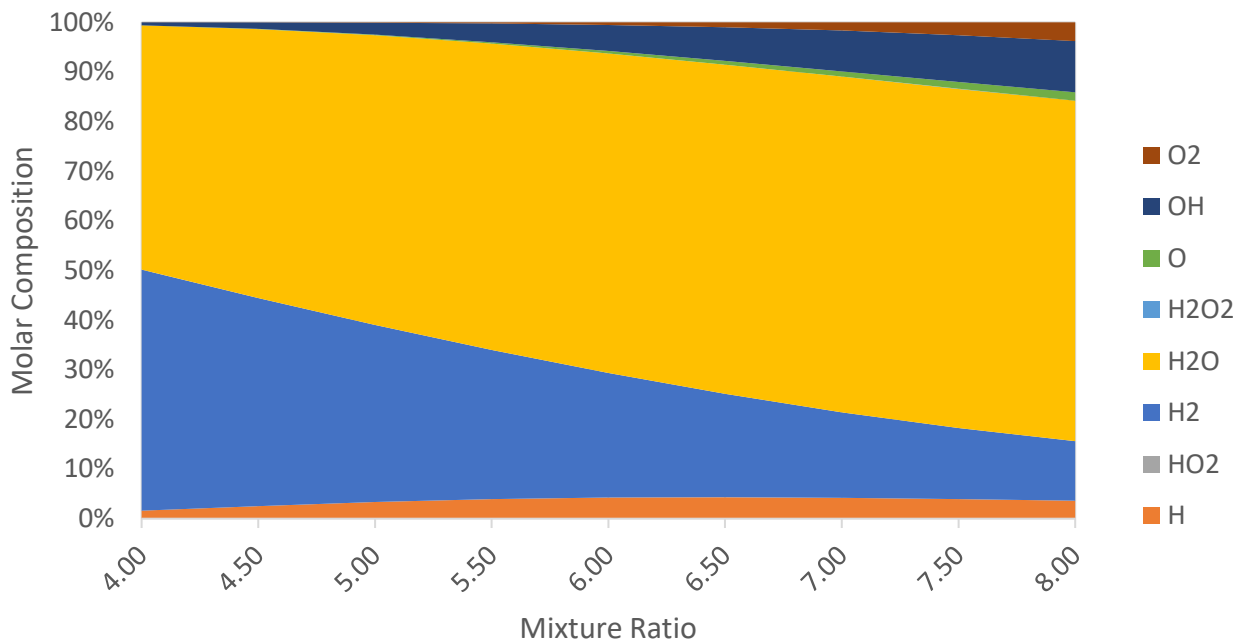
Figure 5-28: Effect of mixture ratio on exhaust gas composition
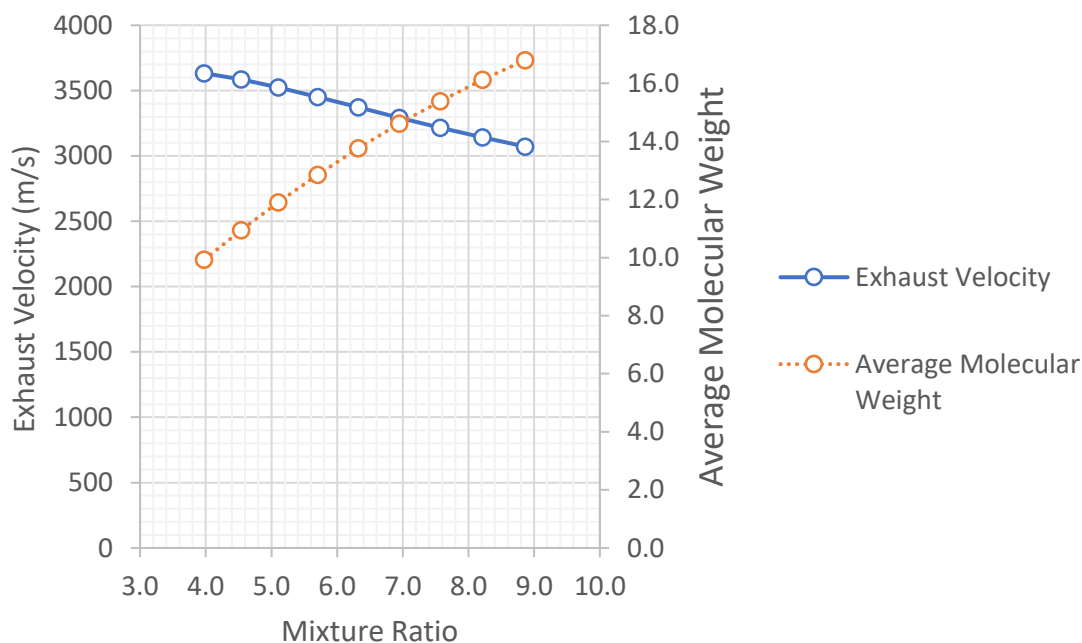
Figure 5-29: Effect of mixture ratio on exhaust gas molecular weight and velocity

5.4.2 Effect on Thrust Chamber Life

Figure 5-30 and Figure 5-31 show the effect of mixture ratio on thrust chamber life. In all three cases, at both the throat and the critical failure point, similar phenomena are evident. Life increases almost linearly with increasing mixture ratio. However, below a mixture ratio of approximately 5.7, this trend ceases, and the number of cycles to failure becomes constant, or starts to increase slightly with decreasing mixture ratio.

(a)   *(b)*
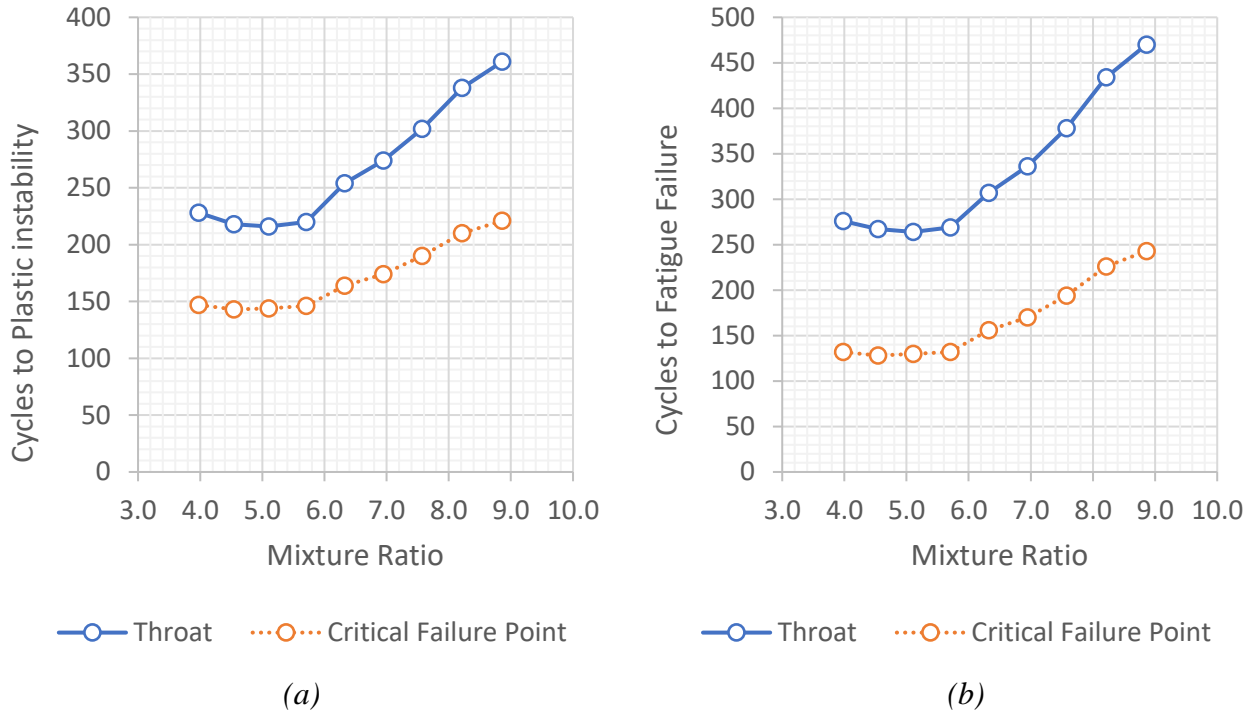
Figure 5-30: Effect of mixture ratio on cycles to (a) plastic instability and (b) fatigue failure
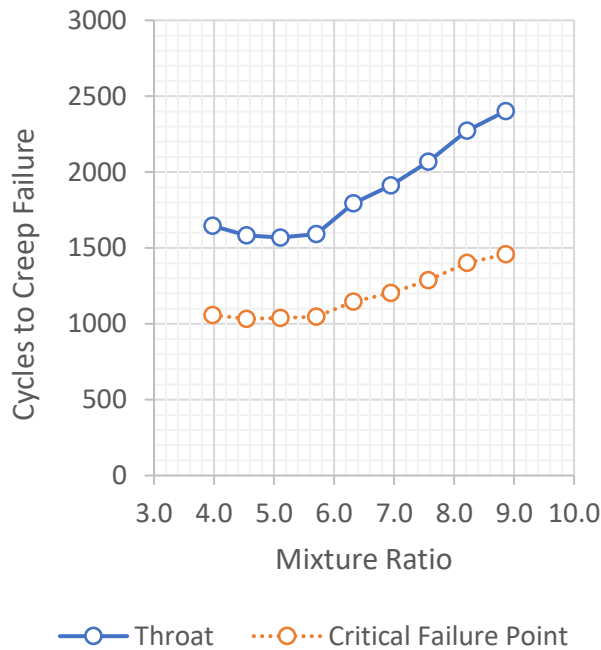
Figure 5-31: Effect of mixture ratio on cycles to creep failure

Figure 5-32 and Figure 5-33 show the effect of changing mixture ratio on the parameters identified in the preliminary analysis results (refer to Equations (3-8) to (3-10), page 38), which affect life. Specifically, Figure 5-32(a) shows the effect on maximum wall temperature, Figure 5-32(b) shows the effect on overall wall (i.e. ligament to closeout wall) temperature difference. Figure 5-33(a) shows

the effect on ligament pressure differential loading. Finally, Figure 5-33(b) shows the effect on ligament temperature difference.

(a)

(b)
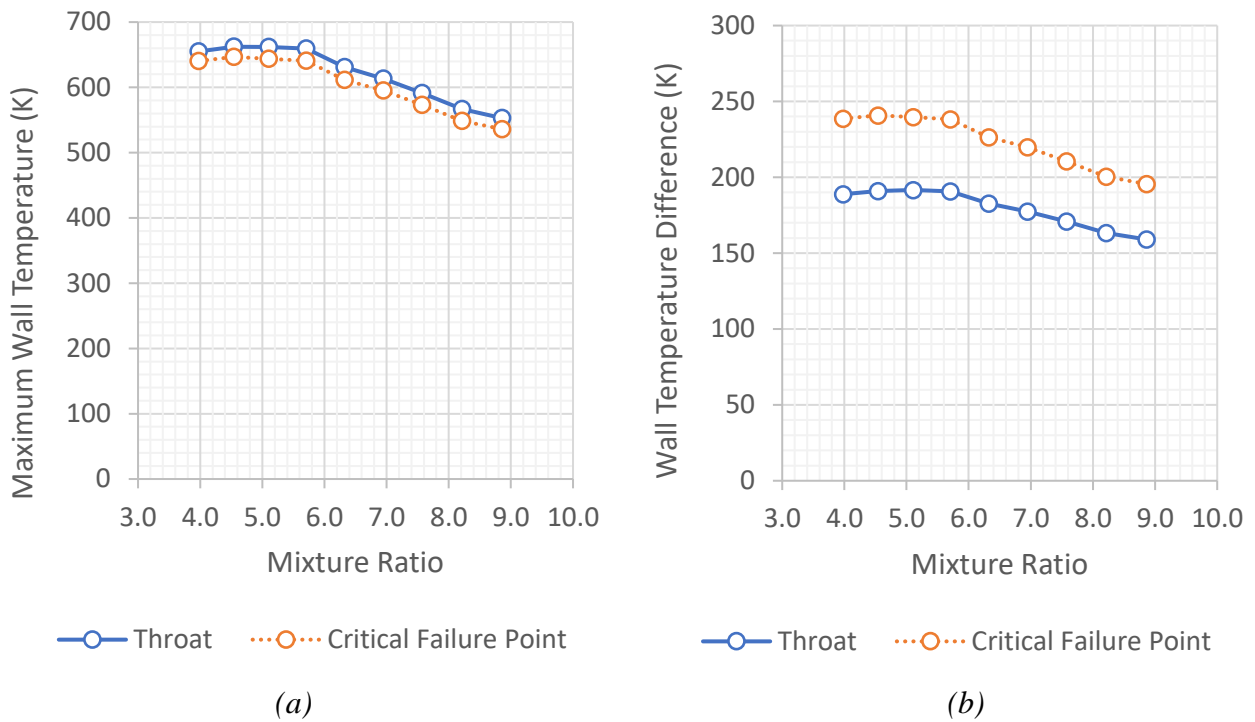
Figure 5-32: Effect of mixture ratio on (a) maximum wall temperature and (b) wall temperature difference

(a)

(b)
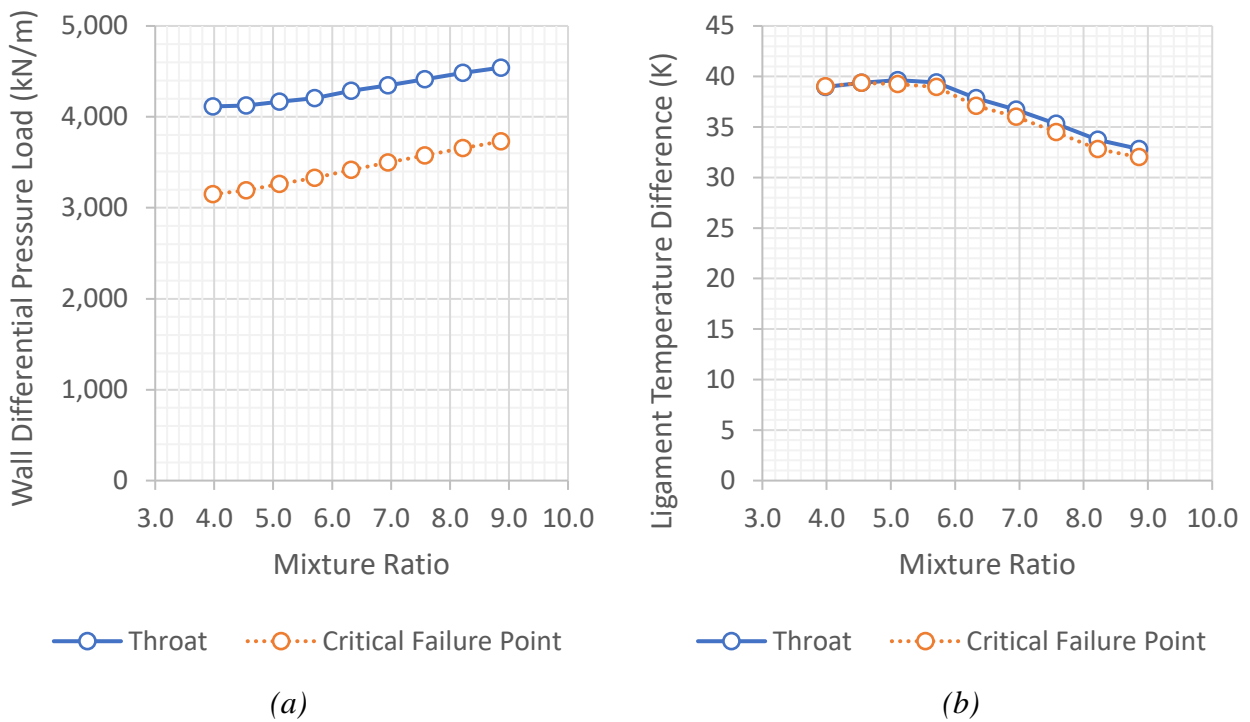
Figure 5-33: Effect of mixture ratio on (a) ligament differential pressure load and (b) ligament temperature difference

Figure 5-32(a), Figure 5-32(b) and Figure 5-33(b) show the effect of changing mixture ratio on the thermal environment in the wall. Similar trends are visible in all three plots, at both the throat and the critical failure point: maximum wall temperature, overall wall temperature difference and ligament temperature difference all increase with decreasing mixture ratio, but at a mixture ratio of approximately 5.7, these trends level off. The temperature distributions remain constant or start to decrease as mixture ratio is further decreased. On the other hand, Figure 5-33(b) shows a much more straightforward correlation between mixture ratio and ligament differential pressure load. At both the throat and the critical failure point, differential pressure load increases slightly with increasing mixture ratio.

The correlation between the temperature distribution plots in Figure 5-32(a), Figure 5-32(b) and Figure 5-33(b), and the thrust chamber life plots in Figure 5-30 and Figure 5-31 is clear. It is evident that the variations in thrust chamber life are being influenced by the temperature distribution in the wall, which is in-turn being influenced by heat transfer from the thrust chamber. Logically, decreasing the temperature of the gasses in the thrust chamber should reduce the temperature gradient between the exhaust gasses and the wall, in turn reducing heat transfer into the wall. Mixture ratio is an effective way of controlling combustion temperature. However Figure 5-34 demonstrates that mixture ratio-induced reductions in combustion temperature do not become significant until the mixture ratio is reduced below a mixture ratio of approximately 5.7.
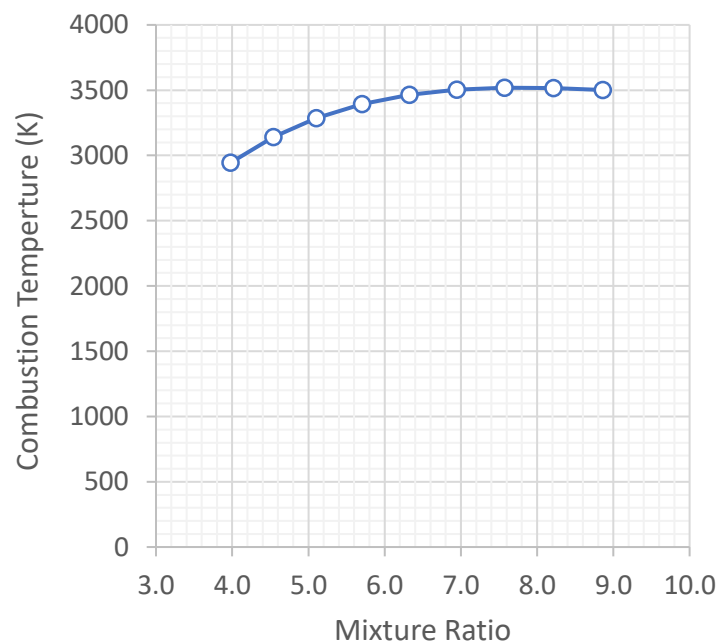
Figure 5-34: Effect of mixture ratio on combustion temperature

The Bartz correlation, shown in Equation (2-50) (page 28) shows that heat transfer from the thrust chamber into the wall is also influenced by fluid stagnation properties, namely constant-pressure specific heat, Prandtl number and viscosity. Additionally, Equation (2-52) (page 28) shows that Prandtl number is inversely proportional to thermal conductivity. Figure 5-35 shows how changing mixture ratio affects the constant-pressure specific heat, thermal conductivity and viscosity at combustion. Specifically, as mixture ratio is decreased, constant-pressure specific heat and thermal conductivity increase, while viscosity decreases. Based on Equations (2-50) and (2-52), increasing specific heat can be expected to increase heat transfer. Also, increasing thermal conductivity can be expected to reduce the Prandtl number, which will also increase heat transfer. Decreasing viscosity can be expected to reduce heat transfer, but the viscosity term is raised to a power of 0.2, indicating that this term does not have a strong influence on heat transfer.

(a)   *(b)*
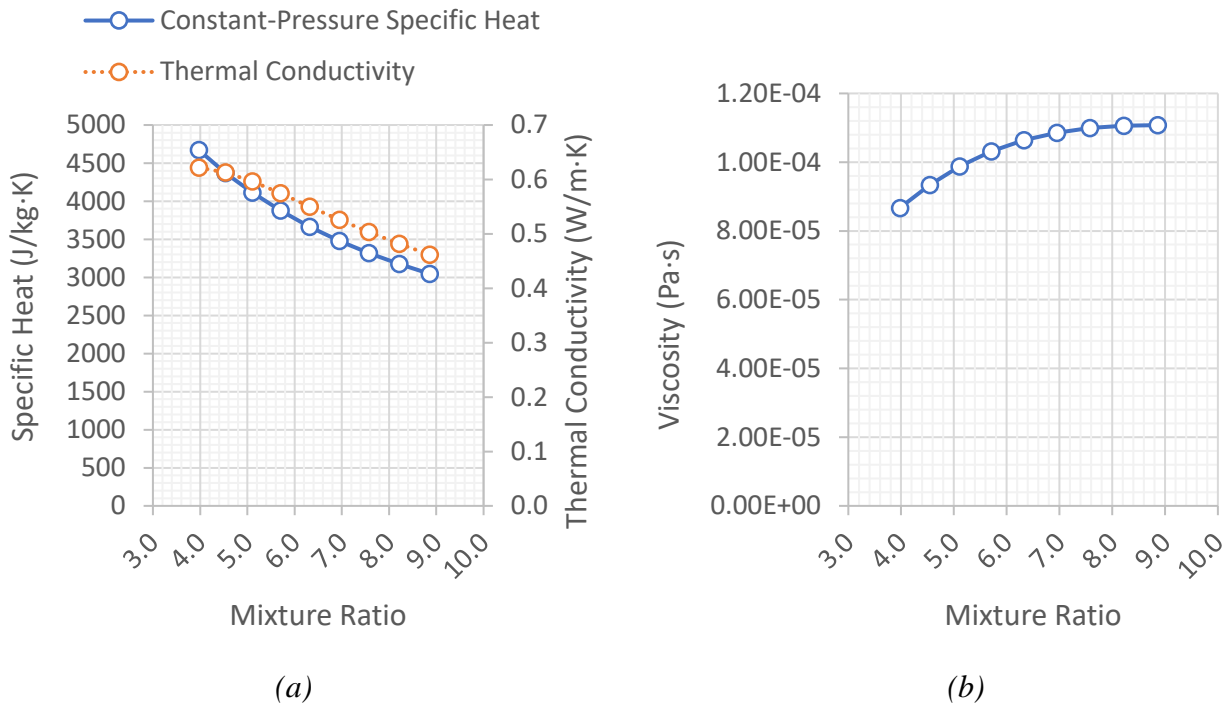
Figure 5-35: Effect of mixture ratio on (a) combustion gas specific heat & thermal conductivity and (b) viscosity

Taken together, the effects of the fluid property changes shown in Figure 5-35 could reasonably be expected to increase heat transfer into the walls as mixture ratio is reduced. However, as mixture ratio decreases below a value of approximately 5.7, the reduction in combustion temperature becomes increasingly significant. It is possible that the change in gas properties causes heat transfer to increase as mixture ratio decreases, but at a value of approximately 5.7, the decrease in gas temperature begins to reduce the rate of heat transfer significantly, overcoming the net effect of the gas properties which would otherwise increase heat transfer.

5.4.3 Operating Limits

Mixture ratio can be increased to a maximum value of 8.9. This upper limit is constrained by bleed flow rate. As described in Subsection 5.3.3, there is no fuel turbine bypass valve in the JAXA reusable rocket engine, so all oxidizer turbine working fluid must first flow through the fuel turbine. Figure 5-36 shows that at the maximum mixture ratio, the fuel turbine flow rate decreases, and the oxidizer turbine flow rate increases to a point where they become equal. As such, the engine cannot operate at a higher mixture ratio without over-powering the fuel turbine, or under-powering the oxidizer turbine.
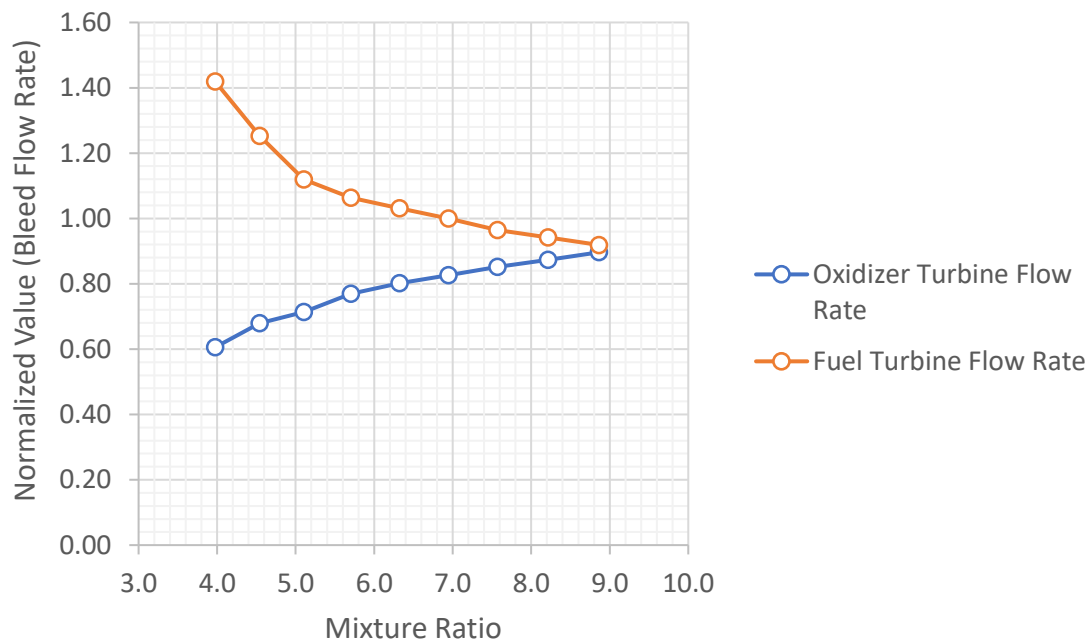
Figure 5-36: Effect of mixture ratio on required turbine flow rates

Mixture ratio can be reduced to a minimum value of 4.0. This lower limit is constrained by OTP shaft speed, as shown in Figure 5-37. At a mixture ratio of 4.0, the OTP shaft speed reaches its maximum allowable limit for the JAXA reusable rocket engine.
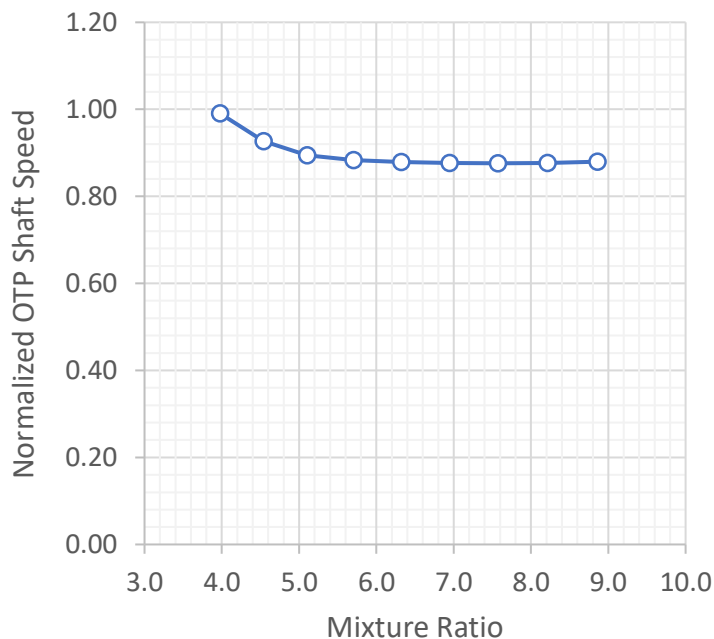
Figure 5-37: Effect of mixture ratio on oxidizer turbopump shaft speed

5.5   Variable Combustion Pressure

In this section, the results of the variable combustion pressure case are presented. Subsection 5.5.1 shows the effect of varying combustion pressure on engine performance. Subsection 5.5.2 shows the effect of varying combustion pressure on thrust chamber life. Finally, Subsection 5.5.3 shows the extent to which combustion pressure can be varied within the engine operating limits. Note that, as described in Section 3.4, propellant flow rate is intrinsically coupled to combustion pressure. The relationship between these variables is linear, as shown in Figure 5-38.
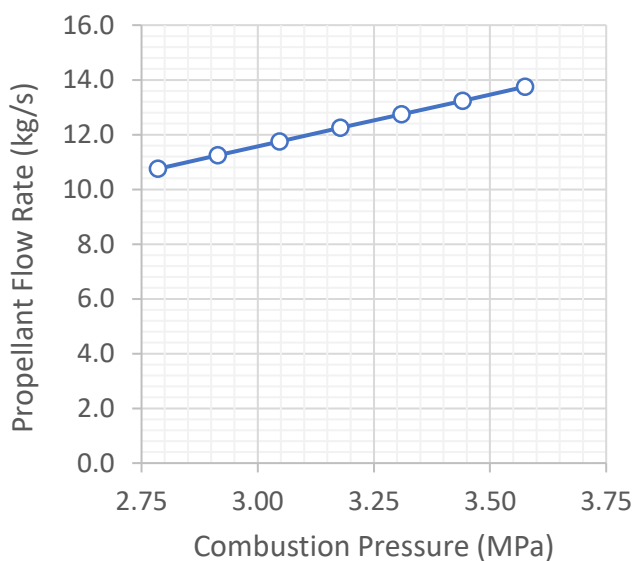
Figure 5-38: Relationship between propellant flow rate and combustion pressure

5.5.1 Effect on Engine Performance

Figure 5-39 shows the effect of changing combustion pressure on engine performance. It can be seen that changing combustion pressure (and therefore propellant flow rate) has a linear effect on both thrust and specific impulse: increasing the combustion pressure will increase both thrust and specific impulse, while reducing combustion pressure will decrease performance. Figure 5-39 shows that thrust is more sensitive to changes in propellant flow rate than specific impulse. This is an intuitive result – by definition, the formula for specific impulse shown in Equation (2-2) (page 15) is normalized by propellant flow rate. As such, the observed variance in specific impulse may be due to the changes in combustion pressure alone, whereas changes in thrust might be influenced by changes in both combustion pressure and propellant flow rate.
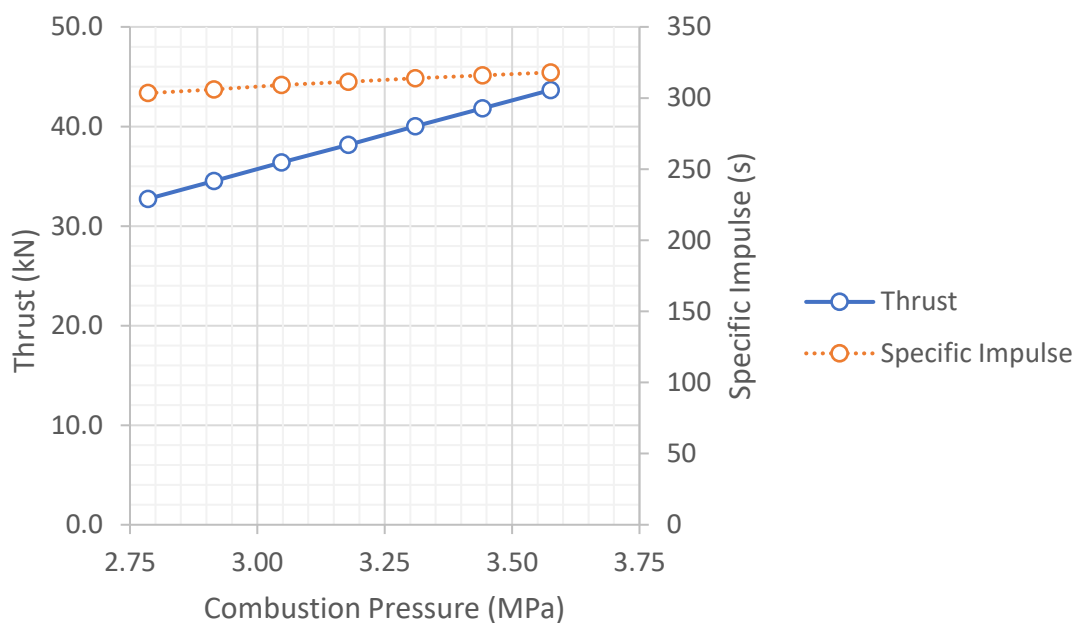
Figure 5-39: Effect of combustion pressure on thrust & specific impulse

5.5.2 Effect on Thrust Chamber Life

Figure 5-40 and Figure 5-41 show the effect of changing combustion pressure on thrust chamber life. In all three cases, at both the throat and the critical failure point, similar phenomena are evident. Life decreases almost linearly with increasing combustion pressure. Additionally, the life calculated at the critical failure point is significantly lower than the life calculated at the throat for all three failure modes.
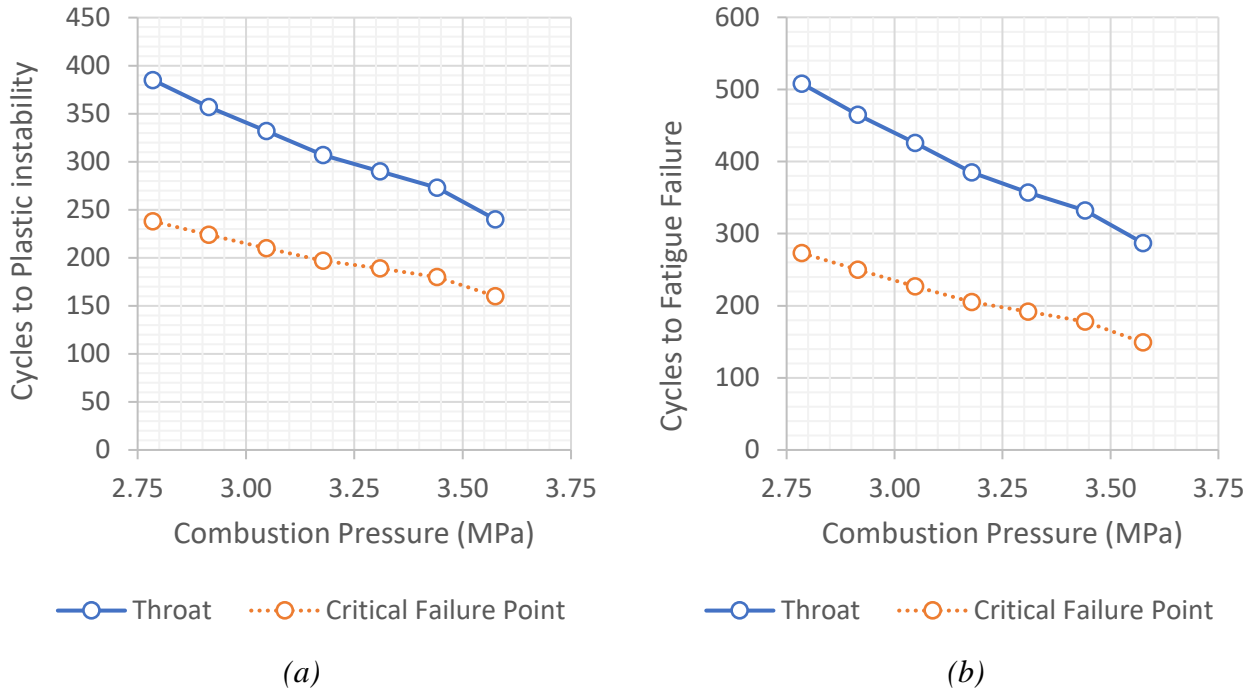
Figure 5-40: Effect of combustion pressure on cycles to (a) plastic instability and (b) fatigue failure
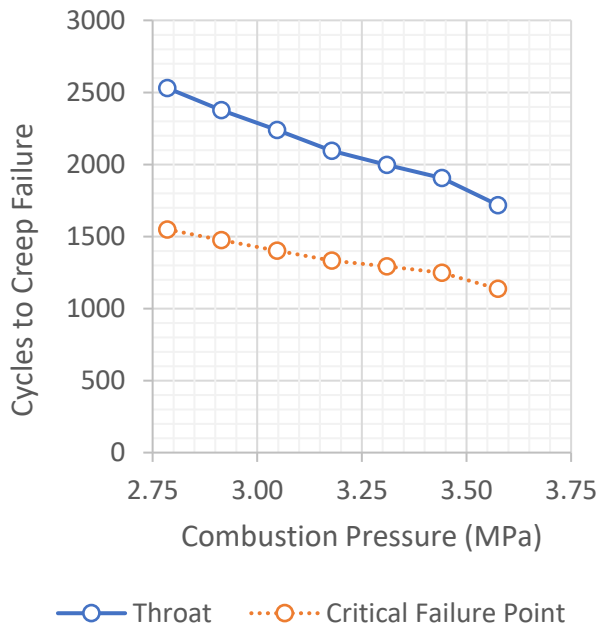
Figure 5-41: Effect of coolant flow rate on cycles to creep failure

Figure 5-42 and Figure 5-43 show the effect of changing combustion pressure on the parameters identified in the preliminary analysis results (refer to Equations (3-8) to (3-10), page 38), which affect life. Specifically, Figure 5-42(a) shows the effect on maximum wall temperature, Figure 5-42(b) shows the effect on overall wall (i.e. ligament to closeout wall) temperature difference. Figure 5-43(a) shows the effect on ligament pressure differential loading. Finally, Figure 5-43(b) shows the effect on ligament temperature difference.

(a)   *(b)*
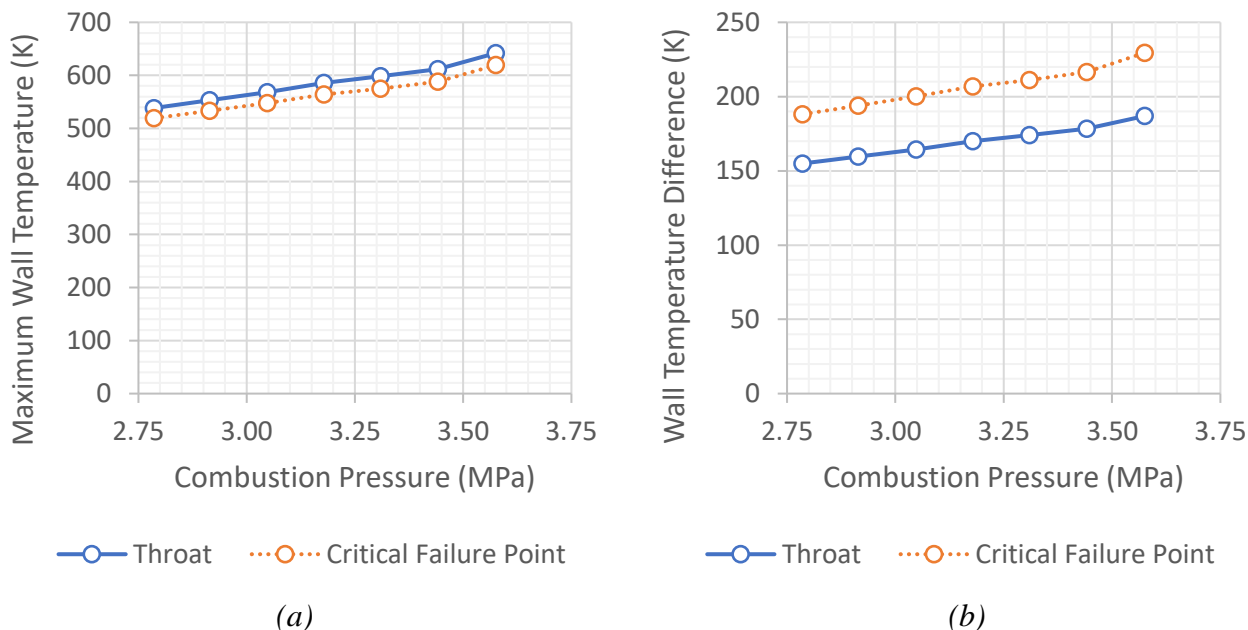
Figure 5-42: Effect of combustion pressure on (a) maximum wall temperature and (b) wall temperature difference

(a)   *(b)*
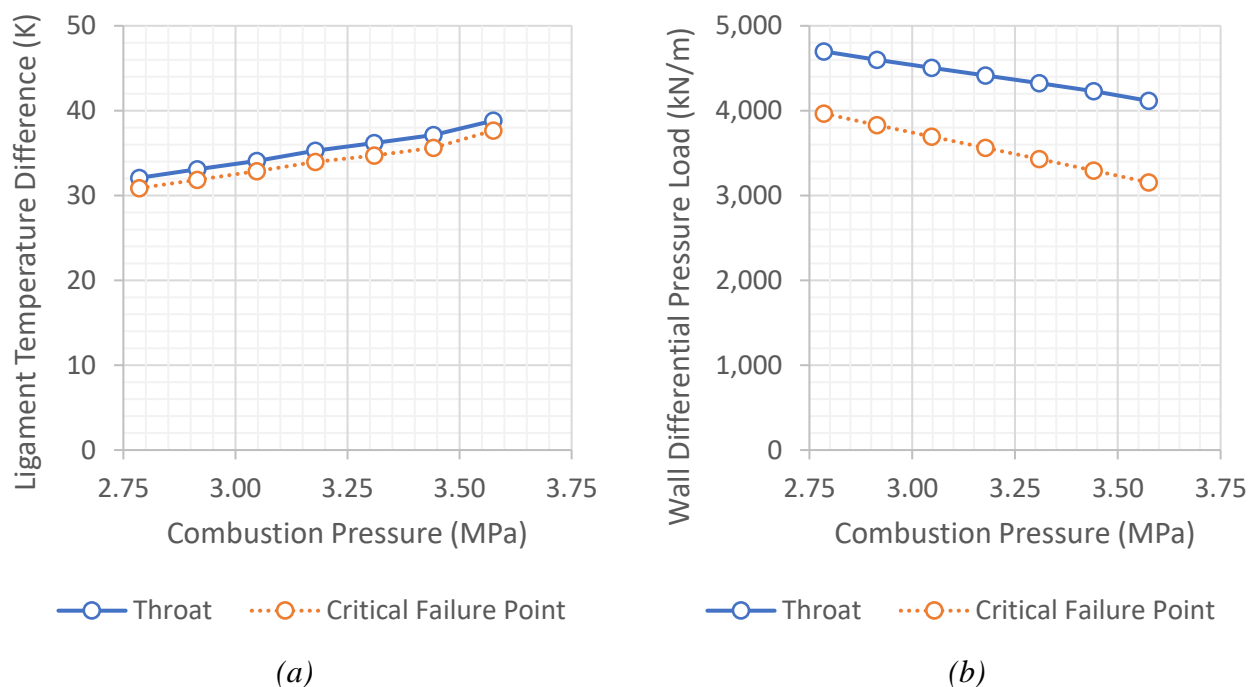
Figure 5-43: Effect of combustion pressure on (a) ligament differential pressure load and (b) ligament temperature difference

All parameters shown in Figure 5-42 and Figure 5-43 vary linearly with combustion pressure. Figure 5-42(a), Figure 5-42(b) and Figure 5-43(b) show that maximum wall temperature, overall wall temperature difference and ligament temperature difference all increase linearly with increasing combustion pressure. This result indicates that increasing combustion pressure increases the heat transfer into the walls. Such a result would be anticipated based on the Bartz correlation, which is

shown in Equation (2-50) (page 28). The Bartz correlation indicates that heat transfer increases with increasing combustion pressure.

Figure 5-43(a) shows that increasing combustion pressure causes a reduction in ligament differential pressure loading. This is also an expected result. Cooling channel pressure is higher than thrust chamber pressure. As such the differential pressure load acts inwards towards the centre of the combustion chamber. Any increase in combustion pressure would act against the pressure loading from the cooling channel, acting to reduce the net magnitude of the differential pressure loading. Despite the reduction in pressure loading, however, it appears that the higher heat transfer at increased propellant flow rates has a more significant effect on all failure modes, resulting in a linear decrease in thrust chamber life as combustion pressure increases.

5.5.3 Operating Limits

Combustion pressure can be increased to a maximum value of 3.58 MPa. This upper limit is constrained by OTP shaft speed, as shown in Figure 5-44. At a combustion pressure of 3.58 MPa, the OTP shaft speed reaches its maximum allowable limit for the JAXA reusable rocket engine. Combustion pressure can be decreased to a minimum value of 2.79 MPa. This lower limit is constrained by bleed flow rate. As described in Subsection 5.3.3, there is no fuel turbine bypass valve in the JAXA reusable rocket engine, so all oxidizer turbine working fluid must first flow through the fuel turbine. Figure 5-45 shows that at the minimum propellant flow rate, the oxidizer turbine flow rate increases to a point where it matches the fuel turbine flow rate. As such, the engine cannot operate at a higher mixture ratio without over-powering the fuel turbine, or under-powering the oxidizer turbine.
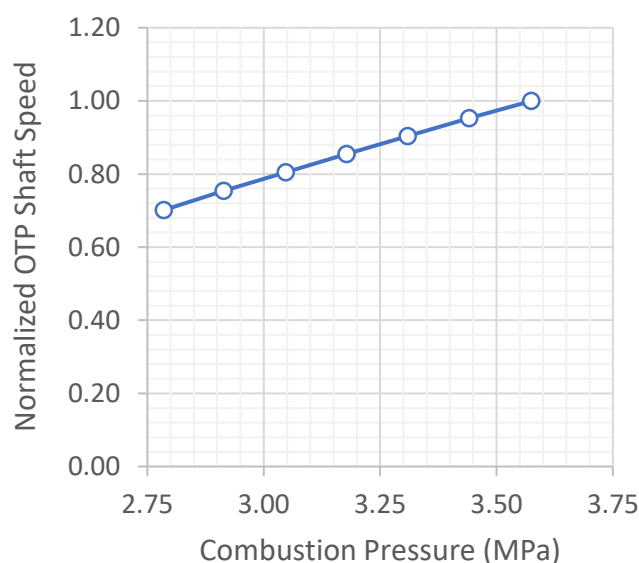
Figure 5-44: Effect of propellant flow rate on oxidizer turbopump shaft speed
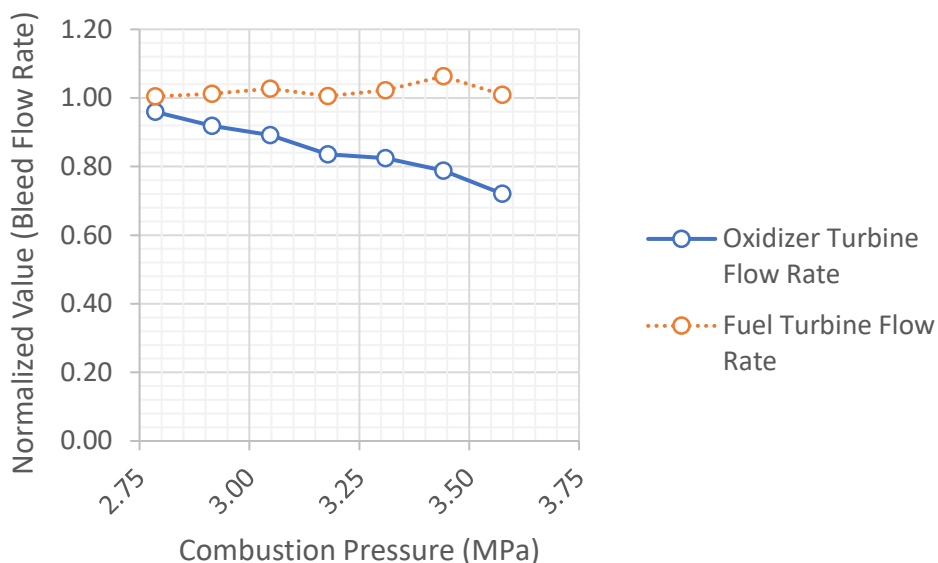
Figure 5-45: Effect of propellant flow rate on required turbine flow rates

5.6   Results Summary

A summary of the operating limits for the cases presented in this chapter is provided in Table 5-2. A summary of the key results presented in this chapter is provided in Table 5-3. Note that the "Maximum Life Increase" in Table 5-3 refers to life at the critical failure point, not the throat.

Table 5-2: Summary of Operating Limits

Case	Lower Limit - Value	Lower Limit - Constraint	Upper Limit - Value	Upper Limit - Constraint
Variable Coolant Pressure	5.72 MPa	OTP Shaft Speed	8.13 MPa	FTP Shaft Speed
Variable Coolant Flow Rate	0.45 kg/s	Fuel Turbine Flow Rate	1.25 kg/s	(OTP) Bleed Flow Enthalpy
Variable Mixture Ratio	3.98	OTP Shaft Speed	8.86	Fuel Turbine Flow Rate
Variable Combustion Pressure	2.79 MPa	Fuel Turbine Flow Rate	3.58 MPa	OTP Shaft Speed

Table 5-3: Summary of Results

Case	Failure Mode	Maximum Life Increase	Change in Thrust	Change in Specific Impulse
Variable Coolant Pressure	Plastic Instability	+ 5.8%	+ 0.2%*	+ 0.4%*
	Low-Cycle Fatigue	+ 5.9%		
	Creep Deformation	+ 6.7%		
Variable Coolant Flow Rate	Plastic Instability	+ 17.9%	+ 0.1%*	- 1.9%*
	Low-Cycle Fatigue	+ 13.0%		
	Creep Deformation	+ 8.6%		
Variable Mixture Ratio	Plastic Instability	+ 27.7%	- 7.6%*	- 7.4%*
	Low-Cycle Fatigue	+ 43.8%		
	Creep Deformation	+ 21.8%		
Variable Combustion Pressure	Plastic Instability	+ 40.5%	- 15.9%*	- 2.8%*
	Low-Cycle Fatigue	+ 51.2%		
	Creep Deformation	+ 32.6%		

Note: Maximum life for all three failure modes occurs at the same operating point in this case.

6. Results Analysis

In this chapter, further analysis of the results introduced in Chapter 5 is presented. Specifically, optimizations have been performed to maximize life without sacrificing performance. This optimization is discussed in Section 6.1. Based on the results of the optimization, a sensitivity analysis was performed based on the limiting constraint. This analysis is discussed in Section 6.2.

6.1 Optimization

The results introduced in Chapter 5 show that each of the identified operating conditions (coolant pressure, coolant flow rate, mixture ratio and propellant flow rate) can impact thrust chamber life. However, there is usually a trade-off between extending thrust chamber life and maintaining high engine performance. This is most evident in the variable mixture ratio and propellant flow rate cases. For example, Table 5-3 shows that a thrust chamber life can be increased by up to 50% (for low-cycle fatigue with variable propellant flow rate), but this would result in in a loss of almost 16% thrust, and almost 3% specific impulse.

Rather than considering the operating conditions in isolation, it may be possible to vary the operating conditions together to maximize thrust chamber life without sacrificing engine performance. As such, three multi-variable optimizations were performed: one for each failure mode. In each optimization, the combustion cycles to failure (i.e. life) was treated as the objective function. To maintain performance, constraints were set on thrust and specific impulse. Specifically, thrust was constrained to be equal to the control case result. Specific impulse was constrained to be greater than or equal to the control case result.

Coolant pressure, coolant flow rate, mixture ratio and propellant flow rate were used as variables. Constraints were placed on the range of these variables based on the respective operating limitations established in Chapter 5. Using the results presented in Chapter 5 for the critical failure point, regressions were performed on data sets for engine performance (thrust & specific impulse), and thrust chamber life (maximum wall temperature overall wall temperature difference, ligament differential pressure load & ligament temperature difference). Based on these regressions, a set of performance and life functions for each of the variables was established. These functions are described in detail in Section 6.1.1.

A deterministic optimization method was used, with data collected at a set of predetermined variables. At each point, the performance and life functions described above. Data was collected at four different cooling channel pressures, at equal intervals over the range of possible values. At each

cooling channel pressure, data was collected at five different coolant flow rates, at equal intervals over the range of possible values. At each coolant flow rate, ten different mixture ratio values were evaluated, at equal intervals over the range of possible values. With three of the four variables constrained, the final variable (propellant flow rate) was adjusted such that the thrust and specific impulse constraints could be met. A summary of the optimization results is presented in Subsection 6.1.2. The full set of results data is presented in graphical form in Appendix C.

6.1.1 Performance and Life Functions

Figure 6-1 shows the normalized results data from the variable coolant pressure case, as introduced in Section 5.2. Figure 6-1 also shows the regression trendlines fitted to these results. The resulting functions based on these regressions are shown in Equation (6-1) (for thrust), Equation (6-2) (for specific impulse), Equation (6-3) (for maximum wall temperature), Equation (6-4) (for ligament temperature difference), Equation (6-5) (for wall temperature difference) and Equation (6-6) (for ligament differential pressure loading).
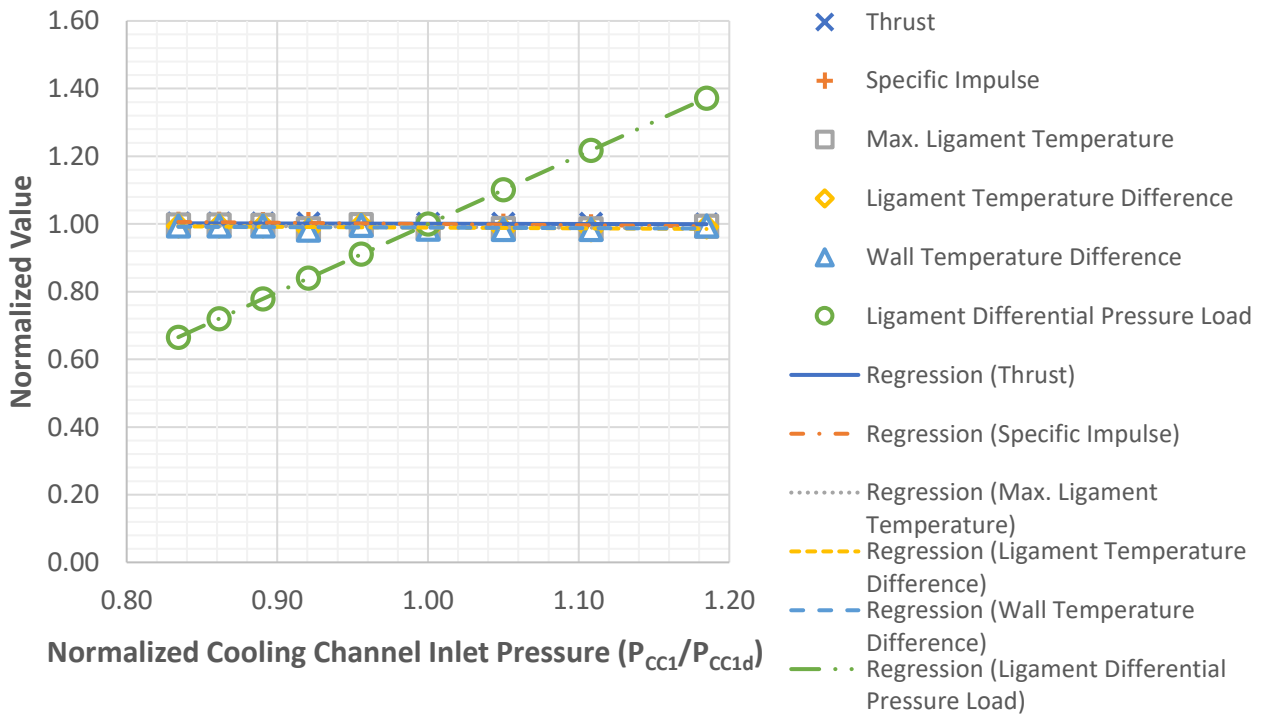
Figure 6-1: Performance and life function regressions – variable coolant pressure

$$\frac{F_T}{F_{T,d}}(p_{CC}) = -7.159 \times 10^{-3} \cdot \left(\frac{p_{CC}}{p_{CC,d}}\right) + 1.008 \tag{6-1}$$

$$\frac{I_{SP}}{I_{SP,d}}(p_{CC}) = -3.626 \times 10^{-2} \cdot \left(\frac{p_{CC}}{p_{CC,d}}\right) + 1.036 \tag{6-2}$$

$$\frac{T_{l1}}{T_{l1,d}}(p_{CC1}) = -2.185 \times 10^{-2} \cdot \left(\frac{p_{CC1}}{p_{CC1,d}}\right) + 1.013 \tag{6-3}$$

$$\frac{\Delta T_l}{\Delta T_{l,d}}(p_{CC1}) = -2.188 \times 10^{-2} \cdot \left(\frac{p_{CC1}}{p_{CC1,d}}\right) + 1.011 \tag{6-4}$$

$$\frac{\Delta T_w}{\Delta T_{w,d}}(p_{CC1}) = -1.445 \times 10^{-2} \cdot \left(\frac{p_{CC1}}{p_{CC1,d}}\right) + 1.004 \tag{6-5}$$

$$\frac{\Delta p_w}{\Delta p_{w,d}}(p_{CC1}) = 2.016 \cdot \left(\frac{p_{CC1}}{p_{CC1,d}}\right) - 1.016 \tag{6-6}$$

Figure 6-2 shows the normalized results data from the variable coolant flow rate case, as introduced in Section 5.3. Figure 6-2 also shows the regression trendlines fitted to these results. The resulting functions based on these regressions are shown in Equation (6-7) (for thrust), Equation (6-8) (for specific impulse), Equation (6-9) (for maximum wall temperature), Equation (6-10) (for ligament temperature difference), Equation (6-11) (for wall temperature difference) and Equation (6-12) (for ligament differential pressure loading).
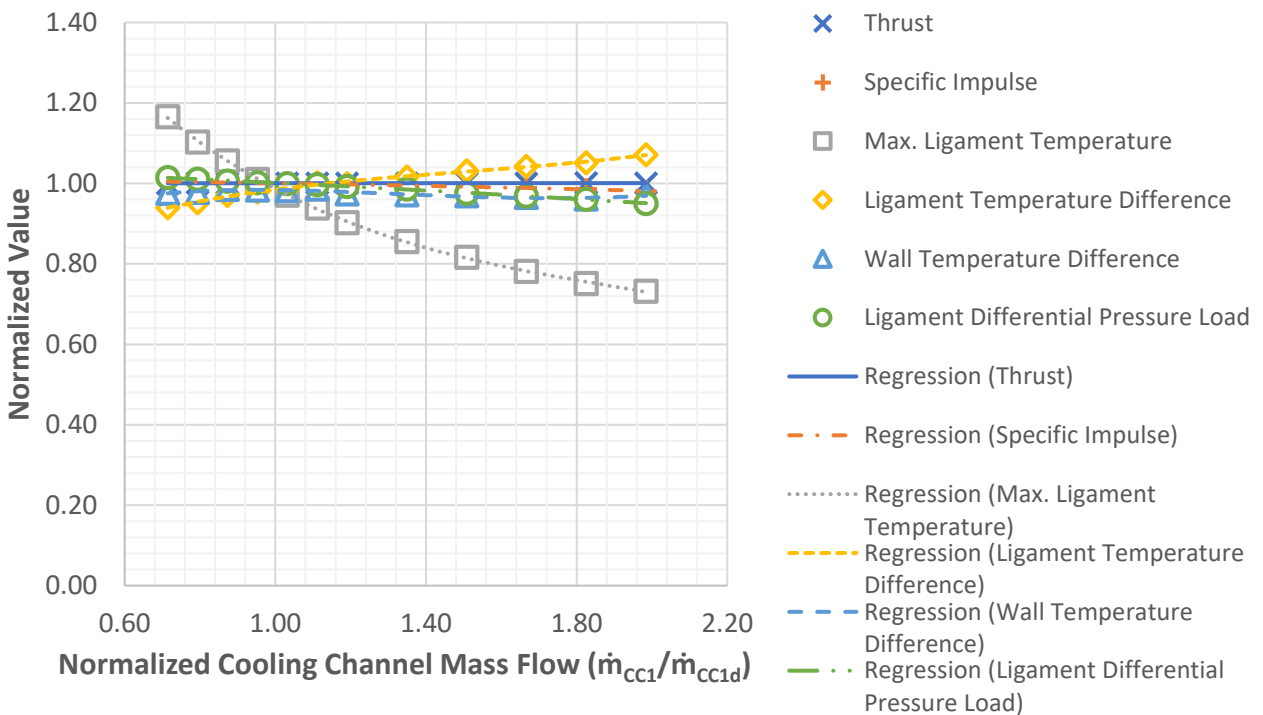
Figure 6-2: Performance and life function regressions – variable coolant flow rate

$$\frac{F_T}{F_{T,d}}(\dot{m}_{C,c}) = 3.037 \times 10^{-4} \cdot \left(\frac{\dot{m}_{CC}}{\dot{m}_{CC1,d}}\right) + 1.000 \tag{6-7}$$

$$\frac{I_{SP}}{I_{SP,d}}(\dot{m}_{CC}) = -4.439 \times 10^{-3} \cdot \left(\frac{\dot{m}_{CC}}{\dot{m}_{CC,d}}\right)^2 - 6.161 \times 10^{-3} \cdot \left(\frac{\dot{m}_{CC}}{\dot{m}_{CC,d}}\right) + 1.011 \tag{6-8}$$

$$\frac{T_{l1}}{T_{l1,d}}(\dot{m}_{CC}) = -1.411 \times 10^{-3} \cdot \left(\frac{\dot{m}_{CC}}{\dot{m}_{CC,d}}\right)^3 + 0.8008 \cdot \left(\frac{\dot{m}_{CC}}{\dot{m}_{CC,d}}\right)^2 - 1.674$$
$$\cdot \left(\frac{\dot{m}_{CC}}{\dot{m}_{CC,d}}\right) + 2.001 \tag{6-9}$$

$$\frac{\Delta T_l}{\Delta T_{l,d}}(\dot{m}_{CC}) = -4.952 \times 10^{-3} \cdot \left(\frac{\dot{m}_{CC}}{\dot{m}_{CC,d}}\right)^4 + 9.532 \times 10^{-2} \cdot \left(\frac{\dot{m}_{CC}}{\dot{m}_{CC,d}}\right)^3$$
$$- 0.3618 \cdot \left(\frac{\dot{m}_{CC}}{\dot{m}_{CC,d}}\right)^2 + 0.5801 \cdot \left(\frac{\dot{m}_{CC}}{\dot{m}_{CC,d}}\right) + 0.6761 \tag{6-10}$$

$$\frac{\Delta T_w}{\Delta T_{w,d}}(\dot{m}_{CC}) = -3.022 \times 10^{-2} \cdot \left(\frac{\dot{m}_{CC}}{\dot{m}_{CC,d}}\right)^4 + 0.2463 \cdot \left(\frac{\dot{m}_{CC}}{\dot{m}_{CC,d}}\right)^3 - 0.6554$$
$$\cdot \left(\frac{\dot{m}_{CC}}{\dot{m}_{CC,d}}\right)^2 + 0.6819 \cdot \left(\frac{\dot{m}_{CC}}{\dot{m}_{CC,d}}\right) + 0.7410 \tag{6-11}$$

$$\frac{\Delta p_w}{\Delta p_{w,d}}(\dot{m}_{CC}) = -6.306 \times 10^{-3} \cdot \left(\frac{\dot{m}_{CC}}{\dot{m}_{CC,d}}\right)^2 - 3.256 \times 10^{-2} \cdot \left(\frac{\dot{m}_{CC}}{\dot{m}_{CC,d}}\right) + 1.040 \tag{6-12}$$

Figure 6-3 shows the normalized results data from the variable mixture ratio case, as introduced in Section 5.4. Figure 6-3 also shows the regression trendlines fitted to these results. The resulting functions based on these regressions are shown in Equation (6-13) (for thrust), Equation (6-14) (for specific impulse), Equation (6-15) (for maximum wall temperature), Equation (6-16) (for ligament temperature difference), Equation (6-17) (for wall temperature difference) and Equation (6-18) (for ligament differential pressure loading).
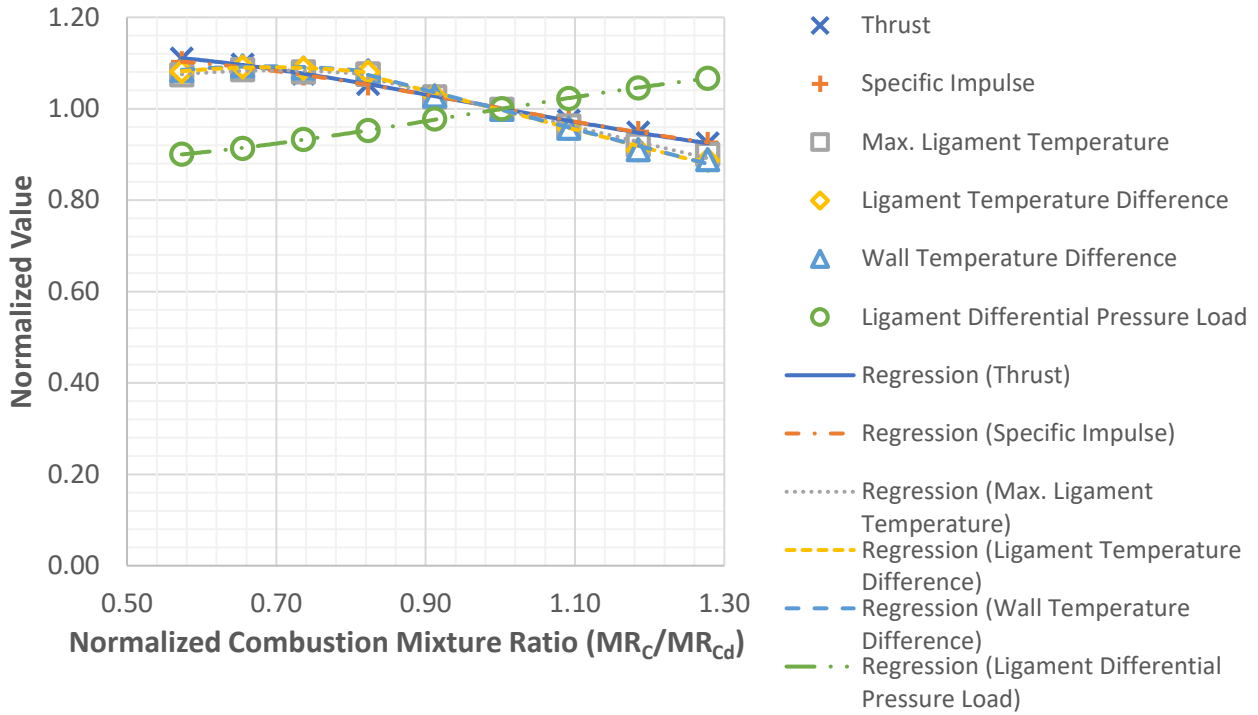
Figure 6-3: Performance and life function regressions – variable mixture ratio

$$\frac{F_T}{F_{T,d}}(MR_C) = 0.2897 \cdot \left(\frac{MR_C}{MR_{C,d}}\right)^3 - 0.8506 \cdot \left(\frac{MR_C}{MR_{C,d}}\right)^2 + 0.5299 \cdot \left(\frac{MR_C}{MR_{C,d}}\right) + 1.032 \quad (6\text{-}13)$$

$$\frac{I_{SP}}{I_{SP,d}}(MR_C) = 0.3435 \cdot \left(\frac{MR_C}{MR_{C,d}}\right)^3 - 1.025 \cdot \left(\frac{MR_C}{MR_{C,d}}\right)^2 + 0.7208 \cdot \left(\frac{MR_C}{MR_{C,d}}\right) + 0.9619 \quad (6\text{-}14)$$

$$\frac{T_{l1}}{T_{l1,d}}(MR_C) = \begin{cases} -0.5651 \cdot \left(\frac{MR_C}{MR_{C,d}}\right)^2 + 0.7872 \cdot \left(\frac{MR_C}{MR_{C,d}}\right) + 0.8096 & \left(\frac{MR_C}{MR_{C,d}} \leq 0.82\right) \\ -0.3874 \cdot \left(\frac{MR_C}{MR_{C,d}}\right) + 1.387 & \left(\frac{MR_C}{MR_{C,d}} > 0.82\right) \end{cases} \quad (6\text{-}15)$$

$$\frac{\Delta T_l}{\Delta T_{l,d}}(MR_C) = \begin{cases} -0.6370 \cdot \left(\frac{MR_C}{MR_{C,d}}\right)^2 + 0.8794 \cdot \left(\frac{MR_C}{MR_{C,d}}\right) + 0.7872 & \left(\frac{MR_C}{MR_{C,d}} \leq 0.82\right) \\ -0.4266 \cdot \left(\frac{MR_C}{MR_{C,d}}\right) + 1.424 & \left(\frac{MR_C}{MR_{C,d}} > 0.82\right) \end{cases} \quad (6\text{-}16)$$

$$\frac{\Delta T_w}{\Delta T_{w,d}}(MR_C) = \begin{cases} -0.5936 \cdot \left(\frac{MR_C}{MR_{C,d}}\right)^2 + 0.8165 \cdot \left(\frac{MR_C}{MR_{C,d}}\right) + 0.8119 & \left(\frac{MR_C}{MR_{C,d}} \leq 0.82\right) \\ -0.4281 \cdot \left(\frac{MR_C}{MR_{C,d}}\right) + 1.426 & \left(\frac{MR_C}{MR_{C,d}} > 0.82\right) \end{cases} \quad (6\text{-}17)$$

$$\frac{\Delta p_w}{\Delta p_{w,d}}(MR_C) = -0.2413 \cdot \left(\frac{MR_C}{MR_{C,d}}\right)^3 + 0.6992 \cdot \left(\frac{MR_C}{MR_{C,d}}\right)^2 - 0.4085 \cdot \left(\frac{MR_C}{MR_{C,d}}\right) + 0.9500 \quad (6\text{-}18)$$

Figure 6-4 shows the normalized results data from the variable propellant flow rate case, as introduced in Section 5.5. Figure 6-4 also shows the regression trendlines fitted to these results. The resulting functions based on these regressions are shown in Equation (6-19) (for thrust), Equation (6-20) (for specific impulse), Equation (6-21) (for maximum wall temperature), Equation (6-22) (for ligament temperature difference), Equation (6-23) (for wall temperature difference) and Equation (6-24) (for ligament differential pressure loading).
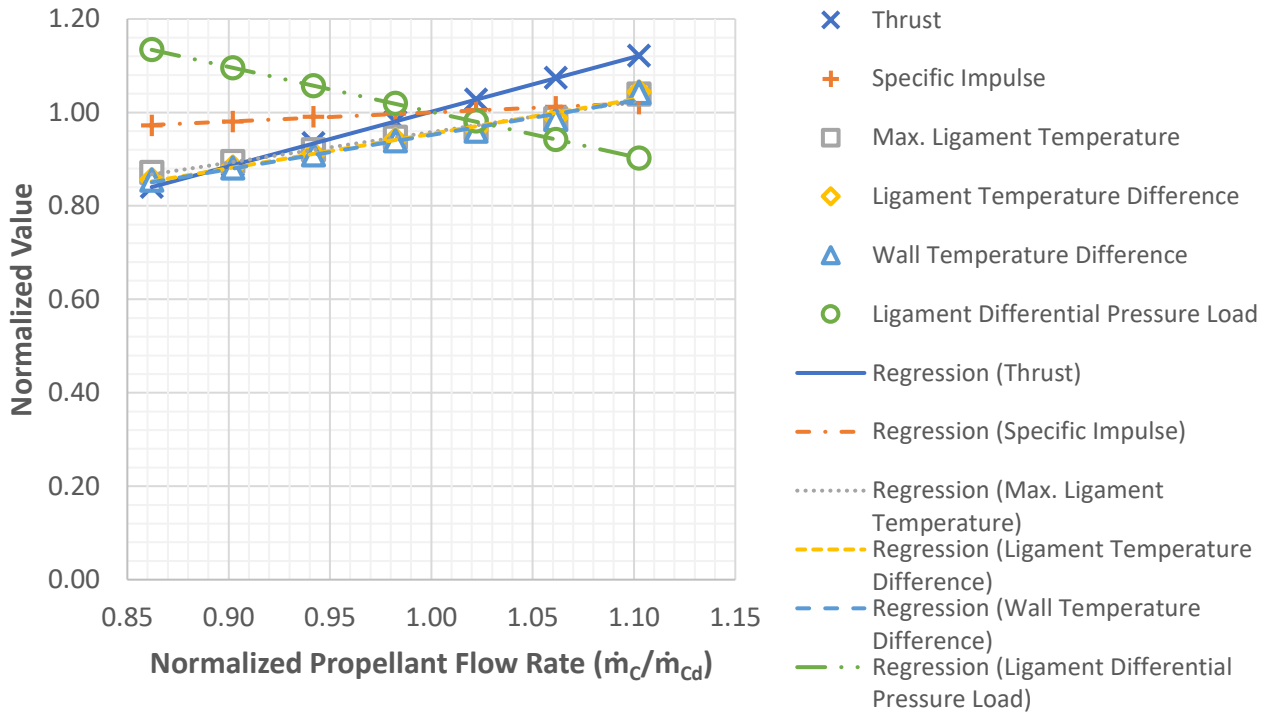
Figure 6-4: Performance and life function regressions – variable propellant flow rate

$$\frac{F_T}{F_{T,d}}(\dot{m}_C) = 1.169 \cdot \left(\frac{\dot{m}_C}{\dot{m}_{C,d}}\right) - 0.1678 \tag{6-19}$$

$$\frac{I_{SP}}{I_{SP,d}}(\dot{m}_C) = 0.1947 \cdot \left(\frac{\dot{m}_C}{\dot{m}_{C,d}}\right) + 0.8053 \tag{6-20}$$

$$\frac{T_{l1}}{T_{l1d}}(\dot{m}_C) = 0.6548 \cdot \left(\frac{\dot{m}_C}{\dot{m}_{Cd}}\right) + 0.3031 \tag{6-21}$$

$$\frac{\Delta T_l}{\Delta T_{ld}}(\dot{m}_C) = 0.7372 \cdot \left(\frac{\dot{m}_C}{\dot{m}_{Cd}}\right) + 0.2169 \tag{6-22}$$

$$\frac{\Delta T_w}{\Delta T_{wd}}(\dot{m}_C) = 0.7339 \cdot \left(\frac{\dot{m}_C}{\dot{m}_{Cd}}\right) + 0.2179 \tag{6-23}$$

$$\frac{\Delta p_w}{\Delta p_{wd}}(\dot{m}_C) = -0.9623 \cdot \left(\frac{\dot{m}_C}{\dot{m}_{Cd}}\right) + 1.964 \tag{6-24}$$

Based on Equations (6-1), (6-7), (6-13) and (6-19), a function for estimating thrust has been established. This function is used as a constraint, as shown in Equation (6-25).

$$\frac{F_T}{F_{T,d}} = \frac{F_T}{F_{T,d}}(p_{CC1}) \cdot \frac{F_T}{F_{T,d}}(\dot{m}_{CC}) \cdot \frac{F_T}{F_{T,d}}(MR_C) \cdot \frac{F_T}{F_{T,d}}(\dot{m}_C) = 1.0 \tag{6-25}$$

Based on Equations (6-2), (6-8), (6-14) and (6-20), a function for estimating specific impulse has been established. This function is used as a constraint, as shown in Equation (6-26).

$$\frac{I_{SP}}{I_{SP,d}} = \frac{I_{SP}}{I_{SP,d}}(p_{CC1}) \cdot \frac{I_{SP}}{I_{SP,d}}(\dot{m}_{CC1}) \cdot \frac{I_{SP}}{I_{SP,d}}(MR_C) \cdot \frac{I_{SP}}{I_{SP,d}}(\dot{m}_C) \geq 1.0 \tag{6-26}$$

Equations (6-27) to (6-30) show the other constraints used in the optimization. These constraints are established based on the operating range limits presented in Chapter 5.

$$0.834 \leq \frac{p_{CC1}}{p_{CC1,d}} \leq 1.185 \tag{6-27}$$

$$0.714 \leq \frac{\dot{m}_{CC1}}{\dot{m}_{CC1,d}} \leq 1.984 \tag{6-28}$$

$$0.573 \leq \frac{MR_C}{MR_{C,d}} \leq 1.278 \tag{6-29}$$

$$0.862 \leq \frac{\dot{m}_C}{\dot{m}_{C,d}} \leq 1.102 \tag{6-30}$$

Equations (6-31) to (6-33) show the objective functions for each optimization. These functions are calculated using the Porowski model. The life functions described above are used to calculate the inputs for the Porowski model by combining them, as shown in Equations (6-34) to (6-37).

$$\max\left[\frac{N_{F,PI}}{N_{F,PI,d}}(T_{l1}, \Delta T_l, \Delta T_w, \Delta p_w)\right] \tag{6-31}$$

$$\max\left[\frac{N_{F,f}}{N_{F,f,d}}(T_{l1}, \Delta T_l, \Delta T_w, \Delta p_w)\right] \tag{6-32}$$

$$\max\left[\frac{N_{F,cr}}{N_{F,cr,d}}(T_{l1}, \Delta T_l, \Delta T_w, \Delta p_w)\right] \tag{6-33}$$

$$T_{l1} = T_{l1,d}\cdot\left[\frac{T_{l1}}{T_{l1,d}}(p_{CC1})\cdot\frac{T_{l1}}{T_{l1,d}}(\dot{m}_{CC})\cdot\frac{T_{l1}}{T_{l1,d}}(MR_C)\cdot\frac{T_{l1}}{T_{l1,d}}(\dot{m}_C)\right] \tag{6-34}$$

$$\Delta T_l = \Delta T_{l,d}\cdot\left[\frac{\Delta T_l}{\Delta T_{l,d}}(p_{CC1})\cdot\frac{\Delta T_l}{\Delta T_{l,d}}(\dot{m}_{CC})\cdot\frac{\Delta T_l}{\Delta T_{l,d}}(MR_C)\cdot\frac{\Delta T_l}{\Delta T_{l,d}}(\dot{m}_C)\right] \tag{6-35}$$

$$\Delta T_w = \Delta T_{w,d}\cdot\left[\frac{\Delta T_w}{\Delta T_{w,d}}(p_{CC1})\cdot\frac{\Delta T_w}{\Delta T_{w,d}}(\dot{m}_{CC})\cdot\frac{\Delta T_w}{\Delta T_{w,d}}(MR_C)\cdot\frac{\Delta T_w}{\Delta T_{w,d}}(\dot{m}_C)\right] \tag{6-36}$$

$$\Delta p_w = \Delta p_{w,d}\cdot\left[\frac{\Delta p_w}{\Delta p_{w,d}}(p_{CC1})\cdot\frac{\Delta p_w}{\Delta p_{w,d}}(\dot{m}_{CC})\cdot\frac{\Delta p_w}{\Delta p_{w,d}}(MR_C)\cdot\frac{\Delta p_w}{\Delta p_{w,d}}(\dot{m}_C)\right] \tag{6-37}$$

6.1.2 Optimization Results

For all three optimization cases, the optimal point was determined to be the same: a normalized pressure of 0.951, a normalized coolant flow rate of 1.667, a normalized mixture ratio of 0.961 and a normalized propellant flow rate of 0.987. To increase computational efficiency, the optimizations were based on regression functions of model output data, rather than using the model itself. In this sense, the optimizations were essentially an estimate of general vicinity of the optimal point. Thus, once the optimal point had been established, the full engine model was run in the vicinity of that point to confirm that it was a "local maximum". Using the full model also gives a more accurate method of determining optimum life at this point. Verification using the full engine model confirmed that the optimal point was at the following operating conditions: a normalized pressure of 0.951, a normalized coolant flow rate of 1.786, a normalized mixture ratio of 0.933 and a normalized propellant flow rate of 0.984.

Given the high number of variables, it is not possible to plot all the optimization data on a single chart. Figure 6-5 shows some of the results of the plastic instability optimization, specifically the chart containing the optimum point. The optimization provided an estimated optimum plastic instability life increase of 30.1%. Figure 6-5 also shows the "optimal solution" as verified by the full engine model. The engine model predicted an optimum plastic instability life increase of 26.6%. A full set of plastic instability optimization results data is provided in Appendix C-1.

Figure 6-6 shows some of the results of the fatigue optimization, specifically the chart containing the optimum point. The optimization provided an estimated optimum fatigue life increase of 32.5%. Figure 6-6 also shows the "optimal solution" as verified by the full engine model. The engine model predicted an optimum plastic fatigue life increase of 24.3%. A full set of fatigue optimization results data is provided in Appendix C-2.
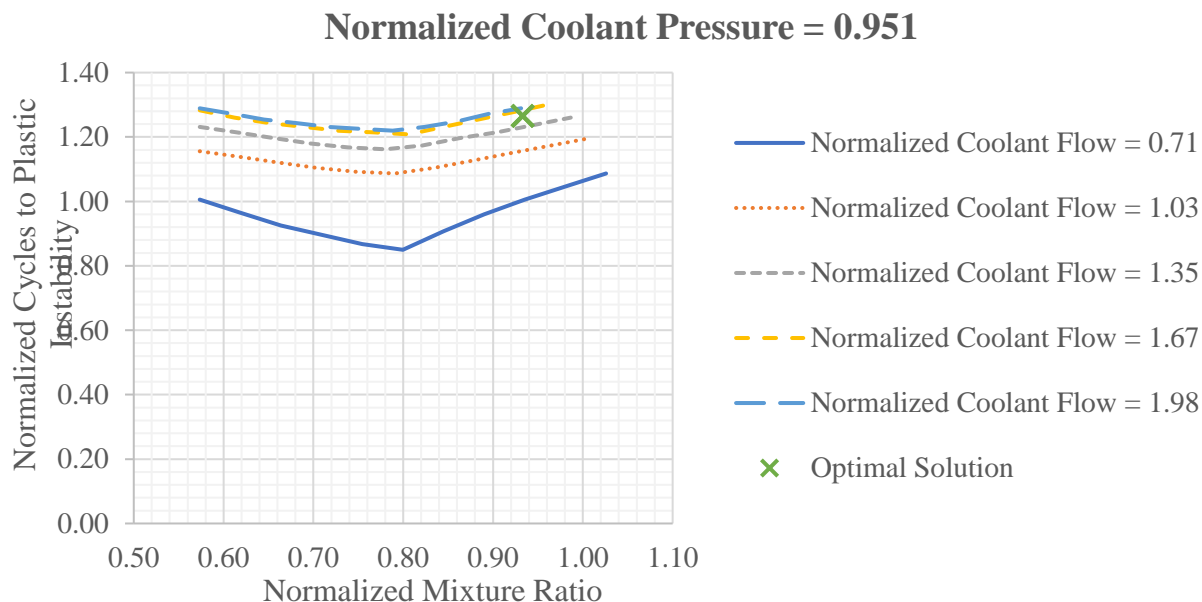
Figure 6-5: Optimization results – plastic instability
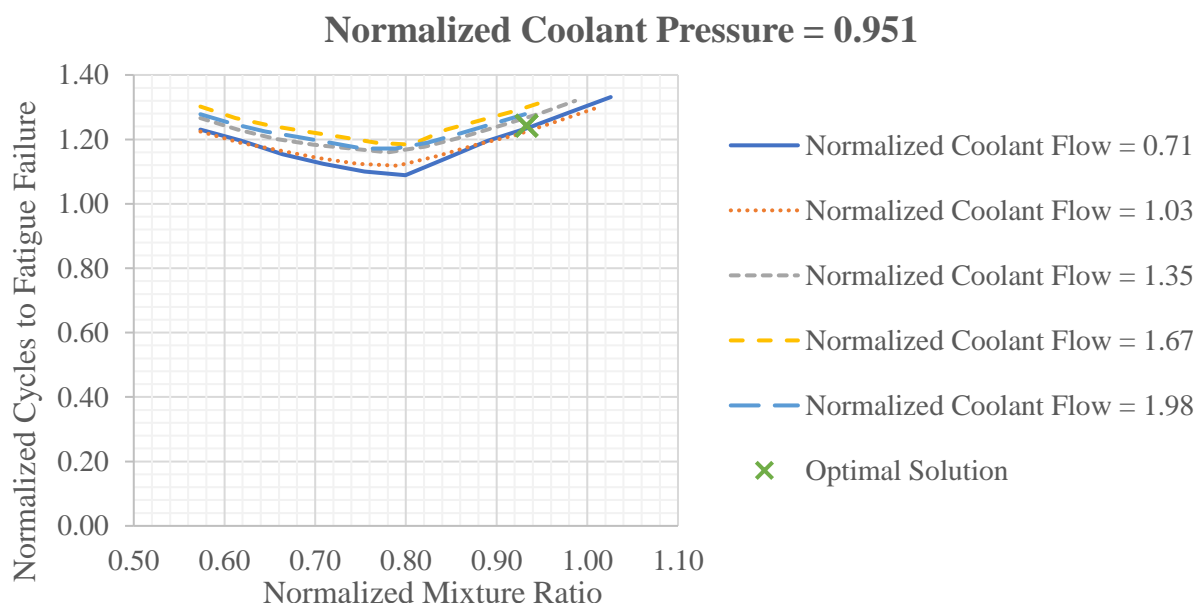
Figure 6-6: Optimization results – low-cycle fatigue

Figure 6-7 shows some of the results of the creep optimization, specifically the chart containing the optimum point. The optimization provided an estimated optimum creep life increase of 21.0%. Figure 6-7 also shows the "optimal solution" as verified by the full engine model. The engine model

predicted an optimum creep life increase of 18.3%. A full set of creep optimization results data is provided in Appendix C-3.

Normalized Coolant Pressure = 0.951

Legend:
— Normalized Coolant Flow = 0.71
······ Normalized Coolant Flow = 1.03
----- Normalized Coolant Flow = 1.35
– – – Normalized Coolant Flow = 1.67
— – Normalized Coolant Flow = 1.98
✕ Optimal Solution
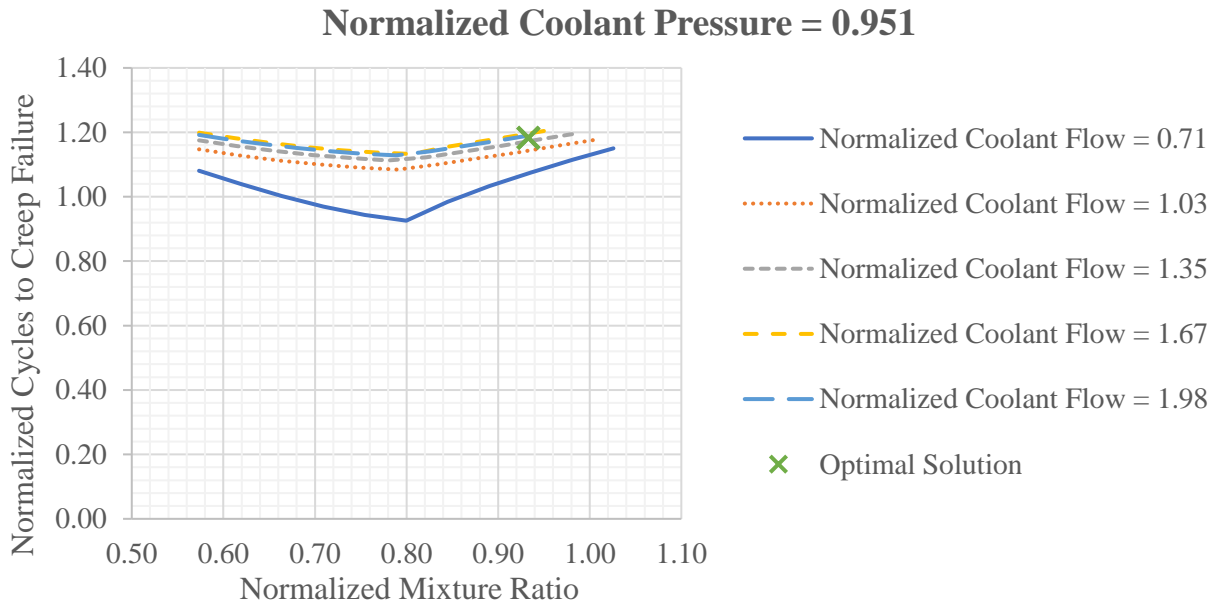
Figure 6-7: Optimization results – creep deformation

Table 6-1 shows a comparison of the baseline operating conditions for the engine (based on the control case results presented in Section 5.1) and the optimized operating conditions. Note that, as described above, the optimal point is identical for all three failure modes.

Table 6-1: Summary of Optimization Results

Case	Baseline (Control Case)	Optimized Result	Change
Coolant Pressure (MPa)	6.86	6.29	− 8.31%
Coolant Flow Rate (kg/s)	0.630	1.125	+ 78.6%
Mixture Ratio	5.990	6.511	+ 8.70%
Combustion Pressure (MPa)	3.480	3.479	− 0.03%
Propellant Flow Rate (kg/s)	12.472	12.290	− 1.46%
Thrust (kN)	38.94	38.97	+ 0.08%
Specific Impulse (s)	312.2	312.4	+ 0.06%
Cycles to Plastic Instability	173	219	+ 26.6%
Cycles to Fatigue Failure	169	210	+ 24.3%
Cycles to Creep Failure	1,198	1,417	+ 18.3%

6.2 Specific Impulse Constraint Sensitivity

As discussed above, the optimal point was determined to be under the same operating conditions for all three failure mode operations. The critical constraint on this optimization was the specific impulse constraint shown in Equation (6-26). This is shown in Figure 6-8, which plots the range of the optimization functions. The requirement that specific impulse be maintained at least the same level as the control case is the key factor limiting further increases in thrust chamber life. Figure 6-8 shows that the "optimal solution" point is being constrained by the specific impulse requirement. If this requirement were relaxed, it may be possible to increase thrust chamber life even further for only a small performance penalty.
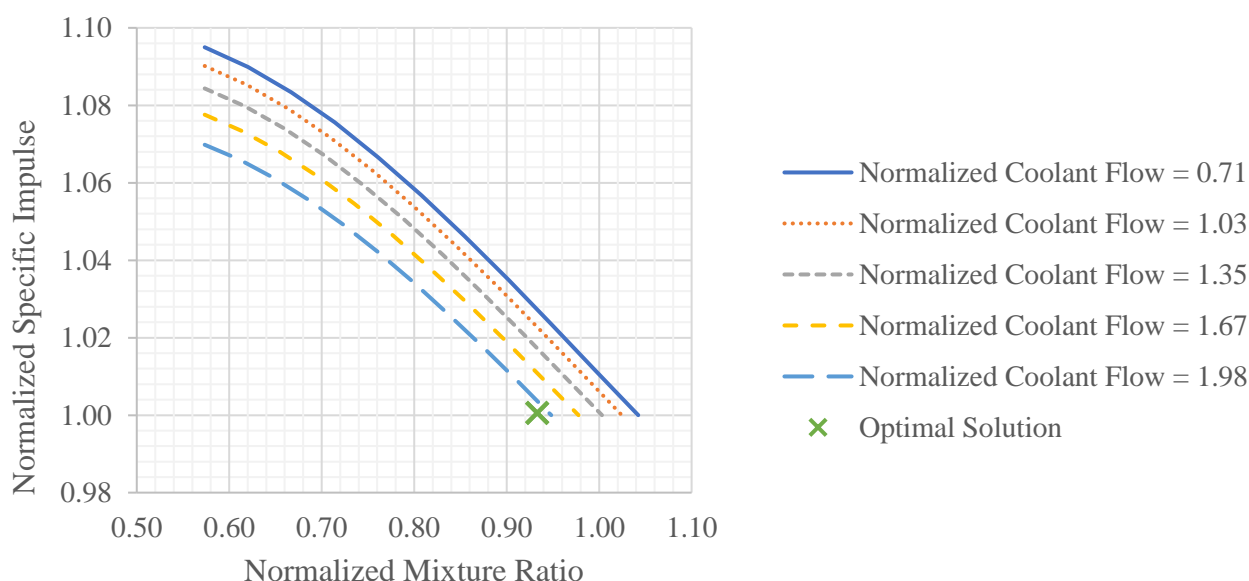
Figure 6-8: Optimization – specific impulse constraint

To investigate this trade-off, a sensitivity analysis was performed. Starting at the "optimal point" result of the optimization, the specific impulse constraint was relaxed, and the full engine model was used to predict performance and estimate life. Figure 6-9 shows the results for all three failure modes. Specific impulse could only be relaxed by less than 4% before another constraint (OTP shaft speed) prevents further relaxation. Regardless of the small size of this change, Figure 6-9 shows a relatively large impact on optimum life for all three failure modes. A specific impulse reduction of 3.6% results in an increase in optimum plastic instability life of 8.7% (from 26.6% to 35.3% higher than the baseline), an increase in optimum fatigue life of 14.2% (from 24.3% to 38.5% higher than the baseline), and an increase in optimum creep life of 6.0% (from 18.3% to 24.3% higher than the baseline).

To achieve the results shown in Figure 6-9, both coolant pressure and flow rate are held constant, while mixture ratio and propellant flow rate are increased with decreasing specific impulse. This trade-off between mixture ratio and propellant flow rate is an important one. Figure 5-30 and

Figure 5-31 show that increasing mixture ratio will extend life. However, Figure 5-27 shows that this will result in a near-identical loss in both thrust and specific impulse. Conversely, Figure 5-39 shows that increasing propellant flow rate will increase both thrust and specific impulse, but the change in thrust is more pronounced. Thus, decreases in thrust resulting from a mixture ratio increase can be offset by increases in propellant flow rate. However, increasing propellant flow rate is not sufficient for offsetting decreases in specific impulse. In addition, Figure 5-40 and Figure 5-41 show that increasing propellant flow rate will decrease life, however the sensitivity analysis results show that any decrease in life from increasing propellant flow rate is more than offset by increases in life from increasing mixture ratio.
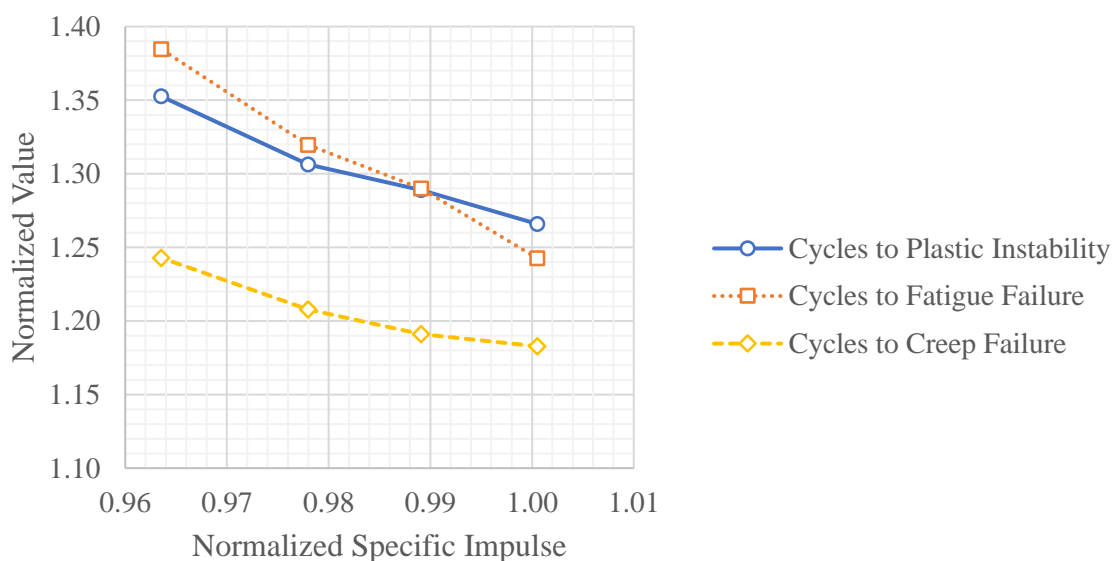
Figure 6-9: Sensitivity of minimum specific impulse constraint - results
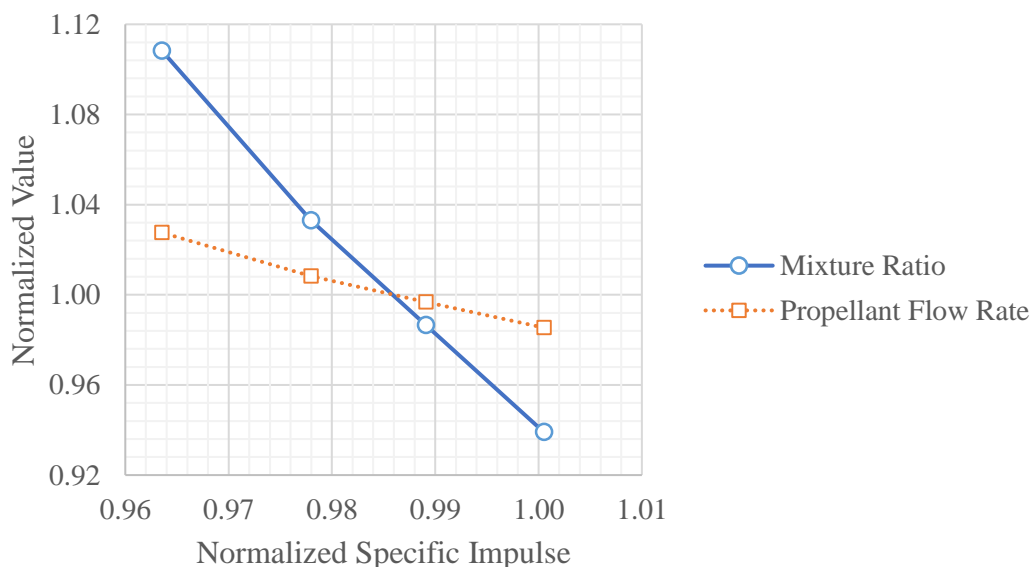
Figure 6-10: Sensitivity of minimum specific impulse constraint – mixture ratio & propellant flow rate adjustments

Table 6-2 shows a comparison of the baseline operating conditions for the engine (based on the control case results presented in Section 5.1) and the results if the sensitivity analysis.

Table 6-2: Summary of Sensitivity Analysis Results

Case	Baseline (Control Case)	Sensitivity Analysis Result	Change
Coolant Pressure (MPa)	6.86	6.52	− 4.95%
Coolant Flow Rate (kg/s)	0.630	1.125	+ 78.6%
Mixture Ratio	5.990	7.685	+ 28.3%
Combustion Pressure (MPa)	3.480	3.479	− 0.03%
Propellant Flow Rate (kg/s)	12.472	12.816	+ 2.76%
Thrust (kN)	38.94	38.97	+ 0.08%
Specific Impulse (s)	312.2	300.8	− 3.65%
Cycles to Plastic Instability	173	234	+ 35.3%
Cycles to Fatigue Failure	169	234	+ 38.5%
Cycles to Creep Failure	1,198	1,489	+ 24.3%

7.   Discussion

In this chapter, the outcomes of this study are discussed. Section 7.1 highlights several key findings of note which have arisen from the results of this study. Section 7.2 describes how the results and findings of this study are applicable to thrust chamber design and analysis more generally. Finally, Section 7.3 recommends some future work to continue the development of long-life, high-performance reusable thrust chambers.

7.1   Key Findings

In this section, several key findings are distilled from the results of the present study. These findings include the importance of finding the "critical failure point", the effectiveness of regenerative cooling for thrust chamber life extension, the effect of changing mixture ratio on gas properties, temperature and wall heat transfer, and the trade-off between mixture ratio and propellant flow rate in terms of both engine performance and thrust chamber life.

Convention dictates that thrust chamber life must be analysed at the nozzle throat. The throat, or the region near the throat, is typically where maximum heat flux occurs, thus it is considered to be the "critical failure point" for thrust chamber structural analysis. The results of the control case presented in Subsection 5.1.2, however, show another critical failure point in the converging section of the nozzle, immediately upstream of a change in cooling channel and ligament geometry. A high wall temperature difference at this point results in a section of the thrust chamber where the life may be as low as half that which might be expected at the throat. Generally speaking, every thrust chamber is different. Different geometries, materials and manufacturing processes will change the structural dynamics and failure modes dramatically between designs. However, this result highlights the danger in assuming that the throat is the critical failure point.

It is important to analyse multiple locations along the length of the thrust chamber to confirm the location of the failure point, rather than assuming its location at the throat. Fortunately, the Porowski model provides a simple and computationally efficient method of predicting thrust chamber wall life. Given its simplicity, the Porowski model is an ideal tool for analysing a large number of locations along the thrust chamber wall to provide localized life estimates. This data can be used to at least identify potential critical failure points not located at the throat. More comprehensive tools, such as FEM models, could then be used to analyse the thrust chamber structure at these critical points. This is considered especially important if the thrust chamber features variable-geometry cooling channels or ligaments, as changes in geometry may increase the risk of critical failure points which may be overlooked in thrust chamber failure analysis.

The results presented in Section 5.2 (variable coolant pressure) and Section 5.3 (variable coolant flow rate) indicate that while there is some correlation between coolant pressure & flow rate and combustion cycles to failure for creep defamation or plastic instability, the effect is not as strong as may be expected. Further, there is almost no correlation between combustion cycles to failure for low-cycle fatigue. Based on the results of this study in general, it would seem that the overall wall temperature difference (between the ligament and the closeout wall) is the greatest contributing factor to increasing or decreasing thrust chamber life. It also seems that changing coolant flow or pressure is not an effective method of reducing this temperature. Even as maximum wall temperature decreases, the temperature difference between the ligament and closeout wall remains consistent.

While it seems to have little effect on wall temperature difference, changing coolant flow rate is important for reducing maximum wall temperature. This makes it crucial for mitigating or preventing creep damage. At very low coolant flow rates, where it appears that a creep threshold is reached, there is a dramatic increase in plastic deformation per cycle. This reduces thrust chamber life for all three failure modes. The creep threshold might be different for different alloys, but generally speaking, coolant flow rate plays an important role in keeping the wall temperature below this threshold. However, outside of creep prevention, the role of coolant flow and pressure in increasing thrust chamber life is marginal. Reducing the wall temperature on the thrust chamber side would seem to be a more effective method of lowering the wall temperature difference.

The results of the variable mixture ratio case presented in Section 5.4 depict a complex relationship between gas temperature, gas composition and wall heat transfer. From the inception of this study, it was argued that mixture ratio would be an important parameter for extending thrust chamber life. Mixture ratio is the most effective method of controlling combustion temperature. Reducing combustion temperature would subsequently reduce exhaust gat temperature throughout the nozzle. This in turn would reduce the temperature gradient between the exhaust gas and the thrust chamber wall, thereby retarding heat transfer into the wall and reducing temperatures. However, in considering convective heart transfer, this hypothesis did not account for changes in exhaust gas composition as a result of the changing mixture ratio. Relevant fluid properties such as specific heat, thermal conductivity and viscosity change as the gas composition changes. The net effect of these property changes appears to be an increase in the heat transfer coefficient as the mixture ratio is reduced. This increased heat transfer coefficient outweighs any reduction in heat transfer due to a lower combustion temperature, at least until the mixture ratio reaches a point far enough from stoichiometry that the combustion temperature starts to change significantly.

In addition to affecting heat transfer, the exhaust gas composition also influences engine performance. As discussed in Subsection 5.4.1, changing the mixture ratio causes a difference in average molecular weight at the exhaust, which affects exhaust velocity. As a result, there is a negative correlation between engine performance and thrust chamber life when considering mixture ratio. Decreasing mixture ratio will lead to a lower average exhaust molecular weight, which increases engine performance. At the same time, however, changes in the exhaust gas composition improve nozzle heat transfer, thereby reducing thrust chamber life. A similar relationship is evident when considering thrust chamber propellant flow rate. Increasing the propellant flow rate increases momentum flux at the exhaust, which increases thrust. For a constant-geometry thrust chamber, increases in propellant flow rate are accompanied by an increase in combustion pressure, which also improves engine performance. At the same time, increased pressure leads to increased heat transfer (as per the Bartz correlation), which reduces thrust chamber life.

Given that variations in mixture ratio and propellant flow rate have similar impacts on thrust and specific impulse, these two operating conditions should be considered together in the design of long-life reusable rocket engine thrust chambers. The results of the optimization described in Section 6.1 indicate that for the case study used in this research, thrust chamber life can be improved by as much as 30% without sacrificing engine performance. Further, the results of the sensitivity analysis described in Section 6.2 indicate that thrust chamber life is very sensitive to a relaxation in performance requirements. Reducing the specific impulse by less than 4% was found to increase thrust chamber life by almost 40% over the control case baseline. This trade-off between life and performance, realized through careful adjustment of mixture ratio and propellant flow rate, is the most significant outcome of this study. It shows that careful selection and control of these particular operating conditions is important to ensuring the long life of reusable rocket engine thrust chambers.

7.2   Applicability

The primary focus of this research was a case study of the JAXA reusable rocket engine. As such, the specific quantitative results are only applicable to this particular engine. However, there are also qualitative results if this study that are broadly applicable to the design of any reusable LH_2/LOx thrust chamber. Specifically, the key findings identified in the previous section form the basis of considerations which future thrust chamber designers should take into account.

One such finding is the necessity of locating the "critical failure point". This is widely assumed to be the wall at the nozzle throat. Such a critical failure point could be present in any reusable liquid rocket engine thrust chamber – regardless of propellant type, power cycles or thrust rating. The

presence or absence of a critical failure point which is not at the throat is likely governed by thrust chamber geometry and material selection, as well as engine operating conditions. For all reusable thrust chamber designs, it is recommended that the Porowski model be used to evaluate a wide variety of thrust chamber wall locations due to its computational efficiency. From there, if a critical failure point is identified at a location other than the throat, then the presence of the critical failure point can be verified with more in-depth FEM modelling focused on the point of interest. Destructive testing is also an option for verifying the location of critical failure points, if funding permits.

Another example of a key finding with applicability to other rocket engines concerns the complex relationship between mixture ratio and heat transfer in LH_2/LOx-fuelled rocket engines. As described in Section 7.1, there appears to be competing effects due to exhaust gas temperature and composition changes as mixture ratio is varied. These changes can affect heat transfer from the exhaust gas into the walls. Mixture ratio is an important design consideration in rocket engine performance, but this result suggests that, through its influence on wall heat transfer, mixture ratio has a significant effect on thrust chamber life. The effect of mixture ratio on thrust chamber convective heat transfer is of interest in the design of any reusable LH_2/LOx-fuelled rocket engine, regardless of power cycle, thrust rating or thrust chamber design. Such effects may also be evident for other common propellants.

Finally, the trade-off and optimization of mixture ratio and combustion pressure as the primary means of maximizing thrust chamber life while minimizing the detrimental impact on engine performance is a key qualitative finding of this study. This finding suggests that any LH_2/LOx-fuelled reusable rocket engine thrust chamber design can be optimized for maximum life by considering this trade-off. The quantitative results of such an optimization may vary based on thrust chamber design and thrust rating (specifically considering the higher combustion pressure in high-thrust engines), but the basic premise for conducting such a study is sound. Similar trade-offs may also be applicable to other common propellants.

7.3   Future Work

There are several improvements to the CFD models which may improve the overall accuracy of the engine plant model, such as introducing combustion or species transport into the thrust chamber model. Improving heat transfer modelling in the cooling channel model may reduce some of the "flow-on" errors due to errors in cooling channel outlet conditions identified in Subsection 5.1.1. A greater focus on modelling transient effects during engine start-up and shut-down would also be improve the accuracy of the results of this study.

The key finding that the critical failure point in a regeneratively-cooled thrust chamber may not be located at the throat challenges conventional wisdom. This finding also has potentially critical implications for not only future reusable rocket engine design, but also for reusable rocket engines which are currently under development or in service which may not have yet reached their life limit. More investigation is required to confirm this finding. Specifically, the transient effects at engine start-up and how they affect cycles to failure at the critical failure point (vs. the throat) should be considered in more detail.

This project has also identified interesting questions about how mixture ratio affects heat transfer into the thrust chamber walls. Between the effects of changing temperature and gas properties, there appears to be competing phenomena at work. This relationship between mixture ratio, gas composition, temperature and heat transfer warrants further investigation. A study analysing the effects of mixture ratio on wall heat transfer rates for a variety of propellants (not just LH_2/LOx) would be a valuable contribution to the liquid rocket engine body of knowledge.

Finally, the literature review in Section 2.1 shows that the study of design improvements to extend thrust chamber life goes back decades. Many innovative solutions for extending thrust chamber life were proposed, including but not limited to thermal barrier coatings, tungsten reinforcement of wall liner alloys, and decreasing the stiffness of closeout walls through material selection. Despite these innovative proposals, progress in recent years has been slow. With the current surge in commercial RLV development, as well as the advent of modern analysis tools and software, it may be time to re-visit some older concepts for thrust chamber design improvements, and analyse them using more powerful modern analysis tools to yield interesting results and improve reusable rocket engine design.

8.   Conclusions

The aim of this research project was to investigate how reusable liquid rocket engine operating parameters could affect thrust chamber life and engine performance. Detailed modelling and simulation of both engine operation and thrust chamber wall structural behaviour has been conducted to this end. The study has yielded a wide variety of important results and key findings, some of which are not directly related to this original goal. The following three fundamental research questions, first introduced in Section 1.2, can now be answered:

1. **Which operating conditions have an effect on thrust chamber life (measured in terms of combustion cycles to failure)?**

   The preliminary analysis described in Chapter 3 identified five engine operating parameters which either affect engine performance, thrust chamber life, or both. These parameters are as follows: mixture ratio, propellant flow rate, combustion pressure, coolant flow rate and coolant pressure. Propellant flow rate and combustion pressure were determined to be intrinsically coupled, due to the requirement to achieve sonic conditions at the thrust chamber throat. These five operating parameters were isolated in four different test cases (with combustion pressure and propellant flow rate coupled together in a single case), which were simulated using the more detailed engine plant and thrust chamber wall structural models described in Chapter 4. The results of these simulations indicated that the effect of coolant pressure on thrust chamber life was marginal. Similarly, the effect of coolant flow rate on thrust chamber life was also mostly marginal, with the caveat that coolant flow rate was an important mechanism for keeping the maximum wall temperature below the creep threshold, which could severely and detrimentally affect thrust chamber life. Conversely, both mixture ratio and combustion pressure (coupled with propellant flow rate) could have a significant effect on thrust chamber life, with increases of up to 50% over baseline life possible, depending on the operating conditions and failure mode.

2. **How and to what extent can these operating conditions be changed?**

   The engine plant model was used to determine both the methods by which the operating conditions could be changed, and limits on the range of operating conditions for each case. The operating ranges are described in Section 4.7, and the operating range limits are summarized in Section 5.6. It was determined that coolant pressure could be varied from 5.72 MPa to 8.13 MPa. This was achieved by scaling the FTP. This range of values was limited by the FTP and OTP shaft speeds. It was determined that coolant flow rate could be varied from 0.45 kg/s to 1.25 kg/s. This was achieved by adjusting the MFVT flow setting. This range of values was

limited by the fuel turbine flow rate and oxidizer turbine flow enthalpy. It was determined that mixture ratio could be varied from 3.98 to 8.86. This was achieved by adjusting various valve flow settings. This range of values was limited by the OTP shaft speed and fuel turbine flow rate. Finally, it was determined that combustion pressure (and by extension, propellant flow rate) could be varied from 2.79 MPa to 3.58 MPa. This was achieved by scaling the OTP and adjusting overall propellant flow rates. This range of values was limited by the fuel turbine flow rate and OTP shaft speed.

3. **What is the effect of these changes on engine performance (measured in terms of thrust and specific impulse)?**

It was determined that both coolant pressure and coolant flow rate have a negligible impact on thrust. Both these operating parameters can influence specific impulse by changing bleed flow requirements, but the overall impact of such changes is minimal. Conversely, both mixture ratio and combustion pressure (propellant flow rate) can influence engine performance significantly. Both thrust and specific impulse are affected in equal measure by changes in mixture ratio. This is primarily due to how changing mixture ratio affects exhaust gas composition, which in turn affects exhaust velocity. On the other hand, changing combustion pressure has a more significant affect on thrust, and a less significant impact on specific impulse. This is likely due to changes in propellant flow rate having a more direct impact on thrust than specific impulse. By considering all of the above-mentioned operating conditions together, it is possible to optimize thrust chamber life without detrimentally affecting engine performance. In the case of the JAXA reusable rocket engine, thrust chamber life can be extended by up to 26.6% over the baseline (depending on the failure mode considered) with no impact on thrust or specific impulse. If the constraint on specific impulse is relaxed, then thrust chamber life can be extended by up to 38.5% over the baseline (depending on the failure mode considered), with a 3.6% decrease in specific impulse, and no impact on thrust.

References

[1] Inatani, Y., Naruo, Y., and Yonemoto, K., "Concept and Preliminary Flight Testing of a Fully Reusable Rocket Vehicle," *Journal of Spacecraft and Rockets,* Vol. 38, No. 1, 2001, pp. 36-42.

[2] Richardson, M.P., and Hardy, D.W.F., "Economic Benefits of Reusable Launch Vehicles for Space Debris Removal," *New Space,* Vol. 6, No. 3, 2018, pp. 227-237.

[3] Ragab, M.M., Cheatwood, F.M., Hughes, S.J., "Launch Vehicle Recovery and Reuse," *AIAA SPACE 2015 Conference and Exposition,* Pasadena, CA, United States, AIAA 2015-4490, American Institute of Aeronautics and Astronautics, 2015.

[4] Federal Aviation Administration, "Commercial Space Transportation: 2011 Year in Review," Federal Aviation Administration, Washington DC, United States, January, 2012.

[5] Pielke, R., and Byerly, R., "Shuttle programme lifetime cost," *Nature,* Vol. 472, 2011, pp. 38.

[6] Federal Aviation Administration, "The Annual Compendium of Commercial Space Transportation: 2017," Federal Aviation Administration, Washington DC, United States, August, 2017.

[7] Joseph, S., and O'Connell, K., "Launch of space shuttle Atlantis STS-132," https://images.nasa.gov/details-sts132-s-059.html [cited May 11, 2019].

[8] SpaceX, "SES-10 Launch—world's first reflight of an orbital class rocket," www.flickr.com/photos/spacex/32915197674 [cited May 11, 2019].

[9] Klerkx, G., "Lost in Space: The Fall of NASA and the Dream of a New Space Age," Pantheon, New York, NY, United States, 2004.

[10] Sato, M., Hashimoto, T., Takada, S., "Development of Main Propulsion System for Reusable Sounding Rocket: Design Considerations and Technology Demonstration," *Transactions of the Japan Society for Aeronautical and Space Sciences, Aerospace Technology Japan,* Vol. 12, 2014, pp. 1-6.

[11] Dai, X., and Ray, A., "Damage-Mitigating Control of a Reusable Rocket Engine: Part II— Formulation of an Optimal Policy," *Journal of Dynamic Systems, Measurement, and Control,* Vol. 118, No. 3, 1996, pp. 409-415.

[12] Ackert, S., "Engine Maintenance Concepts for Financiers: Elements of Turbofan Shop Maintenance Costs," Aircraft Monitor, September, 2011.

[13] Yoshida, M., Takada, S., Naruo, Y., "Design and Operational Concepts for Reusable Rocket Engine," *45th AIAA/ASME/SAE/ASEE Joint Propulsion Conference & Exhibit,* Denver, CO, United States, AIAA 2009-5139, American Institute of Aeronautics and Astronautics, 2009.

[14] Van Hooser, K., and Bradley, D., "Space Shuttle Main Engine - The Relentless Pursuit of Improvement," *AIAA SPACE 2011 Conference & Exposition,* Long Beach, CA, United States, AIAA 2011-7159, American Institute of Aeronautics and Astronautics, 2011.

[15] Olson, E., "Block 5: How SpaceX Re-Engineered its Falcon 9 Rocket to Endure a 100-Launch Lifespan," https://insights.globalspec.com/article/9968/block-5-how-spacex-re-engineered-its-falcon-9-rocket-to-endure-a-100-launch-lifespan [cited July 14, 2019].

[16] Kimura, T., Hashimoto, T., Sato, M., "Reusable Rocket Engine: Firing Tests and Lifetime Analysis of Combustion Chamber," *Journal of Propulsion and Power,* Vol. 32, No. 5, 2016, pp. 1087-1094.

[17] Mattingly, J.D., "Elements of gas turbine propulsion," McGraw-Hill, New York, NY, United States, 1996.

[18] Hacobian, C., "Here's How High Planes Actually Fly, According to Experts," [online database] https://time.com/5309905/how-high-do-planes-fly/ [cited Jul 14, 2019].

[19] Repantis, K., "Why Hasn't Commercial Air Travel Gotten Any Faster Since the 1960s?" [online database] https://alum.mit.edu/slice/why-hasnt-commercial-air-travel-gotten-any-faster-1960s [cited Jul 14, 2019].

[20] GE Aviation, "CF6-80C2 high-bypass turbofan engines," https://www.geaviation.com/sites/default/files/datasheet-CF6-80C2.pdf [cited July 14 2019].

[21] Hannum, N.P., Kasper, H.J., and Pavli, A.J., "Experimental and theoretical investigation of fatigue life in reusable rocket thrust chambers," NASA Lewis Research Center, NASA-TM-X-73413, Cleveland, OH, United States, 1976.

[22] Quentmeyer, R.J., "Experimental fatigue life investigation of cylindrical thrust chambers," NASA Lewis Research Center, NASA-TM-X-73665, Cleveland, OH, United States, 1977.

[23] Andrews, J.S., and Armstrong, W.H., "The 3.3K thrust chamber life prediction," NASA Lewis Research Center, NASA-CR-144048, Cleveland, OH, United States, Aug 01, 1974.

[24] Esposito, J.J., and Zabora, R.F., "Thrust chamber life prediction. Volume 1: Mechanical and physical properties of high performance rocket nozzle materials," NASA Lewis Research Center, NASA-CR-134806, Cleveland, OH, United States, Mar, 1975.

[25] Quentmeyer, R.J., "Rocket combustion chamber life-enhancing design concepts," NASA Lewis Research Center, NASA-CR-185257, Cleveland, OH, United States, Jul, 1990.

[26] Porowski, J.S., Badlani, M., Kasrale, B., "Development of a simplified procedure for thrust chamber life prediction," NASA Lewis Research Center, NASA-CR-165585, Cleveland, OH, United States, October, 1981.

[27] Porowski, J.S., O'Donnell, W.J., Badlani, M.L., "Simplified design and life prediction of rocket thrust chambers," *Journal of Spacecraft and Rockets,* Vol. 22, No. 2, 1985, pp. 181-187.

[28] Badlani, M.L., Porowski, J.S., O'Donnell, W.J., "Development of a simplified procedure for rocket engine thrust chamber life prediction with creep," NASA Lewis Research Center, NASA-CR-168261, Cleveland, OH, United States, October, 1983.

[29] Tokudome, S., Naruo, Y., Yagishita, T., "Recent Advances in LOX / LH$_2$ Propulsion System for Reusable Vehicle Testing," *Transactions of the Japan Society for Aeronautical and Space Sciences, Space Technology Japan,* Vol. 7, 2009, pp. 19-25.

[30] Yoshida, M., Takada, S., Hashimoto, T., "Reusable sounding rocket engine and its tribological subjects," Malaysian Tribology Society,

[31] Nonaka, S., Ito, T., and Inatani, Y., "Technology Demonstrations and System Design for Reusable Rocket Flight Experiment," *68th International Astronautical Congress,* Adelaide, South Australia, Australia, IAC-17-D2.5.4, International Astronautical Federation,

[32] Popp, M., and Schmidt, G., "Rocket engine combustion chamber design concepts for enhanced life," *32nd Joint Propulsion Conference and Exhibit,* Lake Buena Vista, FL, United States, 96-3303, American Institute of Aeronautics and Astronautics, 1996.

[33] Chen, T., Yang, J., Jin, P., "Design and Analysis for Reusable Liquid Rocket Engine Chamber," *49th AIAA/ASME/SAE/ASEE Joint Propulsion Conference,* San Jose, CA, United States, AIAA 2013-4062, American Institute of Aeronautics and Astronautics, 2013.

[34] Oates, G.C., "Aerothermodynamics of gas turbine and rocket propulsion," 3rd ed. AIAA, Reston, VA, United States, 1997.

[35] Sforza, P.M., "Theory of Aerospace Propulsion," Butterworth-Heinemann, Waltham, MA, United States, 2011.

[36] Huzel, D.K., and Huang, D.H., "Modern Engineering for Design of Liquid-Propellant Rocket Engines," American Institute of Aeronautics and Astronautics, Washington DC, United States, 1992.

[37] Binder, M., Tomsik, T., and Veres, J.P., "RL10A-3-3A Rocket Engine Modeling Project," NASA Lewis Research Center, NASA-TM-107318, Cleveland, OH, United States, January, 1997.

[38] White, F.M., "Fluid Mechanics," 7th ed. McGraw-Hill, New York, NY, United States, 2009.

[39] Gordon, S., and McBride, S.J., "Computer program for calculation of complex chemical equilibrium compositions and applications. Part 1: Analysis," NASA Lewis Research Center, NASA-RP-1311, Cleveland, OH, United States, October, 1994.

[40] National Institute of Standards and Technology, "NIST Reference Fluid Thermodynamic and Transport Properties Database (REFPROP)," [Software], Version 7.0, 2004, Gaithersburg, MD, United States.

[41] ANSYS Inc., "ANSYS Fluent," [Software], Version 19.1, 2018, Canonsburg, PA, United States.

[42] Orszag, S.A., Yakhot, V., Flannery, W.S., "Renormalization Group Modeling and Turbulence Simulations," *International Conference on Near-Wall Turbulent Flows,* Tempe, AZ, United States, 1993.

[43] Sutherland, W., "LII. The Viscosity of Gases and Molecular Force," *Philosophical Magazine,* Vol. 5, 1893, pp. 507-531.

[44] Soave, G., "Equilibrium constants from a modified Redlich-Kwong equation of state," *Chemical Engineering Science,* Vol. 27, No. 6, 1972, pp. 1197-1203.

[45] Higashino, K., Sugioka, M., Kobayashi, T., "LNG サルファーアタック/コーキングに関する研究（サルファーアタック分）：共同研究報告（JAXA 宇宙基幹システム本部），" Muroran Institute of Technology, Aerospace Plane Research Center, Muroran, Hokkaido, Japan, Sep 2008.

[46] European Copper Institute, "CuCr1Zr," http://www.conductivity-app.org/alloy-sheet/19 [cited Sep 6, 2018].

[47] Kim, S.E., and Choudhhury, D., "A Near-Wall Treatment Using Wall Functions Sensitized to Pressure Gradient," *Fluids engineering and laser anemometry conference, Separated and complex flows,* Hilton Head, SC , United States, American Society of Mechanical Engineers, 1995.

[48] National Institute of Standards and Technology, "NIST Reference Fluid Thermodynamic and Transport Properties Database (REFPROP)," [Software], Version 9.1, 2013, Gaithersburg, MD, United States.

[49] Barabash, V.R., Kalinin, G.M., Fabritsiev, S.A., "Specification of CuCrZr alloy properties after various thermo-mechanical treatments and design allowables including neutron irradiation effects," *Journal of Nuclear Materials,* Vol. 417, No. 1, 2011, pp. 904-907.

[50] Li, G., Thomas, B.G., and Stubbins, J.F., "Modeling creep and fatigue of copper alloys," *Metallurgical and Materials Transactions A,* Vol. 31, No. 10, 2000, pp. 2491-2502.

Appendix A Preliminary Investigation Functional Analysis

This appendix described the detailed process used in the functional analyses described in Sections 3.1, 3.2 and 3.3. Formulas based on fundamental theory described in Section 2.2 are converted to function notation, and by inspection are exposed to a process of substitution and elimination. The end result of these analyses are a set of functions with only engine operating conditions as variables.

A-1 Engine Performance Functions

Both thrust and specific impulse are functions of thrust chamber mass flow rate, exhaust velocity, atmospheric pressure, exhaust nozzle exit pressure and exhaust nozzle exit area. Specific impulse is also a function of total propellant flow rate and standard gravity. These relationships are shown in Equations (A-1-1) and (A-1-2), respectively.

$$F_T = f(A_E, \dot{m}_{TC}, p_E, p_a, u_E) \tag{A-1-1}$$

$$I_{SP} = f(A_E, g, \dot{m}_{TC}, \dot{m}_{ET}, p_E, p_a, u_E) \tag{A-1-2}$$

Equation (2-4) shows that exhaust nozzle exit pressure is a function of combustion pressure, specific heat ratio and exhaust nozzle exit Mach number. Thus, the relationships in Equations (A-1-1) and (A-1-2) can be rewritten as shown in Equations (A-1-3) and (A-1-4).

$$F_T = f(A_E, Ma_E, \dot{m}_{TC}, p_C, p_a, u_E, \gamma) \tag{A-1-3}$$

$$I_{SP} = f(A_E, g, Ma_E, \dot{m}_{TC}, \dot{m}_{ET}, p_C, p_a, u_E, \gamma) \tag{A-1-4}$$

Equation (2-6) shows that exhaust nozzle exit velocity is a function of exhaust nozzle exit Mach number, specific heat ratio, specific gas constant and exhaust nozzle exit temperature. Thus, the relationships in Equations (A-1-3) and (A-1-4) can be rewritten as shown in Equations (A-1-5) and (A-1-6).

$$F_T = f(A_E, Ma_E, \dot{m}_{TC}, p_C, p_a, R, T_E, \gamma) \tag{A-1-5}$$

$$I_{SP} = f(A_E, g, Ma_E, \dot{m}_{TC}, \dot{m}_{ET}, p_C, p_a, R, T_E, \gamma) \tag{A-1-6}$$

Equation (2-9) shows that exhaust nozzle exit temperature is a function of combustion temperature, specific heat ratio and exhaust nozzle exit Mach number. Thus, the relationships in Equations (A-1-5) and (A-1-6) can be rewritten as shown in Equations (A-1-7) and (A-1-8).

$$F_T = f(A_E, Ma_E, \dot{m}_{TC}, p_C, p_a, R, T_{TC}, \gamma) \qquad \text{(A-1-7)}$$

$$I_{SP} = f(A_E, g, Ma_E, \dot{m}_{TC}, \dot{m}_{ET}, p_C, p_a, R, T_{TC}, \gamma) \qquad \text{(A-1-8)}$$

Equation (2-7) shows that exhaust nozzle exit Mach number is a function of specific heat ratio, exhaust nozzle exit area and throat area. Thus, the relationships in Equations (A-1-7) and (A-1-8) can be rewritten as shown in Equations (A-1-9) and (A-1-10).

$$F_T = f(A_E, A^*, \dot{m}_{TC}, p_C, p_a, R, T_{TC}, \gamma) \qquad \text{(A-1-9)}$$

$$I_{SP} = f(A_E, A^*, g, \dot{m}_{TC}, \dot{m}_{ET}, p_C, p_a, R, T_{TC}, \gamma) \qquad \text{(A-1-10)}$$

Exhaust nozzle exit area and throat area are "design values" for any given engine, and can therefore be considered constant. Similarly, standard gravity is a constant value. Atmospheric pressure varies with altitude, but can be considered constant at sea level for the purposes of this analysis. By removing these "constant" values from the set of functional variables for thrust and specific impulse, Equations (A-1-9) and (A-1-10) can be rewritten as shown in Equations (A-1-11) and (A-1-12).

$$F_T = f(\dot{m}_{TC}, p_C, R, T_{TC}, \gamma) \qquad \text{(A-1-11)}$$

$$I_{SP} = f(\dot{m}_{TC}, \dot{m}_{ET}, R, p_C, T_{TC}, \gamma) \qquad \text{(A-1-12)}$$

Finally, specific heat ratio and specific gas constant are dependent on the properties of the combustion product gasses. Likewise, combustion temperature is dependent upon the combustion reaction. Assuming an isobaric, adiabatic combustion reaction with discrete, specified reactants (fuel and oxidizer) in the thrust chamber, a simulation code such as NASA's Chemical Equilibrium with Applications (CEA)[39] can estimate these values by taking combustion pressure, mixture ratio and propellant temperatures as inputs. Considering these inputs, the relationships in Equations (A-1-11) and (A-1-12) can be rewritten as shown in Equations (A-1-13) and (A-1-14).

$$F_T = f(MR_C, \dot{m}_{TC}, p_C, T_{FI}, T_{OI}) \qquad \text{(A-1-13)}$$

$$I_{SP} = f(MR_C, \dot{m}_{TC}, \dot{m}_{ET}, p_C, T_{FI}, T_{OI}) \qquad \text{(A-1-14)}$$

A-2 Thrust Chamber Life

As described in Subsection 2.2.3, the Porowski model considers three separate failure modes in measuring thrust chamber life: plastic instability, low-cycle fatigue and creep deformation. Life is

quantified as the number of cycles to failure. The number of cycles to plastic deformation failure is governed by the minimum thickness in the ligament (Equation (2-31)) and the critical thickness (Equation (2-33)). Thus, the number of cycles to plastic deformation failure can be expressed as a function of ligament half-thickness, total deflection, rib width, ligament width and strain hardening parameter, as shown in Equation (A-2-1).

$$N_{F,PI} = f(H, l, n, w, \delta_{tot}) \tag{A-2-1}$$

Equation (2-39) shows that the strain hardening parameter is a function of ultimate and yield strengths. Thus, Equation (A-2-1) can be rewritten as shown in Equation (A-2-2).

$$N_{F,PI} = f(H, l, S_U, S_Y, w, \delta_{tot}) \tag{A-2-2}$$

The number of cycles to low-cycle fatigue failure is governed by total strain range, which is required to determine cumulative damage using a fatigue curve. Thus, based on Equation (2-35), the number of cycles to low-cycle fatigue failure is a function axial and hoop strains in the minimum-thickness section of the ligament, as shown in Equation (A-2-3).

$$N_{F,f} = f(\epsilon_{x,min}, \epsilon_{y,min}) \tag{A-2-3}$$

Equation (2-36) shows that axial strain in the minimum-thickness section of the ligament is a function of thermal coefficient and the temperature differential between the ligament and the close-out wall. Also, Equation (2-37) shows that hoop strain in the minimum-thickness section of the ligament is a function of average hoop strain, strain hardening parameter and minimum & maximum ligament thicknesses. Thus, Equation (A-2-3) can be rewritten as shown in Equation (A-2-4).

$$N_{F,f} = f(n, \alpha, \Delta T_w, \epsilon_{x,avg}, \tau_{min}, \tau_{max}) \tag{A-2-4}$$

Equation (2-38) shows that, like axial strain, average hoop strain is a function of thermal coefficient and the temperature differential between the ligament and the close-out wall. Also, Equation (2-39) shows that the strain hardening parameter is a function of ultimate and yield strengths. Thus, Equation (A-2-4) can be rewritten as shown in Equation (A-2-5).

$$N_{F,f} = f(S_U, S_Y, \alpha, \Delta T_w, \tau_{min}, \tau_{max}) \tag{A-2-5}$$

Equations (2-31) and (2-32) show that both minimum and maximum ligament thickness are functions of ligament half-thickness, total deflection, rib width and ligament width. Thus, Equation (A-2-5) can be rewritten as shown in Equation (A-2-6).

$$N_{F,f} = f(H, l, S_U, S_Y, w, \alpha, \delta_{tot}, \Delta T_w) \tag{A-2-6}$$

The number of cycles to creep deformation failure is governed by initial stress, which is required to determine cumulative damage using a stress-rupture curve. Thus, based on Equation (2-44), the number of cycles to creep deformation failure is a function of differential pressure loading, ligament width, rib width and minimum ligament thickness, as shown in Equation (A-2-7).

$$N_{F,cr} = f(l, w, \Delta p_l, \tau_{min}) \tag{A-2-7}$$

As above, Equation (2-31) shows that minimum ligament thickness is a function of ligament half-thickness, total deflection, rib width and ligament width. Thus, Equation (A-2-7) can be rewritten as shown in Equation (A-2-8).

$$N_{F,cr} = f(H, l, w, \Delta p_l, \delta_{tot}) \tag{A-2-8}$$

Equations (A-2-2), (A-2-6) and (A-2-8) show that the number of cycles to failure for all three failure modes are function of total deflection, among other variables. Equation (2-10) shows that total deflection is the sum of the individual bending, shear and creep inelastic deflections. Thus Equations (A-2-2), (A-2-6) and (A-2-8) can be rewritten as shown in Equations (A-2-9) to (A-2-11).

$$N_{F,PI} = f(H, l, S_U, S_Y, w, \delta_{be}, \delta_{sh}, \delta_{cr}) \tag{A-2-9}$$

$$N_{F,f} = f(H, l, S_U, S_Y, w, \alpha, \delta_{be}, \delta_{sh}, \delta_{cr}, \Delta T_w) \tag{A-2-10}$$

$$N_{F,cr} = f(H, l, w, \delta_{be}, \delta_{sh}, \delta_{cr}, \Delta p_l) \tag{A-2-11}$$

Equation (2-30) shows that inelastic creep deflection is a function of Norton law constant, combustion time, ligament width, ligament half-thickness, differential pressure loading and Norton law exponent. Thus, Equations (A-2-9) to (A-2-11) can be rewritten as shown in Equations (A-2-12) to (A-2-14).

$$N_{F,PI} = f(B, C, H, l, S_U, S_Y, t_C, w, \delta_{be}, \delta_{sh}, \Delta p_l) \tag{A-2-12}$$

$$N_{F,f} = f(B, C, H, l, S_U, S_Y, t_C, w, \alpha, \delta_{be}, \delta_{sh}, \Delta p_l, \Delta T_w) \tag{A-2-13}$$

$$N_{F,cr} = f(B, C, H, l, t_C, w, \delta_{be}, \delta_{sh}, \Delta p_l) \tag{A-2-14}$$

Equations (2-25) and (2-26) show that inelastic shear deflection is a function of normalized shear force, normalized bending moment, normalized hoop force and total thermal strain range. Thus, Equations (A-2-12) to (A-2-14) can be rewritten as shown in Equations (A-2-15) to (A-2-17).

$$N_{F,PI} = f(B, C, f_{ho}, f_{sh}, H, l, m_{be}, S_U, S_Y, t_C, w, \delta_{be}, \Delta p_l, \Delta\epsilon_{Th}) \qquad \text{(A-2-15)}$$

$$N_{F,f} = f(B, C, f_{ho}, f_{sh}, H, l, m_{be}, S_U, S_Y, t_C, w, \alpha, \delta_{be}, \Delta p_l, \Delta T_w, \Delta\epsilon_{Th}) \qquad \text{(A-2-16)}$$

$$N_{F,cr} = f(B, C, f_{ho}, f_{sh}, H, l, m_{be}, t_C, w, \delta_{be}, \Delta p_l, \Delta\epsilon_{Th}) \qquad \text{(A-2-17)}$$

Equation (2-24) shows that inelastic bending deflection is a function of ligament width and bending radius. Thus, Equations (A-2-15) to (A-2-17) can be rewritten as shown in Equations (A-2-18) to (A-2-20).

$$N_{F,PI} = f(B, C, f_{ho}, f_{sh}, H, l, m_{be}, r_{be}, S_U, S_Y, t_C, w, \Delta p_l, \Delta\epsilon_{Th}) \qquad \text{(A-2-18)}$$

$$N_{F,f} = f(B, C, f_{ho}, f_{sh}, H, l, m_{be}, r_{be}, S_U, S_Y, t_C, w, \alpha, \Delta p_l, \Delta T_w, \Delta\epsilon_{Th}) \qquad \text{(A-2-19)}$$

$$N_{F,cr} = f(B, C, f_{ho}, f_{sh}, H, l, m_{be}, r_{be}, t_C, w, \Delta p_l, \Delta\epsilon_{Th}) \qquad \text{(A-2-20)}$$

Equation (2-23) shows that bending radius is a function of normalized shear force, normalized hoop force, total thermal strain range and ligament half-thickness. Thus, Equations (A-2-18) to (A-2-20) can be rewritten as shown in Equations (A-2-21) to (A-2-23).

$$N_{F,PI} = f(B, f_{ho}, f_{sh}, H, l, m_{be}, S_U, S_Y, t_C, w, \Delta p_l, \Delta\epsilon_{Th}, \kappa) \qquad \text{(A-2-21)}$$

$$N_{F,f} = f(B, f_{ho}, f_{sh}, H, l, m_{be}, S_U, S_Y, t_C, w, \alpha, \Delta p_l, \Delta T_w, \Delta\epsilon_{Th}, \kappa) \qquad \text{(A-2-22)}$$

$$N_{F,cr} = f(B, f_{ho}, f_{sh}, H, l, m_{be}, t_C, w, \Delta p_l, \Delta\epsilon_{Th}, \kappa) \qquad \text{(A-2-23)}$$

Equation (2-17) shows that normalized hoop force is a function of normalized shear force and normalized bending moment. Thus, Equations (A-2-21) to (A-2-23) can be rewritten as shown in Equations (A-2-24) to (A-2-26).

$$N_{F,PI} = f(B, C, f_{sh}, H, l, m_{be}, S_U, S_Y, t_C, w, \Delta p_l, \Delta\epsilon_{Th}) \qquad \text{(A-2-24)}$$

$$N_{F,f} = f(B, C, f_{sh}, H, l, m_{be}, S_U, S_Y, t_C, w, \alpha, \Delta p_l, \Delta T_w, \Delta\epsilon_{Th}) \qquad \text{(A-2-25)}$$

$$N_{F,cr} = f(B, C, f_{sh}, H, l, m_{be}, t_C, w, \Delta p_l, \Delta \epsilon_{Th}) \tag{A-2-26}$$

Equation (2-14) shows that normalized bending moment is a function of bending moment, yield strength and ligament half-thickness. Also, Equation (2-15) shows that normalized shear force is a function of shear force, yield strength and ligament half-thickness. Thus, Equations (A-2-24) to (A-2-26) can be rewritten as shown in Equations (A-2-27) to (A-2-29).

$$N_{F,PI} = f(B, C, F_{sh}, H, l, M_{be}, S_U, S_Y, t_C, w, \Delta p_l, \Delta \epsilon_{Th}) \tag{A-2-27}$$

$$N_{F,f} = f(B, C, F_{sh}, H, l, M_{be}, S_U, S_Y, t_C, w, \alpha, \Delta p_l, \Delta T_w, \Delta \epsilon_{Th}) \tag{A-2-28}$$

$$N_{F,cr} = f(B, C, F_{sh}, H, l, M_{be}, S_Y, t_C, w, \Delta p_l, \Delta \epsilon_{Th}) \tag{A-2-29}$$

Equations (2-12) and (2-13) show that both bending moment and shear force are functions of bending moment, differential pressure loading, ligament width and tangential ligament position. However, as these functions are either solved at a discrete point (i.e. the ligament centre) or integrated over the width of the ligament, the position term can be neglected in this analysis. Thus, Equations (A-2-27) to (A-2-29) can be rewritten as shown in Equations (A-2-30) to (A-2-32).

$$N_{F,PI} = f(B, C, H, l, S_U, S_Y, t_C, w, \Delta p_l, \Delta \epsilon_{Th}) \tag{A-2-30}$$

$$N_{F,f} = f(B, C, H, l, S_U, S_Y, t_C, w, \alpha, \Delta p_l, \Delta T_w, \Delta \epsilon_{Th}) \tag{A-2-31}$$

$$N_{F,cr} = f(B, C, H, l, S_Y, t_C, w, \Delta p_l, \Delta \epsilon_{Th}) \tag{A-2-32}$$

Equation (2-18) shows that total thermal strain range is the sum of hoop strain range due to the ligament to close-out wall temperature differential and bending strain range due to the temperature differential across the ligament. Thus, Equations (A-2-30) to (A-2-32) can be rewritten as shown in Equations (A-2-33) to (A-2-35).

$$N_{F,PI} = f(B, C, H, l, S_U, S_Y, t_C, w, \Delta p_l, \Delta \epsilon_{Th,w}, \Delta \epsilon_{Th,l}) \tag{A-2-33}$$

$$N_{F,f} = f(B, C, H, l, S_U, S_Y, t_C, w, \alpha, \Delta p_l, \Delta T_w, \Delta \epsilon_{Th,w}, \Delta \epsilon_{Th,l}) \tag{A-2-34}$$

$$N_{F,cr} = f(B, C, H, l, S_Y, t_C, w, \Delta p_l, \Delta \epsilon_{Th,w}, \Delta \epsilon_{Th,l}) \tag{A-2-35}$$

Equation (2-19) shows that hoop strain range due to the ligament to close-out wall temperature differential is a function of thermal coefficient, temperature differential between the ligament and the

close-out wall, yield strength and modulus of elasticity. Thus, Equations (A-2-33), (A-2-34) and (A-2-35) can be rewritten as shown in Equations (A-2-36) to (A-2-38).

$$N_{F,PI} = f\left(B, C, E, H, l, S_U, S_Y, t_C, w, \alpha, \Delta p_l, \Delta T_w, \Delta \epsilon_{Th,l}\right) \tag{A-2-36}$$

$$N_{F,f} = f\left(B, C, E, H, l, S_U, S_Y, t_C, w, \alpha, \Delta p_l, \Delta T_w, \Delta \epsilon_{Th,l}\right) \tag{A-2-37}$$

$$N_{F,cr} = f\left(B, C, E, H, l, S_Y, t_C, w, \alpha, \Delta p_l, \Delta T_w, \Delta \epsilon_{Th,l}\right) \tag{A-2-38}$$

Equation (2-21) shows that bending strain range due to the temperature differential across the ligament is a function of modulus of elasticity, thermal coefficient, temperature differential across the ligament, Poisson's ratio and yield strength. Thus, Equations (A-2-36) to (A-2-38) can be rewritten as shown in Equations (A-2-39) to (A-2-41).

$$N_{F,PI} = f(B, C, E, H, l, S_U, S_Y, t_C, w, \alpha, \Delta p_l, \Delta T_l, \Delta T_w, \nu) \tag{A-2-39}$$

$$N_{F,f} = f(B, C, E, H, l, S_U, S_Y, t_C, w, \alpha, \Delta p_l, \Delta T_l, \Delta T_w, \nu) \tag{A-2-40}$$

$$N_{F,cr} = f(B, C, E, H, l, S_Y, t_C, w, \alpha, \Delta p_l, \Delta T_l, \Delta T_w, \nu) \tag{A-2-41}$$

ligament half-thickness, ligament width and rib width are constrained by the geometry of the thrust chamber and can be considered "design values". Also, modulus of elasticity, coefficient of thermal expansion, Norton law exponent and Poisson's ratio are constrained by thrust chamber material selection and can also be considered "design values". The Norton law constant, ultimate strength and yield strength are also material properties, but can vary with material temperature, as described in Subsection 4.6.2. Thus, these values can be considered to be functions of the maximum wall temperature, which occurs on the inner surface of the ligament. If these "design values" are considered to be constant, or functions of temperature, then Equations (A-2-39) to (A-2-41) can be rewritten as shown in Equations (A-2-42) to (A-2-44).

$$N_{F,PI} = f(t_C, T_{l1}, \Delta p_l, \Delta T_l, \Delta T_w) \tag{A-2-42}$$

$$N_{F,f} = f(t_C, T_{l1}, \Delta p_l, \Delta T_l, \Delta T_w) \tag{A-2-43}$$

$$N_{F,cr} = f(t_C, T_{l1}, \Delta p_l, \Delta T_l, \Delta T_w) \tag{A-2-44}$$

A-3 Thrust Chamber Heat Transfer

The definitions for temperature differential between the ligament and the close-out wall, and temperature differential across the ligament are given in Equations (2-20) and (2-22) respectively. These values can be written as functions of temperatures at relevant points in the wall, as shown in Equations (A-3-1) and (A-3-2).

$$\Delta T_w = f(T_{w1}, T_{w2}) \tag{A-3-1}$$

$$\Delta T_l = f(T_{l1}, T_{l2}) \tag{A-3-2}$$

Equation (2-49) shows that the temperature in the close-out wall is a function of wall ligament temperature and the differential constant. Thus, Equation (A-3-1) can be rewritten as shown in Equation (A-3-3).

$$\Delta T_w = f(\bar{A}, T_{w1}) \tag{A-3-3}$$

Equation (2-48) shows that the wall ligament temperature is a function of the inner and outer ligament temperatures. Thus, Equation (A-3-3) can be rewritten as shown in Equation (A-3-4).

$$\Delta T_w = f(\bar{A}, T_{l1}, T_{l2}) \tag{A-3-4}$$

Equation (2-46) shows that the maximum wall temperature (i.e. the temperature on the inner surface of the ligament) can be estimated as a function of ligament inner and outer surface areas, rib surface area, ligament inner and outer heat transfer coefficients, rib heat transfer coefficient, ligament half-thickness, wall thermal conductivity, thrust chamber gas bulk temperature and cooling channel fluid bulk temperature. This is shown in Equation (A-3-5).

$$T_{l1} = f(A_{l1}, A_{l2}, A_{ri}, H, htc_{l1}, htc_{l2}, htc_{ri}, T_{CC}, T_{TC}, \kappa) \tag{A-3-5}$$

Using Equation (A-3-5), Equations (A-3-2) and (A-3-4) can be rewritten as shown in Equations (A-3-6) and (A-3-7).

$$\Delta T_l = f(A_{l1}, A_{l2}, A_{ri}, H, htc_{l1}, htc_{l2}, htc_{ri}, T_{CC}, T_{l2}, T_{TC}, \kappa) \tag{A-3-6}$$

$$\Delta T_w = f(\bar{A}, A_{l1}, A_{l2}, A_{ri}, H, htc_{l1}, htc_{l2}, htc_{ri}, T_{CC}, T_{l2}, T_{TC}, \kappa) \tag{A-3-7}$$

Equation (2-47) shows that the temperature on the outer surface (i.e. cooling channel side) of the ligament can be estimated as a function of ligament inner and outer surface areas, rib surface area, ligament inner and outer heat transfer coefficients, rib heat transfer coefficient, thrust chamber gas

bulk temperature and cooling channel fluid bulk temperature. Thus, Equations (A-3-6) and (A-3-7) can be rewritten as shown in Equations (A-3-8) and (A-3-9).

$$\Delta T_l = f(A_{l1}, A_{l2}, A_{ri}, H, htc_{l1}, htc_{l2}, htc_{ri}, T_{CC}, T_{TC}, \kappa) \tag{A-3-8}$$

$$\Delta T_w = f(\bar{A}, A_{l1}, A_{l2}, A_{ri}, H, htc_{l1}, htc_{l2}, htc_{ri}, T_{CC}, T_{TC}, \kappa) \tag{A-3-9}$$

The differential constant, ligament inner & outer surface areas, rib surface area, ligament half-thickness and wall thermal conductivity are constrained by the geometry and material of the thrust chamber and can be considered "design values". If these "design values" are considered to be constant, then Equations (A-3-5), (A-3-8) and (A-3-9) can be rewritten as shown in Equations (A-3-10) to (A-3-12).

$$T_{l1} = f(htc_{l1}, htc_{l2}, htc_{ri}, T_{CC}, T_{TC}) \tag{A-3-10}$$

$$\Delta T_l = f(htc_{l1}, htc_{l2}, htc_{ri}, T_{CC}, T_{TC}) \tag{A-3-11}$$

$$\Delta T_w = f(htc_{l1}, htc_{l2}, htc_{ri}, T_{CC}, T_{TC}) \tag{A-3-12}$$

Equations (2-54) and (2-55) show that the rib heat transfer coefficient is a function of the same variables as the ligament outer (cooling channel side) heat transfer coefficient. Thus, Equations (A-3-10) to (A-3-12) can be rewritten as shown in Equations (A-3-13) to (A-3-15).

$$T_{l1} = f(htc_{l1}, htc_{l2}, T_{CC}, T_{TC}) \tag{A-3-13}$$

$$\Delta T_l = f(htc_{l1}, htc_{l2}, T_{CC}, T_{TC}) \tag{A-3-14}$$

$$\Delta T_w = f(htc_{l1}, htc_{l2}, T_{CC}, T_{TC}) \tag{A-3-15}$$

Assuming isentropic flow in the nozzle, the local bulk temperature in the thrust chamber can be estimated using thrust chamber stagnation temperature (i.e. combustion temperature), local Mach number and specific heat ratio. Thus, Equations (A-3-13) to (A-3-15) can be rewritten as shown in Equations (A-3-16) to (A-3-18).

$$T_{l1} = f(htc_{l1}, htc_{l2}, Ma, T_{CC}, T_{TC}, \gamma) \tag{A-3-16}$$

$$\Delta T_l = f(htc_{l1}, htc_{l2}, Ma, T_{CC}, T_{TC}, \gamma) \tag{A-3-17}$$

$$\Delta T_w = f(htc_{l1}, htc_{l2}, Ma, T_{CC}, T_{TC}, \gamma) \tag{A-3-18}$$

Equation (2-50) shows that the ligament inner heat transfer coefficient is a function of throat diameter, thrust chamber stagnation viscosity, constant-pressure specific heat, Prandtl number, stagnation pressure (i.e. combustion pressure), standard gravity, characteristic velocity, throat radius of curvature, throat area, local thrust chamber area and boundary layer correction factor. This functional relationship can be rewritten as shown in Equation (A-3-19).

$$htc_{l1} = f\left(A, A^*, c_{P,TC,0}, D^*, g, p_{TC}, Pr_{TC,0}, r^*, u_{char}, \mu_{TC,0}, \phi_{bl}\right) \tag{A-3-19}$$

Equation (2-51) shows that the boundary layer correction factor is a function of thrust chamber stagnation temperature (i.e. combustion temperature), ligament inner temperature, specific heat ratio and local Mach number. Thus, Equation (A-3-19) can be rewritten as shown in Equation (A-3-20).

$$htc_{l1} = f\left(A, A^*, c_{P,TC,0}, D^*, g, Ma, p_{TC}, Pr_{TC,0}, r^*, T_{l1}, T_{TC}, u_{char}, \gamma, \mu_{TC,0}\right) \tag{A-3-20}$$

Equation (2-52) shows that the Prandtl number is a function of constant-pressure specific heat, viscosity and gas thermal conductivity. Thus, Equation (A-3-20) can be rewritten as shown in Equation (A-3-21).

$$htc_{l1} = f\left(A, A^*, c_{P,TC,0}, D^*, g, k_{TC,0}, Ma, p_{TC}, r^*, T_{l1}, T_{TC}, u_{char}, \gamma, \mu_{TC,0}\right) \tag{A-3-21}$$

Equation (2-53) shows that the characteristic velocity is a function of specific heat ratio, specific gas constant and throat stagnation temperature. Specific gas constant can be calculated using constant-pressure specific heat and the specific heat ratio. If flow in the nozzle is assumed to be isentropic, then throat stagnation temperature can be approximated as combustion temperature. Thus, Equation (A-3-21) can be rewritten as shown in Equation (A-3-22).

$$htc_{l1} = f\left(A, A^*, c_{P,TC,0}, D^*, g, k_{TC,0}, Ma, p_{TC}, r^*, T_{l1}, T_{TC}, \gamma, \mu_{TC,0}\right) \tag{A-3-22}$$

Heat transfer is usually analysed at the throat, as this is the point where heat transfer and ligament temperatures reach their maximum values, and thus the critical location in terms of limiting thrust chamber life. If heat transfer calculations are limited to the throat region, and sonic conditions at the throat are assumed, then Equation (A-3-22) can be simplified, as the local thrust chamber area is equal to the throat area ($A = A^*$), and the local Mach number is one. Thus, Equation (A-3-22) can be rewritten as shown in Equation (A-3-23).

$$htc_{l1} = f\left(A^*, c_{P,TC,0}, D^*, g, k_{TC,0}, p_{TC}, r^*, T_{l1}, T_{TC}, \gamma, \mu_{TC,0}\right) \tag{A-3-23}$$

Constant-pressure specific heat, thermal conductivity, combustion temperature, specific heat ratio and viscosity are all dependent on the properties of the combustion product gasses. As described in Section 3.1, CEA can be used to estimate various combustion product gas properties, including the values described above[39]. Assuming an isobaric, adiabatic combustion reaction with discrete, specified reactants (fuel and oxidizer) in the thrust chamber, CEA can estimate these values by taking combustion pressure, mixture ratio and propellant temperatures as inputs. Considering these inputs, Equation (A-3-23) can be rewritten as shown in Equation (A-3-24).

$$htc_{l1} = f(A^*, D^*, g, MR_{TC}, p_{TC}, r^*, T_{FI}, T_{l1}, T_{OI}) \tag{A-3-24}$$

Throat area, diameter and radius of curvature are constrained by thrust chamber geometry, and can be considered "design values". Also, standard gravity is a constant value. If the "design values" and constant are removed as variables from Equation (A-3-24), it can be rewritten as shown in Equation (A-3-25).

$$htc_{l1} = f(MR_{TC}, p_{TC}, T_{FI}, T_{l1}, T_{OI}) \tag{A-3-25}$$

Recall that ligament inner (thrust chamber side) temperature is already accounted for in Equations (A-3-16) to (A-3-18). Thus, the result shown in Equation (A-3-25) can be substituted into Equations (A-3-16) to (A-3-18), as shown in Equations (A-3-26) to (A-3-28).

$$T_{l1} = f(htc_{l2}, Ma, MR_{TC}, p_{TC}, T_{CC}, T_{FI}, T_{OI}, T_{TC}, \gamma) \tag{A-3-26}$$

$$\Delta T_l = f(htc_{l2}, Ma, MR_{TC}, p_{TC}, T_{CC}, T_{FI}, T_{OI}, T_{TC}, \gamma) \tag{A-3-27}$$

$$\Delta T_w = f(htc_{l2}, Ma, MR_{TC}, p_{TC}, T_{CC}, T_{FI}, T_{OI}, T_{TC}, \gamma) \tag{A-3-28}$$

As described above, it is assumed the heat transfer is calculated at the throat, where the local Mach number is one. Also as described above, combustion temperature and specific heat ratio are dependent on the combustion gas properties, which can be calculated using CEA with existing variables as inputs. Thus, Equations (A-3-26) to (A-3-28) can be rewritten as shown in Equations (A-3-29) to (A-3-31).

$$T_{l1} = f(htc_{l2}, MR_{TC}, p_{TC}, T_{CC}, T_{FI}, T_{OI}) \tag{A-3-29}$$

$$\Delta T_l = f(htc_{l2}, MR_{TC}, p_{TC}, T_{CC}, T_{FI}, T_{OI}) \tag{A-3-30}$$

$$\Delta T_w = f(htc_{l2}, MR_{TC}, p_{TC}, T_{CC}, T_{FI}, T_{OI}) \tag{A-3-31}$$

Equation (2-54) shows that the ligament outer (cooling channel side) heat transfer coefficient is a function of cooling channel coolant film thermal conductivity, constant-pressure specific heat and viscosity, as well as cooling channel hydraulic diameter, mass flow rate, area and curvature correction factor. This functional relationship can be written as shown in Equation (A-3-32).

$$htc_{l2} = f(A_{CC}, c_{P,CC,cf}, D_{CC,hyd}, k_{CC,cf}, \dot{m}_{CC}, \mu_{CC,cf}, \phi_{curv}) \tag{A-3-32}$$

Equation (2-57) shows that the curvature correction factor is a function of cooling channel Reynolds number, hydraulic diameter and radius of curvature. Thus, Equation (A-3-32) can be rewritten as shown in Equation (A-3-33).

$$htc_{l2} = f(A_{CC}, c_{P,CC,cf}, D_{CC,hyd}, k_{CC,cf}, \dot{m}_{CC}, r_{CC}, Re_{CC}, \mu_{CC,cf}) \tag{A-3-33}$$

Equation (2-58) shows that the Reynolds number is a function of cooling channel density, velocity, hydraulic diameter and viscosity. Thus, Equation (A-3-33) can be rewritten as shown in Equation (A-3-34).

$$htc_{l2} = f(A_{CC}, c_{P,CC,cf}, D_{CC,hyd}, k_{CC,cf}, \dot{m}_{CC}, r_{CC}, u_{CC}, \mu_{CC}, \mu_{CC,cf}, \rho_{CC}) \tag{A-3-34}$$

Equation (2-59) shows that the cooling channel velocity is a function of cooling channel density, area and mass flow rate. Thus, Equation (A-3-34) can be rewritten as shown in Equation (A-3-35).

$$htc_{l2} = f(A_{CC}, c_{P,CC,cf}, D_{CC,hyd}, k_{CC,cf}, \dot{m}_{CC}, r_{CC}, \mu_{CC}, \mu_{CC,cf}, \rho_{CC}) \tag{A-3-35}$$

If the cooling channel bulk fluid temperature and pressure are known, cooling channel density and viscosity are fluid properties which can be interpolated from a state variable database for the coolant fluid, as described in Subsection 4.3.2. In a similar fashion, the "coolant film" properties shown in Equation (A-3-35) (constant-pressure specific heat, thermal conductivity & viscosity) can be determined if the coolant film temperature and pressure are known. Equation (2-56) shows that coolant film temperature is a function of cooling channel bulk fluid temperature and ligament outer (cooling channel side) temperature. For simplicity, it is assumed that coolant film pressure is equal to cooling channel bulk fluid pressure. Thus, based on coolant fluid property state variable interpolation, Equation (A-3-35) can be rewritten as shown in Equation (A-3-36).

$$htc_{l2} = f(A_{CC}, D_{CC,hyd}, \dot{m}_{CC}, p_{CC}, r_{CC}, T_{CC}, T_{l2}) \qquad \text{(A-3-36)}$$

Cooling channel area, hydraulic diameter and radius of curvature are constrained by thrust chamber geometry, and can be considered "design values". If the "design values" are removed as variables from Equation (A-3-36), it can be rewritten as shown in Equation (A-3-37).

$$htc_{l2} = f(\dot{m}_{CC}, p_{CC}, T_{CC}, T_{l2}) \qquad \text{(A-3-37)}$$

Recall that ligament outer (cooling channel side) temperature is already accounted for in Equations (A-3-29) to (A-3-31). Thus, the result shown in Equation (A-3-37) can be substituted into Equations (A-3-29) to (A-3-31), as shown in Equations (A-3-38) to (A-3-40).

$$T_{l1} = f(MR_{TC}, \dot{m}_{CC}, p_{CC}, p_{TC}, T_{CC}, T_{FI}, T_{OI}) \qquad \text{(A-3-38)}$$

$$\Delta T_l = f(MR_{TC}, \dot{m}_{CC}, p_{CC}, p_{TC}, T_{CC}, T_{FI}, T_{OI}) \qquad \text{(A-3-39)}$$

$$\Delta T_w = f(MR_{TC}, \dot{m}_{CC}, p_{CC}, p_{TC}, T_{CC}, T_{FI}, T_{OI}) \qquad \text{(A-3-40)}$$

Appendix B   Engine Subsystem Models

B-1   Fuel Turbopump Model

In this sub-appendix, the development of the analytic model for the FTP is discussed. In all engine operating conditions, LH_2 enters the FTP pump inlet from the fuel inlet as a cryogenic liquid. The volumetric flow rate at the pump inlet (in litres per second) is required for interpolating pump performance charts. The volumetric flow rate can be determined using the mass flow rate of fuel flowing into the pump, and the density of the fuel at the pump inlet. This calculation is shown in Equation (B-1-1).

$$Q_{FP1} = \frac{\dot{m}_{FP1}}{\rho_{FP1}} \times 1,000 \tag{B-1-1}$$

The normalized FTP shaft speed is related to the normalized volumetric flow rate, as shown by the chart in Figure B-1-1. Using the data in Figure B-1-1, a formula relating normalized FTP shaft speed to normalized volumetric flow rate has been determined through linear regression, as shown in Equation (B-1-2). The regression curve fits the data well, with $R^2 = 0.99701$.

$$\frac{Q_{FP1}}{Q_{FP1,d}} = 1.6724 \left(\frac{\omega_{FTP}}{\omega_{FTP,d}} \right) - 0.6814 \tag{B-1-2}$$
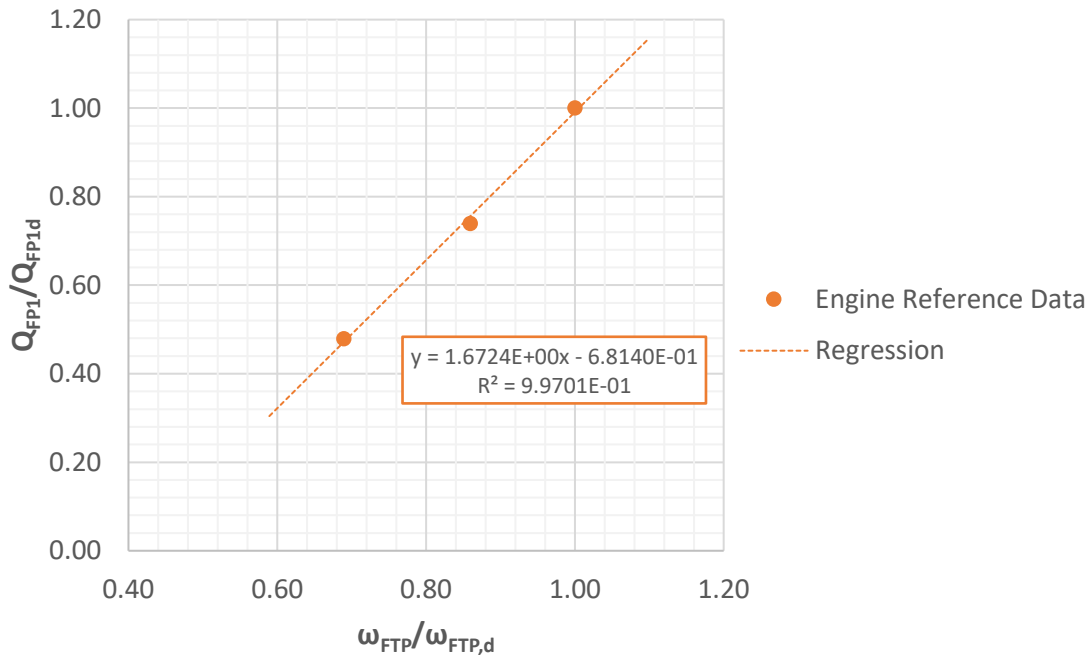

Figure B-1-1: Regression of FTP shaft speed and flow rate

Equation (B-1-2) can be rearranged to give a formula for determining shaft speed based on fuel flow rate. This formula, shown in Equation (B-1-3), is used to determine the shaft speed required to achieve a desired off-design volumetric flow rate. The shaft speed must be either zero or positive, a negative shaft speed is impossible as it would effectively mean running the FTP in reverse. Therefore, the range of this function is all positive and zero values of shaft speed. This is also shown in Equation (B-1-3).

$$\frac{\omega_{FTP}}{\omega_{FTP,d}} = 0.5979 \left[\left(\frac{Q_{FP1}}{Q_{FP1,d}} \right) + 0.6814 \right] \tag{B-1-3}$$

$$(\omega_{FTP} \geq 0)$$

The FTP seal system permits a small amount of leakage from the high-pressure fluid in the pump into the low-pressure gas in the turbine. Engine reference data at three different thrust levels (40%, 70% and 100%) was used to plot the relationship between leakage rate (normalized by fuel mass flow rate), normalized pump inlet volumetric flow rate and normalized pump speed. The resulting chart is shown in Figure B-1-2. A linear regression of the data in Figure B-1-2 has been performed. This regression does not fit the data particularly well, but this is not a significant issue due to the low net flow rates involved. This formula has been adopted to model FTP pump leakage, as shown in Equation (B-1-4). The leakage rate must be either zero or positive, as a negative leakage rate (i.e. fluid "backflowing" from the turbine into the pump) is impossible due to the pressure difference. Therefore, the range of this function is all positive and zero values of leakage rate, as shown in Equation (B-1-4).
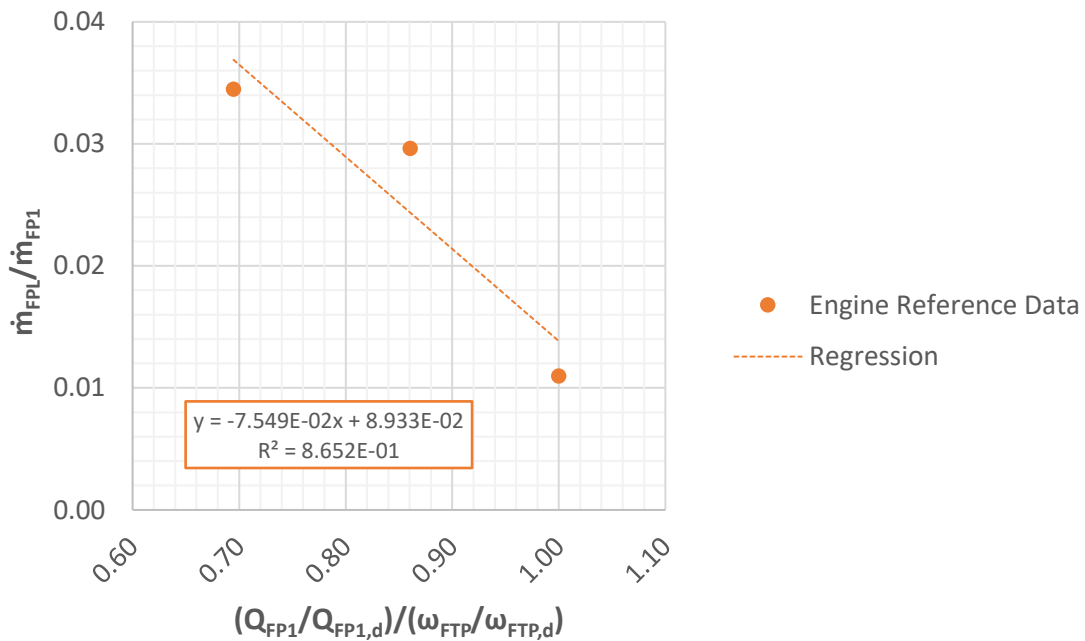
Figure B-1-2: FTP performance – pump leakage rate

$$\frac{\dot{m}_{FPL}}{\dot{m}_{FP1}} = -0.07549 \times \left(\frac{\left(\frac{Q_{FP1}}{Q_{FP1,d}} \right)}{\left(\frac{\omega_{FTP}}{\omega_{FTP,d}} \right)} \right) + 0.08933 \tag{B-1-4}$$

$$(\dot{m}_{FPL} \geq 0)$$

Given that the leaking fuel flows from the pump into the turbine, the leakage rate can be used to estimate the mass flow rate at both the pump and turbine discharge, as shown in Equations (B-1-5) and (B-1-6).

$$\dot{m}_{FP2} = \dot{m}_{FP1} - \dot{m}_{FPL} \tag{B-1-5}$$

$$\dot{m}_{FT2} = \dot{m}_{FT1} + \dot{m}_{FPL} \tag{B-1-6}$$

The FTP pump head increase is related to the normalized volumetric flow rate and normalized shaft speed as shown in Figure B-1-3. A second-order polynomial regression of the reference data has been performed, and the resulting trendline fits the data reasonably well ($R^2 = 0.7620$). This formula has been adopted to model FTP pump head, as shown in Equation (B-1-7). The pump head must be either zero or positive, a negative pump head is impossible as it would effectively mean the pump is depressurizing the fuel. Therefore, the range of this function is all positive and zero values of pump head. This is also shown in Equation (B-1-7).
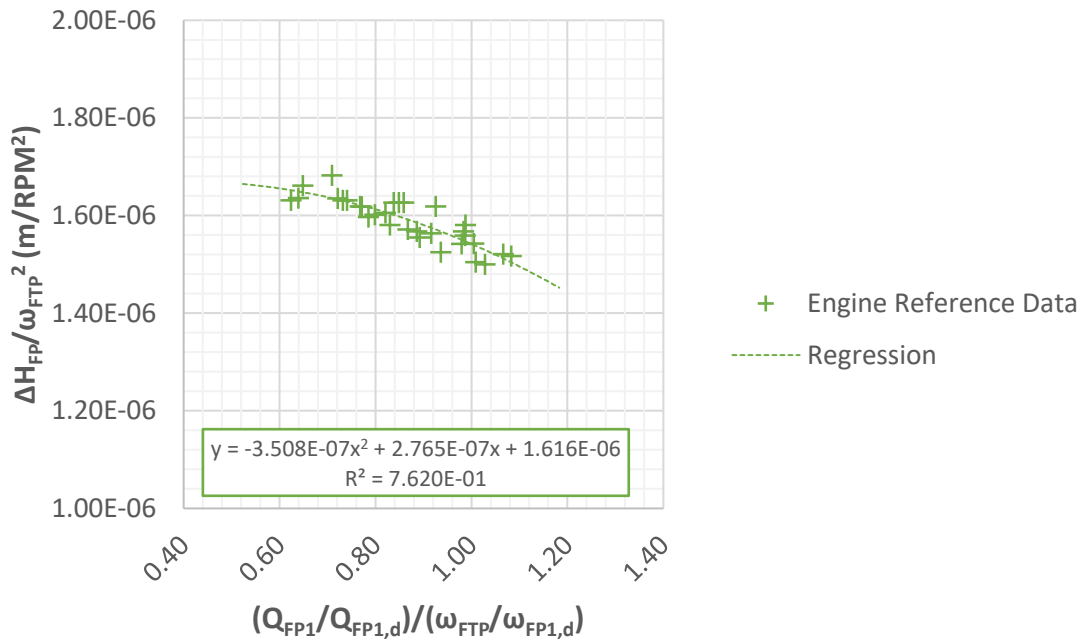

Figure B-1-3: Regression of FTP pump head data

$$\frac{\Delta H_{FP}}{\omega_{FTP}{}^2} = -(3.508 \times 10^{-7}) \times \left(\frac{\left(\frac{Q_{FP1}}{Q_{FP1,d}}\right)}{\left(\frac{\omega_{FTP}}{\omega_{FTP,d}}\right)}\right)^2 + (2.765 \times 10^{-7}) \times \left(\frac{\left(\frac{Q_{FP1}}{Q_{FP1,d}}\right)}{\left(\frac{\omega_{FTP}}{\omega_{FTP,d}}\right)}\right) \quad \text{(B-1-7)}$$

$$+ (1.616 \times 10^{-6})$$

$$(\Delta H_{FP} \geq 0)$$

Assuming an incompressible fluid, the pump head can be used to calculate the increase in LH$_2$ pressure from the pump inlet to the pump discharge, and subsequently the pump discharge pressure, as shown in Equation (B-1-8).

$$p_{FP2} = p_{FP1} + (\rho_{FP1} \times g \times \Delta H_{FP}) \quad \text{(B-1-8)}$$

Equation (B-1-8) provides one of two state quantities (pressure) required to fully define the properties of LH$_2$ at the pump discharge. The second quantity (specific enthalpy) can be determined using isentropic efficiency. The isentropic efficiency of the fuel pump can be defined as shown in Equation (B-1-9), accounting for the difference in inlet and discharge flow rates due to leakage. This formula can be rearranged to make the pump discharge specific enthalpy the subject of the equation, as shown.

$$\eta_{FP,s} = \frac{\dot{m}_{FP2}h_{FP2,s} - \dot{m}_{FP1}h_{FP1}}{\dot{m}_{FP2}h_{FP2} - \dot{m}_{FP1}h_{FP1}}$$

$$\Rightarrow \quad h_{FP2} = \frac{\dot{m}_{FP2}h_{FP2,s} - \dot{m}_{FP1}h_{FP1}}{\dot{m}_{FP2}\eta_{FP,s}} + \frac{\dot{m}_{FP1}h_{FP1}}{\dot{m}_{FP2}} \quad \text{(B-1-9)}$$

The pump inlet specific enthalpy (h_{FP1}) can be interpolated from hydrogen property tables based on the inlet conditions. In the isentropic case, pump discharge specific entropy is equal to pump inlet specific entropy by definition, as shown in Equation (B-1-10).

$$s_{FP2,s} = s_{FP1} \quad \text{(B-1-10)}$$

Using the pump discharge pressure calculated in Equation (B-1-8) and the isentropic discharge specific entropy from Equation (B-1-10), the pump discharge properties for the isentropic case can be determined by interpolation of hydrogen property tables, as described in Subsection 4.3.2. Specifically, pump discharge pressure and isentropic discharge specific entropy can be used to determine isentropic pump discharge temperature ($T_{FP2,s}$). Then pump discharge pressure and isentropic pump discharge temperature can be used to determine isentropic discharge specific enthalpy ($h_{FP2,s}$).

Finally, the only unknown required to solve Equation (B-1-9) is pump isentropic efficiency. However, a chart of pump isentropic efficiency at three different thrust levels (40%, 70% and 100%) is shown in Figure B-1-4. A linear trendline has been fitted to the data, and it fits the data accurately ($R^2 = 0.9773$). The formula for this trendline has been adopted to model the relationship between normalized pump inlet volumetric flow rate, normalized shaft speed and isentropic efficiency, as shown in Equation (B-1-4). Isentropic efficiency must have a value between zero and one. Therefore, the range of this function is all values of isentropic efficiency between zero and one. This is also shown in Equation (B-1-4).
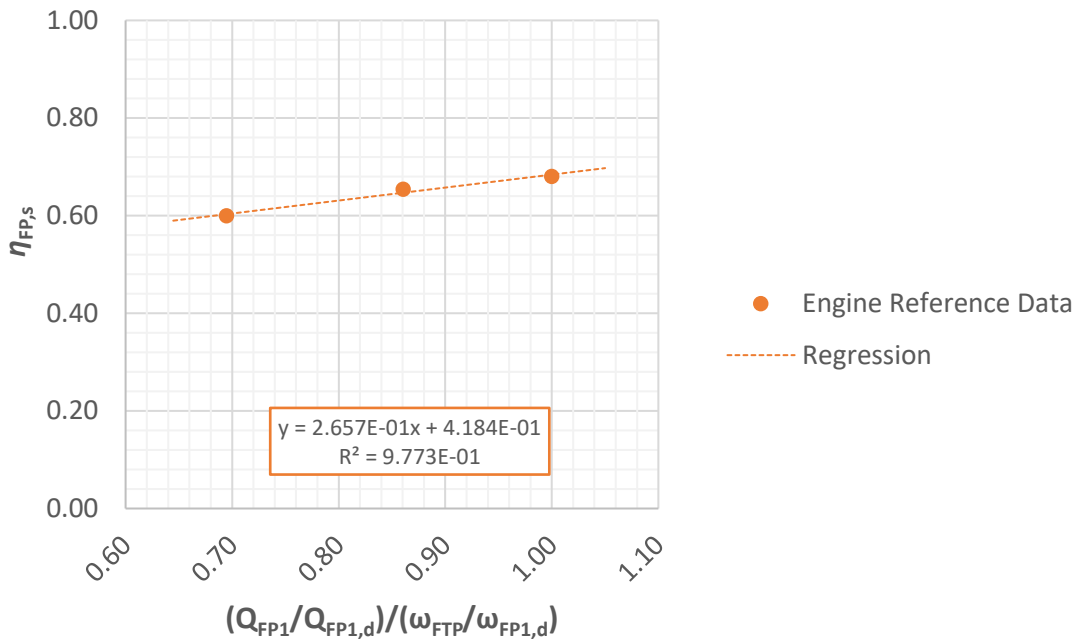
Figure B-1-4: Regression of FTP pump isentropic efficiency data

$$\eta_{FP,s} = 0.2657 \times \left(\frac{\left(\frac{Q_{FP1}}{Q_{FP1,d}} \right)}{\left(\frac{\omega_{FTP}}{\omega_{FTP,d}} \right)} \right) + 0.4184 \tag{B-1-11}$$

$$\left(1 \geq \eta_{FP,s} \geq 0 \right)$$

Substituting in the result of Equation (B-1-4), pump discharge specific enthalpy can be determined using Equation (B-1-9). With two state quantities defined at the pump discharge, other properties at this point can be determined through interpolation of hydrogen property tables, as described in Subsection 4.3.2. This process can be used to determine pump discharge temperature (T_{FP2}).

In order to determine the level of turbine power output required to achieve the fuel pressurization and flow rates described above, it is necessary to estimate how much power is

transmitted from the turbine working fluid to the fuel flowing through the pump. Overall turbopump efficiency is affected by many variables. For the purposes of this model, overall FTP efficiency is defined as the useful work input into the fuel through the pump (i.e. the isentropic pressure increase) divided by the total energy removed from the turbine working fluid. This is shown in Equation (B-1-12). This formula can be rearranged to make turbine energy removal the subject, as shown.

$$\eta_{FTP} = \frac{\dot{m}_{FP1} g \Delta H_{FP}}{\dot{m}_{FT1} h_{FT1} - \dot{m}_{FT2} h_{FT2}}$$

$$\Rightarrow \qquad \dot{m}_{FT1} h_{FT1} - \dot{m}_{FT2} h_{FT2} = \frac{\dot{m}_{FP1} g \Delta H_{FP}}{\eta_{FTP}} \qquad \text{(B-1-12)}$$

Equation (B-1-12) is used as a decision gate for iteratively solving the FTP model, as it can be used ensure that turbine input power and pump output power are balanced. With the exception of overall FTP efficiency (η_{FTP}), the terms on the right-hand side of Equation (B-1-12) are either model inputs or can be determined using methods outlined above. The mass flow rate at the turbine inlet ($\dot{m}_{FT1}$) is also an input into the FTP model from the TCV model. The turbine inlet specific enthalpy (h_{FT1}) can be determined by interpolation of hydrogen property tables using turbine inlet temperature (T_{FT1}) and pressure (p_{FT1}), as described in Subsection 4.3.2. Thus, methods are required to determine overall FTP efficiency, and turbine discharge specific enthalpy (h_{FT2}).

The relationship between overall FTP efficiency and turbine speed ratio is depicted in Figure B-1-5 based on engine reference data at three different thrust levels (40%, 70% and 100%). A linear regression of the data is also shown in Figure B-1-5. The trendline fits the data well ($R^2 = 0.9974$).

Figure B-1-5: Regression of overall FTP efficiency data

The formula for the trendline in Figure B-1-5 has been adopted to model overall FTP efficiency, as shown in Equation (B-1-13). Efficiency must have a value between zero and one. Therefore, the range of this function is all values of efficiency between zero and one. This is also shown in Equation (B-1-13).
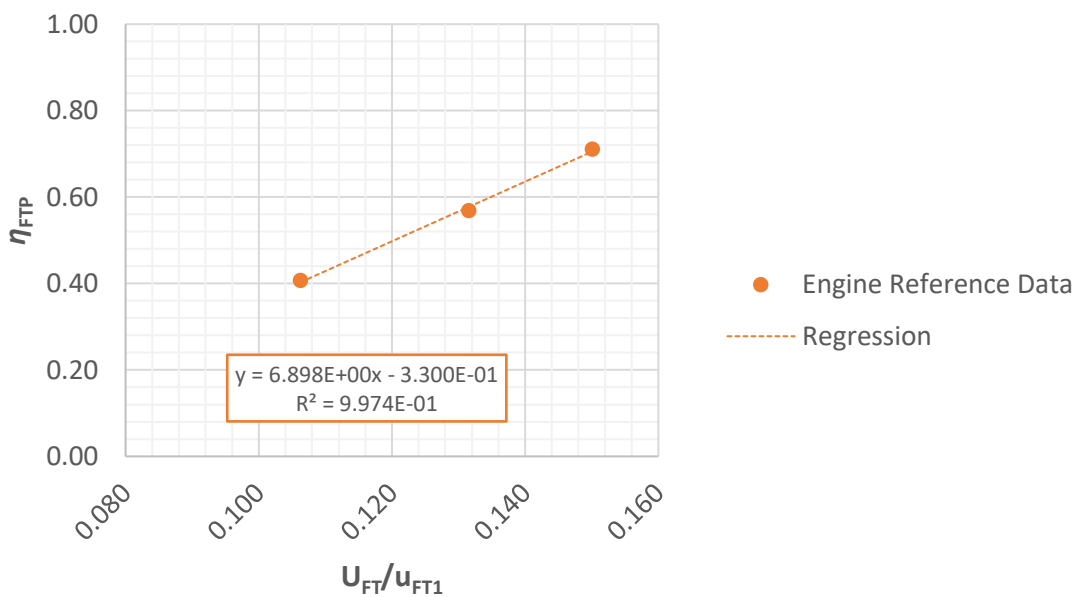
$$\eta_{FTP} = 6.898 \times \left(\frac{U_{FT}}{u_{FT1}}\right) - 0.3300 \tag{B-1-13}$$

$$(1 \geq \eta_{FTP} \geq 0)$$

To solve Equation (B-1-13), turbine speed ratio is required. Turbine speed ratio is defined as turbine tip speed divided by inlet flow velocity for the FTP turbine. Tip speed can be calculated as shown in Equation (B-1-14), while average inlet flow velocity can be calculated as shown in Equation (B-1-15).

$$U_{FT} = r_{FT} \left(\omega_{FTP} \times \frac{2\pi}{60}\right) \tag{B-1-14}$$

$$u_{FT1,avg} = \frac{Q_{FT1} \div 1,000}{A_{FT1}} = \frac{\dot{m}_{FT}}{\rho_{FT1} A_{FT1}} \tag{B-1-15}$$

In order to allow the FTP model to be scalable, it is necessary that the turbine inlet area, and by extension the inlet velocity, also be scalable. Thus, it has been determined that the simplest way to approximate the scaling of the turbine inlet area is to use design pump inlet volumetric flow rate as a scaling variable. This is shown in Equation (B-1-16).

$$A_{FT1} = \left(\frac{Q_{FP1}}{Q_{FP1,d}}\right) \times A_{FT1,d} \tag{B-1-16}$$

Like the specific enthalpy, the density at the turbine inlet can be calculated based on other properties at the turbine inlet, using interpolation of hydrogen property tables as described in Subsection 4.3.2. To allow for fluid velocity profile development when determining inlet velocity, it is necessary to estimate the ratio between maximum inlet velocity and average inlet velocity. The Reynolds number is an appropriate metric for analysing inlet velocity ratio. The Reynolds number at the inlet can be calculated as shown in Equation (B-1-17). Like density, the viscosity at the turbine inlet can be determined using the property table interpolation methods described in Subsection 4.3.2.

$$Re_{FT1} = \frac{\rho_{FT1} u_{FT1,avg} D_{FT1}}{\mu_{FT1}}$$

$$\Rightarrow \qquad Re_{FT1} = \frac{\rho_{FT1} u_{FT1,avg} \sqrt{\dfrac{4 A_{FT1}}{\pi}}}{\mu_{FT1}} \qquad \text{(B-1-17)}$$

The ratio of maximum turbine inlet velocity to average turbine inlet velocity has been plotted against Reynolds number, as shown in Figure B-1-6. A linear regression of the data has also been performed. The regression trendline fits the data well (R^2 = 0.9944). The formula for the regression trendline has been adopted for estimating maximum inlet velocity based on average inlet velocity for the FTP turbine. This formula is shown in Equation (B-1-18). By definition, the maximum inlet velocity cannot be less than the average inlet velocity. Therefore, the range of this function is all values of inlet velocity ratio greater than one. This is also shown in Equation (B-1-18).
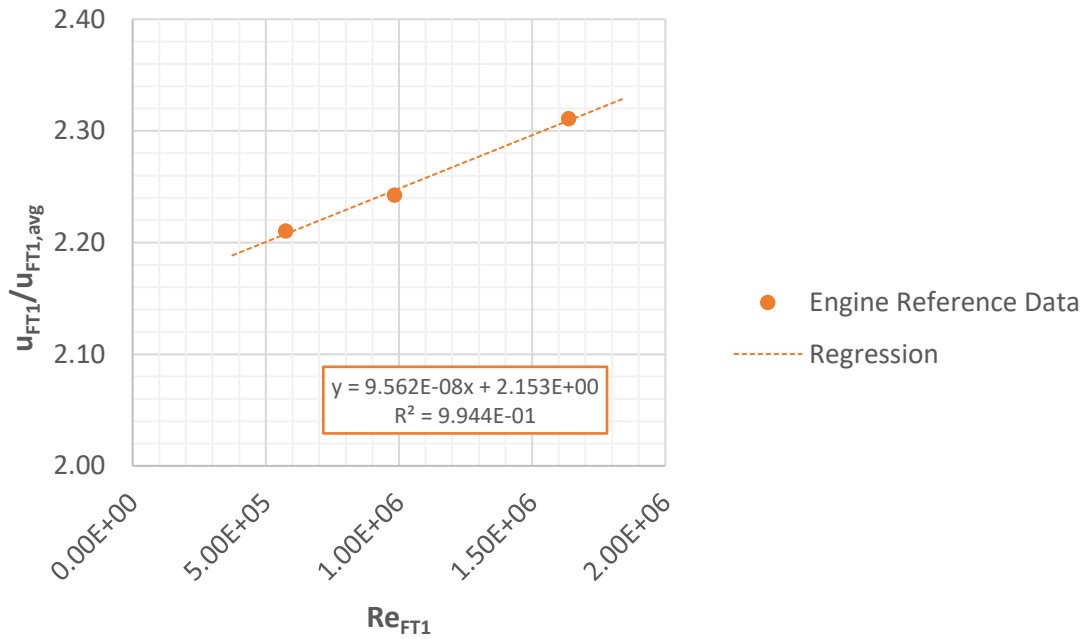
Figure B-1-6: Regression of FTP turbine inlet velocity data

$$\frac{u_{FT1}}{u_{FT1,avg}} = (9.562 \times 10^{-8}) \times Re_{FT1} + 2.153 \qquad \text{(B-1-18)}$$

$$\left(\frac{u_{FT1}}{u_{FT1,avg}} \geq 1 \right)$$

With Equation (B-1-13) establishing a method for determining overall FTP efficiency, the only remaining unknown in Equation (B-1-12) is the turbine discharge specific enthalpy. This property can be determined by estimating the turbine pressure ratio and isentropic efficiency. Turbine pressure ratio

is defined as the ratio of turbine discharge pressure to turbine inlet pressure. Figure B-1-7 shows FTP turbine pressure ratio at three different thrust levels (40%, 70% and 100%). A linear regression of the data has also been performed. The regression trendline fits the data well ($R^2 = 0.9229$). The formula for this trendline has been adopted to model the relationship between FTP turbine speed ratio and pressure ratio, as shown in Equation (B-1-19). In practice, the pressure ratio must be less than one as pressure is always reduced as the turbine extracts work from the fluid. Additionally, the pressure ratio must be greater than or equal to zero because both inlet and discharge pressures are absolute and therefore cannot be negative. Thus, the range of this function is all values of pressure ratio between zero and one. This is also shown in Equation (B-1-19).
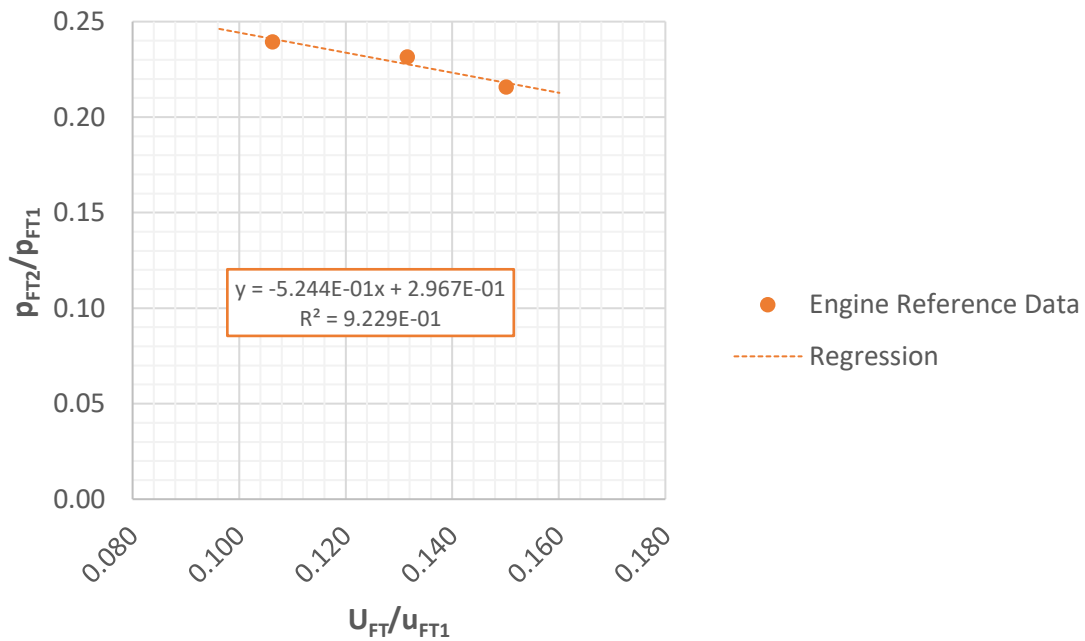
Figure B-1-7: Regression of FTP turbine pressure ratio data

$$\frac{p_{FT2}}{p_{FT1}} = -0.5244 \times \left(\frac{U_{FT1}}{u_{FT}}\right) + 0.2967 \tag{B-1-19}$$

$$\left(1 \geq \frac{p_{FT2}}{p_{FT1}} \geq 0\right)$$

The turbine inlet specific entropy (s_{FT1}) can be determined by interpolation of hydrogen property tables using turbine inlet temperature and pressure, as described in Subsection 4.3.2. In the isentropic case, turbine discharge specific entropy is equal to turbine inlet specific entropy by definition, as shown in Equation (B-1-20).

$$s_{FT2,s} = s_{FT1} \tag{B-1-20}$$

Using the outputs of Equations (B-1-19) and (B-1-20) (specifically turbine discharge pressure and isentropic discharge specific entropy), the isentropic turbine discharge temperature ($T_{FT2,s}$) can be determined by interpolation of the hydrogen property data tables. This value can in turn be used with the turbine discharge pressure to interpolate the hydrogen property tables to determine isentropic turbine discharge specific enthalpy ($h_{FT2,s}$). The isentropic efficiency of the FTP turbine is defined as shown in Equation (B-1-21). Note that total specific enthalpy at turbine discharge includes not only the flow from the turbine, but the leakage flow from the pump, which is combined with the turbine discharge flow at this point. This formula can be rearranged to make turbine discharge specific enthalpy the subject of the equation, as shown.

$$\eta_{FT,s} = \frac{\dot{m}_{FT1}h_{FT1} - \dot{m}_{FT2}h_{FT2}}{\dot{m}_{FT1}h_{FT1} - \left(\dot{m}_{FT1}h_{FT2,s} + \dot{m}_{FPL}h_{FP2}\right)}$$

$$\Rightarrow \qquad h_{FT2} = \frac{\dot{m}_{FT1}h_{FT1} - \eta_{FT,s}\left[\dot{m}_{FT1}h_{FT1} - \left(\dot{m}_{FT1}h_{FT2,s} + \dot{m}_{FPL}h_{FP2}\right)\right]}{\dot{m}_{FT2}} \qquad \text{(B-1-21)}$$

In order to solve Equation (B-1-21), an expression for turbine isentropic efficiency is required. The relationship between turbine efficiency and speed ratio at three different thrust levels (100%, 70% and 40%) is depicted in Figure B-1-8. A second-order polynomial regression of this data has also been performed. As there is only 3 data points, the trendline fits the data perfectly ($R^2 = 1.000$). The formula for this trendline has been adopted to model the relationship between FTP turbine speed ratio and isentropic efficiency, as shown in Equation (B-1-22).

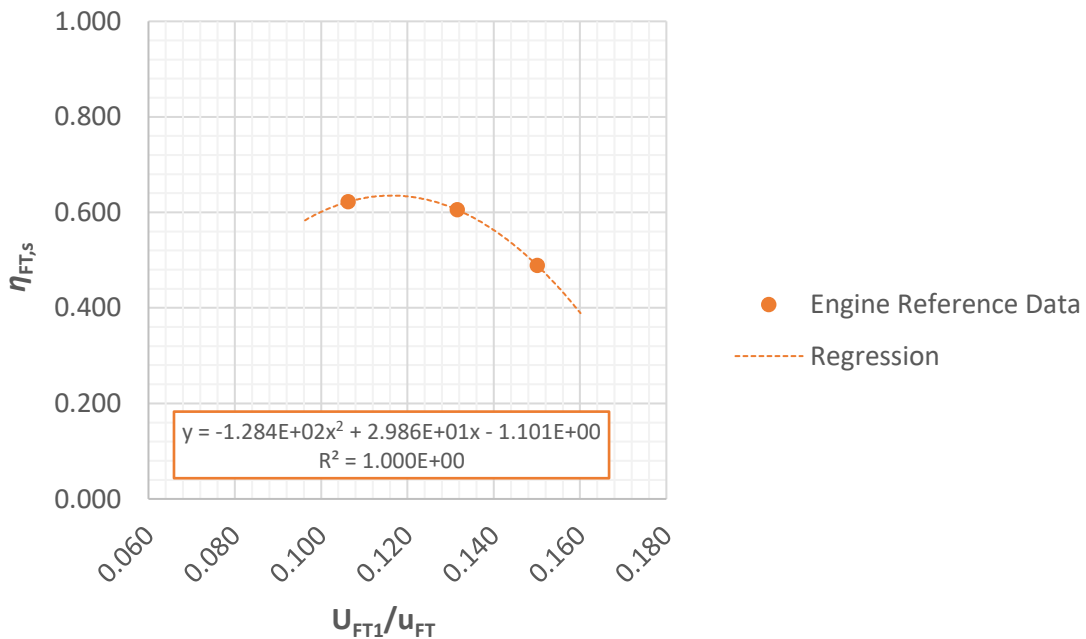$$y = -1.284\text{E}+02x^2 + 2.986\text{E}+01x - 1.101\text{E}+00$$
$$R^2 = 1.000\text{E}+00$$

Figure B-1-8: Regression of FTP turbine efficiency data

$$\eta_{FT,s} = -128.4 \times \left(\frac{U_{FT1}}{u_{FT}}\right)^2 + 29.86 \times \left(\frac{U_{FT1}}{u_{FT}}\right) - 1.101 \qquad \text{(B-1-22)}$$

$$\left(1 \geq \eta_{FT,s} \geq 0\right)$$

The result of Equation (B-1-22) (turbine isentropic efficiency) feeds into Equation (B-1-21) such that turbine discharge specific enthalpy can be determined. This value in turn feeds into Equation (B-1-12), such that the power balance between the turbine and pump is fully defined. Turbine discharge specific enthalpy can also be used with turbine discharge pressure to interpolate hydrogen property data tables and determine discharge temperature, as described in Subsection 4.3.2. Equations (B-1-1) to (B-1-22) provide a full set of formulas required to establish an analytic model of the FTP.

B-2 Oxidizer Turbopump Model

In this sub-appendix, the development of the analytic model for the OTP is described. The volumetric flow rate at the pump inlet (in litres per second) is required for interpolating pump performance charts. The volumetric flow rate can be determined using the mass flow rate of oxidizer flowing through the pump, and the density of the oxidizer at the pump inlet. This calculation is shown in Equation (B-2-1). Note that, unlike the FTP, there is no leakage between the pump and turbine for the OTP. Thus, pump inlet mass flow is equal to discharge mass flow.

$$Q_{OP1} = \frac{\dot{m}_{OP}}{\rho_{OP1}} \times 1{,}000 \qquad \text{(B-2-1)}$$

Figure B-2-1 shows how the normalized OTP shaft speed is related to the normalized pump volumetric flow rate divided by normalized shaft speed at three different thrust levels (100%, 70% and 40%). A linear regression of the data has also been performed. The regression trendline fits the data well ($R^2 = 0.99762$). The formula for this trendline has been adopted to model the relationship between OTP shaft speed and pump volumetric flow rate, as shown in Equation (B-2-2).

$$\frac{\left(\frac{Q_{OP1}}{Q_{OP1,d}}\right)}{\left(\frac{\omega_{OTP}}{\omega_{OTP,d}}\right)} = 0.26173 \left(\frac{\omega_{OTP}}{\omega_{OTP,d}}\right) + 0.74001 \qquad \text{(B-2-2)}$$
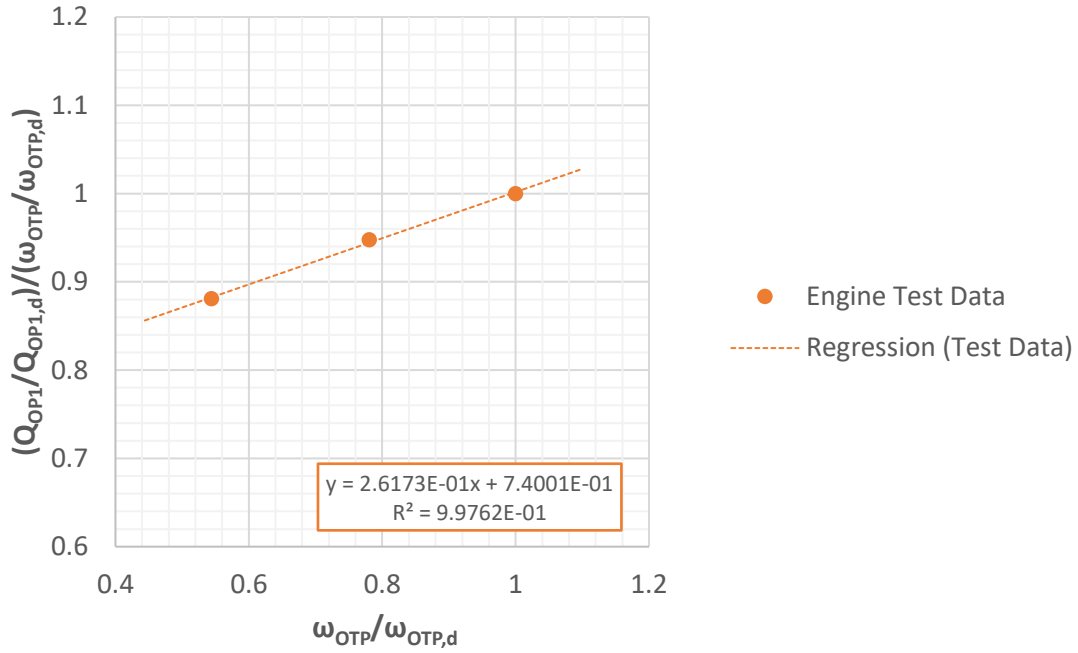
Figure B-2-1: Regression of OTP shaft speed and flow rate

Equation (B-2-2) can be rearranged using the quadratic equation to give a formula for determining shaft speed based on oxidizer flow rate. This formula, shown in Equation (B-2-3), is useful for determining the shaft speed required to achieve a desired off-design volumetric flow rate. The shaft speed must be either zero or positive, a negative shaft speed is impossible as it would effectively mean running the OTP in reverse. Therefore, the range of this function is all positive and zero values of shaft speed. This is also shown in Equation (B-2-3).

$$\frac{\left(\dfrac{Q_{OP1}}{Q_{OP1,d}}\right)}{\left(\dfrac{\omega_{OTP}}{\omega_{OTP,d}}\right)} = 0.26173 \left(\frac{\omega_{OTP}}{\omega_{OTP,d}}\right) + 0.74001$$

$$\Rightarrow \qquad 0 = 0.26173 \left(\frac{\omega_{OTP}}{\omega_{OTP,d}}\right)^2 + 0.74001 \left(\frac{\omega_{OTP}}{\omega_{OTP,d}}\right) - \left(\frac{Q_{OP1}}{Q_{OP1,d}}\right)$$

$$\Rightarrow \qquad \frac{\omega_{OTP}}{\omega_{OTP,d}} = \frac{-0.74001 \pm \sqrt{(0.74001)^2 - 4 \times (0.26173) \times \left(\dfrac{Q_{OP1}}{Q_{OP1,d}}\right)}}{2 \times 0.26173}$$

$$\Rightarrow \qquad \frac{\omega_{OTP}}{\omega_{OTP,d}} = \frac{-0.74001 + \sqrt{0.54761 + 1.04692 \left(\dfrac{Q_{OP1}}{Q_{OP1d}}\right)}}{0.52346} \qquad \text{(B-2-3)}$$

$$\left(\frac{\omega_{OTP}}{\omega_{OTP,d}} \geq 0\right)$$

The OTP pump head increase is related to the normalized volumetric flow rate and normalized shaft speed as shown in Figure B-2-2. A second-order polynomial regression of the reference data has been performed, and the resulting trendline fits the data well (R^2 = 0.9916). This formula has been adopted to model OTP pump head, as shown in Equation (B-2-4). The pump head must be either zero or positive – a negative pump head is impossible as it would effectively mean the pump is depressurizing the oxidizer. Therefore, the range of this function is all positive and zero values of pump head. This is also shown in Equation (B-2-4).
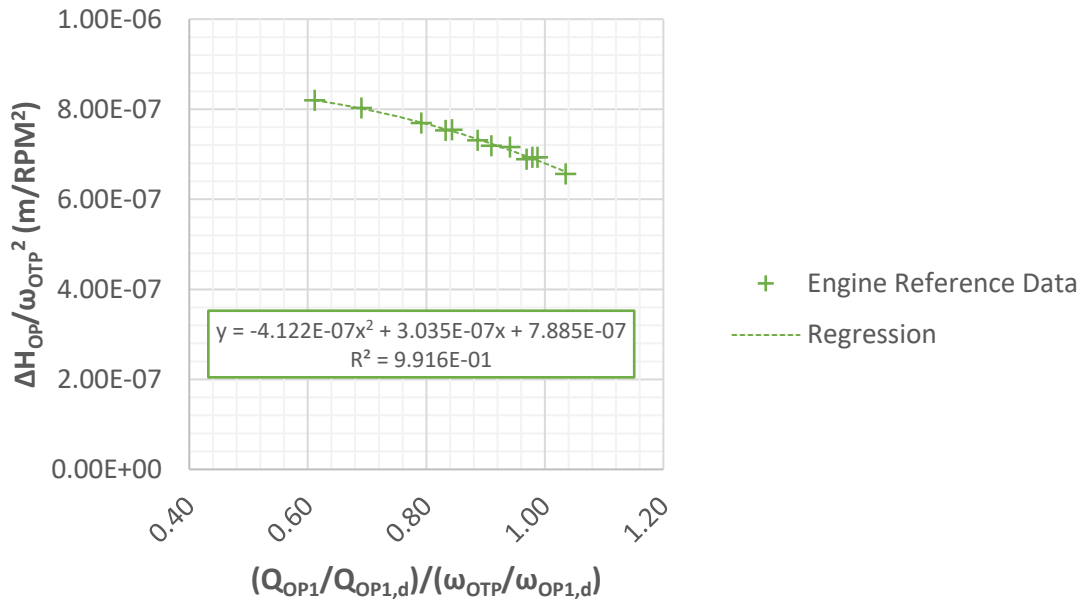

Figure B-2-2: Regression of OTP pump head data

$$\frac{\Delta H_{OP}}{\omega_{OTP}{}^2} = -(4.122 \times 10^{-7}) \times \left(\frac{\left(\frac{Q_{OP1}}{Q_{OP1,d}}\right)}{\left(\frac{\omega_{OTP}}{\omega_{OTP,d}}\right)}\right)^2 + (3.035 \times 10^{-7}) \times \left(\frac{\left(\frac{Q_{OP1}}{Q_{OP1,d}}\right)}{\left(\frac{\omega_{OTP}}{\omega_{OTP,d}}\right)}\right) \quad \text{(B-2-4)}$$
$$+ (7.885 \times 10^{-7})$$
$$(\Delta H_{OP} \geq 0)$$

Assuming that the LO_2 is an incompressible fluid, the pump head can be used to calculate the increase in LO_2 pressure from the pump inlet to the pump discharge, and subsequently the pump discharge pressure, as shown in Equation (B-2-5).

$$p_{OP2} = p_{OP1} + (\rho_{OP1} \times g \times \Delta H_{OP}) \quad \text{(B-2-5)}$$

Equation (B-2-5) provides one of two state quantities (pressure) required to fully define the state of the LO_2 at the pump discharge. The second quantity (specific enthalpy) can be determined using isentropic efficiency. The isentropic efficiency of the oxidizer pump is defined as shown in

Equation (B-2-6). This formula can be rearranged to make the pump discharge specific enthalpy the subject of the equation, as shown.

$$\eta_{OP,s} = \frac{h_{OP2,s} - h_{OP1}}{h_{OP2} - h_{OP1}}$$

$$\Rightarrow \qquad h_{OP2} = \frac{h_{OP2,s} - h_{OP1}}{\eta_{OP,s}} + h_{OP1} \qquad\qquad \text{(B-2-6)}$$

In the isentropic case, pump discharge specific entropy is equal to pump inlet specific entropy by definition, as shown in Equation (B-2-7).

$$\Rightarrow \qquad s_{OP2s} = s_{OP1} \qquad\qquad \text{(B-2-7)}$$

Using the pump discharge pressure calculated in Equation (B-2-5) and the isentropic discharge specific entropy from Equation (B-2-7), the pump discharge properties for the isentropic case can be determined by interpolation of oxygen property tables, as described in Subsection 4.3.2. Specifically, pump discharge pressure and isentropic discharge specific entropy can be used to determine isentropic pump discharge temperature ($T_{OP2,s}$). Then pump discharge pressure and isentropic pump discharge temperature can then be used to determine isentropic discharge specific enthalpy ($h_{OP2,s}$).

Finally, the only unknown required to solve Equation (B-2-6) is pump isentropic efficiency. The relationship between the pump isentropic efficiency, normalized volumetric flow rate and normalized shaft speed at three different thrust levels (40%, 70% and 100%) is shown in Figure B-2-3.
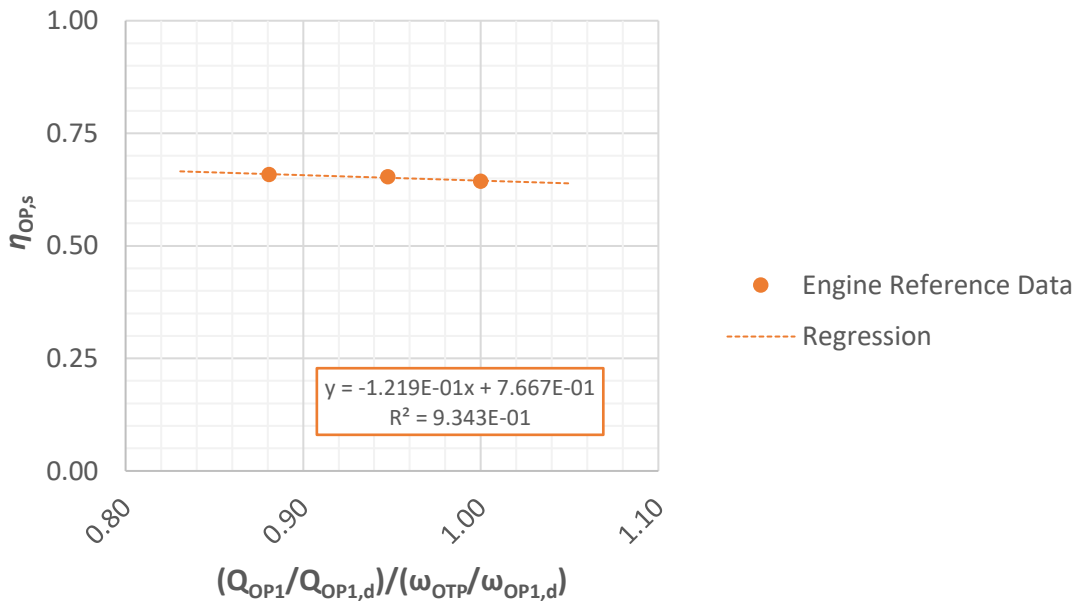

Figure B-2-3: Regression of OTP pump isentropic efficiency data

A linear regression of the data in Figure B-2-3 has also been performed. The regression trendline fits the data well ($R^2 = 0.9343$). The formula for this trendline has been adopted to model the relationship between OTP shaft speed, pump volumetric flow rate, and pump isentropic efficiency, as shown in Equation (B-2-8).

$$\eta_{OP,s} = -0.1219 \times \left(\frac{\left(\frac{Q_{OP1}}{Q_{OP1,d}} \right)}{\left(\frac{\omega_{OTP}}{\omega_{OTP,d}} \right)} \right) + 0.7667 \tag{B-2-8}$$

$$\left(1 \geq \eta_{OP,s} \geq 0 \right)$$

Substituting in the result of Equation (B-2-8), pump discharge specific enthalpy can be determined using Equation (B-2-6). With two state quantities defined at the pump discharge, other properties at this point can be determined through interpolation of oxygen property tables, as described in Subsection 4.3.2. This process can be used to determine pump discharge temperature (T_{OP2}).

In order to determine the level of turbine power output required to achieve the oxidizer pressurization and flow rates described above, it is necessary to estimate how much power is transmitted from the turbine working fluid to the oxidizer flowing through the pump. Overall turbopump efficiency is affected by many variables, including turbine speed ratio (defined as inlet flow velocity divided by turbine blade tip speed), the ratio of pump flow rate to design pump flow rate, seal leakage, turbine pressure ratio, shaft speed and turbine temperature. For the purposes of this model, overall OTP efficiency is defined as the useful work input into the oxidizer through the pump (i.e. the isentropic pressure increase) divided by the total energy removed from the turbine working fluid. This is shown in Equation (B-2-9). This formula can be rearranged to make turbine energy removal the subject, as shown.

$$\eta_{OTP} = \frac{\dot{m}_{OP} g \Delta H_{OP}}{\dot{m}_{OT}(h_{OT1} - h_{OT2})}$$

$$\Rightarrow \qquad \dot{m}_{OT}(h_{OT1} - h_{OT2}) = \frac{\dot{m}_{OP} g \Delta H_{OP}}{\eta_{OTP}} \tag{B-2-9}$$

Equation (B-2-9) is used as a decision gate for iteratively solving the OTP model, as it can be used ensure that turbine input power and pump output power are balanced. With the exception of overall OTP efficiency (η_{OTP}), the terms on the right-hand side of Equation (B-2-9) are either model inputs, or can be determined using methods outlined above. The mass flow rate through the turbine ($\dot{m}_{OT}$) is also an input into the OTP model from the MRCV model. The turbine inlet specific enthalpy

(h_{OT1}) can be determined by interpolation of hydrogen property tables using turbine inlet temperature (T_{OT1}) and pressure (p_{OT1}), as described in Subsection 4.3.2. Thus, methods are required to determine overall OTP efficiency, and turbine discharge specific enthalpy (h_{OT2}).

Figure B-2-4 shows overall OTP efficiency at three different thrust levels (40%, 70% and 100%) as a function of normalized pump flow rate and normalized shaft speed. A linear regression of the results data is also shown in Figure B-2-4. This regression correlates well with the underlying data $(R^2 = 0.9871)$. The formula for this trendline has been adopted to model the relationship between OTP shaft speed, pump volumetric flow rate, and overall OTP efficiency, as shown in Equation (B-2-10).
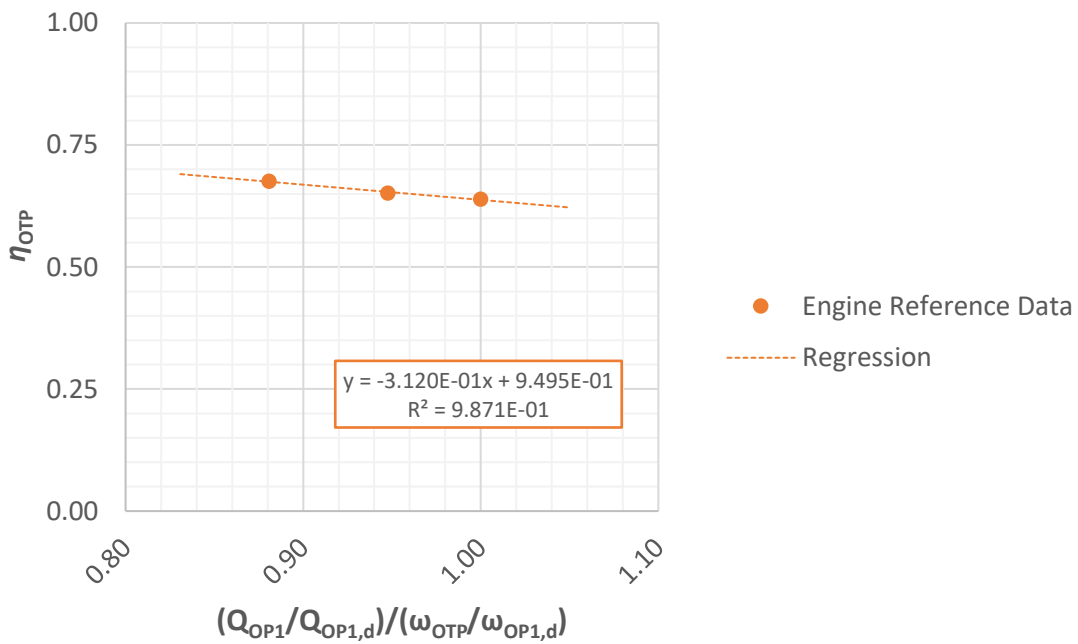

Figure B-2-4: Regression of overall OTP efficiency data

$$\eta_{OTP} = -0.3120 \times \left(\frac{\left(\frac{Q_{OP1}}{Q_{OP1,d}} \right)}{\left(\frac{\omega_{OTP}}{\omega_{OTP,d}} \right)} \right) + 0.9495 \qquad \text{(B-2-10)}$$

$$(1 \geq \eta_{OTP} \geq 0)$$

With Equation (B-2-10) establishing a method for determining overall OTP efficiency, the only remaining unknown in Equation (B-2-9) is the turbine discharge specific enthalpy. This property can be determined by estimating the turbine pressure ratio and isentropic efficiency. When mapping turbine performance parameters such as these, it is common to use the turbine speed ratio (defined as turbine tip speed divided by inlet flow velocity) as a metric, rather than using the flow rate divided by the shaft speed (as was used for calculations involving pump flow). Tip speed can be calculated as

shown in Equation (B-2-11), while average inlet flow velocity can be calculated as shown in Equation (B-2-12).

$$U_{OT} = r_{OT}\left(N_{OTP} \times \frac{2\pi}{60}\right) \tag{B-2-11}$$

$$u_{OT1,avg} = \frac{Q_{OT1} \times 1{,}000}{A_{OT1}} = \frac{\dot{m}_{OT}}{\rho_{OT1}A_{OT1}} \tag{B-2-12}$$

In order to allow the OTP model to be scalable, it is necessary that the turbine inlet area, and by extension the inlet velocity, also be scalable. Thus, it has been determined that the simplest way to approximate the scaling of the turbine inlet area is to use design pump inlet volumetric flow rate as a scaling variable. This is shown in Equation (B-2-13).

$$A_{OT1} = \left(\frac{Q_{OP1}}{Q_{OP1,d}}\right) \times A_{OT1,d} \tag{B-2-13}$$

Like the specific enthalpy, the density at the turbine inlet can be calculated based on other properties at the turbine inlet, using interpolation of oxygen property tables as described in Subsection 4.3.2. To allow for fluid velocity profile development when determining inlet velocity, it is necessary to estimate the ratio between maximum inlet velocity and average inlet velocity. The Reynolds number is an appropriate metric for analysing inlet velocity ratio. The Reynolds number at the inlet can be calculated as shown in Equation (B-2-14). Like density, the viscosity at the turbine inlet can be determined using the property table interpolation methods described in Subsection 4.3.2.

$$Re_{OT1} = \frac{\rho_{OT1}u_{OT1,avg}D_{OT1}}{\mu_{OT1}}$$

$$\Rightarrow \qquad Re_{OT1} = \frac{\rho_{OT1}u_{OT1,avg}\sqrt{\frac{4A_{OT1}}{\pi}}}{\mu_{OT1}} \tag{B-2-14}$$

The ratio of maximum turbine inlet velocity divided by average turbine inlet velocity has been plotted against Reynolds number at three different thrust levels (40%, 70% and 100%), as shown in Figure B-2-5. A linear regression of the data has also been performed, and the data fits the regression well ($R^2 = 0.9902$). The formula for the regression trendline has been adopted for estimating maximum inlet velocity based on average inlet velocity. This formula is shown in Equation (B-2-15). By definition, the maximum inlet velocity cannot be less than the average inlet velocity. Therefore, the range of this function is all values of inlet velocity ratio greater than one. This is also shown in Equation (B-2-15).
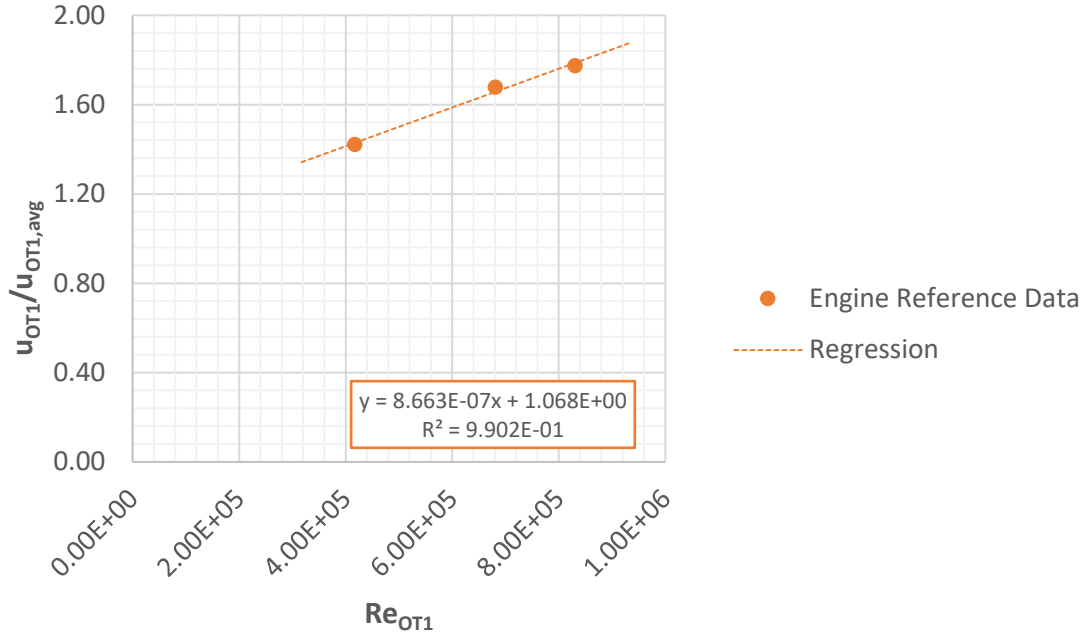
Figure B-2-5: Regression of OTP turbine inlet velocity data

$$\frac{u_{OT1}}{u_{OT1,avg}} = (8.663 \times 10^{-7}) \times Re_{OT1} + 1.068 \tag{B-2-15}$$

$$\left(\frac{C_{OT1}}{C_{OT1,avg}} \geq 1 \right)$$

With a method for accurately estimating turbine speed ratio established, turbine pressure ratio can now be evaluated. Turbine pressure ratio is defined as the ratio of turbine discharge pressure to turbine inlet pressure. It is a measure of the reduction in pressure across the turbine, as pressure work is extracted from the turbine working fluid. A chart of turbine pressure ratio vs. speed ratio is plotted at three different thrust levels (40%, 70% and 100%) in Figure B-2-6. A second-order polynomial trendline has been fitted to the data. As there is only 3 data points, the trendline fits the data perfectly ($R^2 = 1.000$). The formula for this trendline has been adopted to model the relationship between turbine speed ratio and pressure ratio, as shown in Equation (B-2-16). In practice, the pressure ratio must be less than one as pressure is always reduced as the turbine extracts work from the fluid. Additionally, the pressure ratio must be greater than or equal to zero because both inlet and discharge pressures are absolute and therefore cannot be negative. Thus, the range of this function is all values of pressure ratio between zero and one. This is also shown in Equation (B-2-16).
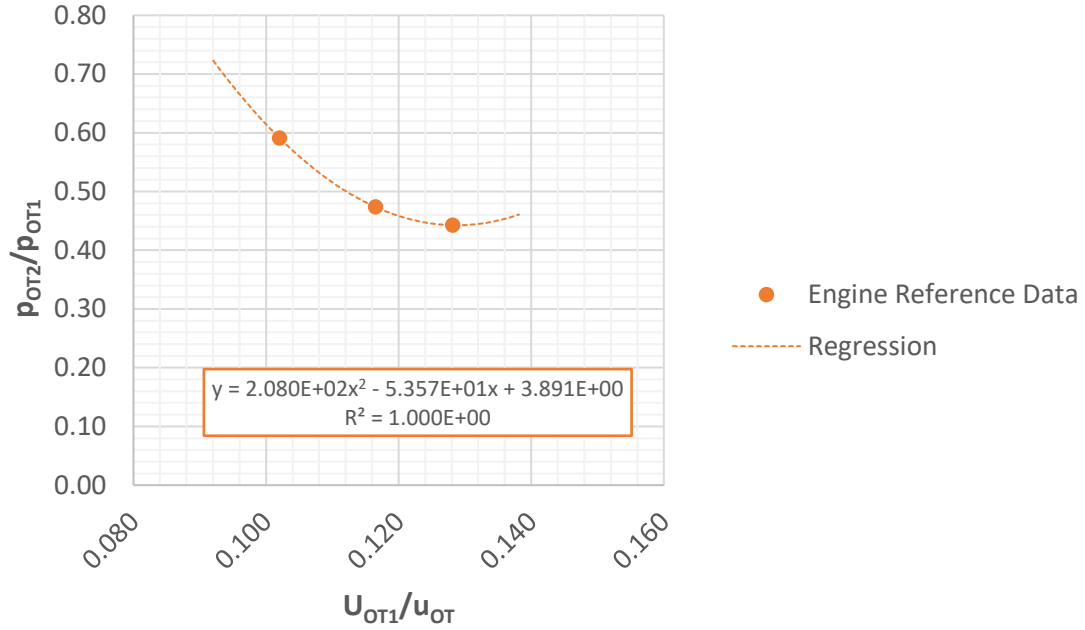
Figure B-2-6: Regression of OTP turbine pressure ratio data

$$\frac{p_{OT2}}{p_{OT1}} = -5.775 \times \left(\frac{U_{OT1}}{u_{OT}}\right) + 1.170 \tag{B-2-16}$$

$$\left(1 \geq \frac{p_{OT2}}{p_{OT1}} \geq 0\right)$$

The turbine inlet specific entropy (s_{OT1}) can be determined by interpolation of hydrogen property tables using turbine inlet temperature and pressure, as described in Subsection 4.3.2. In the isentropic case, turbine discharge specific entropy is equal to turbine inlet specific entropy by definition, as shown in Equation (B-2-17). Using the outputs of Equations (B-2-16) and (B-2-17) (specifically turbine discharge pressure and isentropic discharge specific entropy), the isentropic turbine discharge temperature (T_{OT2s}) can be determined by interpolation of the hydrogen property data tables. This value can in turn be used with the turbine discharge pressure to interpolate the hydrogen property tables to determine isentropic turbine discharge specific enthalpy (hOT2s).

$$s_{OT2s} = s_{OT1} \tag{B-2-17}$$

The isentropic efficiency of the OTP turbine is defined as shown in Equation (B-2-18). This formula can be rearranged to make turbine discharge specific enthalpy the subject of the equation, as shown.

$$\eta_{OT,s} = \frac{h_{OT1} - h_{OT2}}{h_{OT1} - h_{OT2,s}}$$

$$\Rightarrow \qquad h_{OT2} = h_{OT1} - \eta_{OT,s}\left(h_{OT1} - h_{OT2,s}\right) \qquad \text{(B-2-18)}$$

In order to solve Equation (B-2-18), an expression for turbine isentropic efficiency is required. The relationship between turbine efficiency and speed ratio is at three different thrust levels (40%, 70% and 100%) depicted in Figure B-2-7. A second-order polynomial trendline has been fitted to this data. As there is only 3 data points, the trendline fits the data perfectly (R^2 = 1.000). The formula for this trendline has been adopted to model the relationship between turbine speed ratio and pressure ratio, as shown in Equation (B-2-19).
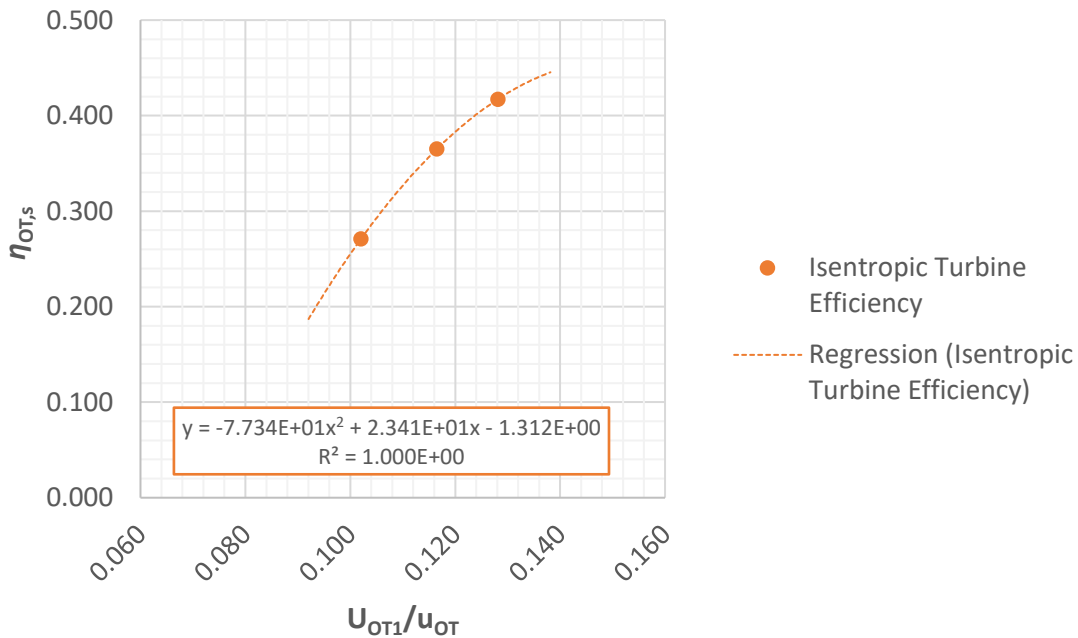

Figure B-2-7: Regression of OTP turbine efficiency data

$$\eta_{OT,s} = -77.34 \times \left(\frac{U_{OT1}}{u_{OT}}\right)^2 + 23.41 \times \left(\frac{U_{OT1}}{u_{OT}}\right) - 1.312 \qquad \text{(B-2-19)}$$

$$\left(1 \geq \eta_{OT,s} \geq 0\right)$$

The result of Equation (B-2-19) (turbine isentropic efficiency) feeds into Equation (B-2-18) such that turbine discharge specific enthalpy can be determined. This value in turn feeds into Equation (B-2-9), such that the power balance between the turbine and pump is fully defined. Turbine discharge specific enthalpy can also be used with turbine discharge pressure to interpolate hydrogen property data tables and determine discharge temperature, as described in Subsection 4.3.2. Equations (B-2-1) to (B-2-19) provide a full set of formulas required to establish an analytic model of the OTP.

B-3 Main Fuel Valve (Throttling) Model

In this sub-appendix, the development of the analytic model for the MFVT is described. This model covers not only the valve itself but surrounding plumbing. Specifically, this model includes one "inlet" (the fuel pump discharge), and two "outlets" (the cooling channel inlet and the liquid inlet to the fuel mixer). Using MFVT bypass flow as a control setting, the fuel properties and flow rates at the two outlets are estimated.

The fuel flowing out of the fuel pump either flows through the MFVT and into the fuel mixer, or bypasses the MFVT and flows into the cooling channels. The ratio of fuel flowing through the MFVT to fuel bypassing the MFVT is controlled by the valve setting. It has been assumed that the MFVT setting can be adjusted to achieved the desired bypass flow rate. With bypass flow (into the cooling channels) as a control variable, and fuel pump discharge flow from the FTP model as an input, the flow through the MVFT (and into the liquid fuel mixer inlet) can be determined using a simple mass balance, as shown in Equation (B-3-1).

$$\dot{m}_{M1L} = \dot{m}_{FP2} - \dot{m}_{CC} \tag{B-3-1}$$

It is assumed that the fuel properties (pressure and temperature) do not exhibit a noticeable change between the fuel pump discharge and the MFVT inlet. Thus, it is assumed that these properties remain constant between these two points. This is shown mathematically in Equations (B-3-2) and (B-3-3).

$$p_{MFVT1} = p_{FP2} \tag{B-3-2}$$
$$T_{MFVT1} = T_{FP2} \tag{B-3-3}$$

From the MFVT inlet to the liquid inlet to the mixer, there is a pressure drop due to either changing pipe cross-section geometry, friction through the valve and in the pipe, or both. Frictional pressure head loss in pipes is correlated with fluid velocity, among other factors. According to the Bernoulli equation, Pressure changes in incompressible fluids is also correlated with velocity changes (if elevation changes are neglected). Velocity is proportional to volumetric flow rate. Thus, there is a correlation between pressure loss and volumetric flow rate which is used to estimate pressure loss across valves and pipes. Volumetric flow rate at the MFVT inlet can be calculated using Equation (B-3-4). The requisite density value in Equation (B-3-4) can be determined by interpolation of hydrogen property tables using the pressure and temperature at the MFVT inlet, as described in Subsection 4.3.2.

$$Q_{MFVT1} = \frac{\dot{m}_{M1L}}{\rho_{MFVT1}} \times 1{,}000 \qquad\qquad (B\text{-}3\text{-}4)$$

Using the concept of "pressure ratio" as discussed in Sub-appendices B-1 and B-2 for modelling the pressure loss across a turbine, the pressure loss across the MFVT and the downstream pipe can be quantified using a similar dimensionless ratio of discharge pressure to inlet pressure. Figure B-3-1 shows the relationship between volumetric flow rate at the MFVT inlet (normalized by the design FTP pump inlet volumetric flow rate) and the pressure ratio through the MFVT and downstream pipe to the liquid inlet of the fuel mixer at three different thrust levels (40%, 70% and 100%). Figure B-3-1 shows that the relationship between MFVT inlet volumetric flow rate and pressure ratio is approximately linear. A linear regression of this data set has been performed, and the resulting trendline is also shown in Figure B-3-1. The trendline matches the data well ($R^2 = 0.9998$), and has therefore been adopted to model the relationship between inlet volumetric flow rate and pressure ratio, as shown in Equation (B-3-1). In practice, the pressure ratio must be less than one as pressure is always reduced as frictional forces act on the fluid. Additionally, the pressure ratio must be greater than or equal to zero because both pressures are absolute and therefore cannot be negative. Thus, the range of this function is all values of pressure ratio between zero and one. This is also shown in Equation (B-3-1).
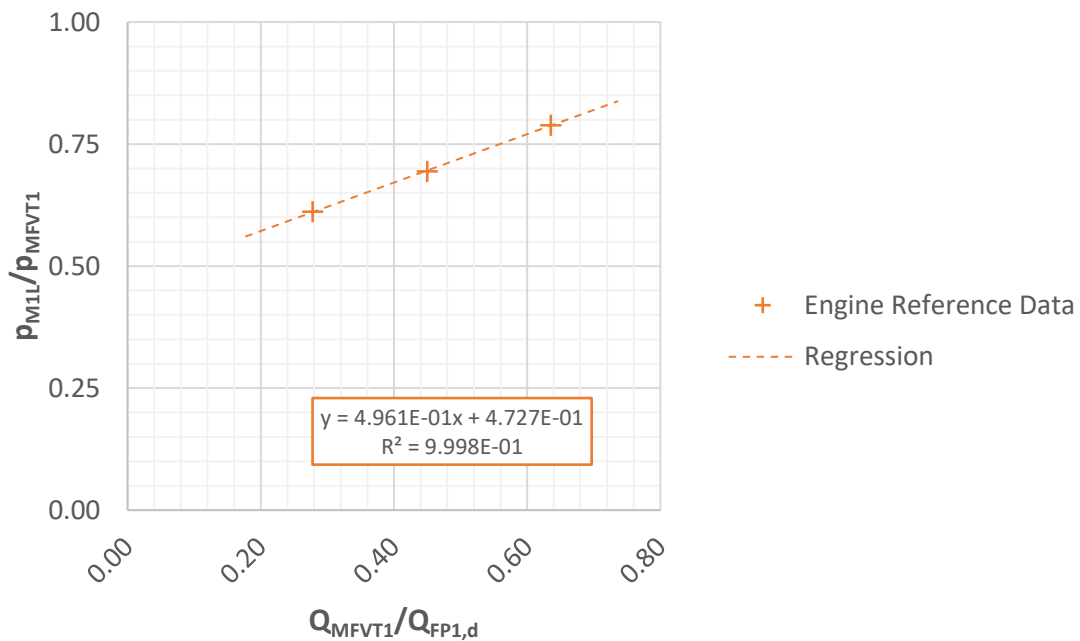

Figure B-3-1: Regression of MFVT pressure ratio

$$\frac{p_{M1L}}{p_{MFVT1}} = 0.4961 \times \left(\frac{Q_{MFVT1}}{Q_{FP1,d}}\right) + 0.4727 \tag{B-3-5}$$

$$\left(1 \geq \frac{p_{M1L}}{p_{MFVT1}} \geq 0\right)$$

Using Equation (B-3-5) to calculate mixer liquid inlet pressure provides one of two state quantities required to fully define the state of the fuel at the liquid inlet of the mixer. Analysis of engine reference data indicates that the change in specific enthalpy is negligible between the MFVT inlet and the mixer liquid inlet. Thus, it has been assumed that specific enthalpy remains constant between the MFVT inlet and the mixer liquid inlet, as shown in Equation (B-3-6). With the specific enthalpy and pressure at the mixer liquid inlet established, the temperature at this point can be determined by interpolation of hydrogen property data tables, as described in Subsection 4.3.2.

$$h_{M1L} = h_{MFVT1} \tag{B-3-6}$$

A similar methodology to that which is described above can be used to estimate the properties of the fuel at the cooling channel inlet. Specifically, a relationship between pressure ratio and volumetric flow rate can be established to estimate cooling channel inlet pressure. Then, fuel pump discharge specific enthalpy can be used to estimate cooling channel inlet specific enthalpy, which can be used with the pressure at this point to interpolate hydrogen property tables to estimate cooling channel inlet temperature. The volumetric flow rate of fuel bypassing the MFVT and flowing into the cooling channels can be determined as shown in Equation (B-3-7).

$$Q_{MFVTB} = \frac{\dot{m}_{CC}}{\rho_{MFVTB}} \times 1{,}000 \tag{B-3-7}$$

In order to solve Equation (53), the density at MFVT bypass is required. For simplicity, it has been assumed that the properties of the fuel flow do not vary between the fuel pump discharge and the MFVT bypass. Thus, temperature and pressure are constant between these points, as shown in Equation (B-3-8) and (B-3-9). Using these properties, density at the MFVT bypass can be determined by interpolation of hydrogen property data tables, as described in Subsection 4.3.2.

$$p_{MFVTB} = p_{FP2} \tag{B-3-8}$$
$$T_{MFVTB} = T_{FP2} \tag{B-3-9}$$

Figure B-3-2 shows a chart of volumetric flow rate at the MFVT bypass (normalized by the design FTP pump inlet volumetric flow rate) against the pressure ratio between this point and the

cooling channel inlet at three different thrust levels (40%, 70% and 100%). Figure B-3-2 shows that the relationship between MFVT bypass volumetric flow rate and pressure ratio is approximately linear. A linear regression of this data set has been performed, and the resulting trendline is also shown in Figure B-3-2. The trendline matches the data well ($R^2 = 0.9989$) and has therefore been adopted to model the relationship between MFVT bypass volumetric flow rate and pressure ratio, as shown in Equation (B-3-10). In practice, the pressure ratio must be less than one as pressure is always reduced as frictional forces act on the fluid. Additionally, the pressure ratio must be greater than or equal to zero because both pressures are absolute and therefore cannot be negative. Thus, the range of this function is all values of pressure ratio between zero and one. This is also shown in Equation (B-3-10).
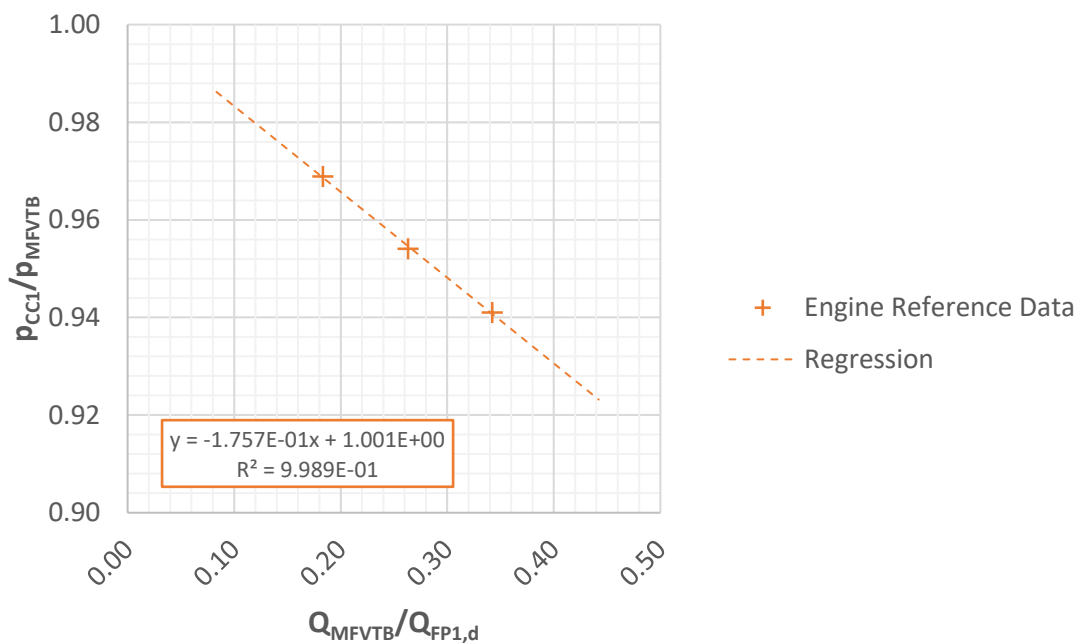

Figure B-3-2: Regression of cooling channel inlet pressure ratio

$$\frac{p_{CC1}}{p_{MFVTB}} = -0.1757 \times \left(\frac{Q_{MFVTB}}{Q_{FP1,d}}\right) + 1.001 \qquad \text{(B-3-10)}$$

$$\left(1 \geq \frac{p_{CC1}}{p_{MFVTB}} \geq 0\right)$$

Using Equation (B-3-10) to calculate mixer liquid inlet pressure provides one of two state quantities required to fully define the state of the fuel at the inlet of the cooling channel. Analysis of engine reference data indicates that the change in specific enthalpy is negligible between the MFVT bypass and the cooling channel inlet. Thus, it has been assumed that specific enthalpy remains constant between the MFVT bypass and the cooling channel inlet, as shown in Equation (B-3-11). With the

specific enthalpy and pressure at the cooling channel inlet established, the temperature at this point can be determined by interpolation of hydrogen property data tables, as described in Subsection 4.3.2.

$$h_{CC1} = h_{MFVTB} \qquad \text{(B-3-11)}$$

The specific enthalpy at the MFVT bypass, which is required to solve Equation (B-3-11), can be determined by interpolation of hydrogen property data tables, as described in Subsection 4.3.2. Equations (B-3-1) to (B-3-11) provide a full set of formulas required to establish an analytic model of the MFVT and associated plumbing.

B-4   Thrust Control Valve Model

In this sub-appendix, the development of the analytic model for the TCV is described. This model covers not only the valve itself but surrounding plumbing. Specifically, this model includes one "inlet" (the cooling channel discharge), and two "outlets" (the fuel turbine inlet and the gas inlet to the fuel mixer). Using flow through the TCV (and into the fuel turbine) as a control setting, the fuel properties and flow rates at the two outlets are estimated.

The fuel flowing out of the cooling channels either flows through the TCV and into the fuel turbine or bypasses the TCV and flows into the fuel mixer. The ratio of fuel flowing through the TCV to fuel bypassing the TCV is controlled by the valve setting. It has been assumed that the TCV setting can be adjusted to achieved the desired flow rate. With TCV flow (into the fuel turbine) as a control variable, and cooling channel discharge flow as an input from the cooling channel model, the flow bypassing the TCV (and into the gas fuel mixer inlet) can be determined using a simple mass balance, as shown in Equation (B-4-1).

$$\dot{m}_{M1G} = \dot{m}_{CC} - \dot{m}_{FT1} \qquad \text{(B-4-1)}$$

From the TCV bypass to the gas inlet to the mixer, there is a pressure drop due to either changing pipe cross-section geometry, friction through the pipe, or both. As described in Sub-appendix B-3, there is a correlation between pressure loss and volumetric flow rate, which can be used to model pressure loss across valves and pipes. Volumetric flow rate at the TCV bypass, which then flows into the gas inlet of the fuel mixer, can be calculated using Equation (B-4-2).

$$Q_{TCVB} = \frac{\dot{m}_{M1G}}{\rho_{TCVB}} \times 1,000 \qquad \text{(B-4-2)}$$

In order to solve Equation (B-4-2), the density at TCV bypass is required. For simplicity, it has been assumed that the properties of the fuel flow do not vary between the cooling channel discharge and the TCV bypass. Thus, temperature and pressure are constant between these points, as shown in Equations (B-4-3) and (B-4-4). Using these properties, density at the TCV bypass can be determined by interpolation of hydrogen property data tables, as described in Subsection 4.3.2.

$$p_{TCVB} = p_{CC2} \tag{B-4-3}$$
$$T_{TCVB} = T_{CC2} \tag{B-4-4}$$

Using the concept of "pressure ratio" as discussed in Sub-appendices B-1 and B-2 for modelling the pressure loss across a turbine, the pressure loss through the pipe can be quantified using a similar dimensionless ratio of discharge pressure to inlet pressure. Figure B-4-1 shows a chart of volumetric flow rate at the TCV bypass (normalized by the design FTP pump inlet volumetric flow rate) against the pressure ratio through the pipe from the TCV bypass to the mixer gas inlet at three different thrust levels (40%, 70% and 100%). Figure B-4-1 shows that the relationship between TCV bypass volumetric flow rate and pressure ratio is approximately linear.
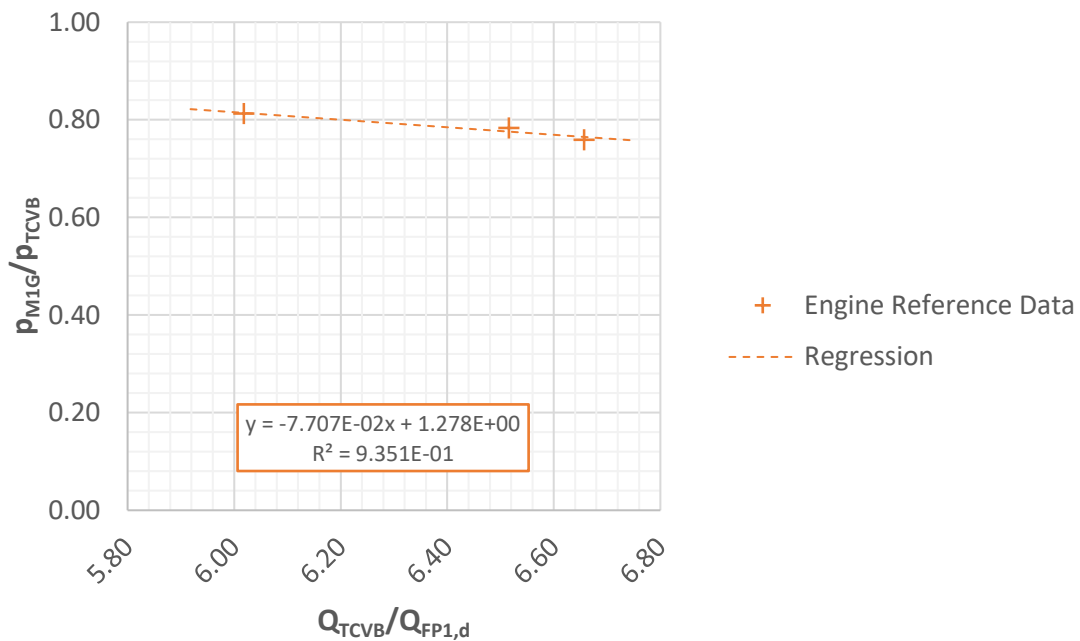

Figure B-4-1: Regression of mixer gas inlet pressure ratio.

A linear regression of the data in Figure B-4-1 has been performed, and the resulting trendline is also shown in Figure B-4-1. The trendline matches the data reasonably well ($R^2 = 0.9351$) and has therefore been adopted to model the relationship between volumetric flow rate and pressure ratio, as shown in Equation (B-4-5). In practice, the pressure ratio must be less than one as pressure is always

reduced as frictional forces act on the fluid. Additionally, the pressure ratio must be greater than or equal to zero because both pressures are absolute and therefore cannot be negative. Thus, the range of this function is all values of pressure ratio between zero and one. This is also shown in Equation (B-4-5).

$$\frac{p_{M1G}}{p_{TCVB}} = -0.07707 \times \left(\frac{Q_{TCVB}}{Q_{FP1,d}}\right) + 1.278 \tag{B-4-5}$$

$$\left(1 \geq \frac{p_{M1G}}{p_{TCVB}} \geq 0\right)$$

Using Equation (B-4-5) to calculate mixer liquid inlet pressure provides one of two state quantities required to fully define the state of the fuel at the gas inlet of the mixer. Analysis of engine reference data indicates that the change in specific enthalpy is negligible between the TCV bypass and the mixer gas inlet. Thus, it has been assumed that specific enthalpy remains constant between the TCV bypass and the mixer gas inlet, as shown in Equation (B-4-6). The specific enthalpy at the TCV bypass, which is required to solve Equation (B-4-6), can be determined by interpolation of hydrogen property data tables, as described in Subsection 4.3.2. With the specific enthalpy and pressure at the mixer liquid inlet established, the temperature at this point can also be determined by hydrogen table interpolation.

$$h_{M1G} = h_{TCVB} \tag{B-4-6}$$

A similar methodology to that which is described above can be used to estimate the properties of the fuel at the fuel turbine inlet. Specifically, a relationship between pressure ratio and volumetric flow rate can be established to estimate fuel turbine inlet pressure. Then, TCV inlet specific enthalpy can be used to estimate fuel turbine inlet specific enthalpy, which can be used with the pressure at this point to interpolate hydrogen property tables to estimate fuel turbine inlet temperature. The volumetric flow rate at the TCV inlet, which then flows into the fuel turbine, can be determined as shown in Equation (B-4-7).

$$Q_{TCV1} = \frac{\dot{m}_{FT1}}{\rho_{TCV1}} \times 1{,}000 \tag{B-4-7}$$

In order to solve Equation (B-4-7), the density at TCV inlet is required. For simplicity, it has been assumed that the properties of the fuel flow do not vary between the cooling channel discharge and the TCV inlet. Thus, temperature and pressure are constant between these points, as shown in

Equations (B-4-8) and (B-4-9). Using these properties, density at the TCV inlet can be determined by interpolation of hydrogen property data tables, as described in Subsection 4.3.2.

$$P_{TCV1} = P_{CC2} \qquad \text{(B-4-8)}$$
$$T_{TCV1} = T_{CC2} \qquad \text{(B-4-9)}$$

Figure B-4-2 shows the relationship between volumetric flow rate at the TCV inlet (normalized by the design FTP pump inlet volumetric flow rate) and the pressure ratio between the TCV inlet and fuel turbine inlet at three different thrust levels (40%, 70% and 100%). Figure B-4-2 shows that the relationship between TCV inlet volumetric flow rate and pressure ratio is approximately linear. A linear regression of this data set has been performed, and the resulting trendline is also shown in Figure B-4-2. The trendline matches the data very well ($R^2 = 1.000$), and as such the formula for this trendline has been adopted to model the relationship between TCV inlet volumetric flow rate and pressure ratio, as shown in Equation (B-4-10). In practice, the pressure ratio must be less than one as pressure is always reduced as frictional forces act on the fluid. Additionally, the pressure ratio must be greater than or equal to zero because both pressures are absolute and therefore cannot be negative. Thus, the range of this function is all values of pressure ratio between zero and one. This is also shown in Equation (B-4-10).
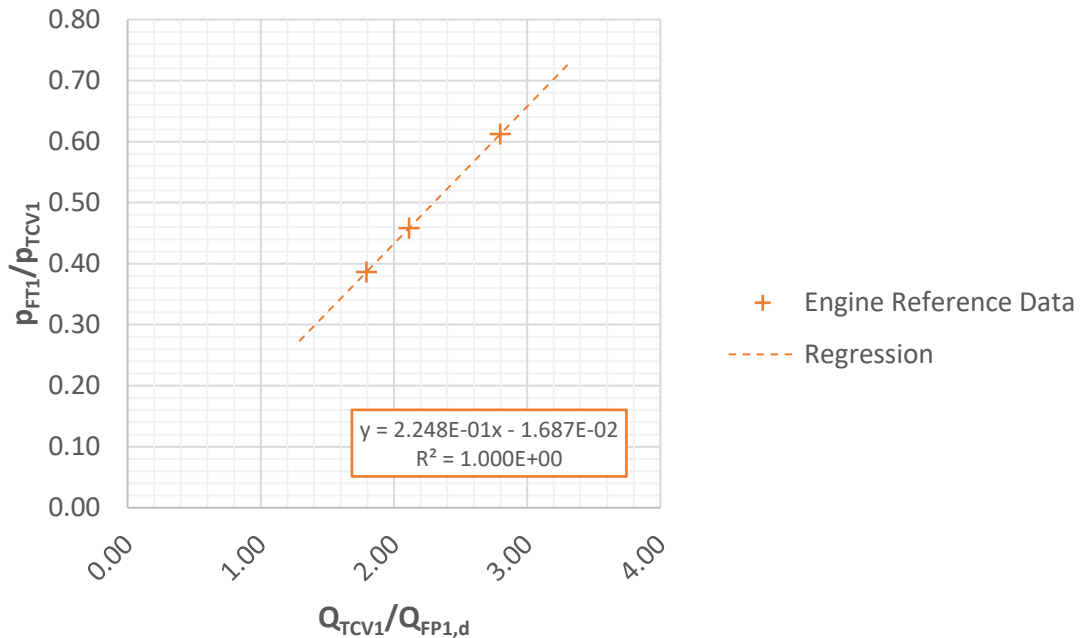

Figure B-4-2: Regression of fuel turbine inlet pressure ratio

$$\frac{p_{FT1}}{p_{TCV1}} = 0.2248 \times \left(\frac{Q_{TCV1}}{Q_{FP1,d}}\right) - 0.01687 \tag{B-4-10}$$

$$\left(1 \geq \frac{p_{FT1}}{p_{TCV1}} \geq 0\right)$$

Using Equation (B-4-10) to calculate fuel turbine inlet pressure provides one of two state quantities required to fully define the state of the fuel at the inlet of the fuel turbine. Analysis of engine reference data indicates that the change in specific enthalpy is negligible between the TCV inlet and the fuel turbine inlet. Thus, it has been assumed that specific enthalpy remains constant between the TCV inlet and the fuel turbine inlet, as shown in Equation (B-4-11). With the specific enthalpy and pressure at the fuel turbine inlet established, the temperature at this point can be determined by interpolation of hydrogen property data tables, as described in Subsection 4.3.2.

$$h_{FT1} = h_{TCV1} \tag{B-4-11}$$

The specific enthalpy at the TCV inlet, which is required to solve Equation (B-4-11), can be determined by interpolation of hydrogen property data tables, as described in Subsection 4.3.2. Equations (B-4-1) to (B-4-11) provide a full set of formulas required to establish an analytic model of the TCV and associated plumbing.

B-5 Mixture Ratio Control Valve Model

In this sub-appendix, the development of the analytic model for the MRCV is described. This model covers not only the valve itself but surrounding plumbing. Specifically, this model includes one "inlet" (the fuel turbine discharge), and two "outlets" (the oxidizer turbine inlet and the MRCV discharge). Using flow bypassing the MRCV (and into the oxidizer turbine) as a control setting, the fuel properties and flow rates at the two outlets are estimated.

The fuel flowing out of the fuel turbine either bypasses the MRCV and flows into the oxidizer turbine or flows through the MRCV and into the exhaust valve. The ratio of fuel flowing through the MRCV to fuel bypassing the MRCV is controlled by the valve setting. It has been assumed that the MRCV setting can be adjusted to achieved the desired flow rate. With MRCV bypass flow (into the oxidizer turbine) as a control variable, and fuel turbine discharge flow as an input from the fuel turbine model, the flow through the MRCV (and directly into the exhaust valve) can be determined using a simple mass balance, as shown in Equation (B-5-1).

$$\dot{m}_{MRCV} = \dot{m}_{FT2} - \dot{m}_{OT} \tag{B-5-1}$$

From the fuel turbine discharge to the oxidizer turbine inlet, there is a pressure drop due to either changing pipe cross-section geometry, friction through the pipe, or both. As described in Sub-appendix B-3, there is a correlation between pressure loss and volumetric flow rate, which can be used to model pressure loss through the pipes. Volumetric flow rate at fuel turbine discharge can be calculated using Equation (B-5-2). In order to solve Equation (B-5-2), the density at the fuel turbine discharge is required. Using the pressure and temperature at this point from the fuel turbine model, density at the fuel turbine discharge can be determined by interpolation of hydrogen property data tables, as described in Subsection 4.3.2.

$$Q_{FT2} = \frac{\dot{m}_{FT2}}{\rho_{FT2}} \times 1{,}000 \qquad (B\text{-}5\text{-}2)$$

Using the concept of "pressure ratio" as discussed in Sub-appendices B-1 and B-2 for modelling the pressure loss across a turbine, the pressure loss through the pipe can be quantified using a similar dimensionless ratio of discharge pressure to inlet pressure. Figure B-5-1 shows a chart of volumetric flow rate at the fuel turbine discharge (normalized by the design fuel pump inlet volumetric flow rate) against the pressure ratio through the pipe from the fuel turbine discharge to the oxidizer turbine inlet at three different thrust levels (40%, 70% and 100%). Figure B-5-1 shows that the relationship between fuel turbine discharge volumetric flow rate and pressure ratio is approximately linear.
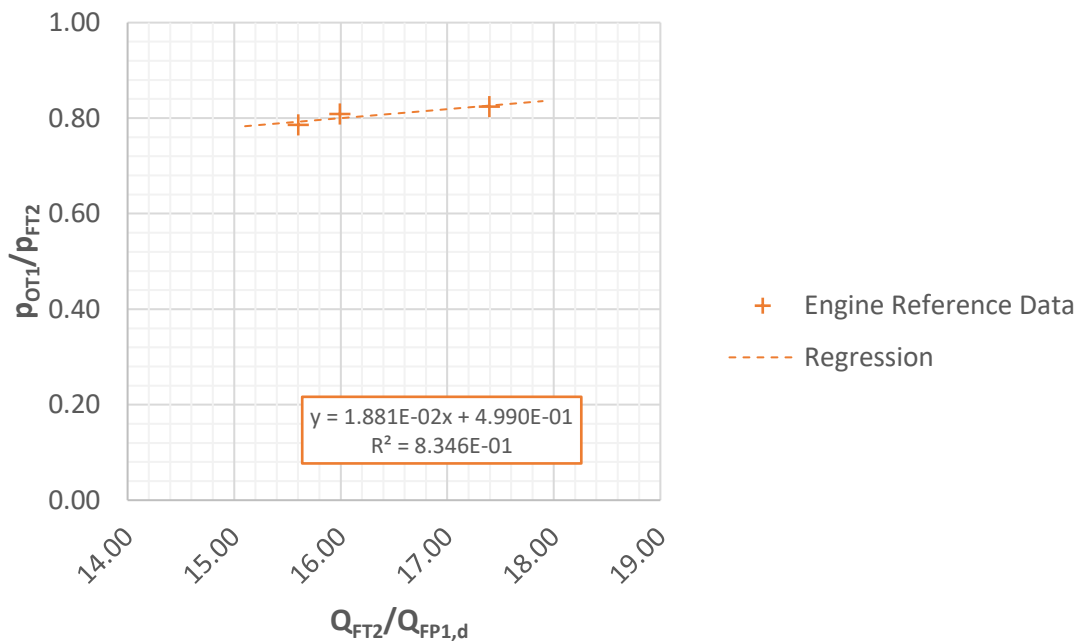

Figure B-5-1: Regression of MRCV pressure ratio

A linear regression of the data in Figure B-5-1 has been performed, and the resulting trendline is also shown in Figure B-5-1. The trendline matches the data reasonably well ($R^2 = 0.8346$). This trendline has been adopted to model the relationship between volumetric flow rate and pressure ratio, as shown in Equation (B-5-3). In practice, the pressure ratio must be less than one as pressure is always reduced as frictional forces act on the fluid. Additionally, the pressure ratio must be greater than or equal to zero because both pressures are absolute and therefore cannot be negative. Thus, the range of this function is all values of pressure ratio between zero and one. This is also shown in Equation (B-5-3).

$$\frac{p_{OT1}}{p_{FT2}} = 0.01881 \times \left(\frac{Q_{FT2}}{Q_{FP1,d}}\right) + 0.4990 \qquad \text{(B-5-3)}$$

$$\left(1 \geq \frac{p_{OT1}}{p_{FT2}} \geq 0\right)$$

Using Equation (B-5-3) to calculate oxidizer turbine inlet pressure provides one of two state quantities required to fully define the state of the fuel at the oxidizer turbine inlet. Analysis of engine reference data indicates that the change in temperature is negligible between the fuel turbine discharge and the oxidizer turbine inlet. Thus, it has been assumed that temperature remains constant between the fuel turbine discharge and the oxidizer turbine inlet, as shown in Equation (B-5-4).

$$T_{OT1} = T_{FT2} \qquad \text{(B-5-4)}$$

There is no data in available literature for the properties at the MRCV inlet. Thus, due to its proximity to the oxidizer turbine inlet, it has been assumed that the properties of the fuel do not vary significantly between these two points. The temperature and pressure at the MRCV inlet are therefore assumed to be equal to the temperature and pressure at the oxidizer turbine inlet, as shown in Equations (B-5-5) and (B-5-6). Equations (B-5-1) to (B-5-6) provide a full set of formulas required to establish an analytic model of the MRCV and associated plumbing.

$$p_{MRCV1} = p_{OT1} \qquad \text{(B-5-5)}$$
$$T_{MRCV1} = T_{OT1} \qquad \text{(B-5-6)}$$

B-6 Turbine Exhaust Valve Model

In this section, the development of the analytic model for the turbine exhaust valve is discussed. This model covers not only the valve itself but surrounding plumbing. Specifically, this model includes two "inlets" (the oxidizer turbine discharge and the MRCV inlet), and one "outlet" (the exhaust valve).

The fuel flowing out of the oxidizer turbine is mixed with the fuel flowing from the MRCV and expelled from the engine through the exhaust valve. The flow through the exhaust valve can therefore be determined using a simple mass balance, as shown in Equation (B-6-1).

$$\dot{m}_{EV} = \dot{m}_{MRCV} + \dot{m}_{OT} \tag{B-6-1}$$

From the oxidizer turbine discharge and MRCV discharge to the exhaust valve, there is a pressure drop due to either changing pipe cross-section geometry, friction through the pipe, or both. As described in Sub-appendix B-3, there is a correlation between pressure loss and volumetric flow rate, which can be used to model pressure loss through the pipes. Volumetric flow rate at the oxidizer turbine discharge can be calculated using Equation (B-6-2). In order to solve Equation (B-6-2), the density at the oxidizer turbine discharge is required. Using the pressure and temperature at this point from the oxidizer turbine model, density at the oxidizer turbine discharge can be determined by interpolation of hydrogen property data tables, as described in Subsection 4.3.2.

$$Q_{OT2} = \frac{\dot{m}_{OT}}{\rho_{OT2}} \times 1{,}000 \tag{B-6-2}$$

In a similar fashion, the volumetric flow rate at the MRCV inlet can be determined as shown in Equation (B-6-3). In order to solve Equation (B-6-3), the density at the oxidizer turbine discharge is required. Using the pressure and temperature at this point from the oxidizer turbine model, density at the oxidizer turbine discharge can be determined by interpolation of hydrogen property data tables, as described in Subsection 4.3.2.

$$Q_{MRCV1} = \frac{\dot{m}_{MRCV}}{\rho_{MRCV1}} \times 1{,}000 \tag{B-6-3}$$

The relative flow rates from the "inlet" streams could be a variable affecting exhaust valve discharge pressure. In most instances, most of the exhaust valve flow is attributable to oxidizer turbine discharge, rather than MRCV discharge. Indeed, it may be possible to operate the engine with the MRCV completely shut-off. As such, the "pressure ratio" between the oxidizer turbine discharge and the exhaust valve is considered to be a more significant predictor of exhaust valve pressure than the "pressure ratio" between the MRCV inlet and exhaust valve. Figure B-6-1 shows the relationship between the relative flow rate (between the MRCV and oxidizer turbine) and the turbine discharge to exhaust valve pressure ratio at three different thrust levels (40%, 70% and 100%).
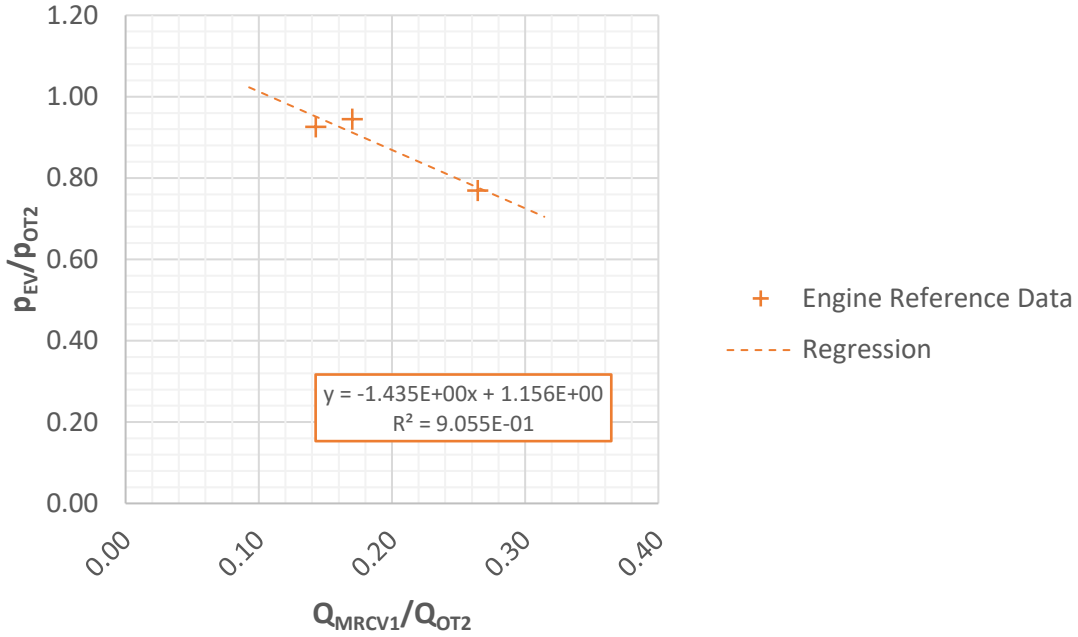
Figure B-6-1: Regression of exhaust valve pressure ratio

Figure B-6-1 shows that the relationship between relative volumetric flow rate and pressure ratio is approximately linear. A linear regression of this data set has been performed, and the resulting trendline is also shown in Figure B-6-1. The trendline matches the data well ($R^2 = 0.9055$), and as such the formula for this trendline has been adopted to model the relationship between relative volumetric flow rate and exhaust valve pressure ratio, as shown in Equation (B-6-4). In practice, the pressure ratio must be less than one as pressure is always reduced as frictional forces act on the fluid. Additionally, the pressure ratio must be greater than or equal to zero because both pressures are absolute and therefore cannot be negative. Thus, the range of this function is all values of pressure ratio between zero and one. This is also shown in Equation (B-6-4).

$$\frac{p_{EV}}{p_{OT2}} = -1.435 \times \left(\frac{Q_{MRCV1}}{Q_{OT2}}\right) + 1.156 \qquad \text{(B-6-4)}$$

$$\left(1 \geq \frac{p_{EV}}{p_{OT2}} \geq 0\right)$$

Using Equation (B-6-4) to calculate exhaust valve pressure provides one of two state quantities required to fully define the state of the fuel at the exhaust valve. Analysis of engine reference data indicates that the change in net enthalpy flux is negligible between the two "inlets" (oxidizer turbine discharge & MRCV inlet) and the single "outlet" (exhaust valve) at all three thrust levels (40%, 70% and 100%). Thus, it has been assumed that net enthalpy flux remains constant between these points, as shown in Equation (B-6-5). With the specific enthalpy and pressure at the exhaust valve established,

the temperature at this point can be determined by interpolation of hydrogen property data tables, as described in Subsection 4.3.2.

$$h_{EV} \dot{m}_{EV} = h_{MRCV1} \dot{m}_{MRCV} + h_{OT2} \dot{m}_{OT}$$

$$\Rightarrow \qquad h_{EV} = \frac{h_{MRCV1} \dot{m}_{MRCV} + h_{OT2} \dot{m}_{OT}}{\dot{m}_{EV}} \qquad \text{(B-6-5)}$$

The specific enthalpy at the oxidizer turbine discharge and MRCV inlet, which are required to solve Equation (B-6-5), can be determined by interpolation of hydrogen property data tables, as described in Subsection 4.3.2. Equations (B-6-1) to (B-6-5) provide a full set of formulas required to establish an analytic model of the exhaust valve and associated plumbing.

B-7 Mixer & Injector Model

In this sub-appendix, the development of the analytic model for the fuel mixer and both the fuel and oxidizer injectors is described. This model covers not only the mixer and injectors themselves but also surrounding plumbing, including the fuel and oxidizer manifolds. This model includes two separate control volumes – one each for the fuel and oxidizer flows.

The fuel control volume includes two "inlets" (the liquid and gas inlets to the fuel mixer), and one "outlet" (the fuel injectors). The liquid and gas fuel streams are combined in the mixer, then flow through the fuel manifold and finally into the injectors. Assuming the fuel flows evenly into all injectors, the flow through a single fuel injector element can be determined using a simple mass balance, as shown in Equation (B-7-1).

$$\dot{m}_{FI} = \frac{\dot{m}_{M1L} + \dot{m}_{M1G}}{i} \qquad \text{(B-7-1)}$$

The relative volumetric flow rates into the fuel mixer has been selected as a metric for modelling mixer performance. Specifically, the ratio of liquid-to-gas inlet volumetric flow rates is used to predict losses in pressure and specific enthalpy through the fuel mixer, manifold and injectors. The volumetric flow rates at the liquid and gas fuel mixer inlets can be determined as shown in Equations (B-7-2) and (B-7-3), respectively. The density values required to solve Equations (B-7-2) and (B-7-3) can be determined by interpolation of hydrogen property data tables, as described in Subsection 4.3.2.

$$Q_{M1L} = \frac{\dot{m}_{M1L}}{\rho_{M1L}} \times 1,000 \qquad \text{(B-7-2)}$$

$$Q_{M1G} = \frac{\dot{m}_{M1G}}{\rho_{M1G}} \times 1{,}000 \tag{B-7-3}$$

In order to model the pressure loss across the fuel mixer and injector, a function accounting for the ratio of inlet volumetric flow rates, as well as the pressure at both inlets is required. Figure B-7-1 shows the relationship between the volumetric flow ratio and the ratio of the square of injector discharge pressure divided by the product of the inlet pressures at three different thrust levels (40%, 70% and 100%). This pressure ratio was selected as a metric because it provides a dimensionless method of relating the single outlet pressure with the two inlet pressures. It also results in a data set that can be accurately modelled with a linear regression ($R^2 = 0.9948$), as the trendline in Figure B-7-1 indicates. The function for this regression trendline has thereby been adopted to model the relationship between inlet volumetric flow rate ratio and pressure loss across the mixer and injector, as shown in Equation (B-7-4). In practice, the pressure ratio must be greater than or equal to zero because both pressures are absolute and therefore cannot be negative. Thus, the range of this function is all values of pressure ratio between zero and one. This is also shown in Equation (B-7-4).
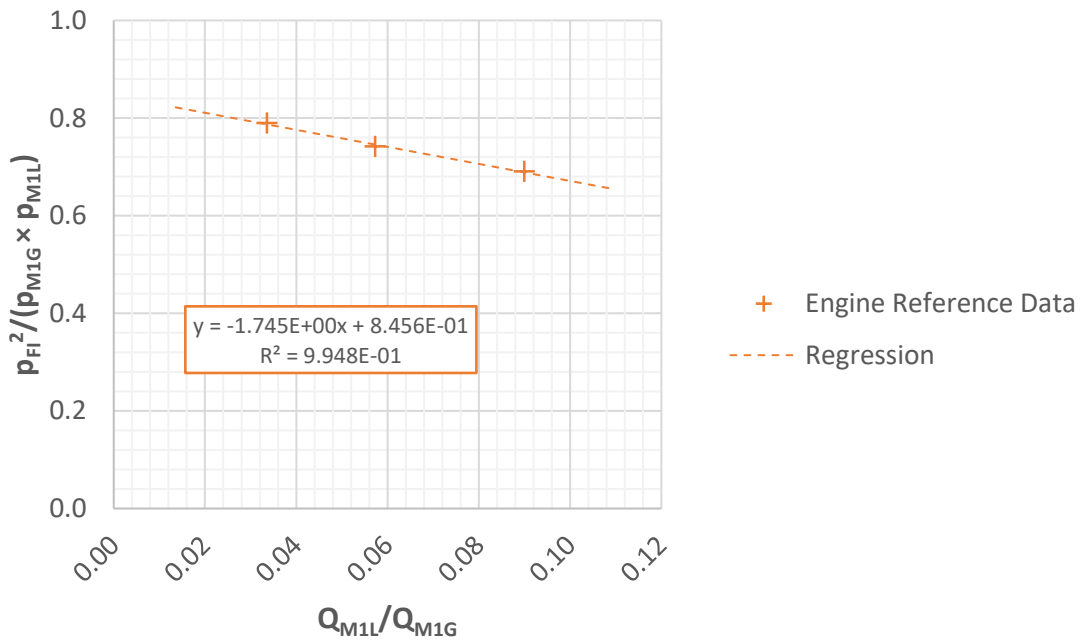
Figure B-7-1: fuel mixer and injector pressure loss

$$\frac{p_{FI}{}^2}{p_{M1G} \times p_{M1L}} = -1.745 \times \left(\frac{Q_{M1L}}{Q_{M1G}}\right) + 0.8456 \tag{B-7-4}$$

$$\left(\frac{p_{FI}{}^2}{p_{M1G} \times p_{M1L}} \geq 0\right)$$

Using Equation (B-7-4) to calculate fuel injector discharge pressure provides one of two state quantities required to fully define the state of the fuel at the injector discharge. Analysis of engine reference data indicates that the change in enthalpy from the mixer inlets to the injector discharge is not negligible. The net enthalpy flux at the mixer inlet (defined as the sum of liquid and gas inlet mass flow rates, multiplied by their respective enthalpies) has been calculated using engine test data at three different thrust levels (40%, 70% and 100%). The net enthalpy flux at the fuel injectors has also been calculated using a similar method. The ratio of these net "outlet-to-inlet" enthalpies is plotted against the inlet volumetric flow ratio in Figure B-7-2.
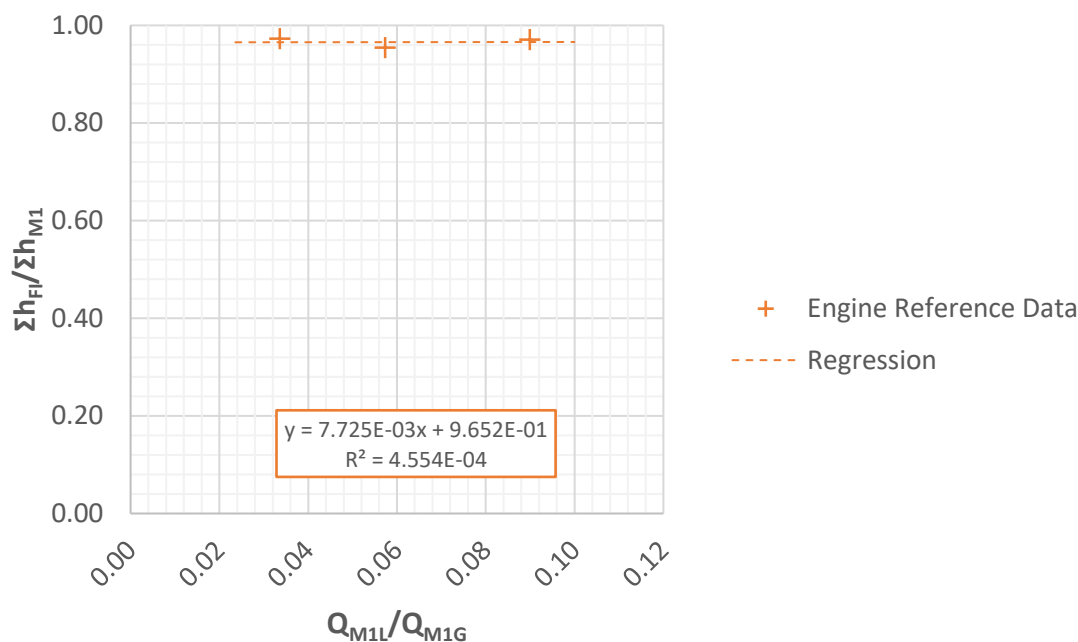
Figure B-7-2: Fuel mixer and injector specific enthalpy loss

Figure B-7-2 shows that a small reduction in net enthalpy flux occurs between the mixer inlets and the injectors, and the relationship to inlet volumetric flow rate is approximately constant. Therefore, a linear regression is used to fit this data to a trendline. The trendline does not fit the data particularly well ($R^2 = 0.4554$), but this is considered acceptable as Figure B-7-2 shows that the enthalpy reduction is roughly constant. This trendline has been adopted to model the relationship between mixer inlet volumetric flow rates and net enthalpy loss in the mixer and injector, as shown in Equation (B-7-5). In practice, the net enthalpy flux ratio must be less than one as there is no mechanism for increasing fluid enthalpy in the injectors or mixer. Thus, only losses in enthalpy can be expected from the inlets to the outlet. The range of this function is all values of enthalpy flux ratio is therefore less than one. This is also shown in Equation (B-7-5). With the specific enthalpy and pressure at the fuel injector established, the temperature at this point can be determined by interpolation of hydrogen property data tables, as described in Subsection 4.3.2.

$$\frac{\sum h_{FI}}{\sum h_{M1}} = \frac{i h_{FI} \dot{m}_{FI}}{h_{M1L} \dot{m}_{M1L} + h_{M1G} \dot{m}_{M1G}} = 0.007725 \times \left(\frac{Q_{M1L}}{Q_{M1G}}\right) + 0.9652 \qquad \text{(B-7-5)}$$

$$\left(1 \geq \frac{\sum h_{FI}}{\sum h_{M1}}\right)$$

The average flow speed of fuel at the injector can be determined using the fuel injector mass flow rate, the fuel injector discharge area and the density of the fuel at the injector. The density at this point can be determined by interpolation of hydrogen property data tables, as described in Subsection 4.3.2. The resulting formula for injector flow speed is shown in Equation (B-7-6).

$$u_{FI,avg} = \frac{\dot{m}_{FI}}{\rho_{FI} A_{FI}} \qquad \text{(B-7-6)}$$

The oxidizer control volume includes one "inlet" (the oxidizer pump discharge), and one "outlet" (the oxidizer injectors). Assuming the oxidizer flows evenly into all injectors, the flow through a single oxidizer injector element can therefore be determined using a simple mass balance, as shown in Equation (B-7-7).

$$\dot{m}_{OI} = \frac{\dot{m}_{OP}}{i} \qquad \text{(B-7-7)}$$

The volumetric flow rate at the oxidizer pump discharge has been selected as a metric for modelling performance of the injector and related plumbing, such as the oxidizer manifold. The volumetric flow rate at the oxidizer pump discharge can be determined as shown in Equation (B-7-8). The density value required to solve Equation (B-7-8) can be determined by interpolation of oxygen property data tables, as described in Subsection 4.3.2.

$$Q_{OP2} = \frac{\dot{m}_{OP}}{\rho_{OP2}} \times 1,000 \qquad \text{(B-7-8)}$$

Figure B-7-3 shows the relationship between oxidizer injector pressure ratio (defined as oxidizer injector discharge pressure divided by oxidizer pump discharge pressure) and pump discharge volumetric flow rate (normalized by the design oxidizer pump inlet volumetric flow rate) at three different thrust levels (40%, 70% and 100%). It can be seen in Figure B-7-3 that a linear regression fits this data accurately ($R^2 = 0.9955$). Thus, the formula for this regression trendline has been adopted to model the relationship between oxidizer pump discharge flow rate and oxidizer injector pressure ratio, as shown in Equation (B-7-9). In practice, the pressure ratio must be less than one as pressure is always reduced as frictional forces act on the fluid. Additionally, the pressure ratio must be greater

than or equal to zero because both pressures are absolute and therefore cannot be negative. Thus, the range of this function is all values of pressure ratio between zero and one. This is also shown in Equation (B-7-9).
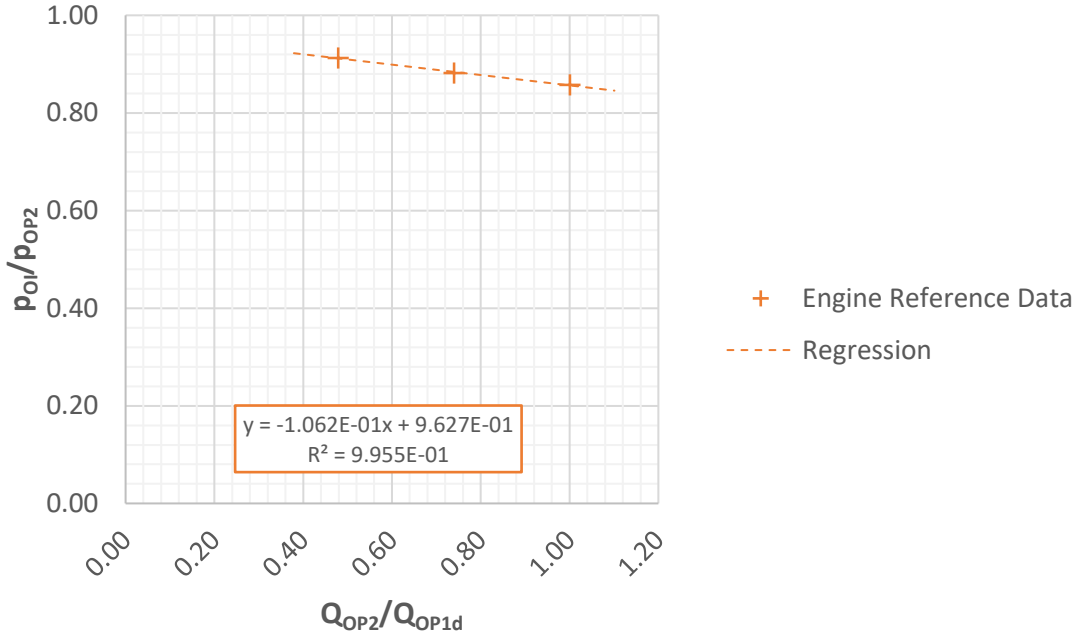

Figure B-7-3: Oxidizer injector pressure loss

$$\frac{p_{OI}}{p_{OP2}} = -0.1062 \times \left(\frac{Q_{OP2}}{Q_{OP1d}}\right) + 0.9627 \tag{B-7-9}$$

$$\left(1 \geq \frac{p_{OI}}{p_{OP2}} \geq 0\right)$$

Using Equation (B-7-9) to calculate oxidizer injector discharge pressure provides one of two state quantities required to fully define the state of the oxidizer at the injectors. Analysis of engine reference data indicates that the change in specific enthalpy is negligible between the oxidizer turbine discharge and the oxidizer injector. Thus, it has been assumed that specific enthalpy remains constant between the oxidizer pump discharge and the oxidizer injector, as shown in Equation (B-7-10). With the specific enthalpy and pressure at the oxidizer injector established, the temperature at this point can be determined by interpolation of oxygen property data tables, as described in Subsection 4.3.2. The specific enthalpy at the oxidizer pump discharge, which is required to solve Equation (B-7-10), can be determined by interpolation of oxygen property data tables, as described in Subsection 4.3.2.

$$h_{OI} = h_{OP2} \tag{B-7-10}$$

The average flow velocity of oxidizer at the injector can be determined using the oxidizer injector mass flow rate, the fuel injector discharge area and the density of the fuel at the injector. The density at this point can be determined by interpolation of oxygen property data tables, as described in Subsection 4.3.2. The resulting formula for injector flow speed is shown in Equation (B-7-11).

$$u_{OI,avg} = \frac{\dot{m}_{OI}}{\rho_{OI} A_{OI}}$$
(B-7-11)

Equations (B-7-1) to (B-7-11) provide a full set of formulas required to establish an analytic model of the exhaust valve and associated plumbing.

Appendix C   Optimization Charts

C-1   Optimization of Cycles to Plastic Instability
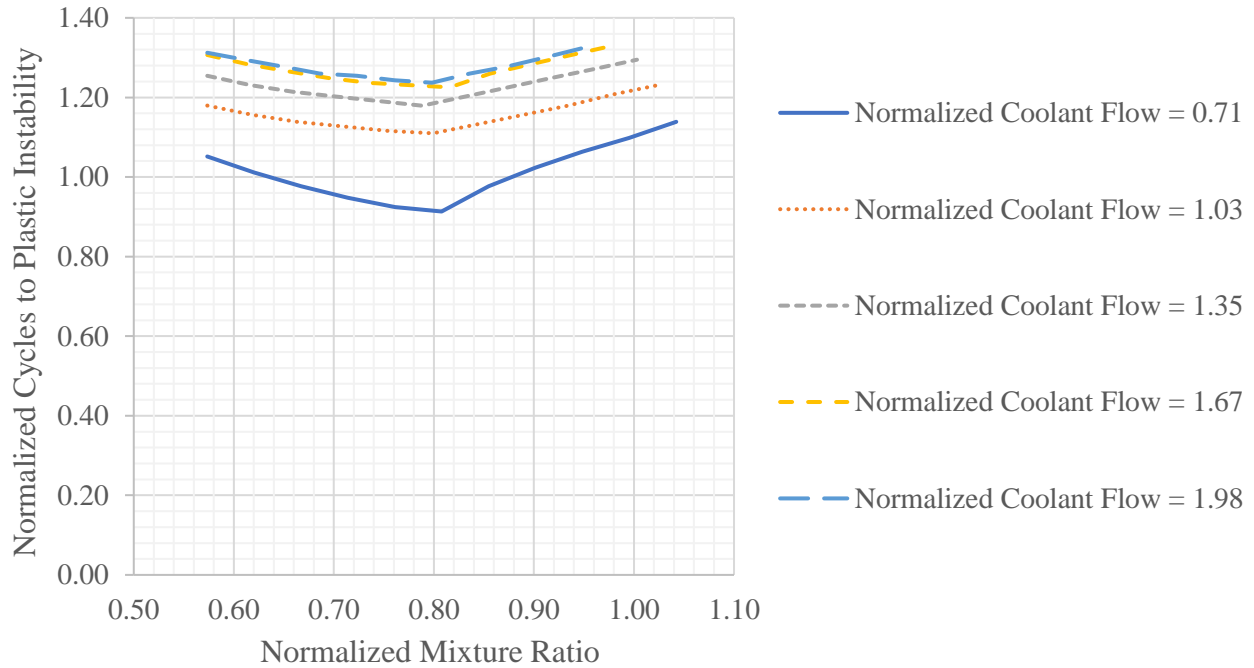
Figure C-1-1: Optimization of plastic instability life at a normalized coolant pressure of 0.834
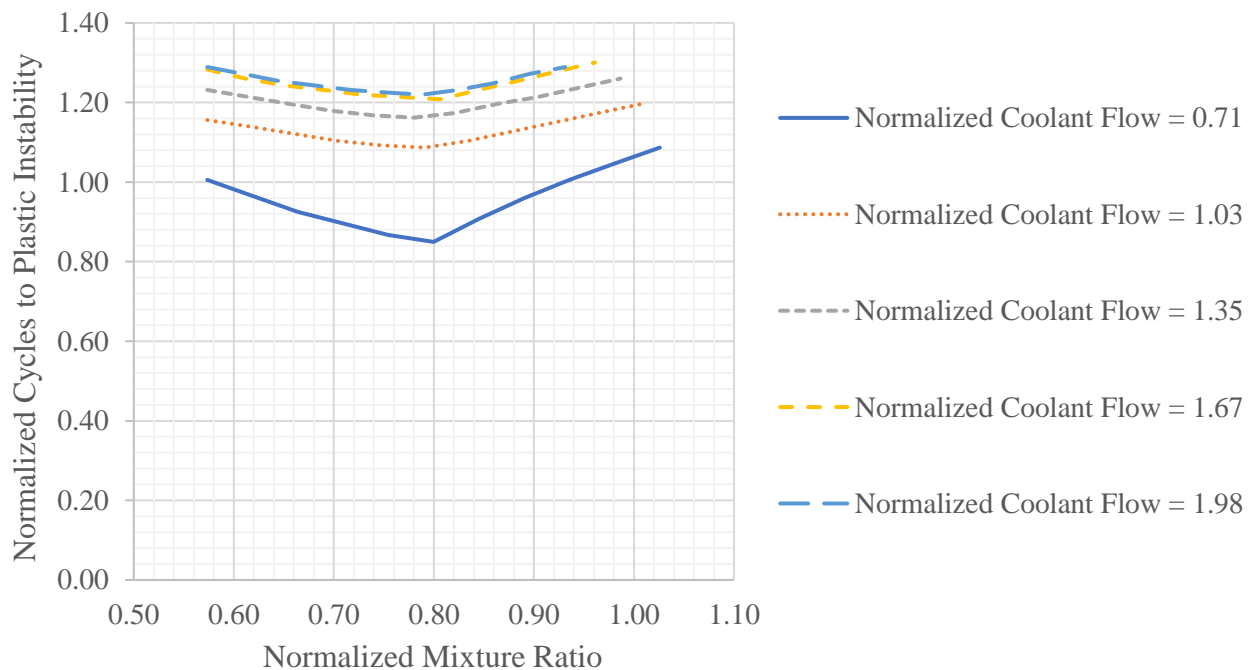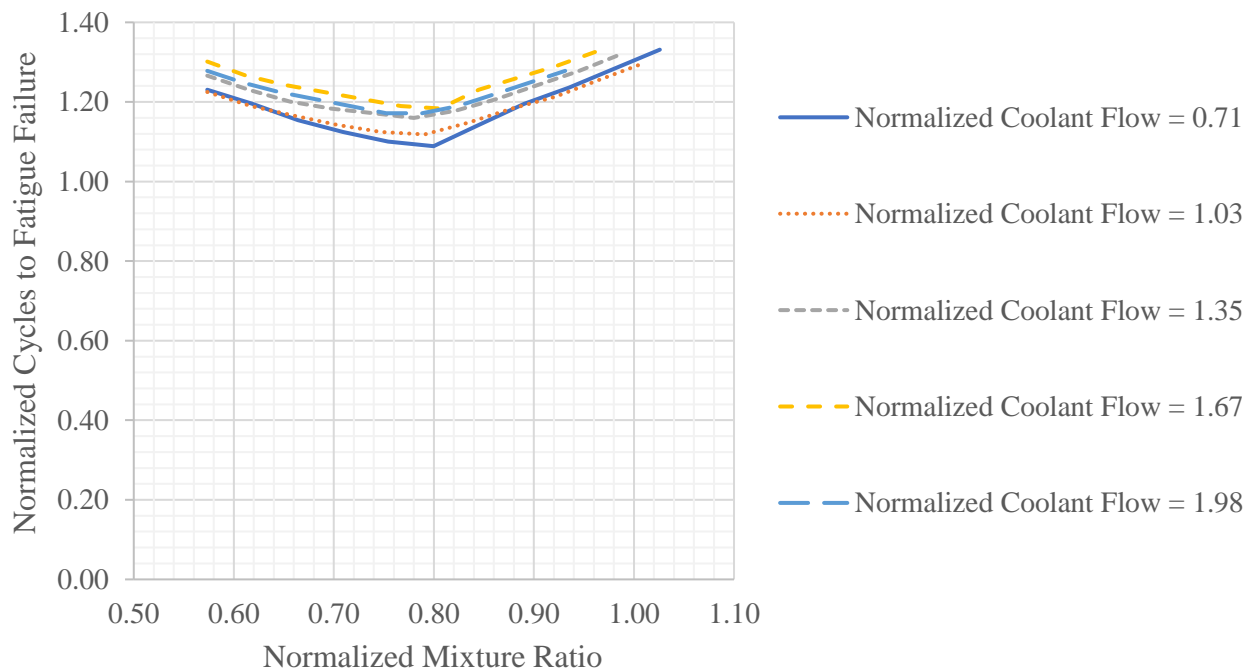

Figure C-1-2: Optimization of plastic instability life at a normalized coolant pressure of 0.951

Normalized Coolant Pressure = 1.068
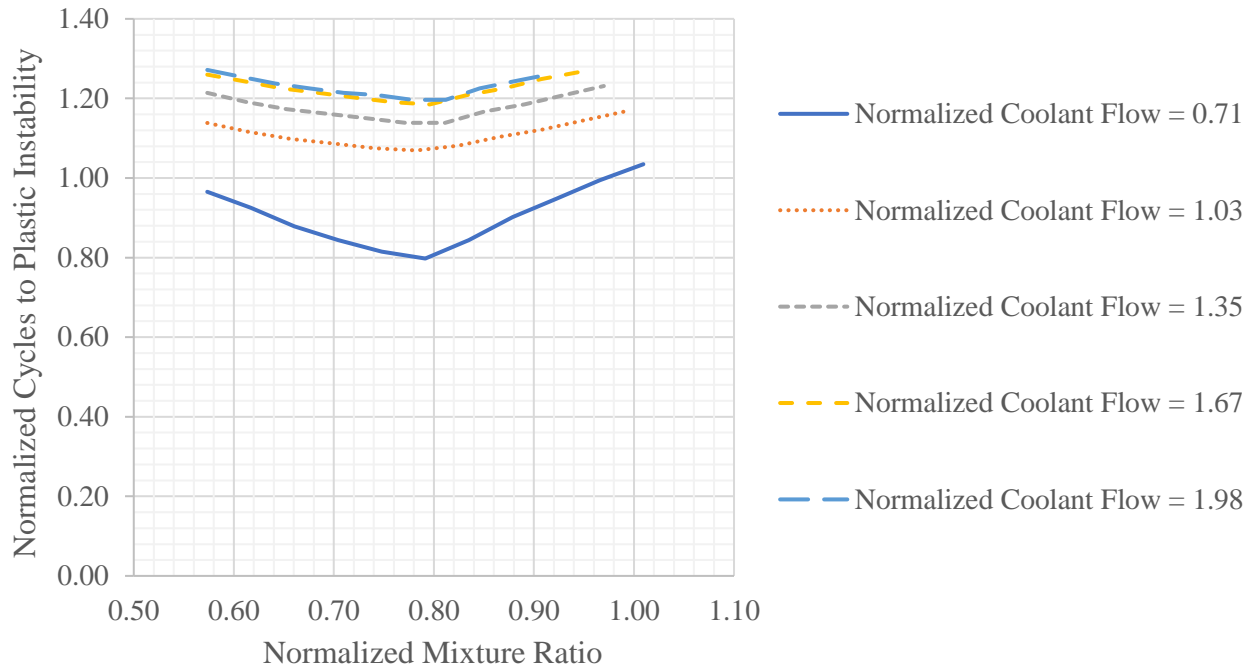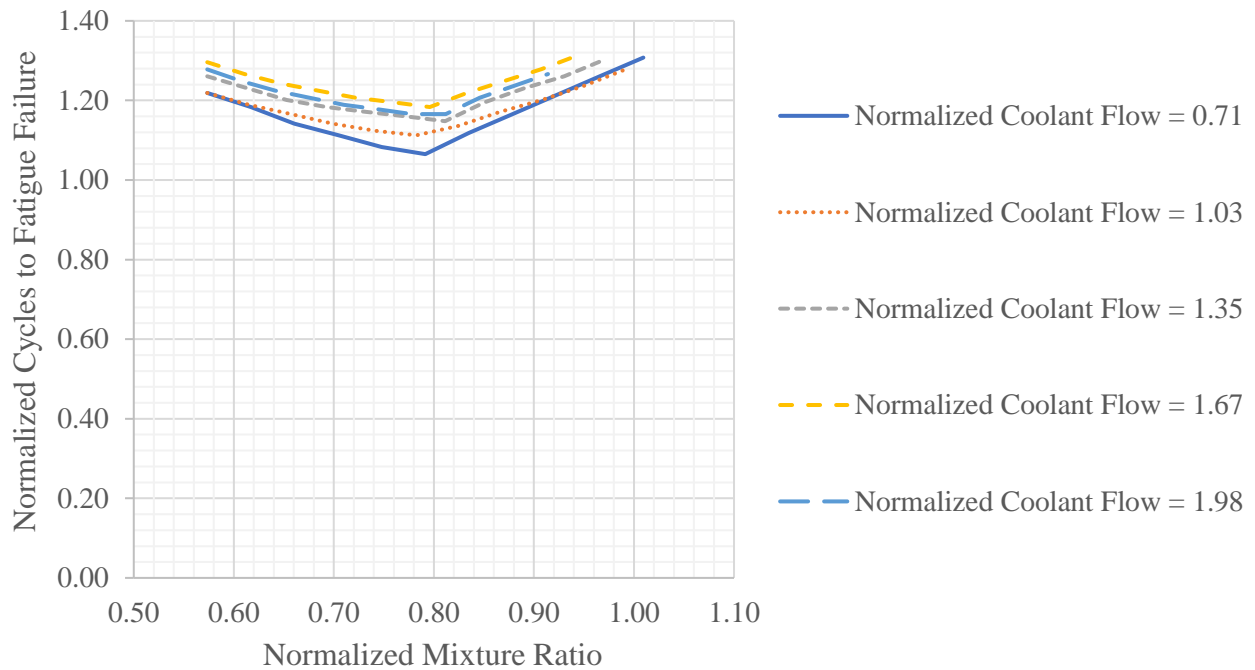

Figure C-1-3: Optimization of plastic instability life at a normalized coolant pressure of 1.068

Normalized Coolant Pressure = 1.185
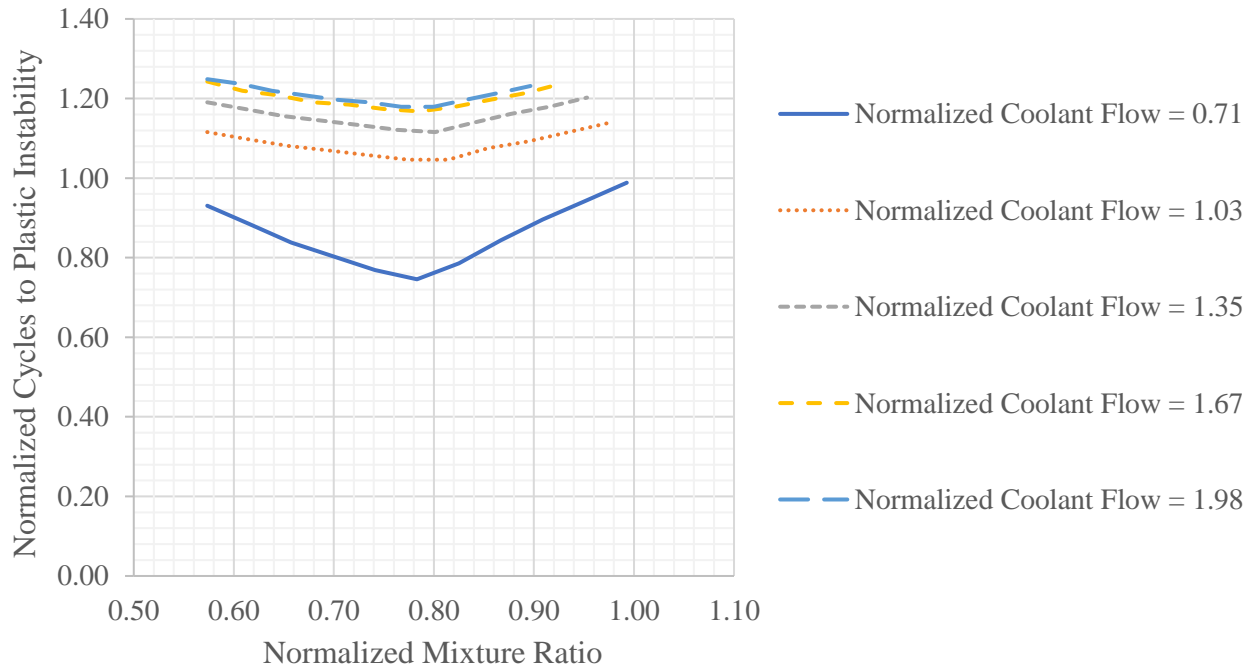
Figure C-1-4: Optimization of plastic instability life at a normalized coolant pressure of 1.185

C-2   Optimization of Cycles to Fatigue Failure

Normalized Coolant Pressure = 0.834
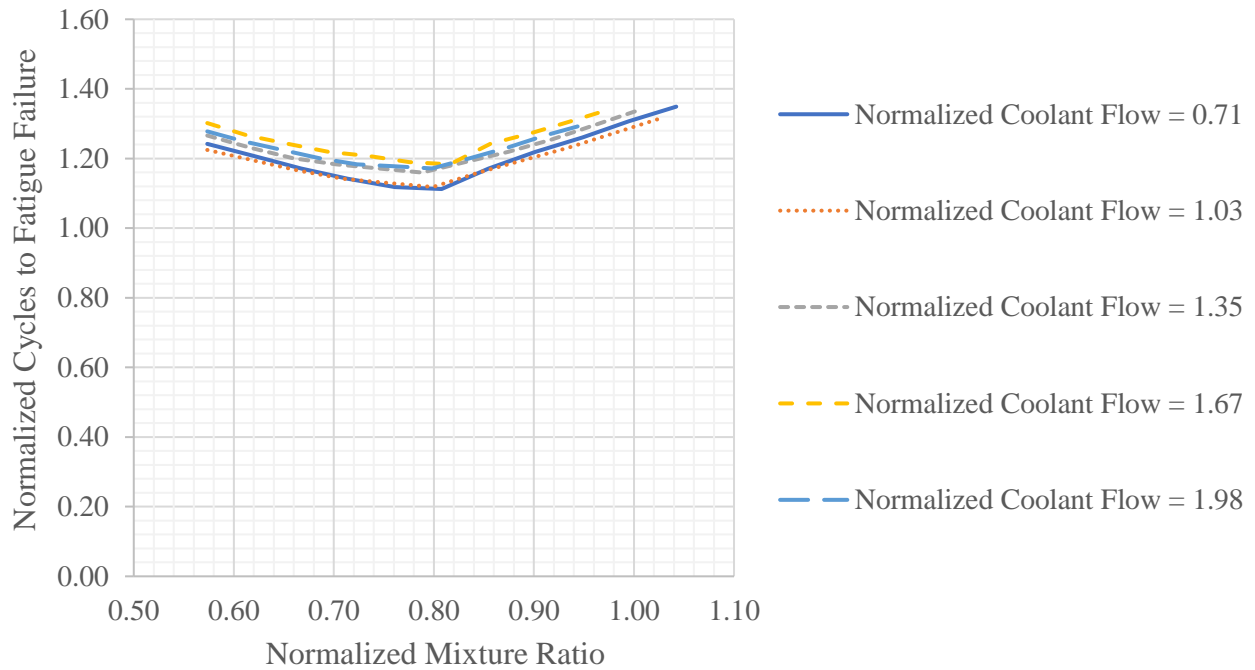
Figure C-2-1: Optimization of fatigue life at a normalized coolant pressure of 0.834
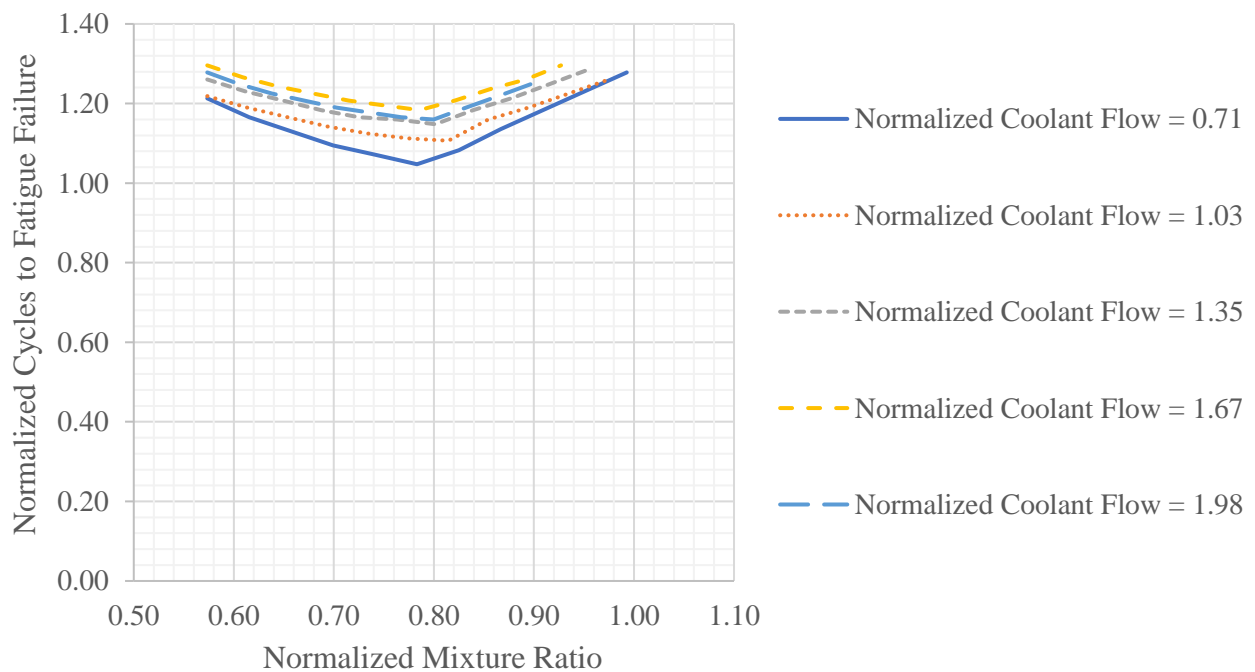
Normalized Coolant Pressure = 0.951

Figure C-2-2: Optimization of fatigue life at a normalized coolant pressure of 0.951

Normalized Coolant Pressure = 1.068

Figure C-2-3: Optimization of fatigue life at a normalized coolant pressure of 1.068

Normalized Coolant Pressure = 1.185

Figure C-2-4: Optimization of fatigue life at a normalized coolant pressure of 1.185

C-3 Optimization of Cycles to Creep Failure
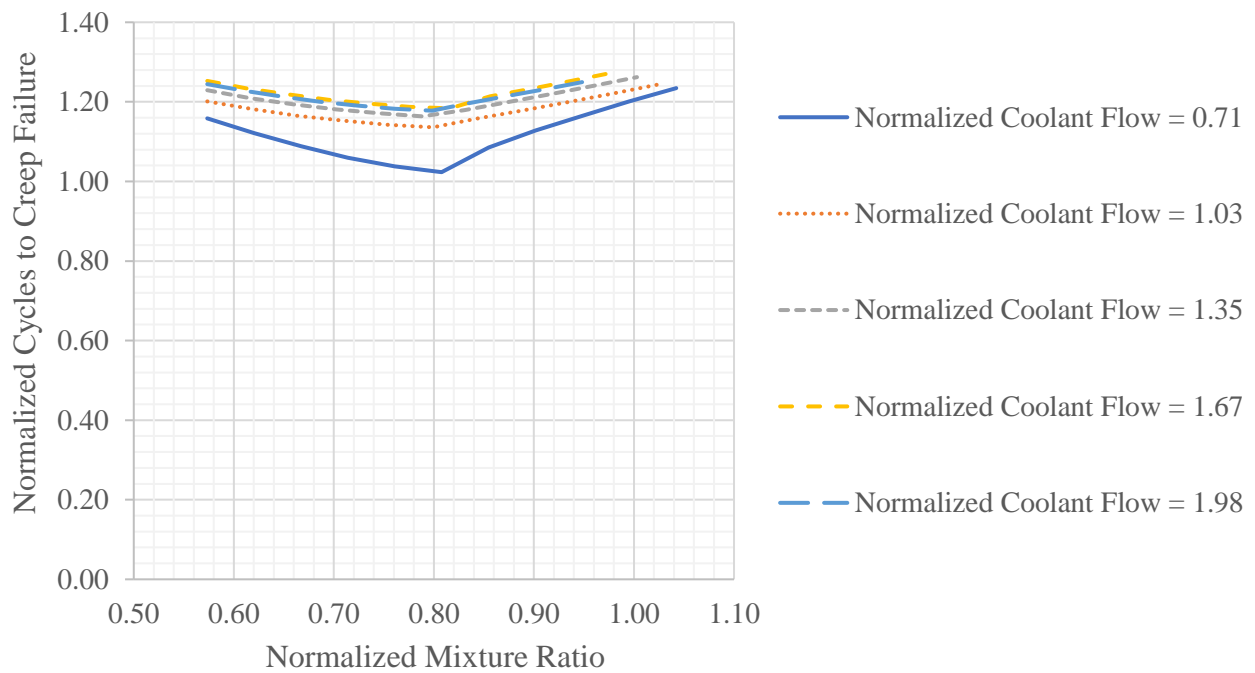
Normalized Coolant Pressure = 0.834

Figure C-3-1: Optimization of creep life at a normalized coolant pressure of 0.834

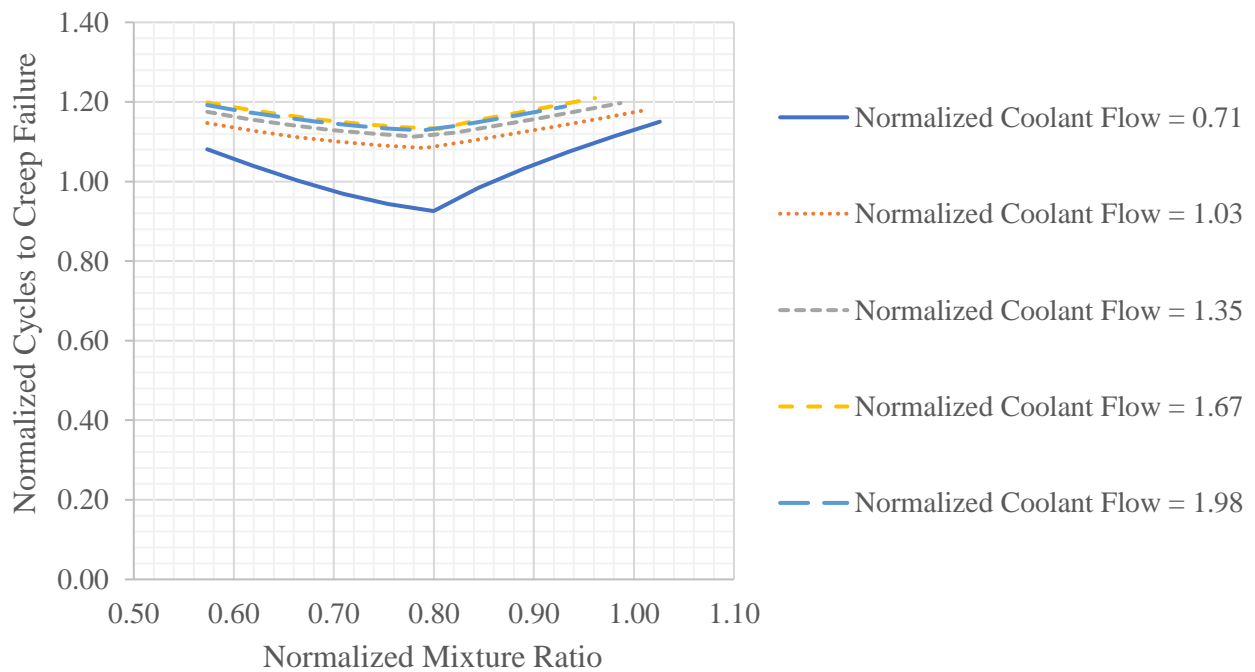### Normalized Coolant Pressure = 0.951

Figure C-3-2: Optimization of creep life at a normalized coolant pressure of 0.951

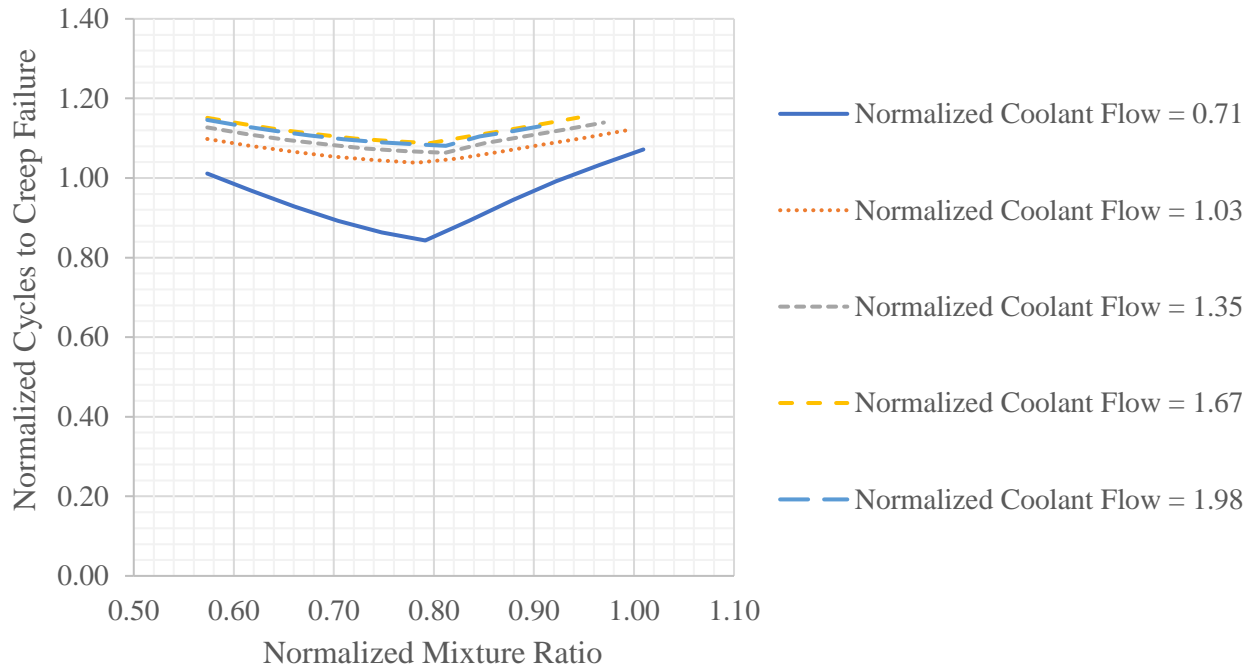## Normalized Coolant Pressure = 1.068

Figure C-3-3: Optimization of creep life at a normalized coolant pressure of 1.068

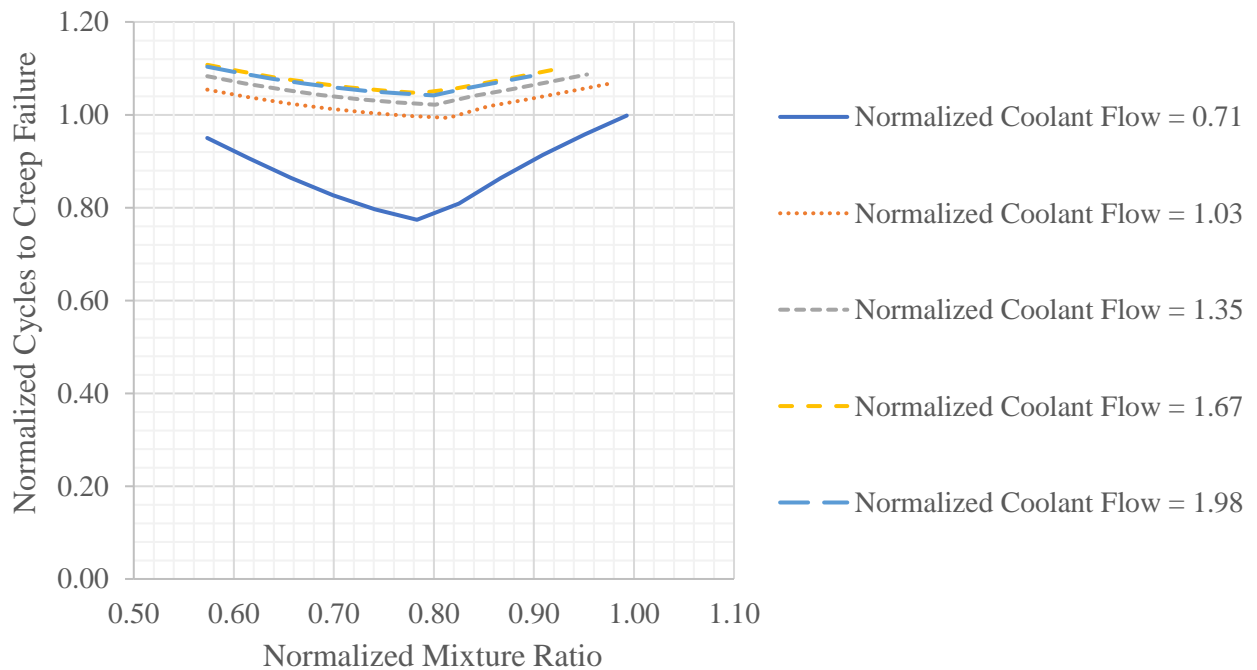## Normalized Coolant Pressure = 1.185

Figure C-3-4: Optimization of creep life at a normalized coolant pressure of 1.185